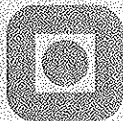


Tore Børvik
**Ballistic Penetration and
Perforation of Steel Plates**

NTNU Trondheim
Norges teknisk-naturvitenskapelige
universitet

Doktor ingeniøravhandling 2000:124
Institutt for konstruksjonsteknikk



669:539,37 B99b

Tore Børvik

**Ballistic Penetration and Perforation
of Steel Plates**

Universitetsbiblioteket i Trondheim
Teknisk hovedbibliotek
Trondheim

Dr. ing. thesis

Structural Impact Laboratory (SIMLab)
Department of Structural Engineering
Norwegian University of Science and Technology
N-7491 Trondheim
Norway

December 2000

CONTENTS

Abstract	5
Acknowledgement	7
Synopsis	9
1. Background	9
2. A Short Introduction to Impact Dynamics	11
3. The Generic Penetration Problem	16
4. Overall Objectives and Method of Research	18
5. Organisation and Summary of the Thesis Work	20
6. Some Main Results	25
7. Concluding Remarks	29
8. Suggestions for Further Work	30
References / Bibliography	31

Part I

T. Børvik, K. Holen, M. Langseth and K.A. Malo,
An experimental set-up used in ballistic penetration.
Proceedings of Fifth International Symposium on Structures under Shock and Impact,
pp. 683 - 692, Thessaloniki, Greece, 24 – 26 June, 1998.

Part II

T. Børvik, M. Langseth, O.S. Hopperstad and K.A. Malo,
Ballistic penetration of steel plates.
International Journal of Impact Engineering, Vol. 22, No. 9-10, pp. 855-886, 1999.

Part III

T. Børvik, O.S. Hopperstad, T. Berstad and M. Langseth,
Computational model of viscoplasticity and ductile damage for projectile impact.
Submitted for possible journal publication, 2000.

Part IV

T. Børvik, J.R. Leinum, J.K. Solberg, O.S. Hopperstad and M. Langseth,
Observations on shear plug formation in Weldox 460 E steel plates impacted by blunt-nosed projectiles.
Accepted for publication in International Journal of Impact Engineering, 2000.

Part V

T. Børvik, O.S. Hopperstad, T. Berstad and M. Langseth,
Numerical simulation of plugging failure in ballistic penetration.
Accepted for publication in International Journal of Solids and Structures, 2000.

Part VI

T. Børvik, M. Langseth, O.S. Hopperstad and K.A. Malo,
Effect of projectile nose shape in structural impact, part I: Experimental study.
Submitted for possible journal publication, 2000.

Part VII

T. Børvik, O.S. Hopperstad, T. Berstad and M. Langseth,
Effect of projectile nose shape in structural impact, part II: Numerical simulations.
Submitted for possible journal publication, 2000.

Part VIII

T. Børvik, O.S. Hopperstad, M. Langseth and K.A. Malo,
Effect of target thickness in blunt projectile penetration of Weldox 460 E steel plates.
Submitted for possible journal publication, 2000.

Abstract

Situations involving impact, i.e. the collision between two or more solids, were at one time primarily of concern to the military. Nowadays, as safety is highlighted within most branches of industry, the field of impact dynamics covers a wide range of situations and is of interest to engineers from a large number of different disciplines. This is in particular true for the oil, transport, space, military, nuclear and metal forming industry.

This thesis describes an experimental and numerical investigation on the ballistic penetration and perforation of Weldox 460 E steel plates, and consists of eight independently published parts that are linked together through a synopsis. The thesis was generated from a project in progress on the behaviour of structural components subjected to impact loading conditions. The work has been carried out at Structural Impact Laboratory (SIMLab), Department of Structural Engineering, Norwegian University of Science and Technology (NTNU), and is supported by the Norwegian Defence Construction Service (NDCS).

The thesis work can be divided into four equally important and quite parallel main research activities. The first part covers the development, building and testing of a new compressed gas gun with instrumentation at SIMLab. This part was necessary for the following parts in the project, since no such equipment was initially available. The gas gun is designed to launch a 250 g sabot mounted projectile to a maximum velocity of about 1000 m/s. During a test, the penetration process is photographed by a computer operated high-speed camera system with a shutter speed of up to 20 million frames per second. Several computer sub-routines have been developed as a part of the project in order to do direct measurements on the digital images.

The second part covers a large number of high-precision component tests on Weldox 460 E steel plates. Here, the gas gun was used to launch the projectiles at impact velocities well above and just below the ballistic limit velocity of the target plates. The primary variables in the tests were the plate thickness (which varied from 6 to 30 mm), the nose shape of the projectile (blunt, hemispherical or conical) and the impact velocity. Measurements were made of initial and final velocities, and the ballistic limit curves were constructed. Microscopic examinations of impacted plates were conducted in order to study the local material behaviour and failure process during penetration.

The development of a coupled constitutive model of viscoplasticity and ductile damage for penetration and impact related problems is covered in the third part. The model, which was implemented in the explicit finite element code LS-DYNA, includes linear thermoelasticity, the von Mises yield criterion, the associated flow rule, non-linear isotropic strain hardening, strain rate hardening, temperature softening due to adiabatic heating, isotropic ductile damage evolution and failure. All material constants were determined through uniaxial tensile tests, and the calibration procedure has been described in detail. The calibrated material model was verified and validated through numerical simulations of the material tests.

Numerical simulations were carried out and the results were compared with the experimental data in the fourth part. From the LS-DYNA simulations it was found that the numerical model was able to describe the structural response even if both the energy absorption mechanisms and failure mode varied, and good agreement was in general obtained between numerical and experimental results. Rezoning was required for conical projectiles, but simulations with fixed meshes and rezoning gave similar results. The experimental results were also compared to some empirical and analytical models found in the literature, showing only limited agreement.

Acknowledgements

This thesis has been carried out at Structural Impact Laboratory (SIMLab), Department of Structural Engineering, Norwegian University of Science and Technology (NTNU), under the supervision of Professor Magnus Langseth and Associated Professor Kjell Arne Malo. I would like to express my deep gratitude for their professional supervision and support during the study. Also, the collaboration and help from Professor Odd Sture Hopperstad throughout these years have also been very important and are hereby gratefully acknowledged. The considerable assistance from Dr. Torodd Berstad during the numerical work is greatly appreciated. He also implemented the constitutive models in LS-DYNA. Finally, thanks are given to my colleagues and fellow Dr.ing.-students at the Department of Structural Engineering, NTNU. The co-operation during these years has been excellent.

During the thesis work the author has been employed by the Norwegian Defence Construction Service (NDCS), Central Staff/Technical Division in Oslo, Norway. Their generous support of the work is gratefully acknowledged. Special credits are also given to Mr. Arnfinn Jenssen for his continual engagement in this thesis and for the initiation of the project.

The help and support from the laboratory staff at the Department of Structural Engineering, especially from Mr. Olav Haldorsen, Mr. Iver Johnsen and Mr. Tore Wisth, during the experimental part of this work is very much appreciated. Special credits are also given to Dr. Tom Engebretsen (SINTEF Energy Research), Mr. Bernt Førre (Department of Physics, NTNU), Mr. Knut Holen (NDCS/OSL) and Mr. Ottar Krest (NDCS) for all sorts of assistance concerning the experimental set-up and instrumentation. Their contributions have been very important, and are therefore gratefully acknowledged.

I also acknowledge the fruitful and instructive collaboration with Mr. John Rasmus Leinum and Professor Jan Ketil Solberg, Department of Materials Technology and Electro Chemistry, NTNU, in connection with the metallurgical investigations.

Finally, I would like to thank my wife, Linda, my two sons, Sindre and Torje, and the rest of my family for supporting and encouraging me throughout these years.



Synopsis

1. Background

Structural impact problems have become increasingly important both for modern industry and society. In design of offshore structures, account is taken for accidental loads such as dropped objects, collisions, explosions and penetration of fragments. Some of these loads are also pertinent in design of protective structures in the process and nuclear industry or fortification installations for defence purposes. The need for lightweight fortification as protection against terrorist attacks and in peacekeeping operations in vulnerable areas of the world is also increasing. Also the request for a lighter and more mobile defence have been a subject during later years. In the transport industry, energy absorption and crashworthiness are today critical issues in the design process of vehicles, vessels and aircrafts. Accidental impacts of space debris and meteoroids are still a major concern for the protection of spacecrafts. In addition, many of the problems found in structural impact are relevant to various types of metal forming operations, such as deep drawing, stamping and forging. Some of these applications where structural impact dynamics are of importance are illustrated in Figure 1.

Even though impact events have become commonplace, regulations and directives treating structural impact are to some extent missing. For most civilian applications, accidental loads are regulated through various national and international standards. However, in later years the general public has become increasingly concerned about safety (Jones, 1989). This is in particular so in the automotive industry, where safety considerations and crashworthiness have become key issues in the manufacturing and marketing process of new vehicles. This is perhaps not so strange when considering the more than 400.000 yearly traffic fatalities worldwide, not to mention the millions of injuries. Such numbers are of course unacceptable both from an economical, political and social point of view. Therefore, it comes as no surprise that the automotive industry is spending enormous resources on safety aspects. Similar arguments may be used for most other civilian applications. According to the regulations of the Norwegian Petroleum Directorate (NPD) for marine structures, unusual events should at most lead to local damage without total collapse. Unusual events refer mainly to accidental loads with a small probability of occurrence, e.g. 10^{-4} per year in permanent operation. Even though such strict limits exist on the paper, history has taught us that major accidents will occur both in the offshore, transport and space industry.

For military installations, the situation is rather different. In contrast to civilian applications, there is only minor public interest in safety questions regarding protective structures during peacetime. This is further increased by the general perception that the danger of war and major crises seems small, at least in our part of the world. This situation leads to a reduced knowledge and interest regarding the design and special needs for protective structures. Also the lack of experience from protective structures that have been in use is a disadvantage for designers of fortification. It follows that defence authorities have a strong obligation to maintain, secure and generate necessary knowledge themselves, since nobody else will.

Protective structures are passive means to improve survivability. Design requirements for fortification installations are usually based upon operational studies. Such studies are carried out by many different organisations, like the SHAPE Technical Centre within NATO and the Norwegian Defence Research Establishment in Norway. The requirements are thereafter often issued as NATO or specific national criteria. These are usually presented as a range of threats

for which the structure is required to protect the operational function with a 90 % probability. It is then up to the defence construction services to come up with the optimal technical-economical solution that will meet the prescribed operational needs. This can only be achieved if the responsible authorities have the necessary knowledge and understanding about the behaviour of materials and structures under high strain rate loading conditions, verified and validated computational tools for the design process and possibilities to test prototypes and components to confirm that the structure meets the required load. In Norway, it is the Norwegian Defence Construction Service (NDCS) that is responsible for the design and construction of protective structures and for the quality control of these installations.

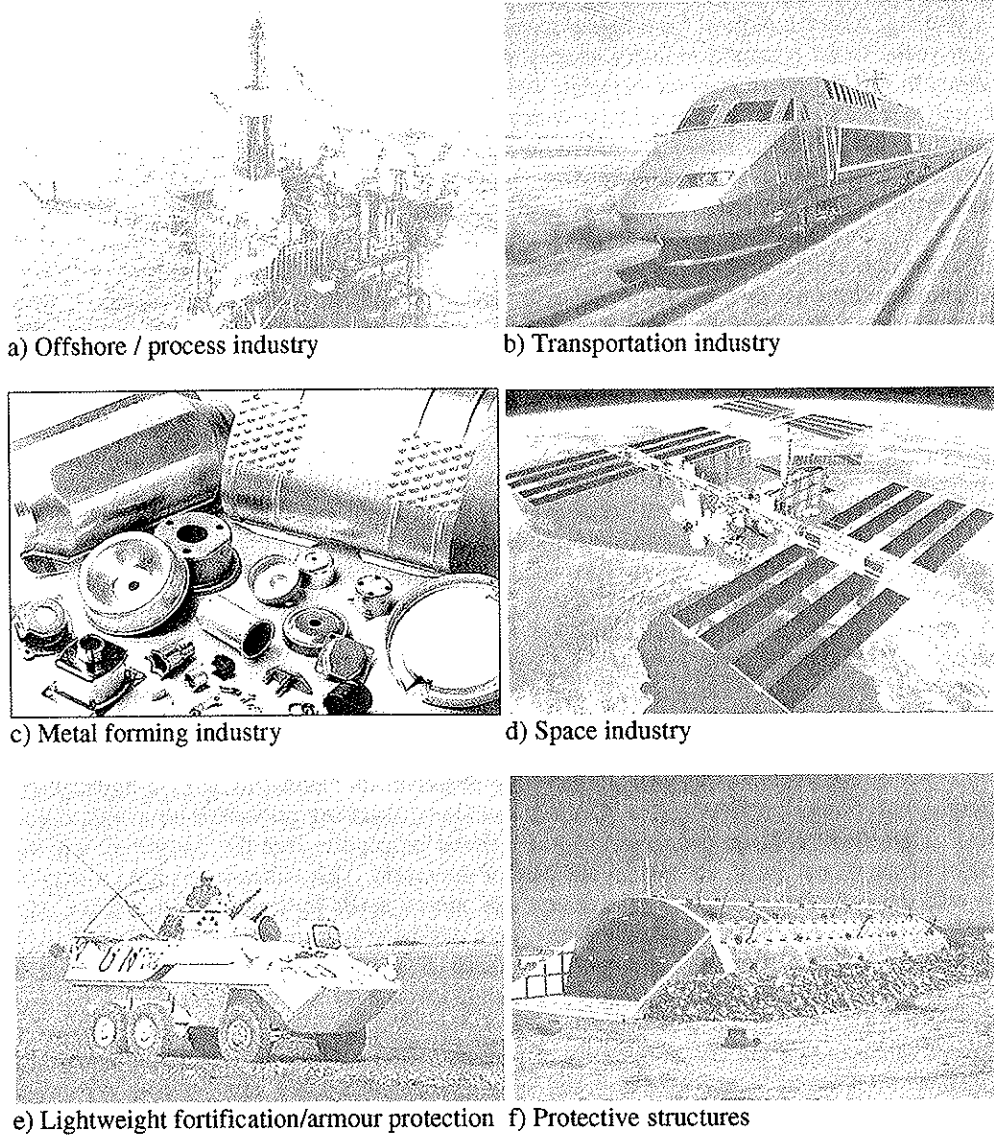


Figure 1: Typical applications where knowledge about structural impact dynamics is required.

Figure 1 illustrates that the science of structural impact dynamics enters into a broad and complex field of engineering. As pointed out by Goldsmith (1999), the enormous work on the subject encompasses a variety of different materials and thicknesses, as well as a host of structural geometries and an impact velocity range from about 5 m/s to the hypervelocity domain of up to 15 km/s. Despite this, impacts remain mysterious. They occur too quickly for us to follow what is happening and the evidence they leave behind is often ambiguous (Macaulay, 1987). The extreme complexity of the penetration problem, especially if dynamic material behaviour and fracture are taken into account, has limited the use of closed-form analytical solutions. For that reason, work done in the area of transient dynamic loading has until now generally been considered as experimental in nature (Zukas et al, 1990).

The development of numerical tools such as the finite element method (FEM) offers new possibilities for attaining further and more generally applicable knowledge to complex problems, and such codes will play an increasingly important role in engineering design. In particular the combination of high precision experiments, advanced numerical algorithms and appropriate constitutive models have been successful. Even so, according to Belytschko (Krauthammer et al, 1996), simulations involving material instabilities and response discontinuities are still among the most difficult problems to solve from a numerical point of view. Therefore, there is a need both to increase our physical understanding of structural impact through material and component tests, to validate the experimental findings through calculations using FE codes and to verify both existing and new computational methods.

This thesis was therefore initiated and supported by NDCS as a part of the ongoing quality control effort for design methods of ballistic penetration and perforation.

2. A Short Introduction to Structural Impact Dynamics

Research into the field of structural impact dynamics has resulted in a large amount of work published in the literature. Many of these investigations have been carried out on generic components under idealised impact conditions, i.e. normal impact of purely translating projectiles against stationary targets. Such idealised situations only occur in the laboratory. In real applications a wide range of different projectile-target configurations exists, and these may differ significantly from generic laboratory investigations. It is therefore not feasible to give a complete listing of all the relevant literature. Nevertheless, important publications and review articles on impact dynamics are given in the bibliography. Textbooks in mathematics, physics or mechanics are not listed. The many publications have resulted in conflicting use of several technical terms, which may cause confusion since their meaning not always are obvious. Some of these terms are therefore defined in the following.

Structural impact dynamics has some features that distinguish it from conventional quasi-static loading conditions. From a physical point of view, inertia effects must be considered in all governing equations. This gives rise to stress wave propagation in the impacting materials, and the recognition that most impact events are transient phenomena where steady-state conditions do not exist (Zukas et al, 1990). From a material point of view, the short time duration of impact phenomena may introduce strain rate effects, thermal softening and hydrodynamic material behaviour, not observed in quasi-statically loaded materials. Also, from an experimental point of view the high rate of loading involves great challenges, as it is far more difficult (and expensive!) both to apply the load and to record the response at 500 m/s than at $5 \cdot 10^{-5}$ m/s.

Impact is defined as the collision between two or more solids, where the interaction between the bodies can be elastic, plastic or fluid, or any combination of these. *Ballistics* is defined as the art of accelerating objects by use of an engine. In modern science, ballistics deals with the motion, forces and impact of projectiles, especially those discharged from firearms and guns. The *ballistic trajectory curve* is often referred to as the path actually travelled by an object, as distinguished from its theoretical parabolic path if gravity was the only force acting on it. The science of ballistics is usually sub-divided into three main research areas. *Interior ballistics* is the study of the motion and forces acting on an object when it is still within the launcher. *Exterior ballistics* is the study of the motion and forces acting on the object during free flight, while *terminal ballistics* describes the interaction between the object and target during impact. Here, most effort is used on the field of terminal ballistics. This is the area of greatest interest with respect to *fortification*, which may be defined as structures used for additional strength or strengthening, especially in military defences. *Penetration* is defined as the entry of the projectile into any region of a target. During impact the projectile may penetrate the target in several ways. Backman and Goldsmith (1978) suggested the following definitions

- 1) *Perforation* if the projectile passes through the target with a final residual velocity.
- 2) *Embedment* if the projectile is stopped during contact with the target.
- 3) *Ricochet* or *rebound* if the projectile is deflected from the target without being stopped.

In the present study the term *penetration* is used to describe the entrance and indentation of the projectile into the target, while the term *perforation* is used to describe the fracture and projectile exit process. These definitions are also reflected in the title of the thesis.

The *ballistic limit velocity* is the average of two striking velocities; the one with the highest velocity only giving partial penetration and the one with the lowest velocity giving complete perforation. This velocity is of major importance in the design of protective structures. There are several criteria used in rating the resistance of structures to penetration, and the three most widely used are the *army ballistic limit* (which is adopted in this study), the *protection ballistic limit* and the *navy ballistic limit*. The essential difference between these definitions is how they define perforation, as illustrated in Figure 2. The terms *critical impact velocity* and *plugging capacity* are also often used to describe the ballistic limit when a part or a plug is separated from the target during impact. In addition to the ballistic limit velocity, the *ballistic limit curve* (or residual velocity curve) is an important measure in structural impact. The ballistic limit curve gives the residual velocity of the projectile as a function of initial projectile velocity. This curve is often compared to the *ballistic limit line* (or residual velocity line), i.e. the ballistic limit curve for a target of zero thickness. The ballistic limit line, curve and velocity used throughout this study are depicted in Figure 3.

The *protection limit* is often used in connection with impact on structures where leak tightness is required, such as pressurised vessels and containers for gases. The protection limit is defined as the highest projectile velocity where daylight can not be seen through the plate at the point of impact, as distinct from the protection ballistic limit seen in Figure 2. Even if the difference between the ballistic limit and the protection limit seems to be small, it is important to notice that such a difference exists.

Hydrodynamic transition velocity is defined as the impact velocity where the projectile and target deformation process will exhibit a dynamic instability that will change its behaviour from an essentially elastic-plastic character to one which is essentially hydrodynamic, such as in meteor impact and similar.

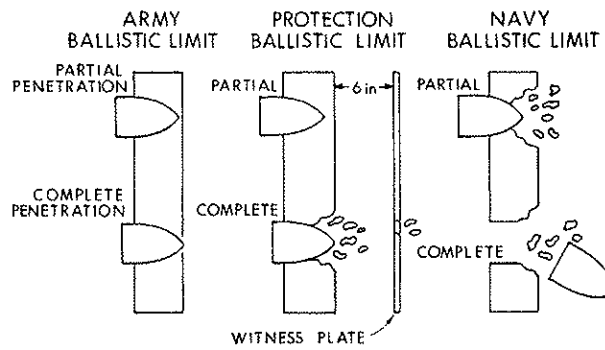


Figure 2: Various definitions of the ballistic limit velocity (Backman and Goldsmith, 1978).

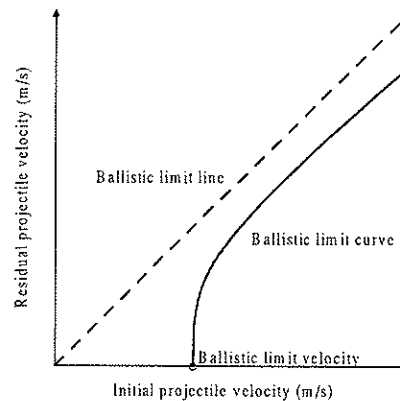


Figure 3: Definition of ballistic limit line, ballistic limit curve and ballistic limit velocity.

Projectiles are normally categorised as soft, semi-hard or hard depending on the material used, the degree of nose deformation (also called mushrooming), and the coupling between target deformation and impact loading. Most work performed in the field of impact dynamics deals with hard projectiles. According to Zukas et al (1982), the term *projectile* is used for any item that can be launched, and this has been adopted as a general term in this work.

- 1) *Projectile* will refer to a device for general ballistic performance that serves specific ballistic functions (bullets, bombs, artillery shells, etc).
- 2) *Missile* is defined as a long-range projectile that may be guided by different sensors or pre-set mechanisms during flight.
- 3) *Penetrator* refers to military projectiles with an exclusively terminal ballistic function.
- 4) *Striker* is defined as any object able to cause an impact.
- 5) *Fragments* are pieces separated from a body by breaking, often generated by failure of pressurised equipment, rotating machinery or detonation of warheads, mines, etc. Such fragments are termed primary, while secondary fragments may be those generated by e.g. a blast wave picking up loose objects and launching them towards the target, etc.

Some commonly occurring projectiles, both military and non-military, are shown in Figure 4, while Figure 7 shows the different geometries and nose shapes used in this particular study.

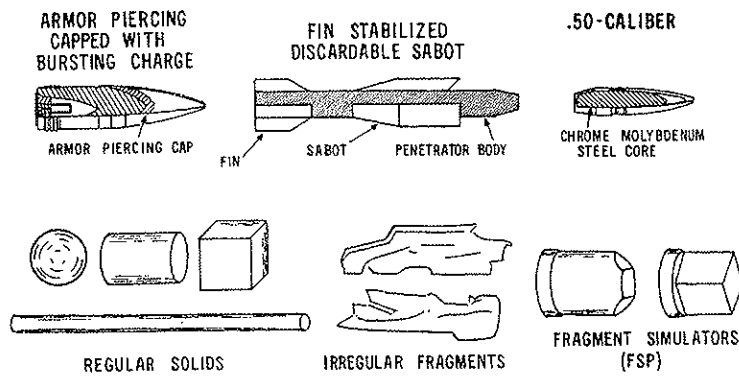


Figure 4: Examples of projectiles (Zukas et al, 1982).

The *target* is defined as any moving or stationary object struck by the projectile and identified by structural and functional unity. Because impact effects in most materials tend to be highly localised for striking velocities exceeding, say 500 m/s, only a small portion of the overall structure needs to be considered in many situations. When the projectile velocity approaches the ballistic limit of the target, it has been shown that target deformation increases and reaches a maximum just below the minimum perforation velocity. This implies that both local and global deformation of the target have to be considered in impact calculations. It is convenient to classify targets by thickness, often by the following operational definitions:

- 1) *Thin*, if stress and deformation gradients throughout its thickness may be neglected.
- 2) *Intermediate*, if the rear surface exerts considerable influence on the deformation process during all (or nearly all) of the penetrator motion.
- 3) *Thick*, if there is influence of the distal boundary on the penetration process only after substantial travel of the projectile into the target element.
- 4) *Infinite*, if there is no influence of the distal boundary on the penetration process.

It is common to divide the target response into non-failure and failure modes. Non-failure modes involves elastic deformation with no damage, plastic deformation that only gives local bulging and global dishing, Figure 6, and cratering for very thick targets. Of particular interest in this study is the many different failure modes of impacted plates. The actual mechanisms depend on such variables as material properties, impact velocity, projectile nose shape and trajectory, target support and relative dimensions of projectile and target. Some of the most common failure modes for thin and intermediate thickness target plates are shown in Figure 5. Although one of these may dominate the failure process, several mechanisms may interact. Ductile hole growth, plugging and petaling are the governing failure modes in ductile materials. Several definitions of the different failure modes exist in the literature, and it is referred to Backman and Goldsmith (1978), Zukas et al (1982) and Langseth (1988) for a more comprehensive description.

Impact velocity is a fundamental quantity in impact dynamics. Even though a variety of other parameters affect the target response, the projectile velocity is so predominant that it overrides most other considerations (Backman and Goldsmith, 1978). This has resulted in that impact classifications are closely connected to a certain velocity range, even though these ranges only should be considered as reference points, and the following definitions are often used:

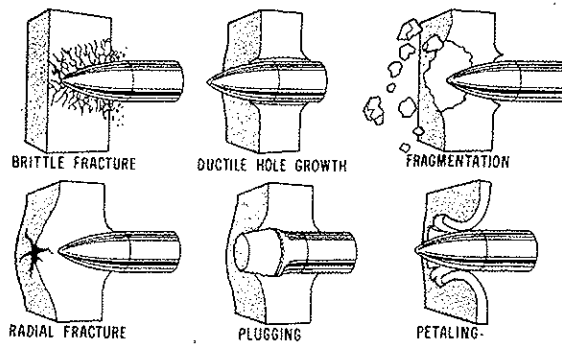


Figure 5: The most common failure modes in impacted plates (Zukas et al, 1982).

1) *Low velocity regime (0-50 m/s)*: Here, elastic and plastic bending controls the deformation. With an increase of projectile mass the response is essentially plastic membrane stretching and bending, and considerable plate deflection will occur which extends to the supports. This velocity range covers dropped objects, vehicle impact, ship collisions, crashworthiness of containers for hazardous materials, etc. 2) *Sub-ordnance velocity regime (50-500 m/s)*: In this range, hard projectiles will normally behave in an elastic manner, while the target response is primarily plastic. The rate of energy dissipated within the target is limited by elastic and plastic waves that will tend to reduce the extent of the deformation in the target compared to a low velocity impact, i.e. the deformation in the target becomes more localised with increasing velocity. The sub-ordnance velocity regime covers the design of nuclear containments, free-falling bombs and missiles, fragments resulting from accidental explosions, etc. 3) *Ordnance velocity regime (500-1300 m/s)*: This range is of special interest for military applications. Here, most of the kinetic energy is converted into plastic work both in the projectile and the target, without any significant material erosion. The material strength is still an important parameter, but material density is getting gradually more important with increasing velocity. The activated part of the target is very small, typically 2-3 projectile diameters from the impact zone, and hardly any global deformation of the target is seen. The ordnance velocity regime covers all kinds of military projectiles like bullets, missiles and high kinetic energy penetrators with or without explosives. 4) *Ultra-ordnance velocity regime (1300-3000 m/s)*: Here, a hydrodynamic description of the material behaviour is necessary since they behave like fluids. The stress level during impact may be many times the material strength of the materials and considerable projectile erosion may occur. The density of the materials is a dominant parameter. This velocity regime covers e.g. warhead fragments and rocket bursted penetrators. 5) *Hypervelocity regime (> 3000 m/s)*: In this velocity regime both the projectile and target behaves like fluids, and the material strength is no longer important. The projectile will often be completely eroded during impact and even totally vaporised if the velocity is high enough. At the highest velocities (> 12000 m/s), impact explosions may occur due to the enormous amount of kinetic energy released. The hypervelocity regime covers all kind of space vessels exposed for meteoroid impact and space debris, and shaped charge penetration.

In view of the complexity of penetration processes, it is not surprising that the bulk of the work in this area has been experimental. To study the physical process during penetration, efficient accelerators and highly sophisticated instrumentation for the laboratory are needed. It is therefore assumed that the limits of these experimental possibilities mark the boundaries of our understanding, at least to some extent. Different gun accelerators, classified after their

velocity range, are given in Table 1. Because of the short time duration involved in impact phenomena, the response of the materials involved strongly influences the impact event. Thus, a study on structural impact requires a study of dynamic material behaviour. Consequently, different material testing techniques have been developed in the wake of the impact tests and some of the most frequently used methods are also listed in Table 1 together with the expected material behaviour at these high strain rates.

Table 1: Experimental methods for terminal ballistics.

<i>Impact Test</i>		<i>Material Test</i>		
Velocity (m/s)	Accelerator	Strain rate (s ⁻¹)	Test method	Dynamic Material Effect
< 50	Drop hammer / Pneumatic accelerator	< 10	Quasi-static / Dynamic hydraulic machine	Inertia forces important, isothermal, plane stress
50 – 500	Compressed air / gas gun	~ 10 – 10 ⁴	Pneumatic / Hydraulic, Taylor-tests, SHPB	Elastic/Plastic stress waves, increasing adiabatic
500 – 1300	Compressed gas gun / Powder gun	~ 10 ³ – 10 ⁵	Split Hopkinson Pressure Bar (SHPB)	Elastic/Plastic stress waves, fluid, adiabatic
1300 – 3000	Powder gun / Two-stage light gas gun	~ 10 ⁴ – 10 ⁶	Plate impact	Shockwaves, plane strain, adiabatic state, fluid
3000 – 12000	Two-stage light gas gun	~ 10 ⁶ – 10 ⁷	Plate impact	Shockwaves, hydrodynamic material
> 12000	Not possible today?	~ 10 ⁸	Not possible today?	Vaporisation

3. The Generic Penetration Problem

As demonstrated in Figure 1, the field of impact dynamics covers a wide range of situations and requires engineering knowledge from a large number of different disciplines. It is for that reason not always adequate to study impact on one particular structural system, where e.g. structural details may influence the overall response. Therefore, basic knowledge is often obtained by studying a generic problem. In this case, the structural component is well defined both in geometry and material. It is also designed in such a way that the generalised structural behaviour is readily evident. When the generic problem is sufficiently understood, the next step is to incorporate this competence into design. Recognising the advantages of generic competence, new structural systems can more easily be studied.

The generic penetration problem studied in this thesis is outlined in Figure 6, showing a blunt-nosed steel projectile impacting a moderately thick flat steel plate. At impact, this type of projectile tends to localise the target deformation in narrow shear zones throughout the target thickness. Within these zones the deformation continues under very high local strains, strain rates and temperatures. Also the stress state changes continuously as the projectile indents the target plate, and this will again influence the damage and fracture process. However, both the global and local structural response of the target (and projectile) will change as the impact conditions are varied, and the list of possible variables in the general penetration problem is long (Baker et al, 1991). In order to establish a reliable experimental database from the generic penetration tests for validation of computational methods, it was found necessary to vary some of the parameters assumed to be most important regarding local versus global structural response, energy absorption and failure. Three different experimental programmes were for that reason carried out and used for validation purposes in this thesis, see Table 2. A sketch showing the different type of projectiles used in this study is given in Figure 7.

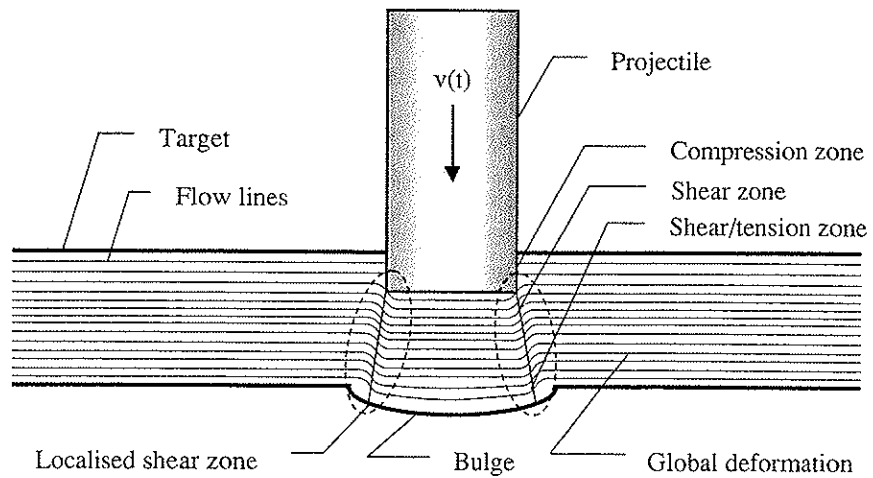


Figure 6: The generic penetration problem.

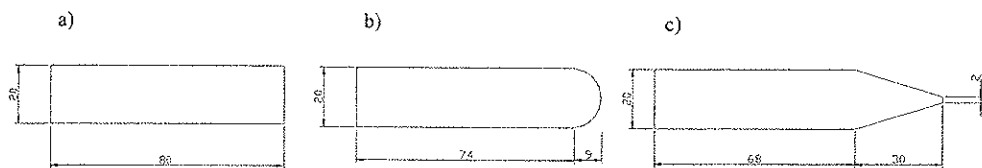


Figure 7: The different projectiles used in the tests; a) blunt, b) hemispherical, c) conical.

A study of structural impact also requires a study of materials behaviour under high strain rate loading conditions. This involves not only the stress-strain response as a function of strain rate, stress state, temperature and history of loading, but also the accumulation of damage and the mode of failure that the material undergoes (Zukas et al, 1990). Since the local material behaviour plays such an important role in the structural impact problem, the material selection process becomes extremely important. However, the selection process is complex and it may be difficult to find the optimal material, Figure 8. In the material selection of this generic study, only mechanical properties have been considered, while several more properties need consideration in design. After some initial tests, projectiles were manufactured from Arne tool steel. This material was chosen due to its excellent hardness properties when heat treated. After machining they were oil hardened to a Rockwell C value of 53 (yield stress of about 1900 MPa) in order to minimise plastic deformations during impact. Nominal hardness (HRC 53), diameter (20 mm) and mass (0.197 kg) of the cylindrical projectiles were kept constant in all tests, while their length/diameter-ratio varied somewhat (Figure 7). Target plates were manufactured from Weldom 460 E steel. This material was chosen due to its combined high strength and ductility, which both are important in structural impact. As an example, the ballistic limit velocity for a 12 mm thick Weldom 700 E steel plate impacted by a blunt projectile was found to be 20 % lower than the ballistic limit velocity for a corresponding Weldom 460 E steel plate, although the yield stress was about 75 % higher. The higher yield stress and the lower strain hardening causes Weldom 700 E to localise into shear bands earlier, which together with the reduced ductility gives an early failure. It follows that knowledge of the problem under investigation is a necessary condition for optimised material selection.

Table 2: Experimental programmes carried out on the generic penetration problem.

Programme #	Experimental Programme	Experimental factors
1	Effect of initial projectile velocity	Blunt nose, $h_t = 8, 10$ and 12 mm, $140 \text{ m/s} \leq v_i \leq 300 \text{ m/s}$
2	Effect of projectile nose shape	Blunt, hemispherical and conical nose (Figure 7), $h_t = 12$ mm, $180 \text{ m/s} \leq v_i \leq 450 \text{ m/s}$
3	Effect of target plate thickness	Blunt nose, $6 \text{ mm} \leq h_t \leq 30 \text{ mm}$, $80 \text{ m/s} \leq v_i \leq 470 \text{ m/s}$

$h_t =$ Target thickness, $v_i =$ initial projectile velocity

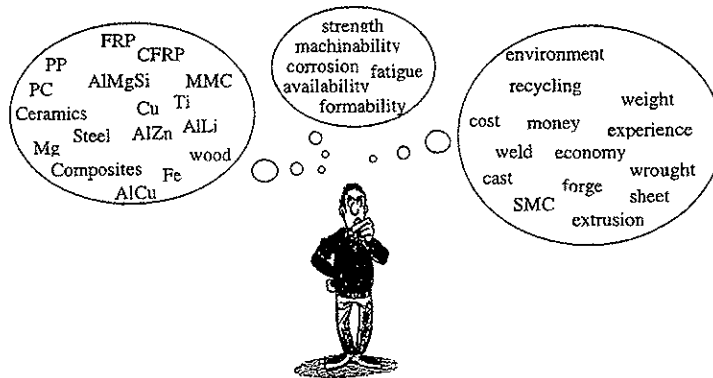


Figure 8: Material selection may be a complex process (Hagström, 1997).

4. Overall Objectives and Method of Research

As already stated, impact dynamics is a complex field of engineering. One main reason is the many (both coupled and uncoupled) physical parameters involved in the problem that may cause highly non-linear and sometimes unexpected structural behaviour when varied, together with a distinct lack of generality in the observations. It is therefore difficult to use statistical methods such as factorial designs (Box et al, 1978) in experimental investigations involving impact and penetration, although these methods have several advantages over the “one-factor-at-a-time” method. In the latter, experimental factors are varied one at a time, while the remaining factors are held constant (see Table 2). Hence, it is difficult in advance to plan in detail all activities within a project as the one described in this thesis. Nevertheless, the following overall objectives have remained fixed throughout the study, and these have been aimed with varying degree of both effort and success.

- To increase the physical understanding of the different phenomena taking place during ballistic penetration and perforation of steel plates.
- To establish precision test methods and to obtain experimental data both for materials and components under impact generated high strain rate loading conditions.
- To evaluate existing empirical and analytical models found in the literature.
- To develop, calibrate, implement and verify a computational material model for the generic penetration problem in a suitable finite element code.
- To establish and validate a finite element model for penetration and perforation studies.

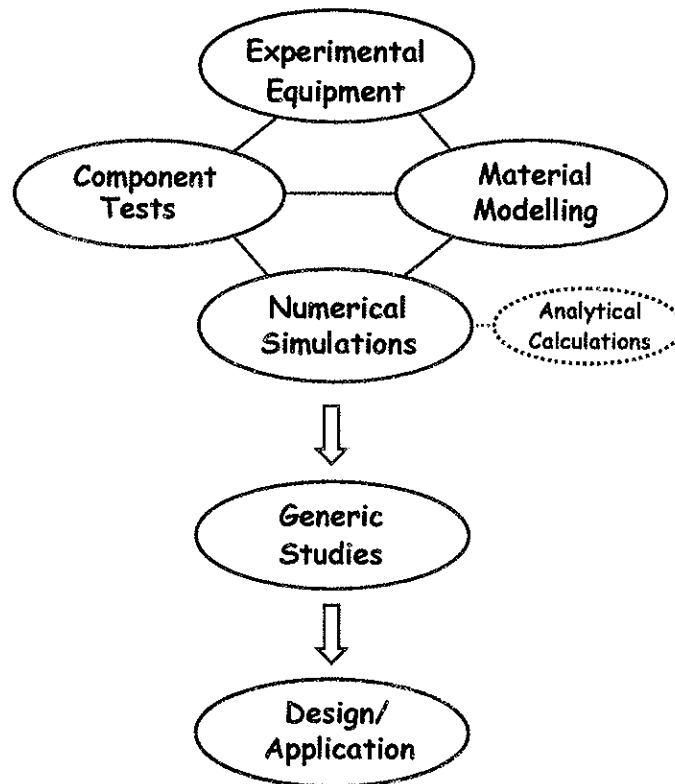


Figure 9: Main research activities

In order to reach these overall objectives, four equally important and quite parallel research activities have been carried out. These are (see Figure 9):

- Experimental equipment
- Component Tests
- Material Modelling
- Numerical Simulations

Knowledge and information gained from these strongly connected and continuously running research activities were then used to study the generic penetration problem in Figure 6. It is important to emphasise that no attempts have been made to incorporate a specific application or design in the thesis work. This is, as also pointed out in Figure 9, a subject for coming studies. Details within each of the main activities will be covered in the next chapter. Finally, it is essential to notice the dotted line to the smaller box named “Analytical Calculations”. This has by no means been a major research activity in the study, but analytical modelling was until recently the primary computational tool in structural impact dynamics and is for that reason still very important. However, during the last decade computer technology has grown tremendously both in power and capability. As a result, numerical simulations using e.g. the finite element method has become commonplace within most branches of industry and is nowadays used to simulate virtually all kinds of non-linear events. This novel situation

involves many new possibilities, but also challenges, not present only a decade ago. It was therefore decided that in this particular study, the finite element method should be the primary computational tool and that possible analytical calculations should only be carried out with models found in the literature.

5. Organisation and Summary of the Thesis Work

The thesis describes an experimental and numerical investigation on the ballistic penetration and perforation of Weldox 460 E steel plates. It is generated from a larger project in progress on the behaviour of structural components under impact loading conditions. The work has been carried out at Structural Impact Laboratory (SIMLab), Department of Structural Engineering, Norwegian University of Science and Technology (NTNU), and was supported by the Norwegian Defence Construction Service (NDCS).

The thesis work consists of eight independently published parts, which are linked together through this synopsis. The different parts are presented at the end of the synopsis and they are completely referred in Table 3. Note that the parts are numbered and presented in the succession as they have been written. The first part was presented at an international conference, while the seven last parts have been separately written and independently submitted for possible publication in various international journals suitable for the topic of the thesis. Thus, some overlap between the different parts was both necessary and inevitable, and must therefore be expected. At this very moment, two parts have been published, two parts have been accepted for publication, while the last four parts are still under review. In order to connect the different parts, and to clarify the governing idea of the thesis work, the synopsis is included. Although conclusions are given at the end of each part, some general conclusions and a suggestion for further work are given at the end of the synopsis. In addition to the eight parts included in the thesis, several other publications have been generated during this project work and a selection is given in Table 4 and Table 5.

This way of organising a thesis has both its advantages and disadvantages. Major advantages may be a more extensive and firm collaboration with “experts” from different departments than what is common when writing a monograph (see the many different co-authors in Table 3 and Table 4) together with international attention around the thesis work at a much earlier stage. The major disadvantage is that some of the governing idea of the thesis may get lost in the process. Also, several important research activities, not necessary of interest to journal readers but of significance for the outcome of the thesis, may never be published. As an example, a lot of resources have been invested in the construction, building and edification of the experimental set-up in this study. This has probably also been the most time-consuming part of the work. In particular the problems associated with the projectile trajectory (pitch and yaw angles) prior to impact was challenging. Even though this work never will be recognised through journal articles, it was absolutely necessary since there was no launcher (and hardly no experience at NTNU) available when the project was initiated. Thus, important reports from the study giving additional background information to the journal articles are referred in Table 5.

The four main research activities defined in Figure 9 can be subdivided into smaller groups in order to outline the different activities and to relate them to the different parts of the thesis presented in Table 3. In coarse features, this is shown in Table 6.

Table 3: Conference paper and journal articles included in the thesis.

Part #	Reference
[1]	Børvik T, Holen K, Langseth M, Malo KA, <i>An Experimental set-up used in Ballistic Penetration</i> , Proceedings of 5 th International Symposium on Structures under Shock and Impact, pp. 683-692, Thessaloniki, Greece, June 24-26, 1998.
[2]	Børvik T, Langseth M, Hopperstad OS, Malo KA, <i>Ballistic Penetration of Steel Plates</i> , International Journal of Impact Engineering, Vol. 22, No. 9-10, pp. 855-886, 1999.
[3]	Børvik T, Hopperstad OS, Berstad T, Langseth M, <i>Computational Model of Viscoplasticity and Ductile Damage for Projectile Impact</i> , Submitted for publication, 2000.
[4]	Børvik T, Hopperstad OS, Berstad T, Langseth M, <i>Numerical Simulation of Plugging Failure in Ballistic Penetration</i> , Accepted for publication in International Journal of Solids and Structures, 2000.
[5]	Børvik T, Leinum JR, Solberg JK, Hopperstad OS, Langseth M, <i>Observations on Shear plug formation in Weldox 460 E steel plates impacted by blunt-nosed projectiles</i> , Accepted for publication in International Journal of Impact Engineering, 2000.
[6]	Børvik T, Langseth M, Hopperstad OS, Malo KA, <i>Effect of Projectile Nose Shape in Structural Impact, Part I: Experimental Study</i> , Submitted for publication, 2000.
[7]	Børvik T, Hopperstad OS, Berstad T, Langseth M, <i>Effect of Projectile Nose Shape in Structural Impact, Part II: Numerical Simulations</i> , Submitted for publication, 2000.
[8]	Børvik T, Hopperstad OS, Langseth M, Malo KA, <i>Effect of Target Thickness in Blunt Projectile Penetration of Weldox 460 E Steel Plates</i> , Submitted for publication, 2000.

Table 4: Conference papers from the study not included in the thesis.

Part #	Reference
[9]	Børvik T, Vestli K, Langseth M, <i>Determination of Projectile Path during Ballistic Penetration by use of a High-Speed Digital Camera</i> , UK Association of High-Speed Photography and Photonics Conference, Cambridge, U.K., 10-11 April, 1997.
[10]	Børvik T, Vestli K, Langseth M, Malo KA, <i>Utilising a Digital High-Speed Camera in Ballistic Penetration</i> , Scandinavian Association of High-Speed Photography Conference, Trondheim, Norway, 5-7 November, 1997.
[11]	Børvik T, Langseth M, Hopperstad OS, Malo KA, <i>Ballistic Penetration of Steel Plates</i> , Proceedings of International Symposium on Transient Loading and Response of Structures (honouring Mr. Arnfinn Jensen), Trondheim, Norway, pp. 241-272, May 25-27, 1998.
[12]	Børvik T, Langseth M, Hopperstad OS, Malo KA, <i>Experimental Determination of the Ballistic Limit in Weldox 460 E Steel Plates</i> , Proceedings of 11 th International Conference on Experimental Mechanics, Oxford, England, pp. 233-238, August 24-28, 1998.
[13]	Børvik T, Hopperstad OS, Langseth M, <i>Penetration of Steel Plates by Fragments Generated from an Accidental Explosion</i> , Proceedings of 11 th Nordic Seminar on Computational Mechanics, pp. 35-38, Stockholm, Sweden, 16-17 October, 1998.
[14]	Børvik T, Langseth M, Hopperstad OS, Malo KA, <i>Penetration of Steel Plates - I. Experimental Study</i> , Proceedings of Third International Symposium on Impact Engineering, Singapore, December 7-9, 1998.
[15]	Hopperstad OS, Børvik T, Berstad T, Aas-Jakobsen K, Langseth M, <i>Penetration of Steel Plates - II. Numerical Simulations</i> , Proceedings of Third International Symposium on Impact Engineering, Singapore, 7-9 December, 1998.
[16]	Børvik T, Hopperstad OS, Berstad T, Malo KA, Langseth M, <i>Numerical Simulation of Plugging Failure in Ballistic Penetration using LS-DYNA</i> , Proceedings of 2nd European LS-DYNA Conference, Gothenburg, Sweden, 14-15 June, 1999.
[17]	Børvik T, Langseth M, <i>Quasi-Static Penetration of Steel Plates</i> , Integrity, Reliability, Failure: An International Conference, University of Porto, Portugal, 19-22 July, 1999.
[18]	Børvik T, Langseth M, Hopperstad OS, Malo KA, <i>Perforation of Steel Plates: Effect of Projectile Nose Shape</i> , Proceedings of 4 th EUROMECH Solid Mechanics Conference, Metz, France, 26-30 June, 2000.
[19]	Børvik T, Hopperstad OS, Langseth M, <i>Experimental and Numerical Studies of Target Plate Failure in Projectile Impact</i> , Proceedings from Symposium on Continuous Damage and Fracture, Cachan, France, 23-27 October, 2000.

Table 5: Selected reports from the study not included in the thesis.

Part #	Reference
[20]	Børvik T, Langseth M, <i>An Investigation of the Scaling Laws for Metal Plates Penetrated by Projectiles</i> , Fortifikatorisk Notat Nr 237 / 96, August, 1996.
[21]	Børvik T, Langseth M, Malo KA, <i>A Compressed Gas Gun for Impact Testing</i> , Fortifikatorisk Notat No. 242 / 97, February, 1997.
[22]	Børvik T, Langseth M, Malo KA, <i>Ballistic Limit Curve of 10 mm Weldox 460 E Steel Plates</i> , Fortifikatorisk Notat No. 252 / 97, September, 1997.
[23]	Børvik T, Langseth M, Malo KA, Hopperstad OS, <i>Empirical Equations for Ballistic Penetration of Metal Plates</i> , Fortifikatorisk Notat No. 260 / 98, September, 1998.
[24]	Børvik T, Hopperstad OS, Aune A, Langseth M, <i>Quasi-Static Tensile Tests of Weldox 460 E Steel Plates - Introductory Study</i> , Fortifikatorisk Notat No. 250 / 97, 1997.
[25]	Børvik T, Aune A, Hopperstad OS, Langseth M, <i>Quasi-Static Tensile Tests of Weldox 460 E Steel Plates - Variation of Material Properties</i> , Fortifikatorisk Notat No. 255 / 97, May, 1998.
[26]	Quick M, Del Grande A, Spinelli R, Albertini C, Børvik T, Langseth M, Hopperstad OS, <i>Tensile Tests at Low, Medium and High Strain-Rate of Weldox 460 E</i> , Fortifikatorisk Notat No. 251 / 97, 1997.
[27]	Hopperstad OS, Børvik T, Berstad T, Langseth M, <i>A Computational Model of Viscoplasticity and Ductile Damage for Perforation Problems</i> , Fortifikatorisk Notat No. 253 / 97, July, 1998.
[28]	Børvik T, Gåsvik KJ, Langseth M, <i>Optical Measurement System for Deformation in Plates</i> , Fortifikatorisk Notat No. 272 / 99, January, 1999.
[29]	Hopperstad OS, Børvik T, Langseth M, <i>Analysis of Plugging Failure in Blunt Projectile Impact of Steel Plates using the Bai-Johnson Model</i> , Report No. R-06-00, SIMLab / Department of Structural Engineering, Norwegian University of Science and Technology, July 2000.

Table 6: Outline of the activities in the different parts in the thesis.

Research Activity	Detailed activities	Thesis part #
1. Compressed gas gun	Development, building, testing and implementation of gas gun. Firing and sabot techniques; pitch/jaw problems; preparation and aligning.	I, II and VIII
2. Instrumentation	Development, building, testing and implementation of instrumentation; high-speed camera set-up; computer sub-routines for velocity/angle measurements from the digital images; 3D spatial camera calibration.	I, II and VIII
3. Component tests	Effect of initial projectile velocity; effect of projectile nose shape; effect of target plate thickness on Weldox 460 E steel (see Table 2).	II, IV, V, VI and VIII
4. Metallurgical investigations	Study of the development and properties of adiabatic shear bands as a function of target thickness; void growth and cracking; different stress states and ductile failure modes with varying projectile nose shapes.	II, IV and VI
5. Material tests	Introductory tests on square specimens; quasi-static tensile tests on smooth and notched specimens; dynamic tensile tests on smooth specimens; quasi-static tensile tests at various temperatures; damage tests; quasi-static tensile tests on hardened projectiles.	II and III
6. Material modelling	Development and implementation of a coupled constitutive model of viscoplasticity and ductile damage in LS-DYNA; a calibration procedure is proposed and the model is calibrated for Weldox 460 E steel; the model is verified and validated through numerical simulations.	II and III
7. Analytical calculations	Typical empirical formulas and three different analytical models found in the literature for steel plates impacted by blunt nosed projectiles are used in calculations and compared with the experimental results.	VI and VIII
8. Numerical simulations	Numerical simulations of all component and material tests; variation in material model (coupled/uncoupled approach); adaptive simulations; mesh size sensitivity.	II, III, V, VII and VIII

Before the different parts are presented, a short summary from each manuscript will be given in the following.

Part I:

T. Børvik, K. Høien, M. Langseth and K.A. Malo. *An experimental set-up used in ballistic penetration*, Proceedings of Fifth International Symposium on Structures under Shock and Impact, pp. 683-692, Thessaloniki, Greece, 24-26 June, 1998.

This paper describes an experimental set-up where a digital high-speed camera is used together with a compressed gas gun in order to study the phenomena associated with ballistic penetration. Until recently, photographic studies of ballistics were limited either by time-consuming film development or a moderate framing rate during testing. These obstacles have been overcome by the introduction of camera systems combining the advantages of an image converter camera and a CCD camera. The image converter camera provides extremely fast shutter speeds (up to 20 million frames per second), while the CCD part provides high quality digital pictures that are available immediately after the experiment. By utilising the advantages of the system, important parameters such as velocities and angles can be determined during penetration. To demonstrate the possibilities of the experimental set-up, some test results are presented.

Part II:

T. Børvik, M. Langseth, O.S. Hopperstad and K.A. Malo. *Ballistic penetration of steel plates*, International Journal of Impact Engineering, Vol. 22, No. 9-10, pp. 855-886, 1999.

This paper presents a research programme where the main objective is to study the behaviour of Weldox 460 E steel plates impacted by blunt-nosed cylindrical projectiles in the lower ordnance velocity regime. A compressed gas gun is used to carry out high-precision tests, and a digital high-speed camera system is used to photograph the penetration process. A coupled constitutive model of viscoplasticity and ductile damage is formulated and implemented into the non-linear finite element code LS-DYNA, and the material constants for the target plate are determined. The proposed model is applied in simulations of the plate penetration problem and the results are compared with test data. Good agreement between the numerical simulations and the experimental results is found for velocities well above the ballistic limit, while the ballistic limit itself is overestimated by approximately 10 % in the numerical simulations.

Part III:

T. Børvik, O.S. Hopperstad, T. Berstad and M. Langseth. *Computational model of viscoplasticity and ductile damage for projectile impact*, submitted for possible journal publication, 2000.

A coupled constitutive model of viscoplasticity and ductile damage for penetration and impact related problems has been formulated and implemented in the explicit finite element code LS-DYNA. The model, which is based on the constitutive model and fracture strain model of Johnson and Cook, and on continuum damage mechanics as proposed by Lemaitre, includes linear thermoelasticity, the von Mises yield criterion, the associated flow rule, non-linear isotropic strain hardening, strain-rate hardening, temperature softening due to adiabatic heating, isotropic ductile damage and failure. For each of the physical phenomena included in the model, one or several material constants are required. However, all material constants can be identified from relatively simple uniaxial tensile tests without the use of numerical simulations. In this paper the constitutive model is described in detail. Then material tests for Weldox 460 E steel and the calibration procedure are presented and discussed. The calibrated model is finally verified and validated through numerical simulations of material and plate perforation tests investigated experimentally.

Part IV:

T. Børvik, J.R. Leinum, J.K. Solberg, O.S. Hopperstad and M. Langseth. *Observations on shear plug formation in Weldox 460 E steel plates impacted by blunt-nosed projectiles*, accepted for publication in International Journal of Impact Engineering, 2000.

Shear plug formation in circular Weldox 460 E steel plates impacted by blunt-nosed cylindrical projectiles with striking velocities between 100 and 500 m/s has been investigated. Target thickness and projectile impact velocity were the primary variables, and for each target thickness the ballistic limit curve of the material was precisely determined. The test at an impact velocity just below the ballistic limit for each target thickness was selected for a microscopic examination of shear localisation and fracture. In these tests, the plug was pushed only partway through the target, and the localised shear zones outlining the fracture were easily recognised both in the optical and scanning electron microscope. Clear evidence of adiabatic shear bands and material damage due to void growth was found in several of the target plates. Analytical models available in the literature were compared with the results from the experimental and microscopic studies. Reasonable agreement was found between calculations and experiments.

Part V:

T. Børvik, O.S. Hopperstad, T. Berstad and M. Langseth. *Numerical simulation of plugging failure in ballistic penetration*, accepted for publication in *International Journal of Solids and Structures*, 2000.

A coupled computational material model of viscoplasticity and ductile damage has been developed and implemented in LS-DYNA. This model gives good agreement between numerical simulations and experimental observations of plugging failure in ballistic penetration, without the use of inverse modeling or predefined defects. However, even if the model constants can be determined from relatively simple uniaxial tensile tests, the computational model is rather comprehensive. In this paper numerical results obtained by using the fully coupled computational model are compared with results obtained from less sophisticated versions of the material model. The differences between the numerical results will be pointed out and discussed, and details from some of the simulations are shown. To validate the accuracy of the computational model, references will be made to experimental observations from gas-gun penetration tests on 8 mm thick Weldox 460 E steel plates.

Part VI:

T. Børvik, M. Langseth, O.S. Hopperstad and K.A. Malo. *Effect of projectile nose shape in structural impact, part I: Experimental study*, submitted for possible journal publication, 2000.

Projectiles with three different nose shapes (blunt, hemispherical and conical) have been used in gas gun experiments to penetrate 12 mm thick Weldox 460 E steel plates. Based on the experimental results, the ballistic limit curves of the target material were constructed and compared. It was found that the nose shape of the projectile significantly affected both the energy absorption mechanism and the failure mode in the target during penetration. The ballistic limit velocity was about equal and close to 300 m/s for hemispherical and conical projectiles, while it was considerably lower for blunt projectiles. Blunt projectiles caused failure by plugging, which is dominated by adiabatic shear banding, while hemispherical and conical projectiles penetrated the target mainly by pushing the material in front of the projectile aside. Also the ballistic limit curves were influenced by nose shape, primarily due to the differences in projectile deformation at impact. The experimental study given in this part of the paper forms the basis for explicit finite element analysis using the commercial code LS-DYNA presented in Part II of the paper.

Part VII

T. Børvik, O.S. Hopperstad, T. Berstad and M. Langseth. *Effect of projectile nose shape in structural impact, part II: Numerical simulations*, submitted for possible journal publication, 2000.

In Part I of this paper, projectiles with three different nose shapes (blunt, hemispherical and conical) were used in gas gun experiments to penetrate 12 mm thick Weldox 460 E steel plates. It was found that the nose shape of the projectile severely affected both the energy absorption and failure mode of the target structure during penetration. This part of the paper describes numerical simulations of the problem investigated experimentally. A constitutive model of viscoplasticity and ductile damage for projectile impact has earlier been developed and implemented in the explicit finite element code LS-DYNA. Numerical simulations involving the model have been carried out, and the results are compared with the experimental data. However, several numerical problems associated with the element mesh were detected, and adaptive meshing was found necessary in order to obtain reliable results for conical projectiles. From the numerical simulations it is seen that the LS-DYNA code is able

to describe the different failure modes without any predefined defects in the element mesh if special care is taken, and good agreement is in general obtained between the numerical and experimental results.

Part VIII

T. Børvik, O.S. Hopperstad, M. Langseth and K.A. Malo. *Effect of target thickness in blunt projectile penetration of Weldox 460 E steel plates*, submitted for possible journal publication, 2000.

This paper describes an experimental, analytical and numerical investigation of blunt projectile penetration of circular Weldox 460 E steel plates when varying the target thickness and projectile impact velocity. In the experimental tests, a compressed gas gun was used to launch a sabot mounted blunt projectile at impact velocities well above and just below the ballistic limit of the target plate. Nominal hardness, diameter, length and mass of the projectile were kept constant in all tests. The target plate was clamped in a rigid circular frame, and the thickness was varied between 6 and 30 mm. Measurements were made of the initial and final velocities, and the ballistic limit curve was constructed for each target thickness tested. In addition, a digital high-speed camera system was used to photograph the penetration event. The experimental findings from the tests are presented and discussed, and the results are used to assess empirical, analytical and numerical models. As will be shown, the method best suited to take the structural response into account when the deformation mode changes from typical thin plate membrane stretching towards thick plate shear localisation, is the finite element approach.

6. Some Main Results

Some of the main results from the thesis work are given in this chapter in order to give the reader an idea of the outcome generated from this type of generic research, and to show the agreement between experimental and numerical data. Plots showing the experimental results are given in Figure 10. Here, the curves in the left figure are constructed based on results from blunt-nosed projectiles used in programme 1 and 3 in Table 2, while the curves in the right figure in Figure 10 are constructed based on experimental results from programme 2 using different nose shapes and a constant target thickness of 12 mm. The solid lines through the data points are based on least square best fits. Corresponding numerical results using the non-linear finite element code LS-DYNA (Hallquist, 1998) are presented in Figure 11. In simulations with different projectile nose shapes both fixed element meshes and adaptive meshing have been used. Figure 12 compares measured and numerical ballistic limit velocities versus target thickness and the effect of mesh sensitivity on the limit velocity for some target thicknesses in simulations with blunt projectiles.

High-speed camera images from typical perforation tests at impact velocities close to the respective ballistic limits are compared to plots from corresponding numerical simulations in Figure 13 (see also Part VI, Part VII and Part VIII for details). Fringes of accumulated plastic strain are plotted on the deformed mesh in Figure 13a) and c), while fringes of accumulated damage are plotted in Figure 13b), d) and f). Here, a red fringe colour indicates a plastic strain of 0.5 or more, or a damage between 0.25 and 0.3 (critical value). Note also that the stated times do not correspond exactly. The times given on the high-speed camera images refer to the time from camera triggering, while the times on the numerical plots refer to the time from impact. Thus, the comparison should be considered as qualitative rather than quantitative.

It is evident that even though the physical mechanisms governing the perforation process from the tests differ significantly, they are captured and described by the numerical simulations. This illustrates that finite element codes can be very powerful tools in research of impact related problems if one recognises their limitations and understand their operations. They can give detailed understanding of physical processes and may in some cases offer the only viable way to obtain necessary information (Andersen Jr., 1987).

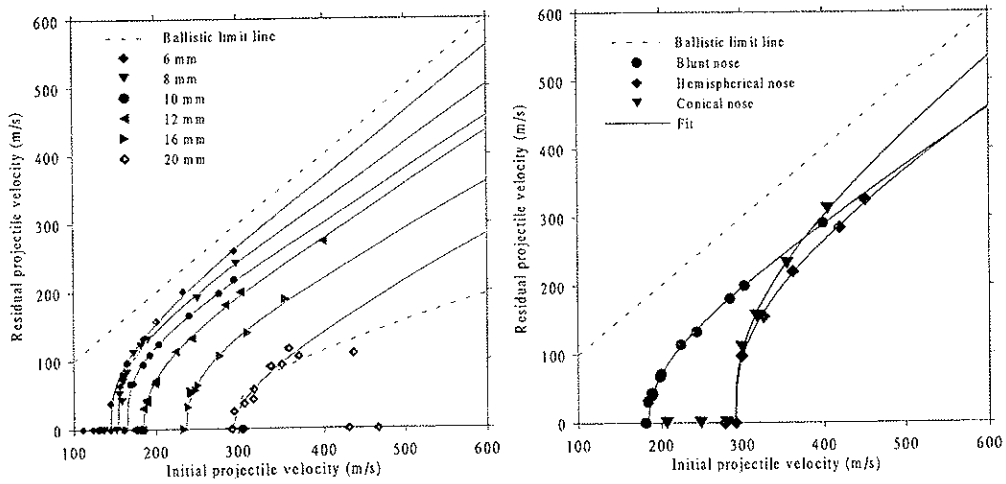


Figure 10: Experimental results for different target thicknesses and projectile nose shapes.

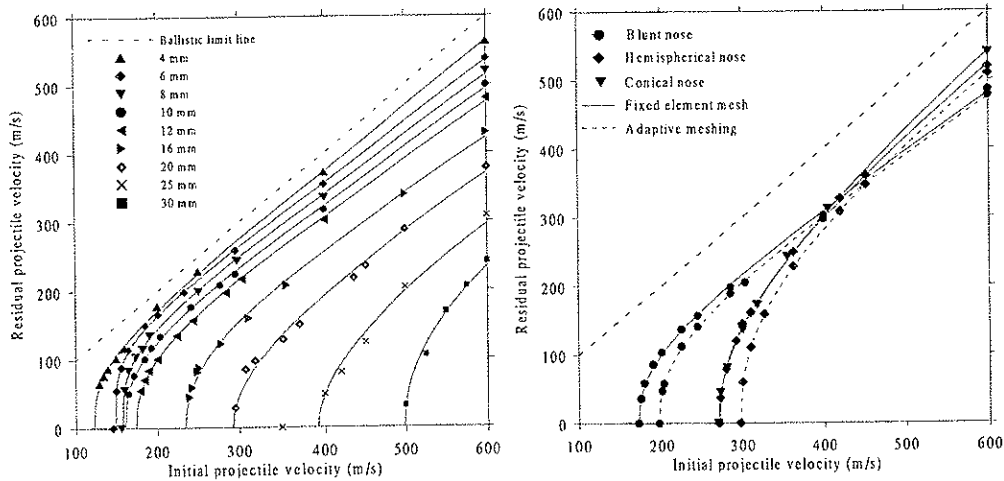


Figure 11: Numerical ballistic limit curves for different target thicknesses and projectile nose shapes.

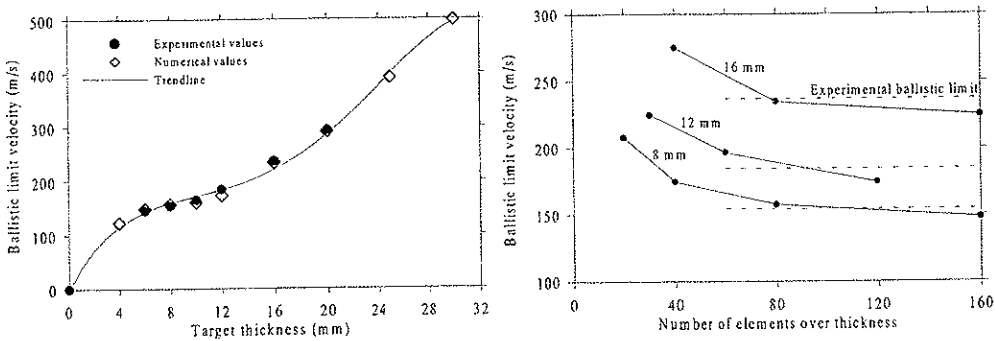
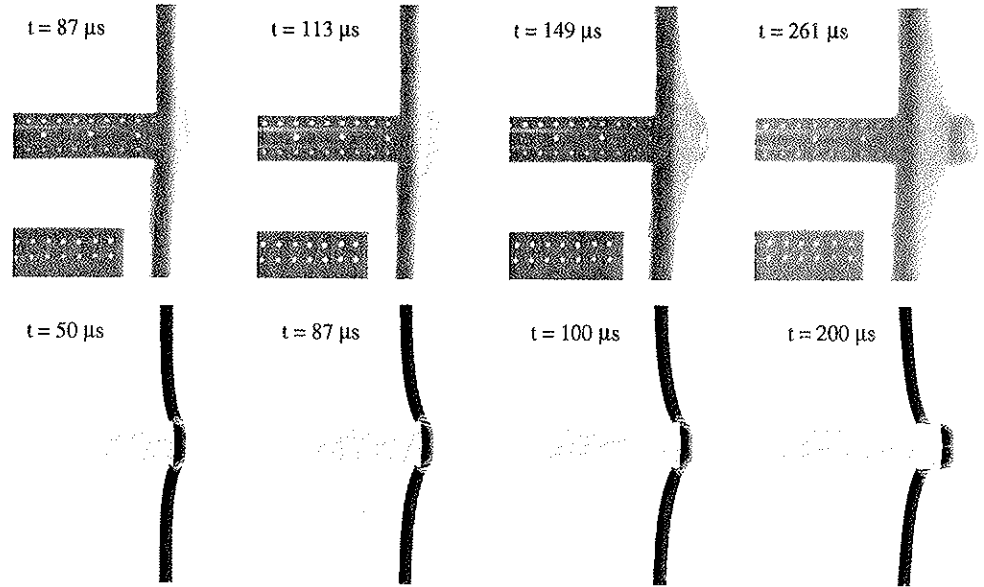
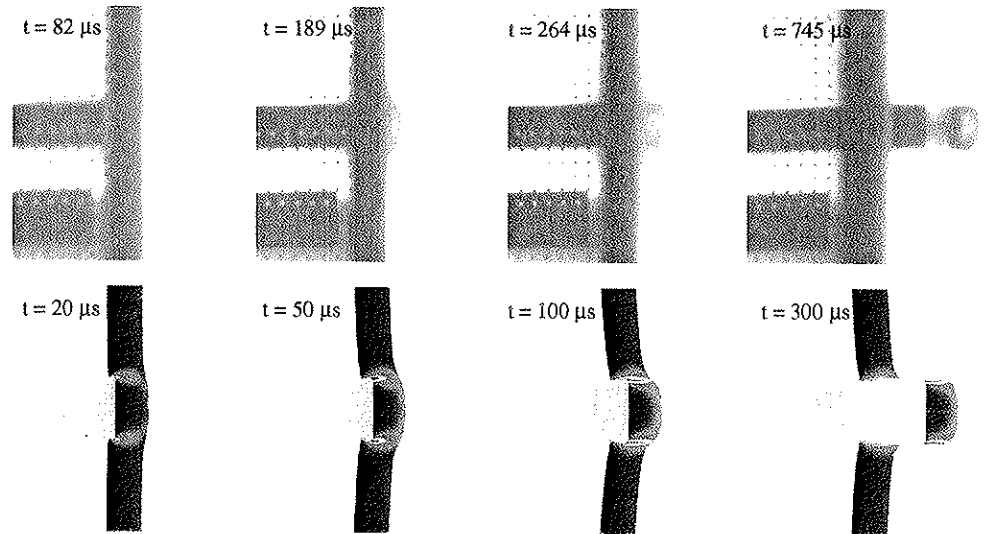


Figure 12: Comparison between measured and numerical ballistic limit velocities versus target thickness and the effect of mesh sensitivity on the ballistic limit velocity for some target thicknesses in simulations with blunt projectiles.

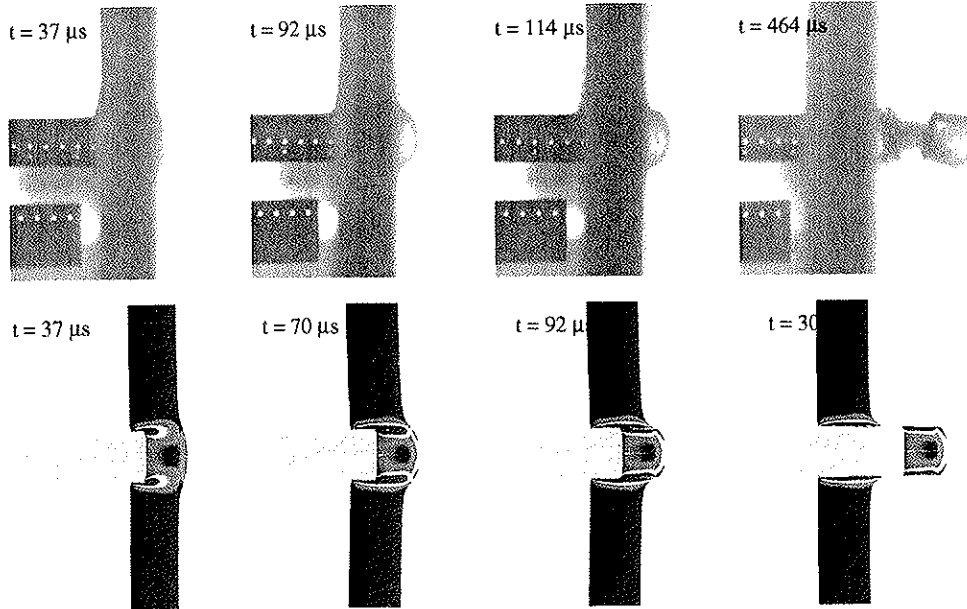
a) Test # 6-11 ($v_i = 156.6$ m/s, $v_r = 63.5$ m/s, $v_{rpl} = 87.0$ m/s, $v_{bl} = 145.5$ m/s)



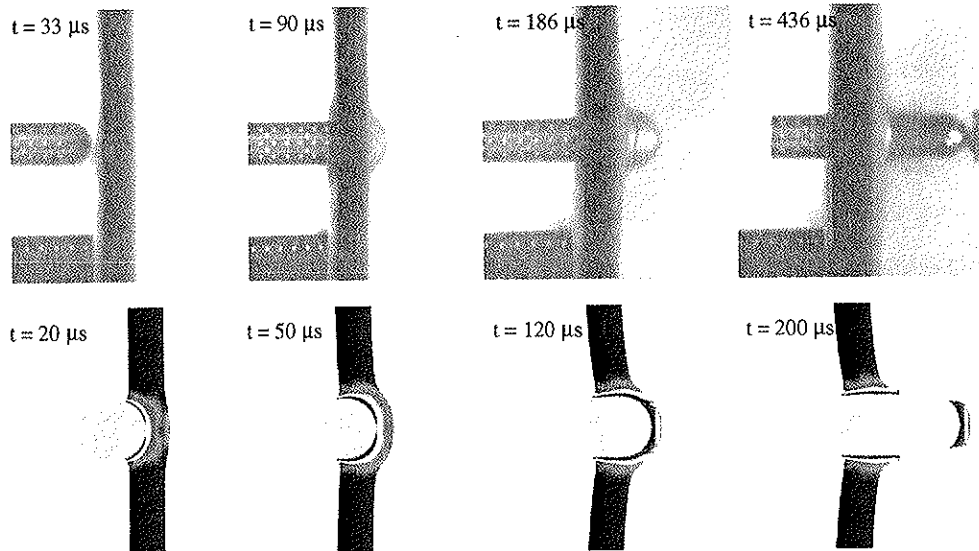
b) Test # 12-16 ($v_i = 189.6$ m/s, $v_r = 42.0$ m/s, $v_{rpl} = 64.0$ m/s, $v_{bl} = 184.5$ m/s)



c) Test # 20-4 ($v_i = 307.2$ m/s, $v_r = 37.1$ m/s, $v_{rpl} = 83.2$ m/s, $v_{bl} = 293.9$ m/s)



d) Test # 12-H1 ($v_i = 300.0$ m/s, $v_r = 97.2$ m/s, $v_{rpl} = 159.5$ m/s, $v_{bl} = 292.1$ m/s)



e) Test # 12-C6 ($v_i = 300.3$ m/s, $v_r = 110.3$ m/s, $v_{bl} = 290.6$ m/s)

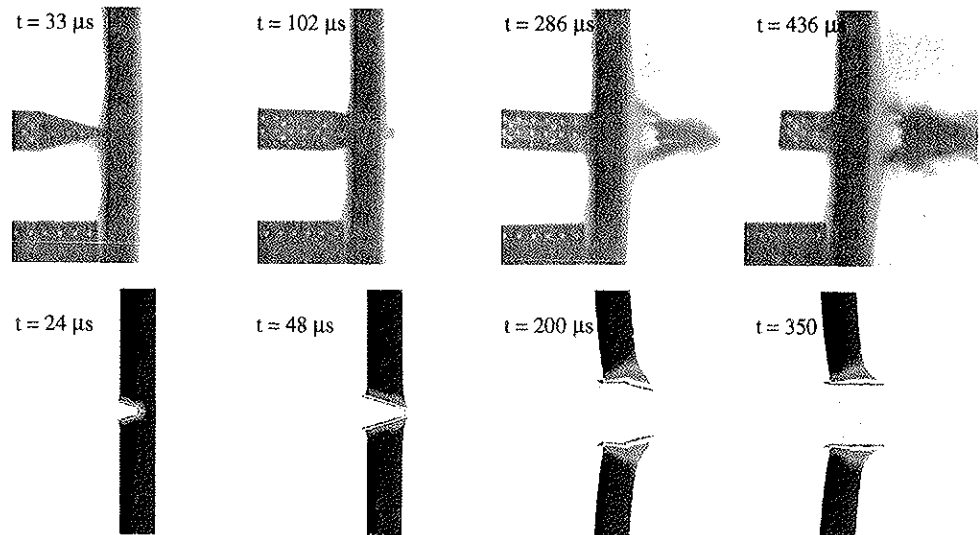


Figure 13: Comparison between high-speed camera images and numerical simulations of the perforation process.

7. Concluding Remarks

This synopsis has been written in order to bring forward the background and some of the main objectives of the thesis, and to establish a closer relation between the different parts dealing with different topics covered in the study. Each part (except for one conference paper) has been submitted for publication in various international journals as independent manuscripts, and at the end of each manuscript a conclusion from that particular part of the work is given. In order not to repeat oneself unnecessarily, and to avoid drawing strict conclusions from the study without relating the results to the specific impact conditions, only general conclusions are given in the following. These are based on a large amount of high-precision impact tests and several hundred large-scale LS-DYNA simulations on the corresponding problem.

It is found that the compressed gas gun, developed and built as a part of this thesis, is an excellent tool in order to carry out high-precision impact tests in the sub-ordnance velocity regime. In addition, experimental results from generic penetration tests have shown to be suitable both for verification and validation of computational methods since both the energy absorption mechanisms and failure mode may easily be changed by varying different impact conditions, such as the projectile nose shape and target thickness.

In computations, it is very important to be able to describe all phenomena occurring in an impact event. This involves a description of the material behaviour under varying stress states, large plastic strains, high strain rates, temperature softening, damage development and local failure. Such complex material behaviour may be the main reason why closed-form analytical models only have had limited success in calculations of penetration and perforation of plated structures. Although computational material models of nearly any degree of

complexity can be incorporated into numerical codes, it is important to remember that model constants have to be extracted from experimental tests. In this study a coupled constitutive model of viscoplasticity and ductile damage has been proposed. All material constants can be identified from relatively simple uniaxial tensile tests without the use of inverse modelling, and a possible calibration procedure has been presented. Of equal importance is the numerical model itself. If for example the element mesh is too coarse or if the element distortion becomes too large during straining, severe errors have to be expected in the simulations.

The LS-DYNA simulations predict with good accuracy the residual projectile velocity as a function of impact velocity, target thickness and projectile nose shapes. The numerical model also describes the correct failure modes for varying impact conditions, but rezoning is needed for conical projectiles. Even though element erosion could be used to remove troublesome elements in these problems, a wrong failure mode was then described. It was also found that simulations with fixed element meshes and rezoning gave similar results.

8. Suggestions for Further Work

In a large project as the one described in this thesis, several related topics are barely touched and many possible extensions of the treated subjects are considered. This generates both new ideas and suggestions for further work. In the same way as for the research methodology defined in Figure 9, these may be divided and sorted into the four main research activities carried out in this study. Some possible topics for further research are briefly presented below.

Experimental equipment part:

- New sabot techniques for impact velocities above 500 m/s, new barrel to prevent the sabot in certain situations.
- Flash x-ray instrumentation for impact tests in brittle materials and laser-curtain based initial velocity measurement station.

Component tests part:

- New materials such as high strength steels, aluminium alloys, high strength concrete, ceramics, composites, etc. Extension of the existing databases on Weldox 460 E steel.
- Lightweight protective structures: compound solutions and material selection.

Material modelling part:

- Dislocation mechanics-based constitutive relations.
- Yield surface and fracture criterion based on the micro-mechanics of voided materials.
- Non-local damage evolution or void growth.
- Calibration of viscoplastic-damage model for the projectile material, calibration of equation-of-state using flyer plate material tests and material tests for new materials.

Numerical simulations part:

- Continued development of adaptive formulation in LS-DYNA.
- Implicit calculations for quasi-static problems of plugging.
- Alternative numerical techniques (such as meshless methods) and 3D simulations.

References / Bibliography

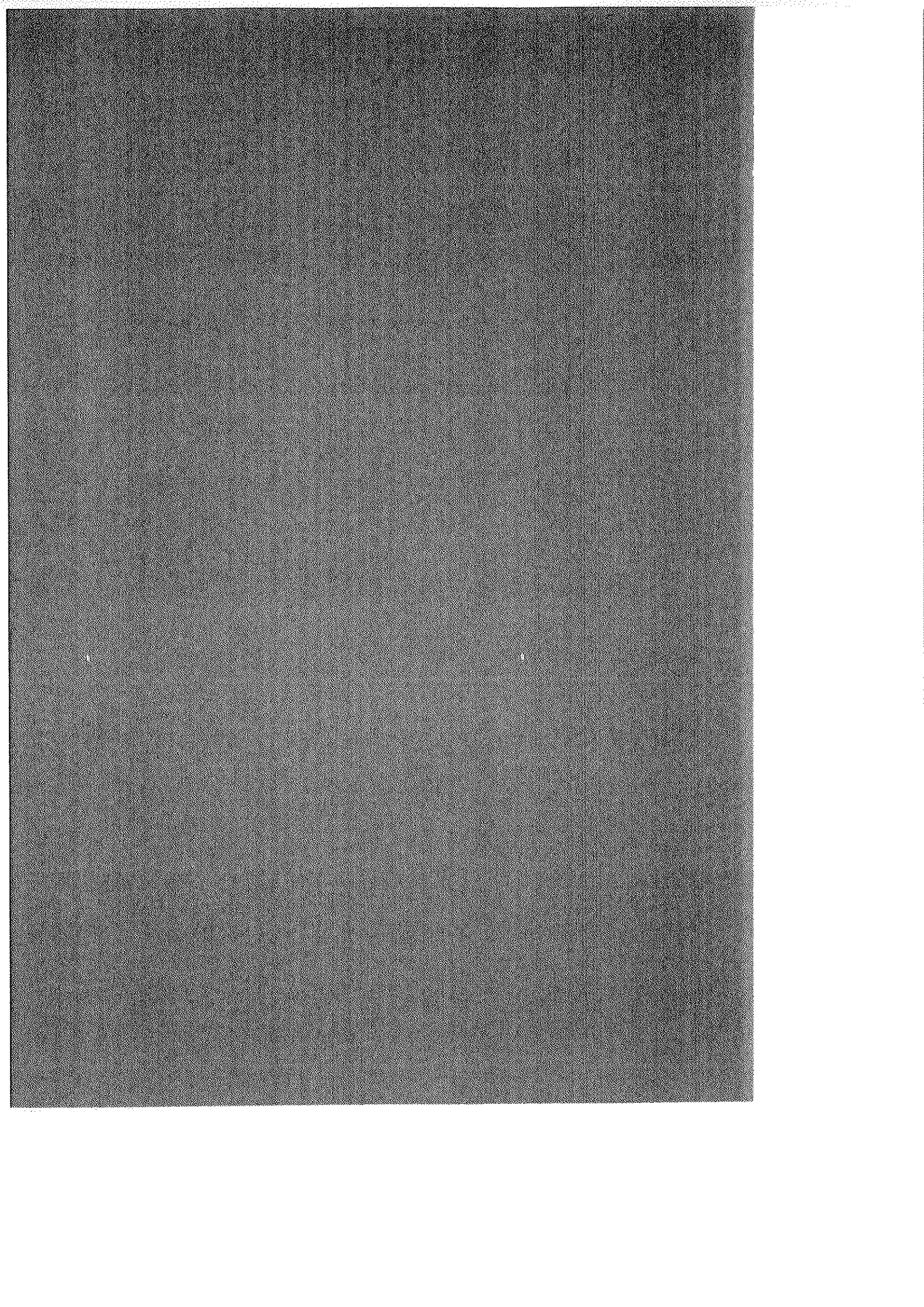
- Anderson Jr CE, 1987. An Overview of the Theory of Hydrocodes, *Int J Impact Engineering* 5, pp 33-59.
- Anderson Jr CE, Bodner SR, 1988. Ballistic Impact: The Status of Analytical and Numerical Modeling, *Int J Impact Engineering* 7 (1), pp 9-35.
- Backman ME, Goldsmith W, 1978. The Mechanics of Penetration of Projectiles into Targets, *Int J Engineering Science* 16, pp 1-99.
- Bai Y, Dodd B, 1992. *Adiabatic Shear Localisation: Occurrence, Theories and Applications*, Pergamon Press.
- Baker WE, Westine PS, Dodge FT, 1991. *Similarity Methods in Engineering Dynamics: Theory and Practice of Scale Modeling*, Revised Edition, Elsevier Science Publishers.
- Bangash MYH, 1993. *Impact and Explosion: Analysis and Design*, Blackwell Scientific Publications.
- Box GEP, Hunter WG, Hunter JS, 1978. *Statistics for Experimenters: An Introduction to Design, Data Analysis and Model Building*, John Wiley and Sons.
- Brown SJ, 1986. Energy Release Protection for Pressurized Systems. Part II. Review of Studies into Impact/Terminal Ballistics, *Appl Mec Rev* 39, pp 177-201.
- Corbett GG, Reid SR, Johnson W, 1996. Impact Loading of Plates and Shells by Free-Flying Projectile, *Int J Impact Engineering* 18 (2), pp 141-230.
- Goldsmith W, 1960. *Impact*, Edward Arnold, Ltd, London.
- Goldsmith W, 1999. Non-ideal projectile impact on targets, *Int J Impact Engineering* 22 (2-3), pp 95-395.
- Hagström J, 1997. *Aluminium Alloy Property Data in Engineering Design*, Doctoral Thesis KTH/AMT-167, Department of Materials Science and Engineering, Royal Institute of Technology (KTH), Stockholm, Sweden, ISSN 0282-9770.
- Johnson W, 1972. *Impact Strength of Materials*, Edward Arnold, Ltd, London.
- Jonas GH, Zukas JA, 1978. Mechanics of Penetration: Analysis and Experiment, *Int J Engineering Science* 16, pp 879-903.
- Jones N, 1989. *Structural Impact*, Cambridge University Press.
- Krauthammer T, Jenssen A, Langseth M, 1996. Precision Testing in Support of Computer Code Validation and Verification, Workshop Report - Fortifikatorisk Notat No. 234/96, The Norwegian Defence Construction Service, Norway.
- Langseth M, 1988. Dropped Objects: Plugging Capacity of Steel Plates, Dr.ing. thesis 1988:25, Department of Structural Engineering, Norwegian Institute of Technology, Trondheim, Norway, ISBN 82-7119-042-3.
- Hallquist JO, 1998. *LS-DYNA: Theoretical manual*, Livermore Software Technology Corporation, CA, USA.
- Macaulay MA, 1987. *Introduction to Impact Engineering*, Chapman and Hall.
- Mayers MA, 1994. *Dynamic Behaviour of Materials*, John Wiley and Sons.
- Mescall J, Weiss V (Eds), 1983. *Material Behaviour under High Stress and Ultrahigh Loading Rates*, Proceedings of the 29th Sagamore Army Materials Conference, 19-23 July, 1982, Lake Placid, New York.
- Stronge WJ, 2000. *Impact Mechanics*, Cambridge University Press.
- Zukas JA (Editor), 1982. *Impact Dynamics*, John Wiley and Son.
- Zukas JA (Editor), 1990. *High Velocity Impact Dynamics*, John Wiley and Sons.

Part I

T. Børvik, K. Holen, M. Langseth and K.A. Måné

An Experimental set-up used in Ballistic Penetration.

Proceedings of Fifth International Symposium on Structures under Shock and Impact, pp. 683 - 692, Thessaloniki, Greece, 24 - 26 June, 1998.



An experimental set-up used in ballistic penetration

T. Børvik¹⁾, K. Holen¹⁾, M. Langseth²⁾ & K. A. Malo²⁾

¹⁾ Norwegian Defence Construction Service, Central Staff / Technical Division, N-0015 Oslo, Norway.

²⁾ Norwegian University of Science and Technology, Dept. of Structural Engineering, N-7034 Trondheim, Norway.

EMail: tore.borvik@bygg.ntnu.no

Abstract

This paper describes an experimental set-up where a digital high-speed camera is used together with a compressed gas gun in order to study the phenomena associated with ballistic penetration. Until recently, photographic studies of ballistics were limited either by time-consuming film development or a moderate framing rate during testing. These obstacles have been overcome by the introduction of camera systems combining the advantages of an image converter camera and a CCD camera. The image converter camera provides extremely fast shutter speeds (up to 20 million frames per sec.), while the CCD part provides high quality digital pictures that are available immediately after the experiment. By utilising the advantages of the system, important parameters such as velocities and angles can be determined during penetration. To demonstrate the possibilities of the experimental set-up, some test results are presented.

1 Introduction

Impact and impact-related problems have been a subject of considerable research for both military and industrial applications since World War II, and substantial effort has been invested in order to physically understand

and mathematically describe the phenomena taking place during ballistic penetration [e.g. 1-2]. So far, most progress has been made during experimental investigations of the normal perforation of metallic plates, and a large number of test results can be found in the literature. However, the experimental details are often limited and not always suitable for validation of analytical or numerical models. To perform high-precision penetration tests, sophisticated and reliable instrumentation is required. The ballistic experimental conditions enforce the use of optical measuring devices, but until recently particularly photographic techniques have been limited either by time-consuming film development or a moderate framing rate during testing. These obstacles have now been overcome by the introduction of a camera system combining the advantages of both an image converter camera and a CCD camera. This paper focuses on a digital high-speed camera that is used both for visualization and measurements during the ballistic penetration of circular steel targets impacted by hardened steel projectiles. Mirrors are used to give a 3D image of the projectile trajectory during testing. Based on the digital images and various computer subroutines, angles and velocities are determined as a function of penetration time immediately after a test. Such information has earlier been hard to obtain. Finally, the paper gives an example from an experimental programme described in [5].

2 Experimental set-up

2.1 Compressed gas gun

The compressed gas gun seen in Fig. 1 and described in [3] is used to launch the projectile. The main components of the gas gun are the 200 bar pressure tank, the specially-designed firing unit for compressed gas, the 10 m long smooth barrel of calibre 50 mm and the closed 16 m³ impact chamber. The gas gun is designed to launch a 250 g sabot mounted projectile to a maximum velocity of approximately 1000 m/s when helium is used as a propellant gas. When the sabot package leaves the muzzle, the sabot is immediately separated from the projectile due to aerodynamic forces. A sabot trap, located about 1.5 m from the muzzle, allows the projectile to pass freely while the sabot parts are stopped. The projectile passes the initial velocity measurement station before it impacts the target after about 2 m of free flight. The target is clamped in a rigid frame, having an inner clamp diameter of 500 mm. To allow pictures to be taken during impact, the clamping system is equipped with a 150 mm

framing window. If the projectile perforates the target, residual velocities are measured before all free flying bodies are stopped without further damage in a rag-box filled with foam and graded plywood. After testing, the impact chamber is opened for final investigations of the target, projectile and plug.

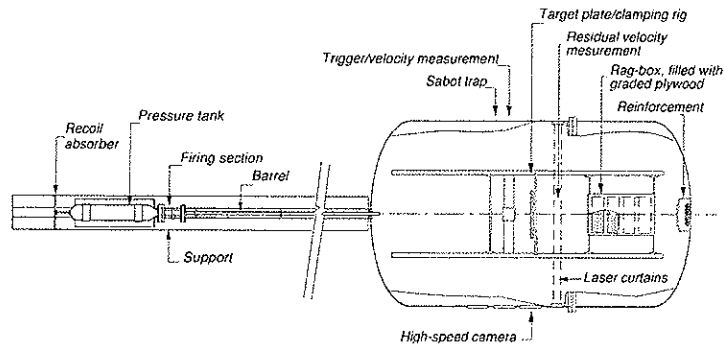


Figure 1: Sketch of compressed gas gun [3]

To measure the initial projectile velocity, a photocell system is used that has light-barriers with LED-light sources on the upper side of the projectile path and detectors on the lower side. When the projectile passes between the sources and detectors in the light-barrier, light is interrupted and signals are given to a nanosecond counter. Furthermore, the digital high-speed camera is triggered when the second light-barrier is disturbed. A similar system is used to measure the residual velocities if perforation takes place. However, instead of using LED-light, each light source consists of six lasers mounted in line to give parallel beams. Detectors are mounted in two lines to match the laser light sources. The detectors feed an amplifier followed by a trigger that detects any abrupt decrease in signal level. When the output signals are stored on a digital oscilloscope, information is obtained regarding velocities and lengths of all passing objects. The accuracy of both systems is found to be very good [3].

2.2 High-speed camera description and set-up

The Ultramac FS 501 high-speed image converter camera shown in Fig. 2 is used in this study. The system is fully computer operated and capable of framing rates from 2,000 to 20,000,000 frames per second with minimum exposure times down to 10 ns. In framing mode each exposure

and interframe time can be independently selected and programmed. The image format may be programmed from 8 to 24 pictures with automatic framing mask selection and positioning. Multi-exposures and streak operation are also available. The CCD readout system used in this camera system utilises a high-resolution chip of 2048×2048 pixels with 16 bits dynamic resolution. Polaroid or negative film may also be used for image recording.

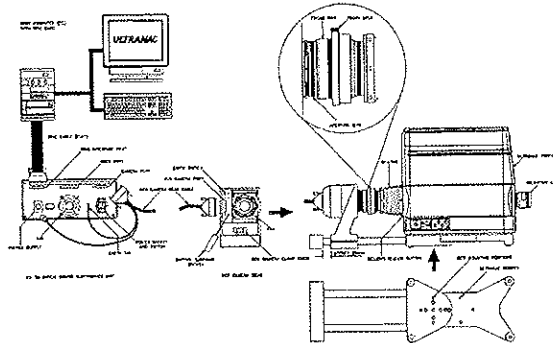


Figure 2: The Ultramac FS 501 high-speed image converter camera

The camera system is set perpendicular to the projectile path in the target plane in order to record the projectile both before and after impact. To reconstruct a full 3D description of the penetration process it is necessary to picture the projectile from at least two different viewpoints simultaneously. Two mirrors are therefore mounted above the projectile path at an angle of 45° with respect to the centreline of the camera, one on each side of the target plate (see Fig. 3).

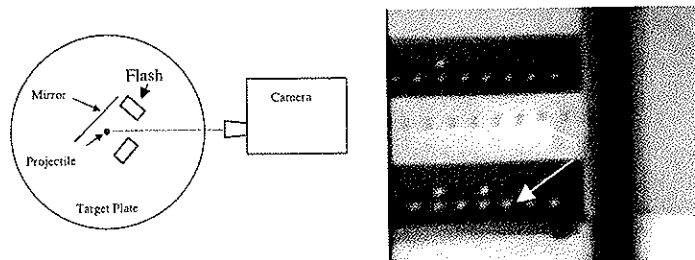


Figure 3: Set-up of high-speed camera giving 3D images [4]

However, the alignment of both the camera system and the mirrors is crucial in order to have good, reliable images. Furthermore, a lot of light is required in order to avoid blur in the images. In this study, 4 flash heads of 60 Joule each are used (2 on each side of the target). In addition, a Cordin model 659 flash lamp system has been installed. The system gives 1100 Joule of extra light divided between two flash heads.

2.3 Spatial camera calibration

Due to aberrations in the image converter tube and the optics, distortions of the digital images are observed. Consequently, it may be necessary to calibrate the camera system, especially if angles are to be measured with high precision. The idea of the calibration routine is to establish a mathematical relationship between the known co-ordinates in object space and the measured co-ordinates in image space (see Fig. 4). The first step is to take a picture of a calibration plate, where fiducial marks are located as drilled holes at a spatial distance of $10 \text{ mm} \pm 0.01$. Secondly, a computer subroutine is used to determine the co-ordinates for the fiducial marks in the digital image. A relationship between the two co-ordinate systems is then established. This information is stored in lookup tables, which are used to correct each pixel within the digital image. Due to non-symmetrical aberrations in the full frame, caused by an imperfect lens system, different lookup tables have to be created for each image. Therefore, the calibration procedure is time consuming and is not carried out prior to every test. However, misalignments of the equipment are always taken into account if angle measurements are of importance [4].

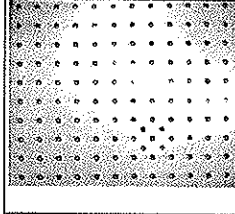
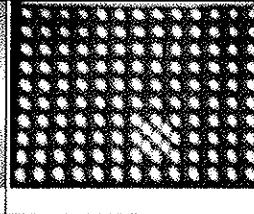
1. Object space	2. Image space	3. Lookup table
		$x_{obj} = f_1(x_{pic}, y_{pic})$ $y_{obj} = f_2(x_{pic}, y_{pic})$
Calibration object with known x_{obj} and y_{obj} co-ordinates of the fiducial marks.	Distorted digital image of the calibration object. The x_{pic} and y_{pic} co-ordinates are determined.	By interpolation every pixel is given a known position in the object space.

Figure 4: High-speed camera calibration routine

2.4 Angle measurements

In most ballistic experiments it is important to control and determine the path of the projectile during penetration. This is necessary because only small angle deviations from the theoretical projectile path at impact can alter the penetration capacity. To be able to make such measurements, the following computer subroutine has been developed. One of the images within the full frame of the test is picked out. By high-pass filtering, all edges in the image are highlighted. The edge of the object to be measured is marked and all pixels within this area with an intensity greater than $(\max + \min)/2$ are selected. The pixel values are plotted in a x-y graph and a least squares method is used to find the best fit line between the points and thereby the angle. By repeating this procedure for all the images within the full frame it is possible to give a full 3D representation of the travelled path as a function of penetration time. The procedure used to calculate the angles is described in Fig. 5.

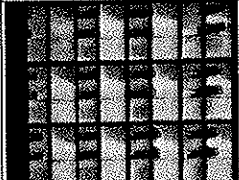
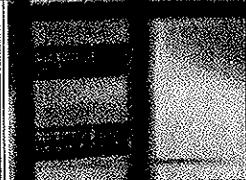
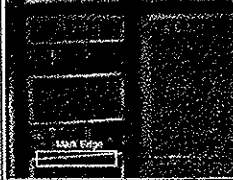



<p>1. Full frame</p> 	<p>2. Select image</p> 	<p>3. High-pass filtering</p> 
<p>The full frame picture of the experiment.</p>	<p>Pick out the image to study.</p>	<p>High-pass filter and mark edge to measure.</p>
<p>4. Plot selected pixels</p>	<p>5. Pixels → Object space</p>	<p>6. Find angle</p>
		
<p>Pixels in the marked area with an intensity greater than $(\max + \min)/2$ are selected.</p>	<p>The correct lookup table transforms each of the selected pixels into object space.</p>	<p>A least squares method is used to find a best-fit line and thereby the angle.</p>

Figure 5: Procedure for the calculation of angles

2.5 Velocity measurements

Based on the digital high-speed camera images, it is also possible to obtain the travelled distance, velocity and acceleration as a function of penetration time for the assumed rigid bodies. This is done by the computer subroutine described in Fig. 6. Both the moving projectile and the stationary support are equipped with fiducial marks, which are typically white dots giving maximum contrast in the image. Each dot is identified by the cursor, and the subroutine calculates the centre of gravity based on the pixel intensity within the detected area. Thus, the coordinates of the fiducial mark are determined. This is done for several fiducial marks both on the moving body and the stationary support. Moving to the next image, the relative distance moved by the body is found if the same fiducial marks are detected as in the previous image.

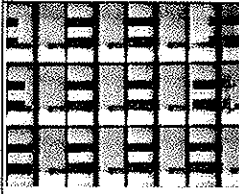
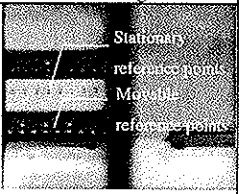
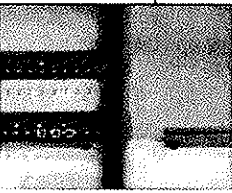
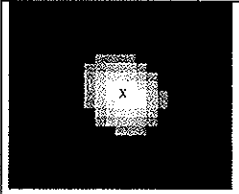
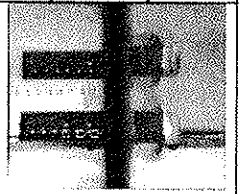
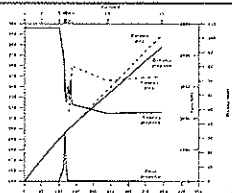
1. Full frame	2. Image	3. Selection of points
		
The full frame picture of the test is shown. The total number of points to measure is selected.	The different images within the full frame are selected and enlarged, one by one.	Fiducial marks on the projectile and support are marked by the cursor, and detected by the program.
4. Centre of gravity	5. Repetition of procedure	6. Results
		
The point is enlarged 10 times. Unwanted pixels are removed, and centre of gravity is calculated based on pixel intensity.	The procedure is repeated for all images in the test. The sub-pixel distance moved between each image is calculated.	Based on the known time interval and a calibration value, distance, velocity and acceleration is found as a function of time.

Figure 6: Procedure for calculation of velocity

The time step Δt between the images is known and set by the user prior to the test. By making use of a known calibration value that transforms pixels into millimetres, the average velocity and acceleration may be calculated. The procedure is repeated for all images within the full frame, and the velocity-time curve is constructed. Due to the sub-pixel resolution, gained by calculating the centre of gravity for each fiducial mark, the accuracy of the velocity measurements is generally very high.

3 Experimental results

One main purpose of the experimental set-up described in this paper is to obtain precision test data for validation of numerical and analytical penetration models. In order to demonstrate the features of the equipment, one test from an experimental programme on the normal penetration of Weldox 460 E steel plates will be shown [5]. In these tests, the compressed gas gun is used to launch a blunt-ended steel projectile at an initial velocity between 130 and 300 m/s, representing impact velocities just below and well above the ballistic limit of the target. The nominal hardness (HRC 53), diameter (20 mm), length (80 mm) and mass (0.197 kg) of the projectile are kept constant for all the tests. The circular target plate, which has an initial thickness of 10 mm and 500 mm in diameter, is clamped in a rigid frame. All targets failed by plugging.

Fig. 7 shows the high-speed camera images of the test. Angles are measured during impact using the procedure described in Fig. 5. The angle measurements just prior to impact show that the total yaw angle, i.e. the vector sum of the pitch and yaw angles as defined in Fig. 3, is insignificant (0.32°). Velocities are measured both using the photocell systems and the digital high-speed camera. The first photocell system measured the initial projectile velocity to be 296 m/s, while the residual velocity for the plug and projectile was measured to be 253 m/s and 219 m/s, respectively. From the high-speed camera images, the residual velocity of the plug and projectile was calculated to be 250 m/s and 217 m/s, respectively. As seen, excellent agreement is found between the two different measuring techniques. Finally, Fig. 8 shows the obtained distance, velocity and force for both the projectile and plug as a function of penetration time. The projectile impacts the target after about 100 μ s. During the next $\sim 40 \mu$ s the projectile penetrates the target, giving a sharp velocity drop, before fracture occurs and a plug is separated from the target. However, it is hard to estimate the perforation time exactly since the camera system only provides a limited number of images. The

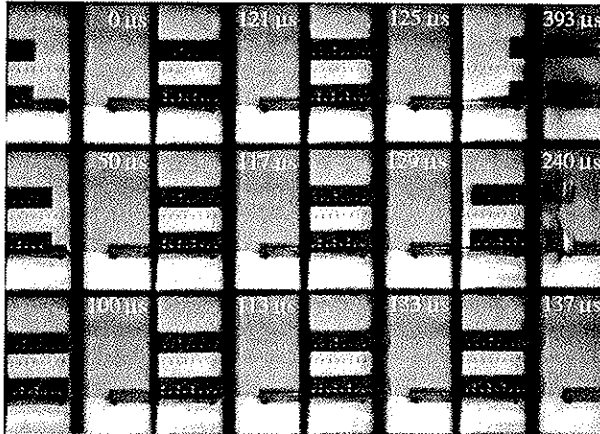


Figure 7: High-speed camera images [5]

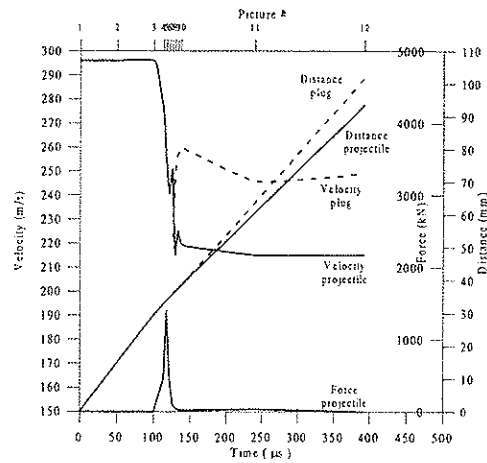


Figure 8: Measured distance, velocity and force

projectile velocity after plugging is almost constant, indicating a negligible sliding friction between the projectile and target after fracture. The plug has a rapid velocity increase due to release of elastic energy, before it stabilises at a velocity approximately 15% higher than the

projectile. The calculated velocity-time curve of the projectile also reveals two peaks, which are believed caused either by a moving stress wave in the projectile or error measurements due to aberrations in the digital images. However, at present this is not known and further investigations are necessary.

4 Conclusions

This paper describes an experimental set-up where a digital high-speed camera is used together with a compressed gas gun to study the phenomena associated with ballistic penetration. During testing, the high-speed camera system is used both for visualisation and measurements of the penetration process. The high quality images that are provided give important information to help understand the complex penetration process. The digital images are also used to measure angles and travelled distance, and velocities and accelerations are calculated as a function of penetration time. These results have been compared to numerical and analytical models, and the agreement is found to be satisfactory [6].

5 References

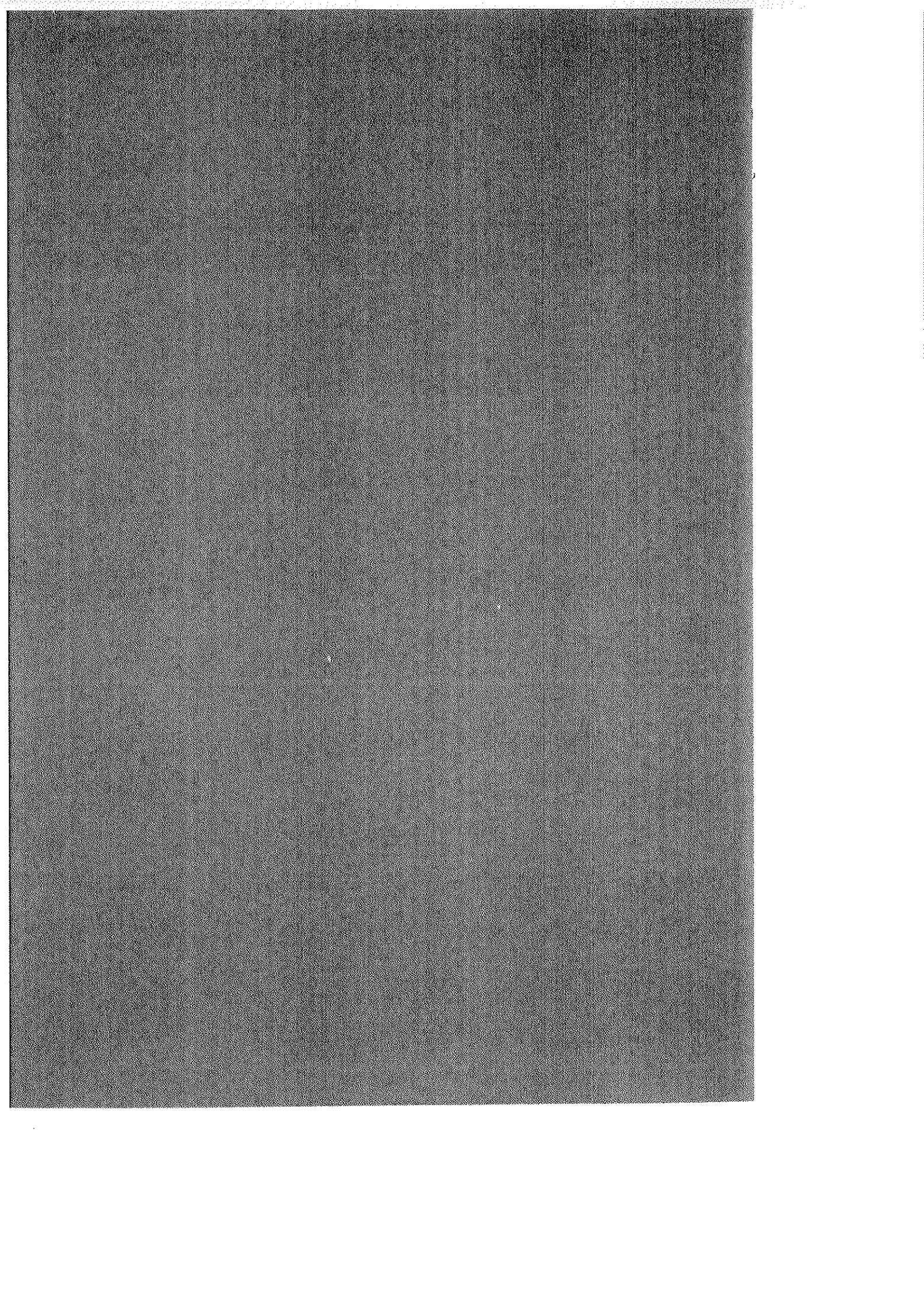
- [1] Backman, M.E. & Goldsmith, W., The Mechanics of Penetration of Projectiles into Targets, *Int. J. Engng. Sci.*, **16**, pp. 1-99, 1978.
- [2] Corbett, G.G., Reid, S.R. & Johnson, W., Impact Loading of Plates and Shells by Free-Flying Projectiles: A Review, *Int. J. Impact Engng.*, **18** (2), pp. 141-230, 1996.
- [3] Børvik, T., Langseth, M. & Malo, K.A., A Compressed Gas Gun for Impact Testing, Technical Report No. 242/97, NDCS, 1997.
- [4] Børvik, T., Holen, K. & Langseth, M., Determination of Projectile Path during Ballistic Penetration by use of a High-Speed Digital Camera, *Paper presented at the Association of High-Speed Photography Conference*, Cambridge, U.K., April, 1997.
- [5] Børvik, T., Langseth, M., Malo, K.A. & Hopperstad, O.S., Experimental Determination of the Ballistic Limit in Weldox 460 E Steel Plates, *Proc. of the 11th Int. Conf. on Experimental Mechanics*, Oxford, U.K., 24-28 August, 1998.
- [6] Børvik, T., Langseth, M., Hopperstad, O.S. & Malo, K.A., Ballistic Penetration of Steel Plates, *Int. Symp. on Transient Loading and Response on Structures*, Trondheim, Norway, 25-27 May, 1998.

Part II

T. Borvik, M. Langseth, O.S. Hopperstad and K.A. Malo

Ballistic Penetration of Steel Plates.

International Journal of Impact Engineering, Vol. 22, No. 9-10,
pp. 855-886, 1999.



Ballistic Penetration of Steel Plates

T. Børvik¹, M. Langseth², O.S. Hopperstad² and K.A. Malo²

¹ *Norwegian Defence Construction Service, Central Staff / Technical Division, N-0015 Oslo, Norway.*

² *Department of Structural Engineering, Norwegian University of Science and Technology, N-7034 Trondheim, Norway.*

Abstract

This paper presents a research programme in progress where the main objective is to study the behaviour of Weldox 460 E steel plates impacted by blunt-nosed cylindrical projectiles in the lower ordnance velocity regime. A compressed gas gun is used to carry out high-precision tests, and a digital high-speed camera system is used to photograph the penetration process. A coupled constitutive model of viscoplasticity and ductile damage is formulated and implemented into the non-linear finite element code LS-DYNA, and the material constants for the target plate are determined. The proposed model is applied in simulations of the plate penetration problem and the results are compared with test data. Good agreement between the numerical simulations and the experimental results is found for velocities well above the ballistic limit, while the ballistic limit itself is overestimated by approximately 10 % in the numerical simulations.

Keywords: Ballistic penetration; Experimental tests; Viscoplasticity; Damage; Numerical simulations

1. Introduction

Impact and impact related problems have been a considerable research topic for decades, and substantial effort has been invested in order to physically understand and mathematically describe the phenomena taking place during ordnance ballistic penetration [1-7]. So far, most progress has been made during experimental investigations of the normal perforation of metal plates, and a large number of studies can be found in the literature [8-15]. However, due to the complexity and costs related to ballistic experiments it is not optimal to base all impact related studies on laboratory tests alone. Therefore, a general solution technique is requested as a supplement to high-precision testing in order to reduce the experimental needs to a minimum.

A number of analytical models have been proposed over the years [16-23], but the complexity of many impact events often limits the general use of closed-form analytical solutions. It may therefore be preferable to use numerical methods in the attempt to solve this class of problems. However, numerical studies involving impact and penetration in the sub-ordnance and ordnance velocity regime are still few in the literature, even though the finite element method has been adopted as a general tool in most communities. The reason may be that the method does not have the accuracy and robustness required for reliable material description and fracture calculation during perforation. Earlier work using e.g. erosion techniques and element-kill options [24] has revealed some weaknesses [25-27], and according to Belytschko [28] finite element simulations including geometrical and material instabilities, combined with discontinuities in space and time, are still very difficult to treat computationally. Thus, special attention is needed to make progress.

This paper is based on a joint research programme in progress between the Norwegian Defence Construction Service and the Department of Structural Engineering, Norwegian University of Science and Technology, where the main objective is to study the behaviour of steel plates impacted by blunt-nosed projectiles. In order to make progress, substantial knowledge regarding the physical phenomena controlling the penetration problem is necessary. Such information is obtained through high-precision penetration tests and material tests under impact generated high strain-rate loading conditions. The experimental findings are used to validate if a computational model of viscoplasticity and ductile damage can be used to numerically predict the target response during penetration.

In the paper, some of the experimental and numerical work carried out so far will be summarised, compared and discussed. Finally, some preliminary conclusions from the project are given.

2. Experimental set-up

The compressed gas gun shown in Figure 1 [29] has been designed in order to launch the projectile. The main components of the gas gun are the 200 bar pressure tank, the purpose-built firing section for compressed gas, the 10 m long smooth barrel of calibre 50 mm and the closed 16 m³ impact chamber. The gas gun is capable of launching a 250 g projectile package to a maximum velocity of 1000 m/s when helium is used as a propellant gas. The projectile is

mounted in an 8-pieced serrated sabot with an obturator and inserted into the rear section of the barrel. To reduce the sabot weight, which is known to be crucial regarding sabot separation and subsequent pitch and yaw, the sabot is manufactured from a combination of polycarbonat and foam. When the sabot package leaves the muzzle, the sabot is immediately separated from the projectile due to aerodynamic forces. A sabot trap, located about 1.5 m from the muzzle, allows the projectile to pass freely while the sabot parts are stopped. The projectile then passes the initial velocity measurement station before it impacts the target after about 2 m of free flight. The circular target is clamped in a rigid frame, having an inner clamp diameter of 500 mm. To allow high-speed photography during impact, the clamping system is equipped with a 150 mm framing window. If the projectile perforates the target, residual velocities are measured before all free flying objects are stopped without further damage in a rag-box. After testing, the impact chamber is opened for final inspections and measurements of the target, projectile and plug.

To measure initial projectile velocity (v_i), a photocell system having two identical light-barriers with LED-light sources on the upper side of the projectile path and detectors on the lower side has been constructed. When the projectile passes between the sources and detectors in the light-barrier, light is interrupted and signals are given to a nanosecond counter. The second light-barrier also works as a trigger for the digital high-speed camera system. A similar system was developed to measure residual velocities (v_r) if perforation takes place. Here, each light source consists of six lasers mounted in line to give parallel beams. Detectors are mounted in two lines to match the laser light sources. The detectors feed an amplifier followed by a trigger that detects any abrupt decrease in signal level. When the output signals are stored on a digital oscilloscope, information regarding velocity and length of all passing objects is obtained. The accuracy of the systems is proven to be high [29].

It is important to be able to observe the different events during ballistic penetration. However, until recently photographic techniques in particular have been limited by time-consuming film development or moderate framing rates during testing. These obstacles have been overcome by camera systems that combine the advantages of an image converter camera and a CCD camera. The image converter camera provides extremely fast shutter speeds, while the CCD camera provides digital images that are available immediately after the experiment. In this study the Ultramac FS 501 digital high-speed image converter camera [30-31] is used both for visualisation and measurements of the penetration process. The system is fully computer operated and capable of framing rates from 2,000 to 20,000,000 frames per second with exposure times down to 10 ns. In framing mode each exposure and interframe time can

be independently selected, and the image format may be chosen from 8 to 24 pictures. The CCD readout system uses a high-resolution chip of 2048 x 2048 pixels with 16 bit dynamic resolution. The camera system is set perpendicular to the projectile path in the target plane in order to record the projectile both before and after perforation. To reconstruct a full 3D description of the penetration process, mirrors are mounted above the projectile path at an angle of 45° with respect to the centreline of the camera, one on each side of the target plate (see Figure 2). However, both the aligning of the system and the luminance during testing are crucial parameters in order to have good, reliable images. In this study, 4 flash heads of 60 Joule and 2 flash heads of 550 Joule have been used to get sufficient lighting.

As indicated above, the high-speed camera system is also used for measurements. This is made possible by advanced image processing of the digital pictures, and several computer sub-routines have been developed [31]. The most important feature is the possibility to obtain travelled distance, velocity and acceleration as a function of penetration time for the assumed rigid bodies. This is illustrated in Figure 3. Both the moving projectile and the stationary support are equipped with fiducial marks, which typically are white dots giving maximum contrast in the image. Each dot is identified by the cursor, and the sub-routine calculates the centre of gravity of the fiducial mark based on the intensity of the pixels within the defined area. Thus, the co-ordinates of the fiducial mark are determined. This is done for several fiducial marks both on the moving body and the stationary support. Moving to the next image, the relative distance moved by the body is found if the same fiducial marks as in the previous image are detected. The time step Δt between the images is known and set by the user prior to the test. By making use of a known calibration value that transforms pixels into millimetres, the average velocity and acceleration can be calculated. The procedure is repeated for all images within the full frame, and the velocity-time curve is constructed. Due to the sub-pixel resolution, gained by calculating the centre of gravity for each fiducial mark, the accuracy of the velocity measurements is generally high. Also angles can be measured as a function of penetration time [30-31], and a comprehensive high-speed camera calibration routine has been developed in order to correct aberrations known to appear in the digital images [31].

3. Experimental results

The main objective of the experimental investigations performed in this project is to study the different phenomena taking place during ballistic penetration. At the same time, high-precision test data becomes available for validation of solution methods. In this particular paper, emphasis will be on an experimental programme carried out to determine the ballistic limit curve of a 12 mm thick Weldox 460 E steel plate. Data and observations from a similar experimental programme on a 10 mm thick Weldox 460 E steel plate [32] are in addition given for comparison.

Blunt-nosed cylindrical projectiles are machined from Arne tool steel, having a nominal mass (m_p), diameter (d_p) and length (l_p) of 197 g, 20 mm and 80 mm, respectively. The total mass of the sabot is in addition approximately 90 gram for all tests. After machining, the projectiles are oil-hardened to a nominal Rockwell C value of 53 ($\sigma_0 \approx 1850$ MPa). Even if this represents an upper limit for projectile hardness, plastic deformation may appear in the nose part. Finally, the projectiles are painted dead black, measured and equipped with fiducial marks. All targets are manufactured from the same Weldox 460 E steel plate, having a nominal plate thickness (h_p) of 12 mm and material properties as given in Table 2. After careful cutting from the larger plate and sandblasting on both sides, 21 equally spaced holes are drilled on a 550 mm diameter bolt circle and the target is clamped in a rigid frame with an inner clamp diameter of 500 mm. Finally, geometrical imperfections, thickness and initial oblique are measured.

The experimental programme and some important test results are given in Table 1, while Figure 4 shows a graphical representation of the most interesting response parameters obtained during testing. All parameters are kept constant in the tests except for the impact velocity (v_i), which are varied between 170 and 310 m/s, representing velocities just below and well above the ballistic limit velocity (v_{bl}) of the target material.

Pitch and yaw angles are measured from the digital high-speed camera images just prior to impact in order to determine the projectile's path during free flight [31]. From all tests, the total yaw angle at impact is found to be small and normally between $0.5 - 1^\circ$. These values are well below the critical value of $3 - 4^\circ$, known to give an increase in the ballistic limit velocity as reported in e.g. [4, 33]. Also target oblique is measured and found negligible.

The ballistic limit curve for the 12 mm thick Weldox 460 E steel plate shown in Figure 4a) is constructed based on the measured initial (v_i) and residual (v_r) projectile velocities given in

Table 1. Several tests are performed in an attempt to determine the ballistic limit velocity as closely as possible, and the difference between the highest velocity not giving perforation (test # 12-16) and the lowest velocity giving complete perforation (test # 12-14) is found to be less than 0.5 m/s. The residual velocity of the plug (v_{rpl}), which is plotted in Figure 4a) for comparison, is always found to be higher than that of the projectile even if the velocities seem to be similar immediately after fracture. This sudden increase in plug velocity after fracture is assumed caused by elastic stress waves in the projectile and plug. The ratio between the velocity curves is found to decrease with increasing velocity.

From the plotted data points it is not clear if a distinct jump as indicated in [34] is present in these experiments. A small jump at the ballistic limit seems to appear, but this may be due to scatter in the target material properties. However, it has been noticed that the target material is sensitive to variations in velocity near the ballistic limit, and that the residual velocity of the projectile is never small.

The experimental data points have been fitted to a model proposed by Lambert [4] in order to calculate residual projectile velocity (v_r) as a function of the measured initial projectile velocity (v_i) and the experimentally obtained ballistic limit velocity (v_{bl})

$$v_r = \begin{cases} 0 & 0 \leq v_i \leq v_{bl} \\ a (v_i^p - v_{bl}^p)^{1/p} & v_i > v_{bl} \end{cases} \quad (1)$$

By using the method of least squares the model constants a and p are found to be 0.76 and 2.36, respectively, and as seen from Figure 4a) excellent agreement between the experimental data and the model fit is obtained. If p is chosen equal to 2, a curve fit gives a equal to 0.85. These values of a and p lead us to the model proposed by Recht and Ipson [35], where conservation of energy and momentum is used to determine an expression for residual projectile velocity. In the Recht - Ipson model, p is equal to 2 and a is given as the mass ratio

$$a = \frac{m_p}{m_p + m_{pl}} \quad , \quad m_{pl} \approx \pi r_p^2 \rho_t h_t \quad (2)$$

Under the conditions described in this programme the mass ratio a becomes 0.87, which is close to the fitted value. A comparison between the experimental data and the Recht - Ipson model is shown in Figure 18. Another observation is that the ballistic limit velocity can be

found from only a few experimental tests using Eq. (1), when v_{bl} is taken as the unknown. If e.g. test # 12-9 in Table 1 is selected, the ballistic limit velocity is calculated to be 182.8 m/s, which is close to the measured ballistic limit of 184.5 m/s. Even if the accuracy of the method is questionable in other situations, it shows that simple energy balances can give reasonable estimates of the overall target response.

Projectile kinetic energy is transformed into target and projectile work through a complex stress wave transfer at impact, and it is difficult to quantitatively address the energy dissipation during penetration. However, the total amount of energy absorbed may easily be calculated using conservation of energy. This is indicated in Figure 4b), where the amount of initial kinetic energy converted into work is plotted as a function of initial kinetic energy. As seen, the percentage of work carried out by the system decreases with increasing impact velocity. At the highest projectile velocities the energy absorption seems to flatten out, indicating that no more energy can be absorbed by the projectile-target system. At the ballistic limit, the total amount of energy absorbed during impact is found to be 35 % less than the amount of energy absorbed under similar quasi-static plugging conditions [36].

The target deformation consists of a combination of localised bulging and global dishing, and the importance of impact velocity is demonstrated in Figure 4c). In the case of static loading [36], the plastic deformation reaches out to the boundary and energy is absorbed as membrane stretching. In the dynamic case, the deformation is much more localised. The permanent target deformation, measured after the test, increases with increasing velocity until it reaches a maximum at the ballistic limit. The maximum deformation (w_{max}) is less than half the plate thickness, indicating that the global response during impact is dominated by bending stresses. After perforation, the deformation decreases with velocity until it stabilises at a velocity well above the ballistic limit. However, the maximum deformation during penetration is observed to be higher. Both from the static and dynamic tests evidence is found that the maximum deformation close to fracture is about twice as large as the permanent deformation, indicating a considerable elastic rebound in the target. Although the permanent deformation is found to be small, global target deformation dissipates a considerable amount of the initial kinetic energy during impact. Some typical cross-sections of penetrated target plates at increasing initial projectile velocity are shown in Figure 5.

Figure 4d) shows measured geometrical values as a function of initial projectile velocity. The permanent target deformation decreases from a maximum value at the ballistic limit towards a constant value at higher projectile velocities, as also indicated in Figure 4c). The plug thinning due to compression, defined as the difference between the initial target

thickness and the final plug thickness, is seen to increase slightly with increasing projectile velocity. However, the plug mass (m_{pl}) is almost constant for all velocities. This is caused by an increase in plug diameter with velocity due to projectile mushrooming, which takes place during the first stage of penetration. The diameter of the front side of the plug is equal to the final diameter of the projectile and always larger than the target cavity diameter (θ_f). The rear side diameter of the plug and target cavity (θ_r) is somewhat larger due to tensile stretching. Even if maximum hardened, the projectile is plastically deformed at impact. Above this hardness limit, the projectile will fracture. During deformation, the projectile length is decreased and the projectile nose diameter is increased as a function of velocity. Furthermore, it seems that there exists a threshold velocity for projectile deformation. Above this velocity considerable mushrooming in the projectile starts to appear. By making post-impact measurements of the deformed shape [37], it is possible to estimate the amount of energy absorbed in the projectile during impact. At the highest velocities used in this study, as much as 10 - 15 % of the total energy is assumed dissipated in projectile plastic deformation.

Finally, the Rockwell C (HRC) hardness of the projectile is measured both before and after impact. It is always found that the hardness is reduced by 2 - 3 HRC during penetration. This indicates damage in the nose part as a result of the impact. Figure 6 shows a typical projectile and plug after perforation.

The indentation of the projectile gives rise to a relative velocity within the target, and the global deformation mode changes into a mechanism of highly localised shear around the projectile nose. The width of the shear zone is a function of the relative velocity, and may turn into an intense shear band if the velocity becomes sufficiently high. The shear failure is isothermal, adiabatic or in the transition stage from isothermal to fully adiabatic depending on the rate of loading. According to Lindholm [38], the failure in steel will be adiabatic if the strain-rate exceeds 100 s^{-1} . From the high-speed camera measurements, evidence is found that the perforation time is less than $100 \mu\text{s}$, except for the tests very close to the ballistic limit. This indicates that the strain-rate in the shear zone has been much higher than 100 s^{-1} , and that the process can be considered as adiabatic. In an adiabatic process, where the conduction of heat generated by the plastic deformation is negligible, strain-hardening effects may be overcome by thermal softening, giving a thermal instability.

In order to investigate the possible influence of thermal effects and the local stress-state in the target during penetration, a micromechanical investigation is in progress [39]. So far, only 10 mm thick targets have been investigated, but an examination involving thicker plates at

higher velocities will be carried out. Sign of temperature effects has been investigated using a scanning electron microscope. No proof of appreciable adiabatic overheating, visible as molten material, intensive white shear bands, recrystallisation or recovery, has been found in the shear zone. This indicates that the temperature in the material has not exceeded 400 °C. By assuming adiabatic conditions, the temperature rise in the target caused by conversion of plastic work into heat can be calculated as [38]

$$\Delta T = \frac{\alpha}{\rho C_p} \int_0^{\gamma_c} \tau d\gamma \quad (3)$$

where α is the proportionality constant, ρ is the density and C_p is the specific heat (see Table 2). This equation gives a temperature rise in the target material during impact of 300 – 350 °C. From the numerical simulations in Chapter 5, where the energy dissipation is calculated and converted into heat, approximately the same result is obtained. A clear blue colour, characteristic for the blue brittle region described in Chapter 4, is clearly seen on the fracture surface of the targets. In Figure 11d), the blue brittle region appears at a temperature of about 300 °C. All this experimental evidence indicates that the temperature rise in the target under the conditions described in this study is about 300 – 350 °C.

The stress-state in the target and the mode of failure during perforation has also been investigated in the microscope. Figure 7 shows the cross-section of a 10 mm thick target at the ballistic limit [39], and several important observations are found. First of all, the dark lines of pearlite running parallel to the plate surface as a result of the manufacturing process show that there are at least three different stress-states in the target during perforation. The first stage, where the flow lines are hardly distorted, is due to compression. This stage is rapidly overcome when the plug is set in motion by the moving projectile and the deformation mechanism changes into a localised shear zone throughout the target thickness. As seen in Figure 7, the width of the intense shear zone is rather constant. When the plug has moved approximately half a plate thickness, fracture occurs. This final stage includes a combination of shear and tensile stresses. It is also seen that the fracture starts at the projectile-plug interface and propagates towards the rear surface. Finally, note that when the plug is completely free on one side, cracking has just started on the other side. This unsymmetrical fracture mode is responsible for the observed plug rotation after complete separation.

The fracture surfaces and the different fracture morphology regions have been studied in

detail in the scanning electron microscope. Two typical images from this study are also presented in Figure 7. From the front face to the rear side of the target one can see a sharp edge of the indentation without any frontal bulge, followed by a shear region smoothed by the passing projectile. Towards the rear side, a region of shear dimples appears. In the concentrated shear zone, voids are initiated. Due to the continuous straining, the voids grow and elongate. The voids then coalesce due to fracture of the thin walls separating the voids, giving the obtained dimples, and the crack is allowed to grow. This type of behaviour denotes ductile fracture [40]. Of even more interest, the area in front of the crack tip has been investigated. A number of elliptical cavities are found along the localised shear zone, showing how the voids nucleate, grow and coalesce in front of the crack to form the ductile fracture. This observation justifies the assumption of using continuum damage mechanics in order to describe the ductile fracture, as presented in Chapter 4.

Two typical perforation tests are selected for a more detailed study. The results from these tests will be compared to the numerical simulations given in Chapter 5. High-speed camera images from the tests are shown in Figure 8 and 9. In Figure 8, a 10 mm thick Wieldox 460 E steel plate is perforated by a projectile with an initial velocity of 296 m/s, which is well above the ballistic limit (test # 10-9 in [32]). In Figure 9, a 12 mm thick Wieldox 460 E steel plate is perforated by a projectile having an initial velocity of 189.6 m/s, which is close to the ballistic limit (test # 15 in Table 1). In Figure 8 mirrors are used to give a 3D description of the penetration process (see Figure 2) and the camera is operating in a 12 image mode. No mirrors are used in Figure 9, and a 15 image mode is used. In the latter, the stationary reference points are seen in the lower-left corner of the different images.

From these and similar pictures some immediate conclusions can be drawn. The projectile is embedded in the target before any considerable bulging of the rear side appears (Figure 8), justifying the assumption of a stationary compression stage. The bulge is highly localised, showing hardly any radial distribution before fracture. This is valid for most tests, except for those closest to the ballistic limit where perforation is a much slower process and a larger part of the target plate is activated (Figure 9). Furthermore, the plug fractures when the projectile has indented approximately half the target thickness. It is then pushed out of the cavity by the projectile before complete separation occurs. In most cases, the projectile and plug have identical velocities immediately after perforation. Afterwards they separate and the plug leaves the projectile at a higher velocity. Some of the images have revealed considerable plug rotation after complete separation due to the unsymmetrical fracture mode seen in Figure 7. No significant angle deviation of the projectile after perforation is found.

The digital high-speed camera images are also used for direct measurements of travelled distance as a function of penetration time [31]. This is used to calculate projectile and plug velocity and acceleration during testing. The average velocity is defined as a vector quantity equal to the moved distance of the projectile divided by the known time interval. The average acceleration is given as the vector change in velocity divided by the time interval. The high-speed camera measurements are shown in Figure 10. As seen from Figure 10a), the projectile in test # 10-9 (Figure 8) impacts the target after about 100 μ s at a velocity of 296 m/s. During the next \sim 40 μ s the projectile indents the target, giving a sharp velocity drop, and it perforates at a velocity of 218 m/s. However, it is hard to determine the point of impact and the perforation time exactly since the camera system provides only a limited number of images. In test # 10-9 the point of impact seems to be missed by some microseconds, since the final slope of the measured velocity-time curve is steeper than the initial slope. The velocity after perforation is almost constant, indicating a negligible sliding friction between the projectile and target after fracture. However, the possible influence of sliding and sticking friction during penetration is still unknown. The plug shows a rapid velocity increase before it stabilises at a velocity approximately 15% higher than that of the projectile. A similar behaviour is obtained in Figure 10b) for the penetration process in test # 12-15. In this test the camera missed the point of impact due to an inaccurate trigger. However, since the distance from the trigger to the target is known for all these tests, the measured velocity-time curve was corrected according to the assumed point of impact. This gives that the projectile impacts the target after about 114 μ s at a velocity of 189.6 m/s. During the next 100 μ s the projectile perforates the target, having a residual velocity of 42 m/s. As seen, the process is much slower near the ballistic limit. In this test the residual velocity of the plug is found to be 50 % higher than that of the projectile. Finally, the average force on the projectile seems to be considerable higher in Figure 10a) due to a steeper velocity drop. The force calculations are inaccurate since they are based on the measured acceleration from a limited number of images.

The velocities calculated using the high-speed camera images are in close agreement (within 1-2 %) with those obtained by the photocell system described in Chapter 2. However, the measured velocity-time curves show some peaks near the fracture region. This may be due to aberrations in the digital images, or it could as well be caused by a physical effect due to several impacts between the projectile and plug during penetration. The numerical simulations have revealed such impacts between the projectile and plug, but this is for the time being not clear and further investigations are necessary.

4. Material behaviour and modelling

To be able to describe the various phenomena taking place during ballistic penetration, it is necessary to characterise the behaviour of materials under impact-generated high strain-rate loading conditions. The characterisation involves not only the stress-strain response at large strains, different strain-rates and temperatures, but also the accumulation of damage and the mode of failure. Such complex material behaviour involving fracture is difficult to describe in analytical models. In numerical simulations, constitutive models of nearly any degree of complexity can be incorporated into the code. However, due to the many difficulties in obtaining model constants for dynamic material behaviour, engineering models may be preferable to more sophisticated models [5]. Another important feature is the physical difference between plastic flow and fracture. In ductile metals, plastic flow may be viewed macroscopically as a visible shape change, microscopically as the appearance of slip lines, and at the atomic level as the movement of dislocations. It is also known that plastic flow is driven by the deviatoric stress-state in the material. Initiation of damage is due to arrests of dislocations by microdefects or microstress concentrations giving decohesion and subsequently nucleation, growth and coalescence of microcracks and microvoids [41]. The damage evolution is strongly influenced by the hydrostatic stress-state in the material [42-43]. Accordingly, different mathematical models are needed to describe plastic flow and fracture.

In this paper numerical simulations are carried out and compared with experimental data using a coupled material model of viscoplasticity and ductile damage, developed for impact and penetration problems. Here, only the main features of the model will be given, while the details in the formulation are presented by Hopperstad et al. [44]. The model is formulated within the framework of viscoplasticity and continuum damage mechanics [42], allowing for large plastic strains, high strain-rates and adiabatic heating.

By assuming isotropic material behaviour and von Mises plasticity, the engineering model proposed by Johnson and Cook [45] is adopted in the viscoplastic domain [44]. Thus, the equivalent stress σ_{eq} can be expressed as

$$\sigma_{eq} = [A + Bp^n] [1 + C \ln \dot{p}^*] [1 - T^{*m}] \quad (4)$$

where A, B, C, n and m are material constants, p is the accumulated plastic strain, $\dot{p}^* = \dot{p} / \dot{p}_0$ is a dimensionless strain-rate, \dot{p} is the plastic strain-rate, \dot{p}_0 is a user defined reference strain-

rate, $T^* = (T-T_0) / (T_m-T_0)$ is the homologous temperature, T is the actual temperature, T_0 is the room temperature and T_m is the melting temperature. Since the strain-rate and temperature effects on the flow stress are uncoupled, the Johnson-Cook model is easy to calibrate with a minimum of experimental data, and model constants can be found for several metals in the literature [5]. However, in contrast to the model, rate sensitivity is found experimentally to increase with increasing temperature, while the flow stress is decreasing [54]. Nevertheless, the model is generally accepted and has been implemented into several finite element codes.

To describe ductile fracture, Johnson and Cook also proposed a model including the effects of stress triaxiality, temperature, strain-rate and strain path [43] on the failure strain. The model assumes that damage accumulates in the material element during plastic straining, and that the material breaks immediately when the damage reaches a critical value. In other words, the damage has no effect on the stress field as long as fracture has not taken place. Since it is known that damage degrades material strength during deformation, a coupled model is found necessary. Continuum damage mechanics [42], which is an attempt to treat ductile fracture quantitatively, may therefore be used to give a failure criterion. The main advantage of using this approach is that the damage model is coupled with the constitutive equation. In [42], the strain equivalence principle states that any constitutive equation for a damaged material can be derived in the same way as for the virgin material except that the usual stress is replaced by the effective stress. This implies that a unified model for damaged viscoplastic materials can be written as

$$\sigma_{eq} = (1 - D) \left[A + B r^n \right] \left[1 + C \ln \dot{r} \right] \left[1 - T^{*m} \right] \quad (5)$$

where D is the damage variable, defined in [42], and r is the damage accumulated plastic strain given as $\dot{r} = (1 - D) \dot{p}$. The damage variable takes values between 0 and 1, where $D = 0$ for an undamaged material and $D = 1$ for a fully broken material. However, the critical value of the damage variable, i.e. the value at which a macrocrack occurs, is less than 1. Hence, the failure criterion simply becomes

$$D = D_c \leq 1 \quad (6)$$

The evolution of damage is always related to irreversible strains, and may therefore be taken as a function of the accumulated plastic strain. Furthermore, experiments indicate that the

damage remains equal to zero during the build-up of dislocations generating microcracks. Accordingly, it may exist a threshold of the accumulated plastic strain at which damage starts to evolve. Based on observations like these, a damage evolution rule is proposed as

$$\dot{D} = \begin{cases} 0 & \text{when } p < p_d \\ \frac{D_c}{p_f - p_d} \dot{p} & \text{when } p \geq p_d \end{cases} \quad (7)$$

where D_c is the critical damage, p_d is the damage threshold and p_f is a fracture strain depending on stress triaxiality, strain-rate and temperature. Johnson and Cook [43] proposed an expression for the fracture strain as

$$p_f = [D_1 + D_2 \exp(D_3 \sigma^*)] [1 + D_4 \ln \dot{p}^*] [1 + D_5 T^*] \quad (8)$$

where $D_1 - D_5$ are material constants, $\sigma^* = \sigma_m / \sigma_{eq}$ is the stress triaxiality ratio, and σ_m is the mean stress.

The constitutive model defined by Eqns. (5) - (8) has been implemented in the explicit finite element code LS-DYNA [46] using a fully vectorized backward-Euler integration algorithm [44, 47]. The model is applicable for shell and solid elements in three-dimensional analysis, as well as axisymmetric elements in two-dimensional analysis. In order to allow crack growth during penetration, the model was coupled with an element-kill algorithm available in the code. As the damage variable reaches its critical value D_c the damaged element is removed from the mesh, while the element mass is redistributed to neighbouring nodes.

The model describes linear elasticity, initial yielding, strain hardening, strain-rate hardening, damage evolution and fracture. For each of these phenomena one or several material parameters are required, and the total number of experimentally determined constants may seem considerable at first sight. However, all material constants can be identified from uniaxial tensile tests. In this study all targets are manufactured from Weldox 460 E, which is a thermo-mechanically rolled ferritic structural steel offering high strength combined with a high degree of ductility. Introductory quasi-static tensile tests at a strain-rate of $5 \cdot 10^{-4} \text{ s}^{-1}$ were carried out to determine the elastic constants, and to study anisotropy and scatter in material properties as a function of plate thickness and batch number [48-49]. Tensile tests in three different directions (0° , 45° and 90°) with respect to the rolling direction of the material were

conducted. Longitudinal and transverse strains were measured up to diffuse necking using two extensometers. The elastic properties, E and ν , are as given in Table 2. It was also found that the material could be characterised as isotropic both regarding stress and strain. However, it seems like damage after necking is directional and introduces anisotropy into the previously isotropic material (see also Figure 13) at large plastic strains. The scatter of material properties between the different deliveries was found to be moderate. Nevertheless, it was decided that all material specimens should be manufactured from the same target plate, identical to the material used in the experimental penetration tests. Owing to the isotropic behaviour, only specimens parallel to the rolling direction have been tested.

All laboratory tests needed to calibrate the constitutive model are shown in Figure 11. The data are obtained from a) quasi-static smooth specimen tensile tests at large strains, b) quasi-static notched specimen tensile tests with various notch radii, c) tensile tests at various strain-rates and d) quasi-static tensile tests at various temperatures. The main features of the identification procedure are given below.

Figure 11a) shows the measured quasi-static true stress-strain curve for the target material all the way to fracture. The stress is based on continuous measurements of the applied load and the current area of the cylindrical specimen [50], while the strain is calculated as $\ln(A_0/A)$ where A_0 and A represent the initial and current area of the specimen, respectively. As seen, the target material is very ductile. Due to necking of the cylindrical specimens at large strains, there is a component of hydrostatic tension that tends to make the net tensile stress greater than the equivalent stress. According to Bridgman [51] and LeRoy et al [52] the obtained stress in the smooth specimen should therefore be corrected. A comparison between the measured and the Bridgman-LeRoy corrected curve is shown in Figure 11a). As seen, the correction is considerable at large strains, and the validity of the LeRoy empirical equation for this particular material is unknown. Therefore, only the yield stress constant A is determined from the smooth specimen tests.

In order to determine the strain hardening parameters B and n , and the critical damage parameter D_c , the cylindrical specimens with various notch radii as shown in Figure 11b) are used. Here, the damage evolution threshold p_d is chosen equal to zero. In a similar way as for the smooth specimen, the applied load and cross-sectional area in the notch are measured during testing. It is further assumed that the stress triaxiality ratio σ^* is approximately constant during plastic straining in each notched-specimen tensile test. The stress triaxiality ratio σ^* in the smooth specimen is on the other hand assumed to vary, and is therefore omitted

in the calibration procedure. The different notches give a concentration of hydrostatic tension in the test specimen. For a specified true strain, the stress is seen to increase when the notched radius R is reduced. It is also seen that the presence of hydrostatic tension significantly decreases the strain at which the material fractures. By taking the latter into account, the effect of hydrostatic tension on the failure strain is included in the model. The model constants B , n and D_c are determined from Eq. (5) when $\dot{p}^* = 1$, $T = T_0$ and σ^* is constant, which gives

$$\sigma_{eq} = \left(1 - \frac{D_c}{\bar{p}_f(\sigma_\alpha^*)} p_\alpha \right) (A + B r_\alpha^n) \quad (9)$$

where p_α , r_α and σ_α^* are discrete values of the variables p , r and σ^* , and \bar{p}_f is the measured fracture strain for the different notched specimens. The damage accumulated plastic strain r is calculated as

$$r = p - \frac{1}{2} \frac{D_c}{p_f(\sigma^*)} p^2 \quad (10)$$

for this particular case. The method of least squares is then used to minimise the difference between the experimental determined curves and the model by varying B , n and D_c simultaneously. The obtained material constants are given in Table 2, while Figure 11b) shows a comparison between the experimental curves and the model fit. As seen, good correlation is obtained for the notched specimens. However, the fit is somewhat poorer for the smooth specimen. This is probably caused by the variation in stress triaxiality during testing. The damage threshold p_d and the critical damage D_c can be identified from a tensile test where unloading is prescribed at equal intervals of strain in order to measure the variation of the modulus of elasticity, which may be used as a measure of damage [42]. Although this method is simple in principle, it is difficult to perform. Inverse modelling of the smooth and notched specimens using LS-DYNA will also be carried out in order to determine the damage parameters. The numerical approach, which is believed to give an accurate fit of the model to the measured data, should be used as a control of the simplified calibration procedure described above.

The viscous effect is obtained by means of uniaxial tensile tests at a range of different strain-rates from 10^{-4} to 10^3 s^{-1} [53] as shown in Figure 11c). From these tests an average

effect of strain-rate can be obtained. The figure shows that the strain-rate sensitivity of the material is moderate and almost unaffected by the level of plastic strain. To have an average value of the strain-rate sensitivity the data was fitted to the proposed model using the method of least squares for a plastic strain of $p = 0$ and $p = 0.1$ when $T = T_0$. The mean value of C is then used to describe the viscous effect. This is shown in Figure 11c).

The effect of thermal softening on the true stress is shown in Figure 11d). While the yield stress shows a linear decrease with increasing temperature, the ultimate tensile stress exhibits a local maximum at a temperature of about 300 °C. This temperature region is known as the blue brittle region [40], and is caused by restraining of dislocations due to a release of second-order particles in carbon steels. By assuming adiabatic condition at high strain-rates, the effect of thermal softening is included in the model by fitting the material constant m to the decreasing yield stress ($p = 0$, $\dot{p}^* = \dot{p}/\dot{p}_0 = 1$). A similar behaviour is seen at higher strains if the blue brittle effect is neglected. However, according to Harding [54] this uncoupling between thermal and viscous effects used in the Johnson-Cook model may not represent the correct physical behaviour observed in experiments.

The strain to fracture used in the damage evolution rule is given by Eq. (8). The expression in the first set of brackets gives the effect of hydrostatic stress on the strain to fracture for quasi-static conditions. This is shown in Figure 12a), where the dimensionless triaxiality ratio in the centre of the specimen is calculated based on Bridgman's analysis as [55]

$$\sigma^* = \frac{1}{3} + \ln\left(\frac{a + 2R}{2R}\right) \quad (11)$$

where a and R are the initial radius of the specimen in the neck and the initial neck radius, respectively, since the triaxiality ratio is assumed constant during plastic straining. The strain to failure is calculated as $\ln(A_0/A_f)$, where A_0 is the measured initial area of the specimen, and A_f is the measured area after fracture. All fracture areas have been measured in a light microscope, as seen in Figure 13. The data point at $\sigma^* = 0$ was estimated, based on a model proposed in [42]. The three material constants, D_1 , D_2 and D_3 , in the model have been fitted to the given data, and the curve has been extrapolated into the hydrostatic compression region as seen in Figure 12a). The obtained values of D_1 - D_3 from the curve fit are as given in Table 2.

The effect of strain-rate and temperature on the strain to failure is given in the second and third set of brackets in Eq. (8). The effect of strain-rate is isolated from the temperature effect

by considering the measured fracture strains for smooth specimens ($\sigma^* = 1/3$) at $T^* = 0$. This is shown in Figure 12b), where the strain-rate constant D_4 is fitted to the measured fracture strains. Both Figure 12b) and Figure 13b) indicate that the fracture strain decreases slightly with increasing strain-rate. In a similar way, the effect of temperature on the fracture strain is isolated from the strain-rate when $\dot{p}^* = \dot{p}/\dot{p}_0 = 1$, and the temperature constant D_5 is obtained from Figure 12c). However, due to the blue brittle region the fracture strain is found to be unaffected by temperature up to 300-350 °C. Therefore, D_5 is for this material chosen equal to zero.

As also indicated by Johnson and Cook [43], it appears that the fracture strain as a function of the triaxiality ratio shown in Figure 12a) is of primary importance. This is due to a rapid increase of the strain to fracture under hydrostatic compression. In most penetration problems a compression region will develop in front of the projectile at impact, and the damage evolution and fracture becomes strongly influenced by hydrostatic compression. As no material data is available in this region, the assumed function becomes critical and must be further investigated in coming work.

All material constants needed for the viscoplastic damage mechanics model are given in Table 2. The corresponding stress-strain relationship to fracture when $\sigma^* = 1/3$, obtained by using the constitutive model in Eq. (5), is shown in Figure 12d). Here, adiabatic behaviour is assumed and the strain-rate is chosen as $\dot{\epsilon} = 1000s^{-1}$. If this curve is compared to the quasi-static relationship given in Figure 11a), the significance of adding several physical effects to the material behaviour during impact is shown. The adiabatic temperature rise during plastic deformation is seen in Figure 12e). Both damage and temperature tends to soften the stress-strain curve. The damage evolution is shown in Figure 12f). As seen, under the given conditions the damage develops linearly until the critical damage is reached.

The proposed model is used in the first approach of formulating a computational model of viscoplasticity and ductile damage for penetration problems. Therefore, both the model itself and the calibration procedures are under development. The main advantage of the model compared with most computational fracture models is that the damage evolution, giving material degradation, is fully coupled with the constitutive equation through the strain equivalence principle, i.e. the stress field depends on damage. Hence, damage contributes to the localisation of plastic deformation in the penetration process, and as the critical damage D_c is reached a macrocrack appears and fracture is assumed to occur. In the literature, the Johnson and Cook model has received some criticism. This is mainly due to the uncoupling

between viscoplasticity and temperature. However, the model is here adopted as a first approach due to its relative simple formulation and calibration.

5. Numerical simulations

Preliminary numerical simulations of the penetration problem have been carried out to examine if the computational model of viscoplasticity and ductile damage [44] is able to predict the experimental obtained target response during plugging. However, it is important to emphasise that some work still remains in order to draw final conclusions of the numerical results.

The axisymmetric finite element mesh used in the LS-DYNA [46] simulations is shown in Figure 14. A total of 3550 4-node axisymmetric elements with one-point integration were applied in the model, giving 25 elements through the plate thickness. The required CPU time varied between 5-9 hours per run on a HP 715/100 workstation. Due to the CPU requirement, the analyses were stopped before the elastic rebound of the target plate was completed. Therefore, the final target deformation is not obtained.

The target material was modelled as elastic-viscoplastic coupled with ductile damage, using Eqns. (5)-(8) and the material constants given in Table 2. The projectile of hardened tool steel was modelled as linear elastic with Young's modulus $E_p = 200000$ MPa and Poisson's ratio $\nu_p = 0.33$ due to the lack of reliable projectile material data. At impact velocities near the ballistic limit this assumption seems to be sufficient. However, at higher impact velocities the projectile mushrooming may become considerable. Projectile material data will be included in the next version of the numerical model.

In the simulations, the plate was fully clamped at the support, while the projectile was given an initial velocity v_i as defined in Table 3. The contact between the projectile and target was modelled using a penalty formulation without friction. The effect of friction will be investigated in future work. No attempt has so far been made in order to reveal the possible mesh dependence of the solution. However, according to Needleman [56], pathological mesh size effects do not occur in finite element simulations involving material softening due to e.g. damage if the strain-rate dependence of the material is accounted for. More severe numerical difficulties are associated with the dynamic localisation problem, and a lot of elements are

required over the target thickness. An adaptive solution method under development will be tested in later simulations in order to resolve the narrow shear bands.

The scope of the simulations was to examine run # 10-9 and run # 12-15 in detail regarding a direct comparison with the experimental observations given in Figure 8 - 10, and to construct the ballistic limit curve for the 12 mm thick Weldom 460 E steel target based on the numerical results. Table 3 gives the numerical test programme, together with the major response parameter, which is defined as the residual velocity of the projectile and plug. The agreement between the experimentally and numerically obtained velocities is excellent at the highest velocities. However, in the simulation of test # 12-15 perforation was not obtained. In order to define the ballistic limit velocity, run # 12-N1 to 12-N3 were conducted. From these simulations, the ballistic limit velocity was found from run # 12-N3 to be 205 m/s. This gives a deviation from the experimentally obtained ballistic limit of 10 %, which is acceptable concerning the complexity of the problem. Based on the results, it was decided to compare test # 12-15 with the numerical results of run # 12-N2, since the initial velocity in both cases is approximately 5 m/s above the respective ballistic limit.

Plots of the deformed element mesh during perforation of run # 10-9 and 12-N2 are shown in Figure 15 and 16, respectively. If the results are compared with Figure 8 and 9, where the high-speed camera images from the experiments are shown, excellent agreement is found between the numerical simulations and the experimental observations. In the first phase, the projectile indents the plate due to a large compressive force between the projectile and target. During this short period of time, the target mass in front of the projectile is accelerated, and the deformation mechanism changes into a highly localised shear zone surrounding the projectile nose. Damage develops rapidly in the shear zone due to the severe plastic straining of the elements closest to the projectile-target interface. The critical damage is reached, the elements start to erode, and the crack propagates towards the rear side of the target. In the final stage, the failure mode is combined shear and tensile failure, as also obtained during testing. The bulge is highly localised, with hardly any global target deformation in run # 10-9. In run # 12-N2, where the initial velocity is close to the ballistic limit, the perforation process slows down and a larger part of the plate is activated. This involves a larger global target deformation, as also seen in Figure 4c). The plug is fully fractured before complete separation from the target occurs, and the plug shape seems to be very close to the experimental one (Figure 6). The typical target lip due to tensile straining at the rear side (Figure 5) is described. No frontal bulge is obtained in any of the simulations.

The projectile velocity-time curves from the numerical simulations of run # 10-9 and 12-2N have been compared with the high-speed camera measurements of test # 10-9 and 12-15 (see Figure 10). This is shown in Figure 17. Not only are the residual velocities of the projectile closely described, but also the slope of the curves and the perforation times seem to coincide. From the simulations, it seems like the projectile impacts the plug several times during penetration. At impact, the plug mass is accelerated by stress waves to a higher velocity than that of the projectile. However, due to restraining by the shear zone, the plug is prevented from leaving the target. The projectile catches up with the plug, giving it a new impact, and contact between the bodies are lost once more. At or very close to fracture, this impact becomes a collision between two free bodies, and the plug leaves the target at a higher velocity. This may explain the observed difference in projectile and plug residual velocity, and the measured fluctuations in the velocity-time curves close to fracture. A comparison between the measured and simulated projectile residual velocities given in Table 3 for the 12 mm thick steel target is shown in Figure 18. Due to the disagreement in the ballistic limit velocity of 10 %, the data does not coincide except for the highest impact velocities. In Figure 18, also the model of Recht and Ipson [35] has been plotted for the obtained ballistic limits of 185 m/s and 205 m/s, respectively. As seen, the model gives a close representation of the numerical results.

The simulations indicate that the maximum strain-rate in the shear zone is nearly 200000 s^{-1} for run # 10-9, and 100000 s^{-1} for run # 12-2N. The calculated temperature increase due to adiabatic heating is about 350°C in both runs. Also the energy absorption in the different materials has been calculated, and it is found that most of the work is carried out in global target deformation. However, since the projectile is modelled as an elastic material, the calculated energy distribution becomes inaccurate.

From the preliminary simulations the numerical model seems to capture the main target response during the penetration process, and promising results are obtained. However, to exactly determine the ballistic limit velocity in the penetration problem using numerical simulations is still a challenge. This is in any case the parameter of primary interest in design. Nevertheless, the ballistic limit velocity obtained in the numerical study is within the expected accuracy for such complex problems. In coming work the sensitivity of the numerically determined ballistic limit velocity to variations in the material constants will be studied. The effect of changing model parameters, such as target thickness and projectile nose shape will be investigated both experimentally and numerically.

6. Summary and conclusions

This paper presents a joint research programme in progress between the Norwegian Defence Construction Service and the Department of Structural Engineering, Norwegian University of Science and Technology, where the main objective is to study the behaviour of steel plates impacted by blunt-nosed cylindrical projectiles in the lower ordnance velocity regime.

A compressed gas gun capable of launching a 250 g sabot mounted projectile to a maximum velocity of 1000 m/s has been built during the study. The gas gun is used to obtain high-precision penetration test data for verification of solution methods. During testing, the main instrumentation is provided by a digital high-speed camera system. In addition to visualisation of the impact process, the digital images are used to obtain travelled distance, velocity and acceleration for the assumed rigid bodies as a function of penetration time.

In this paper, emphasis has been on an experimental programme carried out to determine the ballistic limit curve of a 12 mm thick Weldox 460 E steel plate. Some of the most important experimental findings are reported and discussed, and two typical perforation tests are presented in detail. All targets failed by shear plugging. A metallurgical examination of the penetrated target plates is also presented. This study has e.g. revealed void growth and coalescence in the localised shear zone, indicating a ductile fracture.

To be able to predict the different phenomena taking place during penetration, characterisation of the target material under impact generated high strain-rate loading conditions has been found necessary. This involves not only the stress-strain response for large strains, high strain-rates and temperatures, but also the accumulation of damage and the mode of failure. A coupled constitutive model of viscoplasticity and ductile damage was used in order to calculate projectile penetration and failure. The model, which has been implemented into the finite element code LS-DYNA, has been coupled with an element-kill algorithm available in the code that removes the damaged element from the model when the damage variable reaches its critical value.

Even if the total number of material constants required in the model seems considerable at first sight, they can readily be identified from quasi-static and dynamic tensile tests. All laboratory test data needed to calibrate the model is presented and discussed, and the model constants for Weldox 460 E steel are given in tabular form.

Preliminary numerical simulations of the plate penetration problem have been carried out giving promising results, and it seems like the numerical model is capable of describing the main target response and physical behaviour observed during perforation. However, the numerical solution overpredicts the ballistic limit velocity by approximately 10 %. At higher velocities, good agreement between the numerical model and experimental results is obtained. In coming work, the sensitivity of the numerical model to variations in material constants and mesh size will be studied. Also the effect of changing model parameters, such as target thickness and projectile nose shape, will be investigated both experimentally and numerically. In addition, an adaptive solution procedure will be tested in order to resolve the high strain gradients in the plate penetration problem.

Acknowledgements

The authors would like to thank the Norwegian Defence Construction Service for their generous financial support of the research project that forms the basis of the present work. Furthermore, the authors would like to express their gratitude to Mr. Knut Holen for considerable assistance in establishing the high-speed camera measurement techniques and to Dr. Torodd Berstad for model implementation and help in obtaining the numerical results. Finally, Mr. Arnfinn Jenssen is also gratefully acknowledged for his help during the project.

References

- [1] Backman, M.E. and Goldsmith, W., *The Mechanics of Penetration of Projectiles Into Targets*, Int. J. Engng. Sci., Vol. 16, pp. 1 - 99, 1978.
- [2] Corbett, G.G., Reid, S.R. and Johnson, W., *Impact Loading of Plates and Shells by Free-Flying Projectile*, Int. J. Impact Engng., Vol. 18, No. 2, pp. 141 - 230, 1996.
- [3] Anderson Jr., C. E. and Bodner, S. R., *Ballistic Impact: The Status of Analytical and Numerical Modeling*, Int. J. Impact Engng., Vol. 7, No. 1, pp. 9 - 35, 1988.
- [4] Zukas, J.A. et al., *Impact Dynamics*, Krieger Publishing Company, Florida, 1992.
- [5] Zukas, J.A. et al., *High Velocity Impact Dynamics*, John Wiley, New York, 1990.
- [6] Brown, S.J., *Energy Release Protection for Pressurized Systems-Review of Studies into Impact/Terminal Ballistics*, Appl. Mec. Rev., Vol. 39, pp. 177 - 201, 1986.

- [7] Jonas, G.H. and Zukas, J.A., *Mechanics of Penetration: Analysis and Experiment*, Int. J. Engng. Sci., Vol. 16, pp. 879 - 903, 1978.
- [8] Corran, R.S.J., Shadbolt, P.J. and Ruiz, C., *Impact Loading of Plates—An Experimental Investigation*, Int. J. Impact Engng., Vol. 1, No. 1, pp. 3 - 22, 1983.
- [9] Awerbuch, J. and Bodner, S.R., *Experimental Investigation of Normal Perforation of Projectiles in Metallic Plates*, Int. J. Solids Struct., Vol. 10, No. 6, pp. 685–699, 1974.
- [10] Hanchak, S.J., Altman, B.S. and Forrestal, M.J., *Perforation of HY-100 Steel Plates with Long Rod Projectiles*, Proceedings of 13th Army Symposium on Solid Mechanics, 17 - 19 August, Plymouth, Massachusetts, 1993.
- [11] Piekutowski, A.J., Forrestal, M.J., Poormon, K.L. and Warren, T.L., *Perforation of Aluminium Plates with Ogive-Nose Steel Rods at Normal and Oblique Impact*, Int. J. Impact Engng., Vol. 18, Nos. 7-8, pp. 877 - 887, 1996.
- [12] Liss, J. and Goldsmith, W., *Plate Perforation and Phenomena due to Normal Impact by Blunt Cylinders*, Int. J. Impact Engng., Vol. 2, No. 1, pp. 37 - 64, 1984.
- [13] Goldsmith, W. and Finnegan, S.A., *Penetration and Perforation Processes in Metal Targets at and Above Ballistic Velocities*, Int. J. Mech. Sci., Vol. 13, pp. 843 - 866, 1971.
- [14] Lethaby, J.W. and Skidmore, I.C., *The deformation and Plugging of Thin Plates by Projectile Impact*, Mech. Prop. of Materials at High Rates of Strain, Conf. Ser. No. 21, pp. 429 - 441, Oxford, 1974.
- [15] Woodward, R.L. and De Morton, M.E., *Penetration of Targets by Flat-Ended Projectiles*, Int. J. Mech. Sci., Vol. 18, pp. 119 - 127, 1976.
- [16] Shadbolt, P.J., Corran, R.S. and Ruiz, C., *A Comparison of Plate Perforation Models in the Sub-Ordnance Velocity Range*, Int. J. Impact Engng., Vol.1, No.1, pp. 23-49, 1983.
- [17] Awerbuch, J.A. and Bodner, S.R., *Analysis of the Mechanics of Perforation of Projectiles in Metallic Plates*, Int. J. Solids Structures, Vol. 10, pp. 671 - 684, 1974.
- [18] Langseth, M. and Larsen, P.K., *The Behaviour of Square Steel Plates Subjected to a Circular Blunt Ended Load*, Int. J. Impact Engng., Vol. 12, No. 4, pp. 617 - 638, 1992.
- [19] Marom, I. and Bodner, S.R., *Projectile Perforation of Multi-Layered Beams*, Int. J. Mech. Sci., Vol.21, pp. 489 - 504, 1979.
- [20] Wierzbicki, T. and Hoo Fatt, M.S., *Deformation and Perforation of a Circular Membrane due to Rigid Projectile Impact*, AMD-Vol. 127 / PVP-Vol. 225, Dynamic Response of Structures to High-Energy Excitation, ASME, 1991.
- [21] Ravid, M. and Bodner, S.R., *Dynamic Perforation of Viscoplastic Plates by Rigid Projectiles*, Int. J. Engng. Sci., Vol. 21, No. 6, pp. 577 - 591, 1983.
- [22] Liu, J. and Jones, N., *Shear and Bending Response of a Rigid Plastic Circular Plate Struck by a Mass*, Mech. Struct. & Mach., Vol. 24, No. 3, pp. 361 - 388, 1996.
- [23] Liss, J., Goldsmith, W. and Kelly, J.M., *A Phenomenological Penetration Model of Plates*, Int. J. Impact Engng., Vol. 1, No. 4, pp. 321 - 341, 1983.
- [24] Belytschko, T. and Lin, J.L., *A Three-Dimensional Impact-Penetration Algorithm with Erosion*, Computers & Structures, Vol. 25, No. 1, pp. 95 - 104, 1987.

- [25] Sewell, D.A., Ong, A.C.J. and Hallquist, J.O., *Penetration Calculations Using an Erosion Algorithm in Dyna*, Proceedings of 12th International Symposium on Ballistics, San Antonio, USA, pp. 208-217, 1990.
- [26] Schwer, L.E. and Day, J., *Computational Techniques for Penetration of Concrete and Steel Targets by Oblique Impact of Deformable Projectiles*, Nuclear Engng. and Design, No. 125, pp. 215 – 238, 1991.
- [27] Chen, E.P., *Numerical Simulation of Shear Induced Plugging in HY100 Steel Plates*, Int. J. Damage Mech., Vol. 1, pp. 132 – 143, 1992.
- [28] Belytschko, T., *On Difficulty Levels in Non Linear Finite Element Analysis of Solids*, Bulletin for Int. Assoc. Comp. Mech., No. 2, pp. 6 – 8, 1996.
- [29] Børvik, T., Langseth, M. and Malo, K.A., *A Compressed Gas Gun for Impact Testing*, Fortifikatorisk Notat No. 242 / 97, Norwegian Defence Construction Service, 1997.
- [30] Børvik, T., Vestli, K. and Langseth, M., *Determination of Projectile Path during Ballistic Penetration by use of a High-Speed Digital Camera*, Association of High-Speed Photography Conference, Cambridge, U.K., April, 1997.
- [31] Børvik, T., Holen, K., Langseth, M. and Malo, K.A., *An Experimental set-up used in Ballistic Penetration*, Proceedings of Fifth International Symposium on Structures under Shock and Impact, pp. 683 – 692, Thessaloniki, Greece, 24 - 26 June, 1998.
- [32] Børvik, T., Langseth, M., Malo, K.A. and Hopperstad, O.S., *Experimental Determination of the Ballistic Limit in Weldox 460 E Steel Plates*, Proceedings of 11th International Conference on Experimental Mechanics, pp. 233 – 238, Oxford, U.K., 24 - 28 August, 1998.
- [33] Goldsmith, W., Tham, E. and Tomer, D., *Yawing Impact on Thin Plates by Blunt Projectiles*, Int. J. Impact Engng., Vol. 16, No. 3, pp. 479 - 498, 1995.
- [34] Forrestal, M.J. and Hanchak, S.J., *Perforation of HY-100 Steel Plates with 4340 Rc 38 and T-250 Maraging Steel Rod Projectiles*, Proceedings of Int. Symposium on Transient Loading and Response of Structures (honouring Mr. Arnfinn Jenssen), Trondheim, Norway, 25 - 27 May, 1998.
- [35] Recht, R.F. and Ipson, T.W., *Ballistic Perforation Dynamics*, Int. J. Applied Mech. (Trans. ASME), Vol. 30, pp. 384-390, 1963.
- [36] Aune, A., Børvik, T. and Langseth, M., *Quasi-Static Point-Loaded Weldox 460 E Steel Plates (in Norwegian)*, Fortifikatorisk Notat No. 241/96, Norwegian Defence Construction Service, 1996.
- [37] Hawkyard, J.B., Eaton, D. and Johnson, W., *The Mean Dynamic Yield Strength of Copper and Low Carbon Steel at Elevated Temperatures from Measurements of the "Mushrooming" of Flat-Ended Projectiles*, J. Mech. Sci., Vol. 10, pp. 929 – 948, 1968.
- [38] Lindholm, U.S. and Johnson, G.R., *Strain-Rate Effects in Metals at Large Shear Strains*, Proceedings of the 29th Sagamore Army Materials Conference entitled Material Behaviour Under High Stress and Ultrahigh Loading Rates, New York, 1982.
- [39] Solberg, J.K., Børvik, T., Hopperstad, O.S. and Langseth, M., *Metallurgical Examination of Impacted Weldox 460 E Steel Plates*, to appear in a Journal, 1998.
- [40] Dieter, G.E., *Mechanical Metallurgy*, McGraw-Hill Book Company, London, 1988.
- [41] Lemaitre, J. and Chaboche, J.-L., *Mechanics of Solid Materials*, Cambridge University Press, 1990.
- [42] Lemaitre, J., *A Course on Damage Mechanics*, Springer-Verlag, 1992.

- [43] Johnson, G.R., and Cook, W.H., *Fracture Characteristics of Three Metals Subjected to Various Strains, Strain Rates, Temperatures, and Pressures*, Engineering Fracture Mechanics, Vol. 21, pp. 31-48, 1985.
- [44] Hopperstad, O.S., Berstad, T., Børvik, T. and Langseth, M., *Computational Model for Viscoplasticity and Ductile Damage*, Proceedings of 5th International LS-DYNA User Conference, Michigan, USA, 21 – 22 September, 1998.
- [45] Johnson, G.R., and Cook, W.H., *A Constitutive Model and Data for Metals Subjected to Large Strains, High Strain Rates and High Temperatures*, Proceedings of Seventh International Symposium on Ballistics, The Hague, The Netherlands, April, 1983.
- [46] Hallquist, J.O., Stillman, D.W., and Lin, T.-L., *LS-DYNA3D User's Manuals*, Livermore Software Technology Corporation, Report 1007, Rev. 2, 1994.
- [47] Berstad, T., Hopperstad, O.S. and Langseth, M., *Elasto-Viscoplastic Constitutive Models in the Explicit Finite Element Code LS-DYNA3D*, Proceedings of 2nd Int. LS-DYNA3D User Conference, San Francisco, Sept. 20-21, 1994.
- [48] Børvik, T., Aune, A., Hopperstad, O.S. and Langseth, M., *Quasi-Static Tensile Tests of Weldox 460 E Steel Plates - Introductory Study*, Fortifikatorisk Notat No. 250 / 97, Norwegian Defence Construction Service, 1997.
- [49] Børvik, T., Aune, A., Hopperstad, O.S. and Langseth, M., *Quasi-Static Tensile Tests of Weldox 460 E Steel Plates - Variation of Material Properties*, Fortifikatorisk Notat No. 255 / 97, Norwegian Defence Construction Service, 1998.
- [50] Søvik, O.P., *Numerical Modelling of Ductile Fracture - A Damage Mechanics Approach*, Dr. Ing. Thesis, Department of Machine Design and Materials Technology, NTNU, 1996.
- [51] Bridgman, P.W., *Studies in Large Plastic Flow and Fracture*, Harvard Univ. Press, 1964.
- [52] LeRoy, G., Edwards, G. and Ashby, M.F., *A Model of Ductile Fracture based on the Nucleation and Growth of Voids*, Acta Metal, Vol. 29, pp. 1509-1522, 1981.
- [53] Quick, M., Del Grande, A., Spinelli, R., Albertini, C., Børvik, T., Hopperstad, O.S., Langseth, M., *Tensile Tests at Low, Medium and High Strain-Rate of Weldox 460 E*, Fortifikatorisk Notat No. 251 / 97, Norwegian Defence Construction Service, 1997.
- [54] Harding, J., *The Development of Constitutive Relationships for Material Behaviour at High Rates of Strain*, Inst. Phys. Conf. Ser. No 102: Session 5, Oxford, U.K., 1989.
- [55] Hill, R., *The Mathematical Theory of Plasticity*, Oxford University Press, 1950.
- [56] Needleman, A., *Material Rate Dependence and Mesh Sensitivity in Localization Problems*, Computer Methods in Applied Mechanics and Engng. 67, pp. 69-85, 1988.

Table 1: Experimental results of 12 mm thick Weldox 460 E steel plates.

Test #	v_i (m/s)	v_r (m/s)	v_{rpl} (m/s)	m_p (gram)	m_{pl} (gram)	h_t (mm)	w_{max} (mm)	θ_r (mm)	θ_t (mm)
1	303.5	199.7	242.3	196.6	27.6	12.1	1.01	20.65	20.93
2	244.2	132.6	187.7	196.9	28.1	12.1	1.22	20.42	21.18
3	285.4	181.1	224.7	197.3	27.6	12.0	1.22	20.59	20.75
4	200.4	71.4	103.7	197.0	27.8	12.0	2.08	20.35	20.88
5	199.1	67.3	104.0	196.9	27.8	12.1	1.92	20.28	20.65
6	188.8	43.2	66.9	196.9	27.8	12.0	2.32	20.36	20.68
7	173.7	0	0	196.1	-	12.1	2.93	20.19	-
8	181.5	0	0	196.7	-	12.1	2.92	20.21	-
9	224.7	113.7	169.0	196.9	27.3	12.0	-	20.56	20.72
10	179.4	0	0	196.8	-	12.0	2.81	20.14	-
11	189.6	43.7	71.8	196.9	27.9	12.1	1.98	20.40	20.77
12	189.2	40.1	66.8	196.7	28.0	12.1	1.87	20.36	20.63
13	177.3	0	0	197.0	-	12.1	2.95	20.21	-
14	184.3	30.8	45.3	196.8	27.8	12.1	2.04	20.35	20.64
15	189.6	42.0	64.0	196.7	27.7	12.1	2.06	20.34	20.63
16	184.8	0	0	196.9	-	12.1	2.59	20.20	-

Table 2: Preliminary model constants for Weldox 460 E steel.

Elastic constants and density			Yield stress and strain hardening			Strain-rate hardening		Damage Evolution	
E (GPa)	ν	ρ (kg/m ³)	A (MPa)	B (MPa)	n	\dot{p}_0, \dot{t}_0 (s ⁻¹)	C	D_c	p_d
200	0.33	7850	490	807	0.73	$5 \cdot 10^{-4}$	0.012	0.30	0
Adiabatic heating and temperature softening					Fracture strain Constants				
C_p (J/kgK)	α	T_m (K)	T_0 (K)	m	D_1	D_2	D_3	D_4	D_5
452	0.9	1800	293	0.94	0.0705	1.732	-0.54	-0.0123	0

Table 3: Numerical programme and results.

Run #	Input data			Experimental		Numerical	
	v_i (m/s)	m_p (gram)	h_t (mm)	v_r (m/s)	v_{rpl} (m/s)	v_r (m/s)	v_{rel} (m/s)
10-9	296.0	196.7	9.7	218	243	224	232
12-15	189.6	196.7	12.1	42	62	0	0
12-1	303.5	196.6	12.1	200	242	206	265
12-2	244.2	196.9	12.1	133	188	109	142
12-9	224.7	196.9	12.0	114	169	94	123
12-4	200.4	197.0	12.0	71	104	0	0
12-8	181.5	196.7	12.1	0	0	0	0
12-N1	215.0	197.0	12.0	-	-	69	76
12-N2	210.0	197.0	12.0	-	-	38	47
12-N3	205.0	197.0	12.0	-	-	0	0

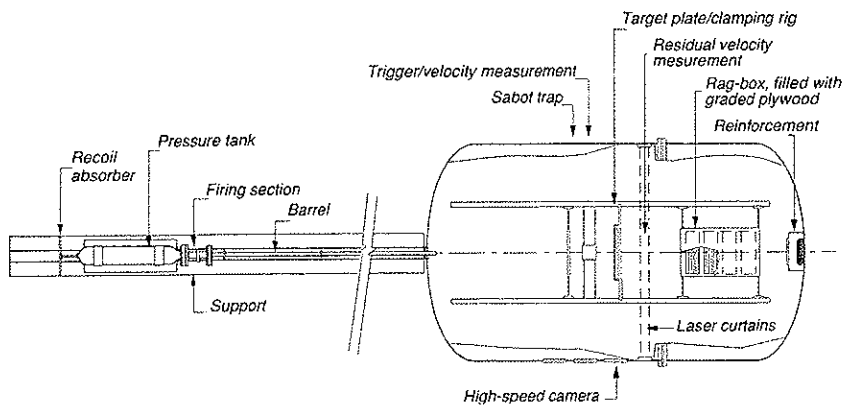


Figure 1: Sketch of compressed gas gun [29].

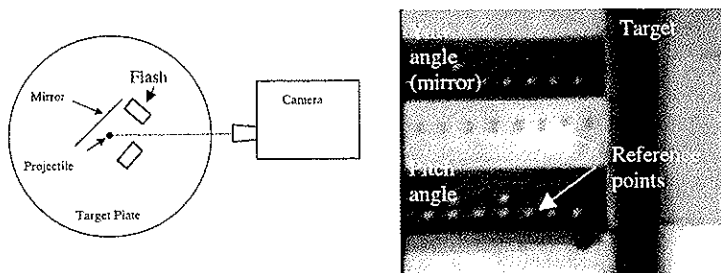


Figure 2: Set-up of high-speed camera system giving 3D images [30].

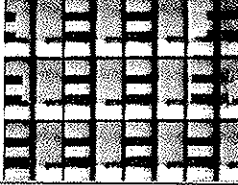
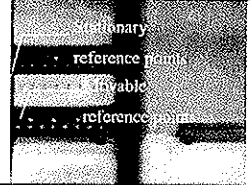
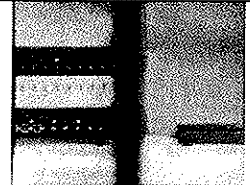
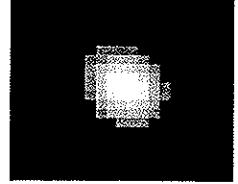

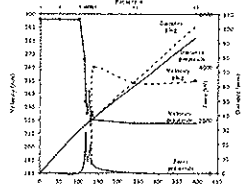
1. Full frame	2. Image	3. Selection of fiducial marks
		
<p>The full frame picture of the test is shown. The total number of points to measure is selected.</p>	<p>The different images within the full frame are selected and enlarged, one by one.</p>	<p>Fiducial marks on the projectile and support are marked by the cursor, and detected by the program.</p>
4. Centre of gravity	5. Repetition of procedure	6. Results
		
<p>The point is enlarged 10 times. Unwanted pixels are removed, and the centre of gravity is calculated based on the pixel intensity.</p>	<p>The procedure is repeated for all images in the test. The sub-pixel distance moved between each image is calculated.</p>	<p>Based on the known time interval and a calibration value, distance, velocity and acceleration are found as a function of time.</p>

Figure 3: Procedure for calculation of velocity as a function of time [31].

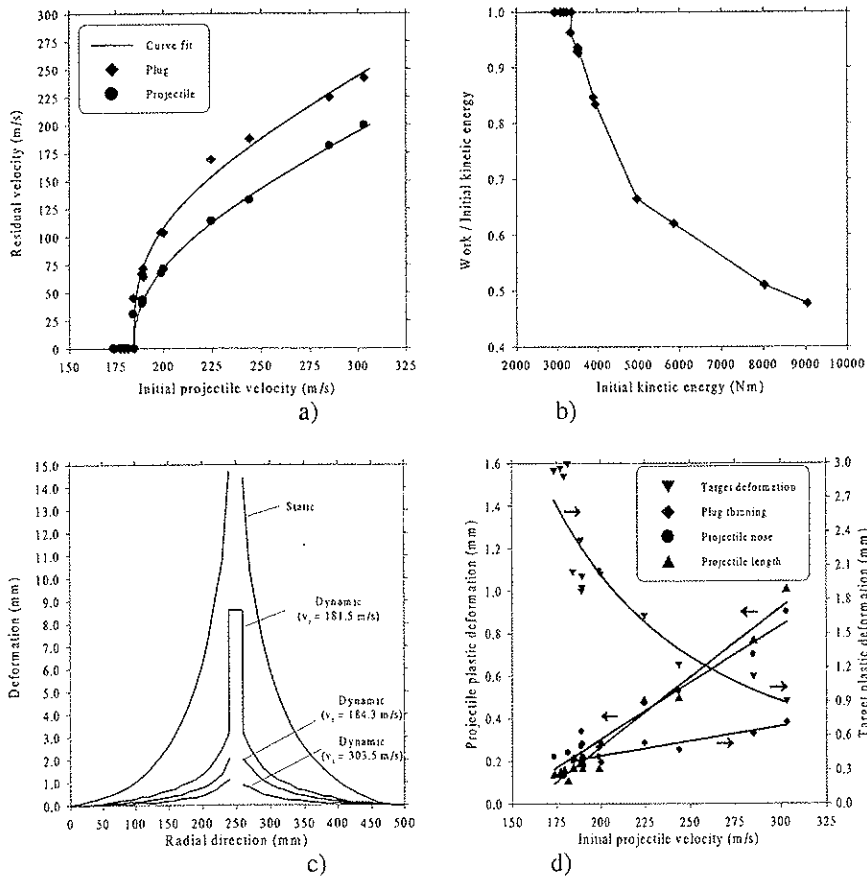


Figure 4: Graphical representation of important response parameters.

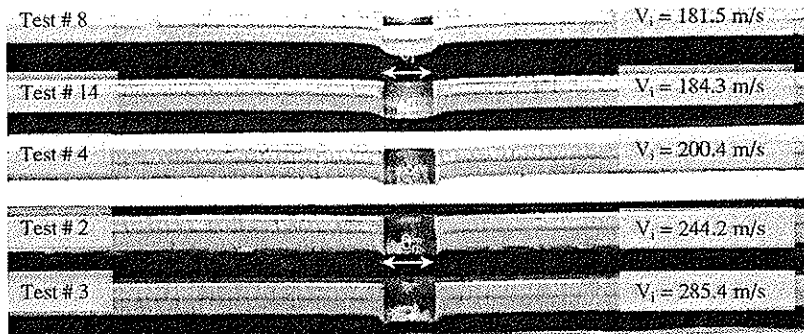


Figure 5: Cross-sections of penetrated 12 mm thick Weldox 460 E steel targets.



Figure 6: Typical projectile and plug after perforation.

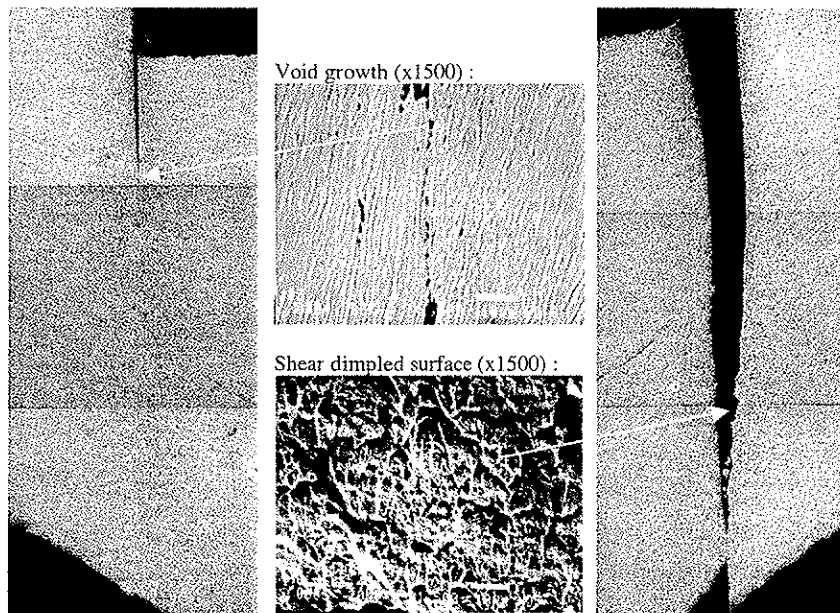
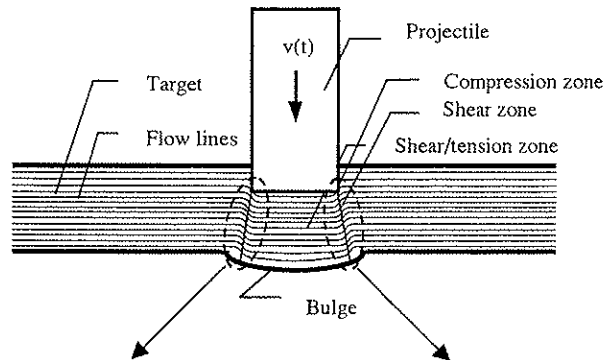


Figure 7: Metallurgical images of the localised shear zone (x32). Note that the pictures showing the shear zones are constructed based on several images.

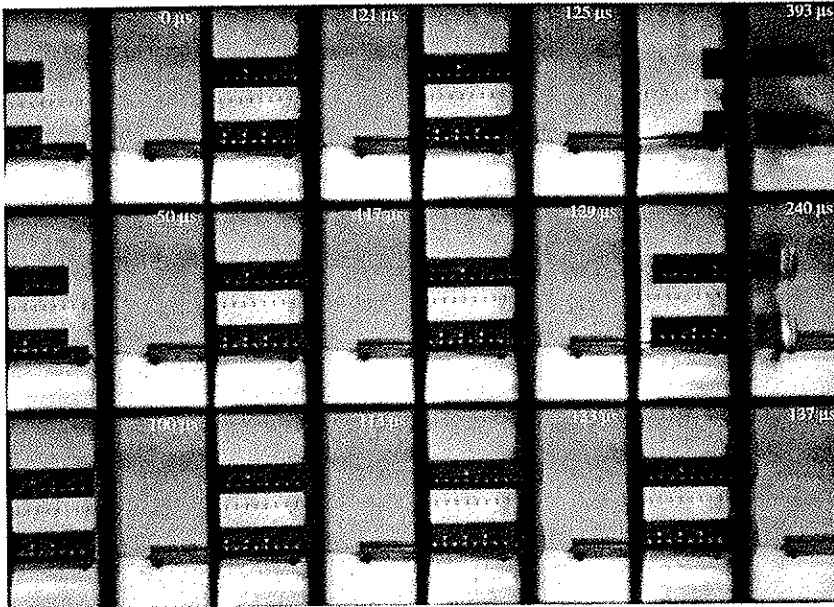


Figure 8: Perforation of 10 mm thick Weldox 460 E steel plate (test # 10-9 in [32]).

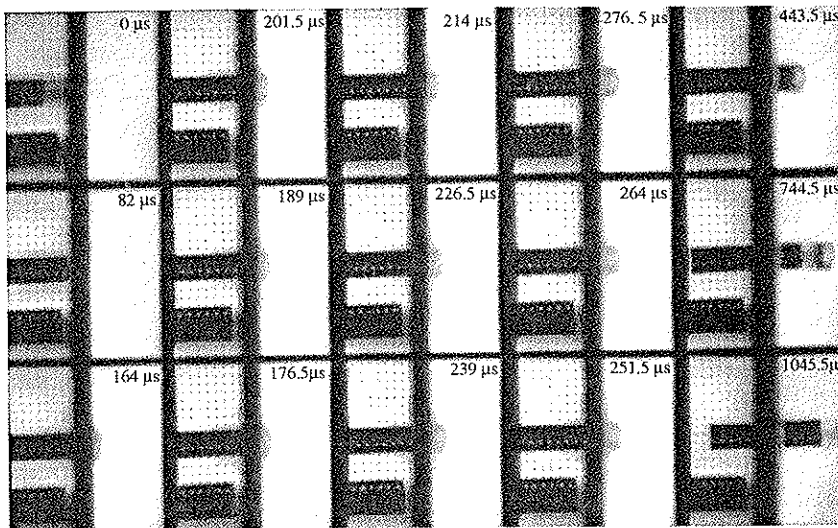


Figure 9: Perforation of 12 mm thick Weldox 460 E steel plate (test # 12-15).

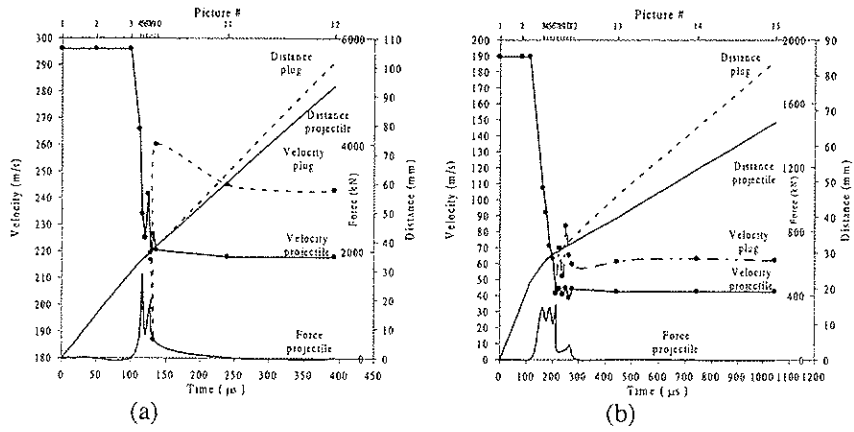


Figure 10: High-speed camera measurements of a) test # 10-9 and b) test # 12-15.

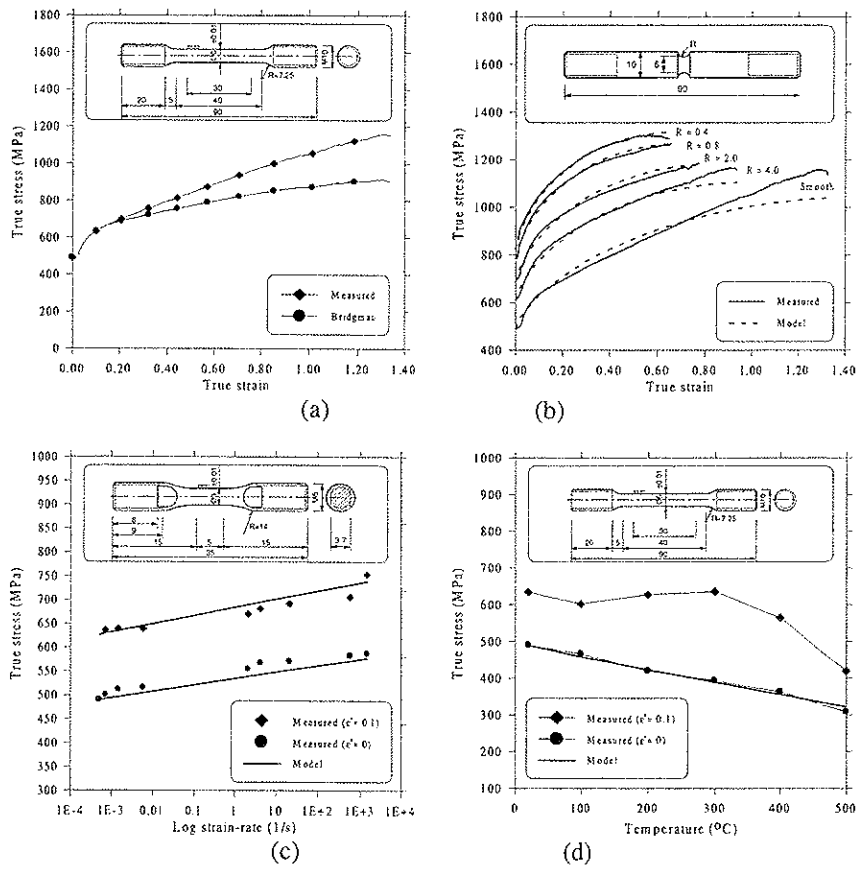


Figure 11: Material test data used for identification of the model constants.

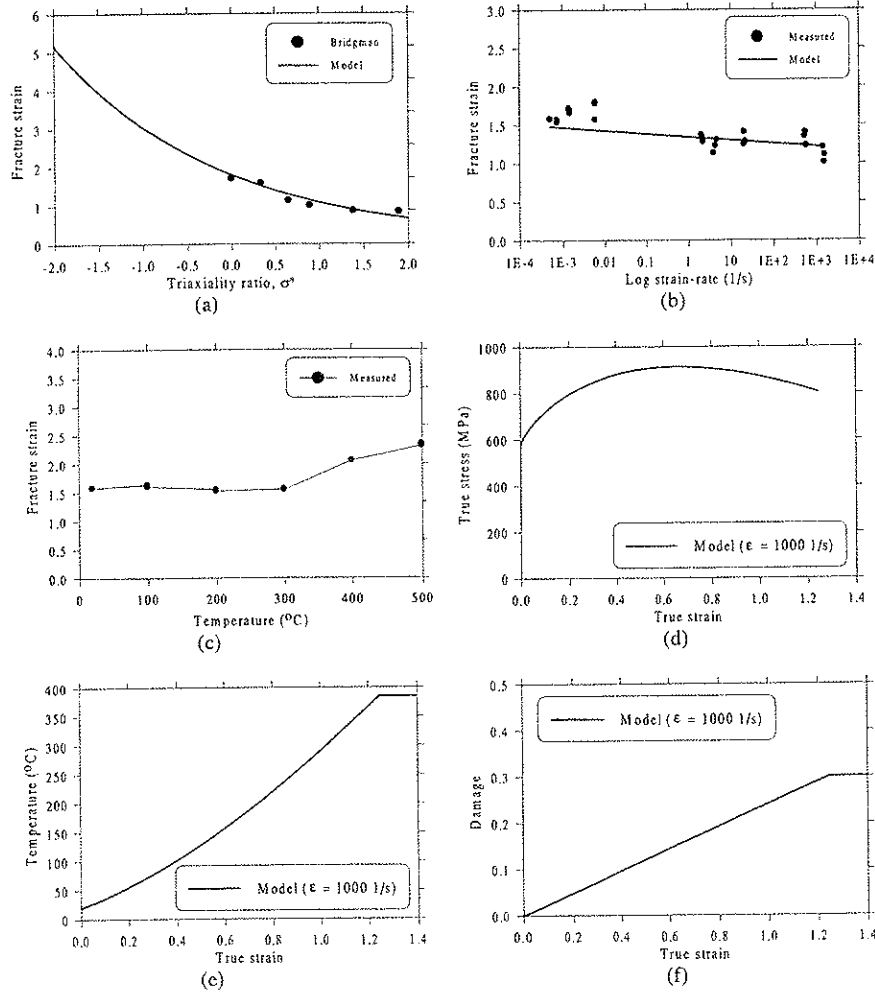
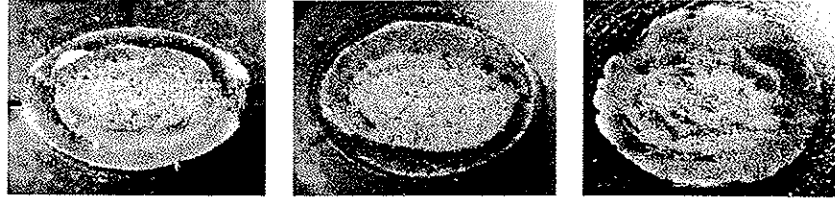


Figure 12: Calibration of material model.

a) Smooth and notched specimen tensile tests:



Smooth, $\epsilon_f = 1.64$

$R = 4.0$, $\epsilon_f = 1.13$

$R = 0.8$, $\epsilon_f = 0.86$

b) Dynamic tensile tests at various strain-rates:



$\dot{\epsilon} = 7.4 \cdot 10^{-4} \text{ s}^{-1}$, $\epsilon_f = 1.57$

$\dot{\epsilon} = 4.4 \text{ s}^{-1}$, $\epsilon_f = 1.22$

$\dot{\epsilon} = 1573 \text{ s}^{-1}$, $\epsilon_f = 1.11$

c) Tensile tests at various temperatures:



$T = 100 \text{ }^\circ\text{C}$, $\epsilon_f = 1.60$

$T = 300 \text{ }^\circ\text{C}$, $\epsilon_f = 1.54$

$T = 500 \text{ }^\circ\text{C}$, $\epsilon_f = 2.34$

Figure 13: Fracture surfaces of some tensile test specimens as a function of a) triaxiality, b) strain-rate and c) temperature. Notice how the specimen geometry changes from isotropic to anisotropic behaviour with increasing strain to fracture.

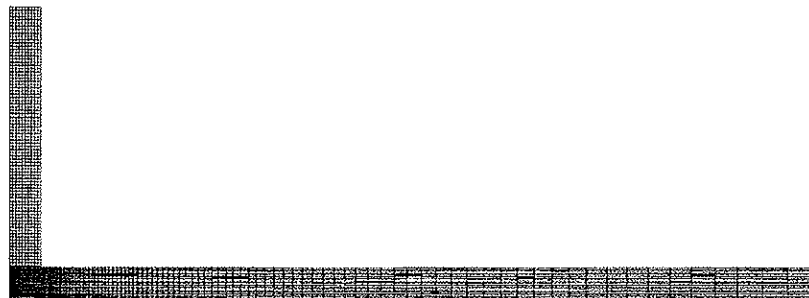


Figure 14: Finite element model of the penetration problem.

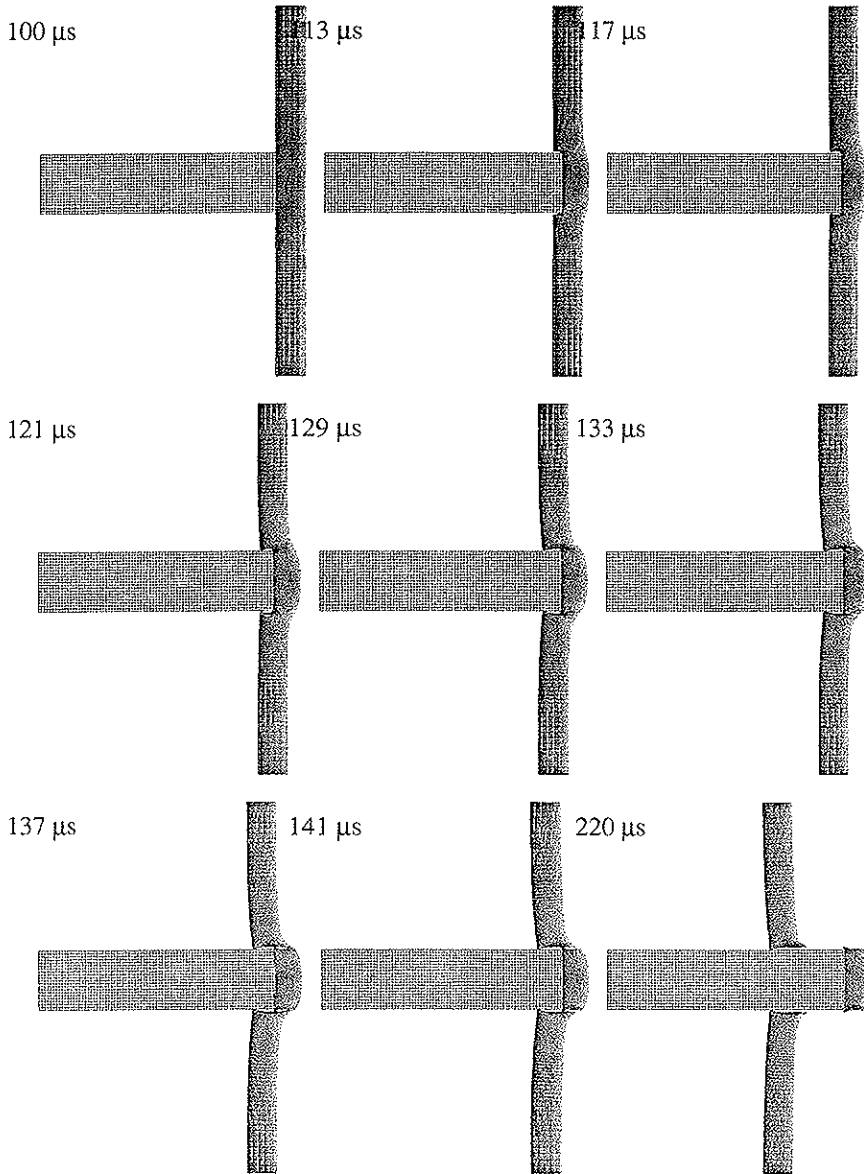


Figure 15: Plots of deformed mesh during perforation from run # 10-9.

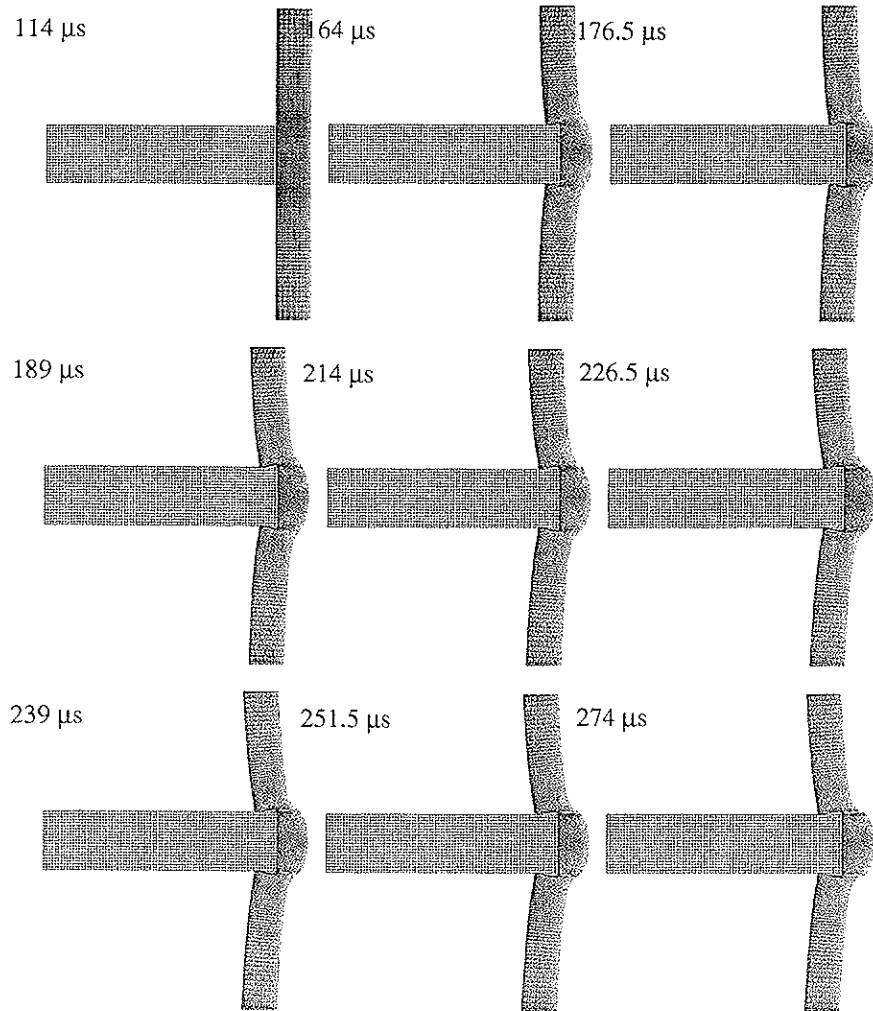


Figure 16: Plots of deformed mesh during perforation from run # 12-2N.

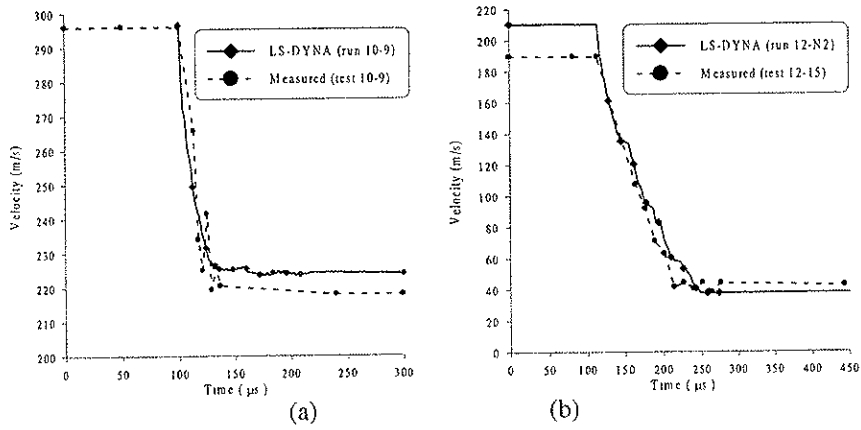


Figure 17: Numerical vs. experimental velocity-time curves for a) test and run # 10-9 and b) test # 12-15 and run # 12-N2.

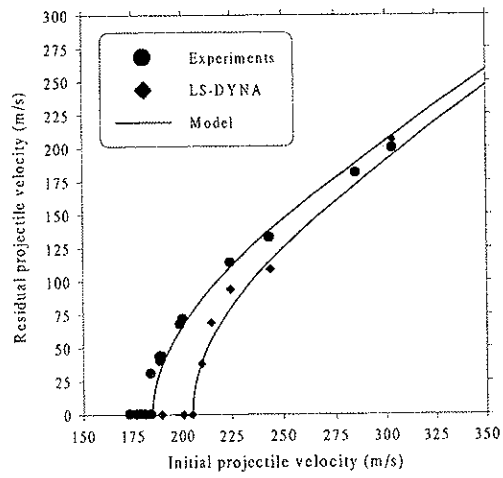


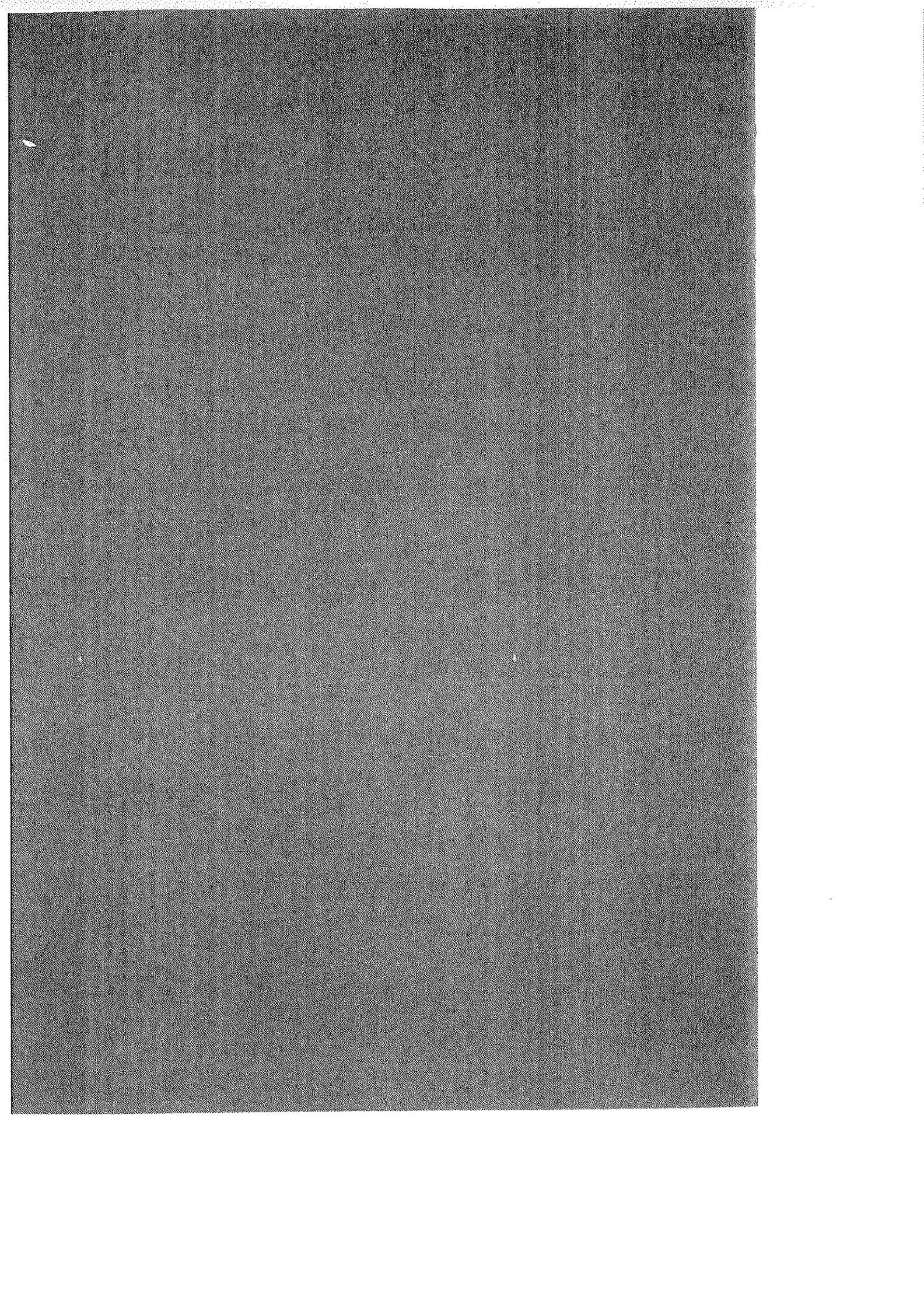
Figure 18: Comparison between calculated and measured ballistic limit curves.

Part III

T. Børvik, O.S. Hopperstad, T. Berstad and M. Langseth

Computational Model of Viscoplasticity and Ductile Damage for Projectile Impact.

Submitted for possible journal publication.



Computational Model of Viscoplasticity and Ductile Damage for Projectile Impact

T. Børvik*, O. S. Hopperstad, T. Berstad and M. Langseth

Structural Impact Laboratory (SIMLab), Department of Structural Engineering, Norwegian University of Science and Technology, N-7491 Trondheim, Norway

Abstract

A coupled constitutive model of viscoplasticity and ductile damage for penetration and impact related problems has been formulated and implemented in the explicit finite element code LS-DYNA. The model, which is based on the constitutive model and fracture strain model of Johnson and Cook, and on continuum damage mechanics as proposed by Lemaitre, includes linear thermoelasticity, the von Mises yield criterion, the associated flow rule, non-linear isotropic strain hardening, strain-rate hardening, temperature softening due to adiabatic heating, isotropic ductile damage and failure. For each of the physical phenomena included in the model, one or several material constants are required. However, all material constants can be identified from relatively simple uniaxial tensile tests without the use of numerical simulations. In this paper the constitutive model is described in detail. Then material tests for Weldox 460 E steel and the calibration procedure are presented and discussed. The calibrated model is finally verified and validated through numerical simulations of material and plate perforation tests investigated experimentally.

Keywords: impact; constitutive behaviour; dynamic fracture; elastic-viscoplastic material; finite elements

1. Introduction

Penetration and impact related problems have been studied for a long time, and substantial effort has been invested in order to understand the phenomena occurring in the abrupt collision between two bodies. In numerical simulations of this type of problems, one particular challenge is to characterise the material behaviour under high strain-rate loading conditions. A complete material description involves not only the stress-strain response as a

* Corresponding author. Tel.: + 47 73 59 46 47; fax: + 47 73 59 47 01
E-mail: tore.borvik@bygg.ntnu.no (T. Børvik)

function of large strains, high strain-rates, high temperatures, varying stress states and history of loading, but also the accumulation of damage and the mode of failure (Zukas et al, 1990).

In addition to plastic flow at high rates of strain, fracture is an important aspect of dynamic material characterisation for engineering applications in structural impact. At impact, a blunt-nosed projectile tends to localise the deformation in narrow shear zones throughout the target thickness. Due to the high strain-rate, the heat generated by plastic work in the localised regions has no time to transfer and the process becomes adiabatic. The temperature rise gives local softening, while the surrounding material continues to strain harden. When further loaded, the soft zones deform more than the surrounding area, making these zones even softer. If the thermal softening overcomes the strain and strain-rate hardening, the deformation takes place in bands of intense plastic shear. This is known as adiabatic shear localisation or thermal-plastic instability. In some situations, the localised zones may become extremely narrow. The local temperature increase may give a phase change in the material that appears in carbon steels as intense white bands of deformed martensite if etched in nital. Such bands are broadly termed transformed adiabatic shear bands (Bai and Dodd, 1992). The effect of softening due to adiabatic heating is widely accepted and often included in impact simulations.

The large strains in the adiabatic shear band may lead to material degradation. The damage and fracture process in ductile metals involves a number of metallurgical events such as nucleation, growth, and coalescence of voids (Dieter, 1988). Such growth of microvoids and microcracks results in a progressive reduction of the load-carrying area of the material. This process, giving a loss in material strength and stiffness, is called damage (Lemaitre, 1990). When the damage process reaches a stage where the voids coalesce to give a macrocrack, fracture is normally assumed. The damage evolution is found to be influenced by strain-rate, temperature, history of loading and stress state (Zukas et al, 1990). In particular the stress state seems to be important, since void growth is found to be very sensitive to hydrostatic stresses in the material during straining. The latter has been proven by e.g. Bridgman (1952), McClintock (1968), Hancock and Mackenzie (1976), and Rice and Tracy (1978). During penetration of blunt nosed projectiles, a compression stage due to inertia occurs while the projectile indents the target. This stage is rapidly overcome once the target mass in front of the projectile starts to move, and the deformation mechanism changes into localised shear at the well-defined periphery of the projectile. When the projectile has penetrated a certain amount of the target thickness, a plug is formed and fracture occurs under a combination of shear and tensile stresses. Hence, the stress state in the target changes continuously during

penetration, which again influence the damage and fracture process. The different stress states have been identified through a metallurgical examination of penetrated steel plates, as shown in Fig. 1 (Børvik et al, 1999).

According to Zukas et al (1990) the nucleation and growth of microvoids and microcracks at impact occur independently at various points in the bulk material due to the short time duration of high intensity stresses generated by transient stress waves. In ductile metals these microvoids, which growth is controlled by the localised plastic flow around them, grow rapidly and coalesce under high tensile mean stresses. A metallographic study by Miller (1970) of ductile fracture in carbon steels also showed that a combination of applied tensile stresses and concentrated shear was required to initiate voids. In Fig. 1, voids have been identified in front of the crack tip along the shear zones (Børvik et al, 1999). Shear dimples formed from numerous elongated voids in the material are also found along all fracture surfaces, indicating a ductile failure. However, Dieter (1988) states that particles as small as 50 Å have been found to nucleate voids, so that the absence of voids during metallographic studies is not a reliable indicator of whether void formation has occurred.

The computational model described in this paper is suitable for large-scale finite element simulations. It is formulated within the framework of viscoplasticity and continuum damage mechanics, allowing for large strains, high strain-rates and adiabatic heating. No predefined defects are required in order to predict fracture. In viscoplasticity, a yield criterion, a flow rule, and rules for strain and strain-rate hardening govern the plastic deformation of the material. In continuum damage mechanics, the main ingredients are the damage measure, the effective stress concept, the principle of strain equivalence and the damage evolution rule. Even if each new phenomenon included in a phenomenological model requires one or several material constants to be determined from material tests, sophisticated models seem to be necessary in order to solve the highly complex penetration problem (Zukas et al, 1990). First, the computational model of viscoplasticity and ductile damage is presented. Then the identification of the model constants from material tests of Weldox 460 E steel is described. Only uniaxial tensile tests are necessary to have a calibrated model for the ductile material. The model is finally verified and validated through numerical simulations of material and plate perforation experiments.

2. Computational Model of Viscoplasticity and Ductile Damage

The proposed computational model includes linear thermoelasticity, viscoplasticity and ductile damage, and is developed for an isotropic material. Assuming negligible elastic strains compared with the plastic strains, it is reasonable to adopt an additive decomposition of the deformation rate tensor \mathbf{d} into an elastic part, a plastic part and a part due to thermal straining (Khan and Huang, 1995). The elastic domain is defined by means of the von Mises yield criterion, and it is assumed that isotropic strain hardening is sufficient to describe the evolution of the yield surface during plastic deformation. Strain hardening is thus described in terms of the damage accumulated plastic strain r (Lemaitre, 1996). It is further assumed that the elastic and viscoplastic properties of the material depend on the temperature T generated by adiabatic heating under high strain-rate loading conditions, while any thermomechanical coupling with the surroundings is not included in the formulation. The damage evolution is described by the damage variable D , representing the surface density of intersections of microcracks and microcavities with any plane in the body (Lemaitre, 1996). For a virgin material D equals zero and for a fully broken element D is equal to one. However, the material element breaks by atomic decohesion before D becomes one, and the criterion for macrocrack initiation and failure is $D = D_C$, where D_C is less than one. The critical value of damage D_C is assumed to be a material characteristic.

The hypothesis of strain equivalence (Lemaitre, 1996) states that any strain constitutive equation for a damaged material may be derived in the same way as for the virgin material except that the Cauchy stress tensor $\boldsymbol{\sigma}$ is replaced by an effective stress tensor

$$\tilde{\boldsymbol{\sigma}} = \frac{\boldsymbol{\sigma}}{1-D} \quad (1)$$

which is the stress defined on the effective area of the material element. This hypothesis is adopted in the following to include damage in the viscoplastic constitutive equations. The additive decomposition of the deformation rate tensor into an elastic part, a plastic part and a thermal part may be given as (Tvergaard and Needleman, 1992)

$$\mathbf{d} = \mathbf{d}^e + \mathbf{d}^p + \mathbf{d}^t \quad (2)$$

where \mathbf{d}^e , \mathbf{d}^p and \mathbf{d}^t are the elastic, plastic and thermal deformation rate tensor, respectively. The material is further assumed to be linear-elastic. The Jaumann rate of the effective stress tensor is thus defined in terms of the elastic deformation rate tensor as (Bammann et al, 1993)

$$\dot{\tilde{\boldsymbol{\sigma}}} = \mathbf{C}:\mathbf{d}^e \quad \text{or} \quad \dot{\tilde{\boldsymbol{\sigma}}} = (1-D)\mathbf{C}:\mathbf{d}^e - \frac{\dot{D}}{(1-D)}\tilde{\boldsymbol{\sigma}} \quad (3)$$

where \mathbf{C} is a fourth-order tensor of elastic constants. Since isotropic linear-elasticity is adopted, \mathbf{C} is thus a function of Young's modulus E and Poisson's ratio ν only. Assuming isotropic thermal expansion, the thermal deformation rate tensor is given as

$$\mathbf{d}^t = \alpha \dot{T} \mathbf{I} \quad (4)$$

where α is the thermal expansion coefficient, \dot{T} is the rate of temperature increase, and \mathbf{I} is a second-order unit tensor. The elastic domain of the material is a convex domain in the effective stress space, defined as

$$F(\tilde{\boldsymbol{\sigma}}, r, T) = f(\tilde{\boldsymbol{\sigma}}) - \sigma_0(T) - R(r, T) \leq 0 \quad (5)$$

where σ_0 is the yield strength, R is the strain hardening function, r is the accumulated damage plastic strain and f is a convex function defining the equivalent stress

$$\sigma_{eq} = f(\boldsymbol{\sigma}) = \sqrt{\frac{3}{2} \boldsymbol{\sigma}' : \boldsymbol{\sigma}'} \quad (6)$$

where $\boldsymbol{\sigma}'$ is the deviatoric stress tensor. It is also convenient to define the damage equivalent stress as

$$\tilde{\sigma}_{eq} = f(\tilde{\boldsymbol{\sigma}}) = \frac{\sigma_{eq}}{1-D} \quad (7)$$

In the viscoplastic domain the yield function F is equal to the viscous stress σ_v , which controls the strain-rate sensitivity of the material (Lemaitre, 1990), i.e.

$$F(\tilde{\sigma}, r, T) = \sigma_v(\dot{r}, r, T) > 0 \Leftrightarrow f(\tilde{\sigma}) = \sigma_0(T) + R(r, T) + \sigma_v(\dot{r}, r, T) \quad (8)$$

This equation may be solved to give the strain-rate \dot{r} for the damaged material as a function of the state variables $\tilde{\sigma}$, r and T . The plastic deformation rate tensor is defined by means of the associated flow rule

$$\mathbf{d}^p = \dot{r} \frac{\partial f(\tilde{\sigma})}{\partial \tilde{\sigma}} = \frac{3}{2} \frac{\dot{r}}{1-D} \frac{\tilde{\sigma}'}{\tilde{\sigma}_{eq}} \quad (9)$$

while the rate of the accumulated plastic strain \dot{p} is defined by

$$\dot{p} = \sqrt{\frac{2}{3} \mathbf{d}^p : \mathbf{d}^p} = \frac{\dot{r}}{1-D} \quad (10)$$

Assuming adiabatic conditions, the rate of temperature increase is usually defined as (Bammann et al, 1993)

$$\dot{T} \approx \chi \frac{\boldsymbol{\sigma} : \mathbf{d}^p}{\rho C_p} \quad (11)$$

where C_p is the specific heat and ρ is the density, and the Taylor-Quinney empirical constant χ is often assigned the value 0.9. However, recent tests have indicated that this parameter may vary with plastic strain (Jones, 1997).

The constitutive relation adopted in the model reads (Hopperstad et al, 1998a)

$$\boldsymbol{\sigma}_{eq} = (1-D) [\sigma_0(T) + R(r, T) + \sigma_v(\dot{r}, r, T)] \quad (12)$$

The well-known Johnson and Cook (1983) model fits into this formulation. Originally, the model was given as

$$\sigma_{eq} = [A + Bp^n] [1 + C \ln \dot{p}^*] [1 - T^*{}^m] \quad (13)$$

where A , B , C , n and m are material constants, $T^* = (T - T_0)/(T_m - T_0)$ is the homologous temperature, where T_0 is the room temperature and T_m is the melting temperature, $\dot{p}^* = \dot{p}/\dot{p}_0$ is a dimensionless strain-rate, and \dot{p}_0 is a user-defined reference strain-rate. Camacho and Ortiz (1997) modified the strain-rate sensitivity term in Eq. (13) to avoid unwanted effects if $\dot{p}^* < 1$. Therefore, a modified version of the Johnson-Cook model can be written as

$$\sigma_{eq} = [A + B\dot{p}^n][1 + \dot{p}^*]^C [1 - T^{*m}] \quad (14)$$

Note that $\dot{p} = \dot{r}$ in Eq. (13) and (14) since $\dot{D} = 0$, i.e. no coupling between damage and the constitutive equation. It is possible to obtain the modified Johnson-Cook model from the constitutive relation defined in Eq. (12) by making the following identifications for the yield stress σ_0 , the strain hardening function R and the viscous stress σ_v

$$\begin{aligned} \sigma_0(T) &= A(1 - T^{*m}) \\ R(r, T) &= Br^n(1 - T^{*m}) \\ \sigma_v(\dot{r}, r, T) &= g(\dot{r}^*)(A + Br^n)(1 - T^{*m}) \end{aligned} \quad (15)$$

where $\dot{r}^* = \dot{r}/\dot{r}_0$ is a dimensionless strain-rate, \dot{r}_0 is a user-defined reference strain-rate, and the function $g(\dot{r}^*)$ is given as

$$g(\dot{r}^*) = (1 + \dot{r}^*)^C - 1 \quad (16)$$

Eq. (15) and Eq. (16) inserted in Eq. (12) gives the constitutive relation used in the model

$$\sigma_{eq} = [1 - D][A + Br^n][1 + \dot{r}^*]^C [1 - T^{*m}] \quad (17)$$

In the Johnson and Cook (1985) fracture strain model, the damage evolution is defined as

$$\dot{D} = \frac{\dot{p}}{p_f} \quad (18)$$

in which p_f is the actual value of the fracture strain in terms of stress triaxiality, strain-rate and temperature. Again, by applying the modified expression for the strain-rate sensitivity, a modified version of the Johnson-Cook fracture strain model becomes

$$p_f = [D_1 + D_2 \exp(D_3 \sigma^*)] [1 + \dot{p}^*]^{D_4} [1 + D_5 T^*] \quad (19)$$

The stress triaxiality ratio is defined as $\sigma^* = \sigma_H / \sigma_{eq}$, where σ_H is the hydrostatic stress, and D_1 to D_5 are material constants. In Eq. (18) it is assumed that $D = 0$ for a virgin material, and that fracture occurs when $D = 1$. Here, the following expression is used to define the damage evolution during plastic straining

$$\dot{D} = \begin{cases} 0 & \text{for } p \leq p_d \\ D_C \frac{\dot{p}}{p_f - p_d} & \text{for } p > p_d \end{cases} \quad (20)$$

where p_d is a damage threshold and D_C is the critical damage, i.e. fracture occurs as D reaches $D_C \leq 1$. For simplicity it is assumed that D_C is a material constant. The unified model of viscoplasticity and ductile damage is implemented in LS-DYNA (1997) using a vectorised backward-Euler integration algorithm (Berstad et al, 1994). The model is applicable for shell and solid elements in three-dimensional analysis, as well as axisymmetric elements in two-dimensional analysis. The model is coupled with an element-kill option available in LS-DYNA, and as the damage variable reaches its critical value D_C , the element is removed. It is referred to Berstad et al (1994) for details about the backward-Euler integration algorithm.

3. Material Characterisation

For each of the phenomena described in the computational model, one or several material constants are required. These can all be identified from relatively simple uniaxial tensile tests. Four types of tensile tests are required: quasi-static smooth specimen tests, quasi-static notched specimen tests, tests at different strain-rates, and tests at elevated temperatures. Due to the model formulation, i.e. no coupling between the different effects, the characterisation procedure becomes straightforward.

3.1. Target Material - Weldox 460 E Steel

Weldox is the brand name of a class of thermomechanically rolled ferritic structural steels that offers both high strength and ductility. These are both assumed as important parameters in order to have an effective energy absorber during structural impact. Especially Weldox 460 E seems to have an optimised combination of strength and ductility, and was therefore chosen as target material in this study. Due to the thermomechanical treatment during hot-working, Weldox 460 E has a very fine microstructure of randomly distributed irregular and acicular shaped grains. This indicates that the macroscopic behaviour of Weldox 460 E is almost isotropic. The supplier has given some general material data, which is presented in Table 1-3.

3.2. Introductory Quasi-Static Tensile Tests

Introductory uniaxial tensile tests at room temperature and a strain-rate of $5 \cdot 10^{-4} \text{ s}^{-1}$ were carried out on 6 mm flat specimens, as shown in Fig. 2a). The experimental programme contained nine tensile test coupons taken in three different directions ($\alpha=0^\circ$, $\alpha=45^\circ$, $\alpha=90^\circ$) to the rolling direction of the material. During the tests, the axial force in the load cell and the displacement of the moving crosshead were measured, and extensometers were used to measure both longitudinal and transverse strains up to diffuse necking.

The purpose of the introductory tests was to determine the elastic constants and to investigate whether the material could be considered as isotropic and homogeneous. Weldox 460 E was found to behave as typical low carbon steels, showing a distinct yield plateau with a constant yield point elongation of about 2.5 % at this strain-rate. After initial yielding, a moderate strain hardening was observed. The material was also found to be very ductile with a true fracture strain of about 1.5. The elastic properties were determined within the central 80 % of the initial linear region of the stress-strain curves. From these measurements the mean value of Young's modulus was found to be approximately 200 GPa. The Poisson's ratio ν , given as the ratio between the elastic stiffness measured in the longitudinal direction divided by the elastic stiffness measured in the transverse direction, was found close to 0.33.

To investigate whether the material was isotropic in yield stress and exhibited isotropic hardening, the true stress-strain curves in different directions were compared. As shown in Fig. 4a), the anisotropy in stress was found to be small. To depict anisotropy in strain, the

ratio between the plastic strains in the width and thickness direction was compared. Assuming proportional strains, the R-ratio is given as (Barlat and Richmond, 1987)

$$R = \frac{\epsilon_w^p}{\epsilon_t^p} = - \frac{\epsilon_w^p}{\epsilon_t^p + \epsilon_w^p} \quad (21)$$

This measure is equal to unity if the material is isotropic in strain. As seen from Fig. 4b), the R-ratio is almost constant and close to 0.9 for all levels of plastic strain. This small anisotropy in strain was ignored. However, the extensometers were removed at approximately 15 % total strain due to diffuse necking. According to Zukas et al (1990), damage is directional and may introduce anisotropy into the previously isotropic material at large plastic strains.

In subsequent penetration tests, target plates with different thicknesses were tested (Børvik et al, 1999). This involved material from several deliveries, having different batch numbers, and it follows that scatter in material properties may appear. In order to reveal such scatter, specimens were machined from 8, 10 and 12 mm thick plates. Coupons were taken at different locations throughout the thickness (both from the mid-section and the edge of the plate), and in two different directions ($\alpha=0^\circ$ and $\alpha=90^\circ$) to the rolling direction of the material. Two repetitions were carried out for each parameter investigated, giving a total of 24 additional tests. It was found that the scatter in material properties was generally small and could be ignored.

Based on the introductory tests it was decided that in the following specimens should be taken from the same 12 mm thick Weldox 460 E steel plate and only parallel to the rolling direction of the material, i.e. $\alpha=0^\circ$. The observed isotropic material behaviour, at least for small strains, justifies the use of an isotropic yield criterion and isotropic strain hardening in the computational model.

3.3. *Quasi-Static Tensile Tests: Smooth and Notched Specimens*

Quasi-static tensile tests were carried out on circular specimens at room temperature with a constant strain-rate of $5 \cdot 10^{-4} \text{ s}^{-1}$. The experimental programme comprised both smooth and notched specimens, with geometry as shown in Fig. 2b) and Fig. 2c). The smooth specimens were given an artificial neck of 0.01 mm in the central region to ensure that necking took place there. The initial neck was assumed to have negligible effects on the tensile properties.

Notched specimens with four different notched root radii were tested ($R = 0.4$ mm, $R = 0.8$ mm, $R = 2.0$ mm and $R = 4.0$ mm). The different notches introduce different levels of hydrostatic tension in the specimens during straining, which distinctly effect both the true stress and the strain to failure of the material. The initial radius in the gauge section was kept constant at $a = 3$ mm for all specimens tested. During the tests, applied load, crosshead displacement and longitudinal strain were measured.

The longitudinal strain is usually measured by an extensometer, which is removed before incipient necking. The true stress-strain curve is then calculated based on the measured engineering values, and extrapolated to higher strains. In the penetration problem where large plastic strains appear, this procedure becomes uncertain. An apparatus that allows true strain to be measured directly to fracture has been developed (Søvik, 1996). This special device consists of four inductive displacement gauges attached to a circular frame, which is used to record the reduction in cross-sectional area of the specimen during straining. The diameter reduction is calculated from the average of the recordings from the four displacement gauges. The frame is kept in position by stiff rods parallel to the specimen. To be able to measure the diameter reduction directly in the neck, the frame is free to move in the vertical direction. Six smooth specimens were tested. For the notched specimens, the number of parallels was three. This gave a total of 18 tests. The first three of the smooth specimens were tested using an extensometer for better registration of strains prior to necking. The last three of the smooth and all the notched specimens were tested using the diameter reduction measurement device. In the range covered by the extensometer, the true uniaxial strain is defined as

$$\varepsilon_1 = \ln(L) - \ln(L_0) \quad (22)$$

where L and L_0 represents the current and initial specimen gauge length, respectively. Assuming volume constancy, the strain during diameter reduction can be related to the current (d) and initial (d_0) diameter of the specimen, i.e.

$$\varepsilon_1 = 2\{\ln(d_0) - \ln(d)\} \quad (23)$$

The true stress is calculated by dividing the applied load F by the current minimum cross-sectional area A . Fig. 5 shows a comparison between the extensometer values and the diameter reduction measurements for smooth tensile specimens to a total strain of 15%.

Excellent agreement was obtained between the different strain measurement methods, which lends confidence to the applied measuring device for diameter reduction. Fig. 6a) shows the mean load versus diameter reduction curves for all specimens tested. The experimental scatter among specimens of identical initial geometry was found negligible. Fig. 6b) gives the calculated true stress – true strain curves for both smooth and notched specimens based on the diameter reduction measurements. As seen, the true stress is increased and the fracture strain is reduced with decreasing notch root radius, i.e. increased level of hydrostatic tension in the material during straining.

3.4. *Dynamic Tensile Tests*

The strain-rate sensitivity of Weldox 460 E was obtained by means of uniaxial tensile tests at room temperature and strain-rates between 10^{-4} and 10^3 s⁻¹. These tests were carried out at the European Commission Joint Research Centre, Ispra, Italy (Quick et al, 1997). The huge variation in strain-rate applied during the tests enforced the use of different experimental techniques. Low strain-rate tensile tests were performed in a Hounsfield Tensometer at strain-rates between 10^{-4} and 10^{-2} s⁻¹. Here, load measurements were made with a strain gauge attached to elastic bars holding the specimen and an inductive displacement transducer measured the displacement of the specimen. Tensile tests at medium strain-rates were performed in a hydro-pneumatic testing machine. By allowing water to flow out of a pressurised chamber through a calibrated orifice at constant speed, the apparatus permitted tensile test at constant strain-rates between 10^{-1} and 50 s⁻¹. Load and displacement were obtained in a similar way as for the low strain-rate tests. Tensile tests at the highest strain-rates were performed in a modified Hopkinson bar. Here, the incident bar was clamped by a brittle bridge and pre-stressed in tension. When the bridge was broken, a uniaxial elastic tension wave propagated along the incident bar and loaded the specimen to fracture. Due to the numerous reflections of elastoplastic waves in the short specimen, stress equilibrium was obtained. Strain gauges placed on the incident and output bar, at equal distances from the specimen, were used for measurements of the incident, reflected and transmitted pulses. The unfiltered data was used to calculate the engineering stress, strain and strain-rate.

The experimental programme consisted of 24 uniaxial tensile tests (9 at low strain-rate, 9 at medium strain-rate and 6 at high strain-rate), and the geometry of the specimen used in all tests is shown in Fig. 2d). The number of parallels for each strain-rate tested was three, and

the repeatability was found to be good. The mean stress-strain curves at different strain-rates are shown in Fig. 7a). Fig. 7b) shows that the strain-rate sensitivity of Weldox 460 E is moderate and hardly affected by the level of plastic strain to a strain-rate of approximately 1500 s^{-1} . Both the yield and flow stresses are seen to increase at a given strain with increasing strain-rate, while the fracture strain decreases (see Fig. 12). However, the strain-rate in the material during projectile penetration is believed to be much higher. Unfortunately, it was not possible to use the modified Hopkinson bar with confidence at higher strain-rates.

3.5. Tensile Tests at Elevated Temperatures

Tensile tests at elevated temperatures were performed on smooth cylindrical specimens in a temperature controlled chamber at a constant strain-rate of $5 \cdot 10^{-4} \text{ s}^{-1}$. During the tests, load, crosshead displacement and temperature were measured. The longitudinal strain was measured using an extensometer until diffuse necking took place, while the crosshead displacement was used at higher strains. Thermocouples were used to measure temperature both in the chamber and directly on the specimen. The temperature was kept constant for about 30 minutes before testing to ensure that both the specimen and grips were fully heated. This was necessary since no rapid heating device was available. In the experimental programme 5 different temperatures between 100 and 500 °C were used, and the number of parallels were two. The experimental scatter between identical tests was found negligible.

Fig. 8a) shows the engineering stress-strain curves at elevated temperatures. At a temperature of 200–300 °C the tensile strength was suddenly increased and equalled the value obtained at room temperature. This is further outlined in Fig. 8b), where the stress at different levels of plastic strain is plotted as a function of temperature. While the yield stress showed a linear decrease with increasing temperature, the flow stress and stiffness exhibited a local maximum at a temperature of about 300 °C. This is known as the blue brittle region (Dieter, 1998), where the strength of carbon steel is increased and the ductility is decreased on heating due to restraining of dislocations caused by a release of second-order particles in the material.

3.6. Fracture Strain Measurements

The true fracture strain was measured in all tests carried out. This parameter, given as

$$\varepsilon_f = \ln\left(\frac{A_0}{A_f}\right) \quad (24)$$

is based on the original cross-section area A_0 and the final cross-section area A_f of the test specimen, and represents the maximum true strain the material withstands before fracture occurs. The original area was exactly measured prior to testing. The final area was measured by photographing the fracture surfaces in a stereo light microscope. Image processing was used on the digital images to determine A_f . Some typical fracture surfaces of the tensile tests are shown in Fig. 9. From the images, it is seen that the fracture strain increases with rising temperature, and decreases with increasing strain-rate and hydrostatic tension. Anisotropy also seems to be introduced into the previously isotropic material at high strains (Zukas et al, 1990). The measured true fracture strains from all tests are plotted in Fig. 12a), d) and f).

3.7. Projectile Material – Arne Tool Steel

In the ballistic penetration tests (Børvik et al, 1999), blunt-nosed cylindrical projectiles were manufactured from Arne tool steel. After machining, the projectiles were oil-hardened to a nominal Rockwell C value of 53, which was controlled by hardness measurements in the nose prior to testing. Component tests had indicated that this hardness number represented an upper limit for projectile capacity, i.e. the projectile could fracture at impact if further hardened. Even so, plastic deformation (mushrooming) was observed in the nose of the projectile, especially at the highest velocities. In order to have reliable material data, test coupons were eroded directly from hardened projectiles to the geometry shown in Fig. 3, and quasi-static tensile tests were carried out at room temperature. Longitudinal strains were measured up to 2 % using an extensometer, while the displacement of the moving crosshead was used at higher strains. Stresses were obtained based on the applied load and the initial cross-section area of the circular specimens. A total of 5 identical tensile tests were carried out, and the mean stress-strain curve is shown in Fig. 10. The yield stress σ_0 was found to be 1900 MPa, while the fracture strain was about 2.5 %, indicating a rather brittle behaviour.

4. Identification of Material Constants

The basic idea of the identification procedure was to determine all material constants without the use of numerical simulations. This was found possible using a direct curve fit to the experimental data, assuming proportional straining and constant strain-rate, temperature and triaxiality ratio during each test. The method of least squares requires the residual sum between the experimental observations and model results to be minimised. This implies that the proposed model of viscoplasticity and ductile damage can be completely calibrated by minimising the residuals

$$\mathfrak{R}(\sigma_{eq}) = \sum_{\alpha=1}^{N_{\alpha}} \sum_{\beta=1}^{N_{\beta}} \sum_{\delta=1}^{N_{\delta}} \sum_{\gamma=1}^{N_{\gamma}} \left\{ \sigma_{eq}^{exp}(p_{\alpha}, \sigma_{\beta}^*, \dot{p}_{\delta}, T_{\gamma}) - \left(1 - D_C \frac{P_{\alpha}}{p_f(\sigma_{\beta}^*)} \right) (A + Br_{\alpha}^n) (1 + i_{\delta}^*)^c (1 - T_{\gamma}^{*m}) \right\}^2 \quad (25)$$

$$\mathfrak{R}(p_f) = \sum_{\beta=1}^{N_{\beta}} \sum_{\delta=1}^{N_{\delta}} \sum_{\gamma=1}^{N_{\gamma}} \left\{ p_f^{exp}(\sigma_{\beta}^*, \dot{p}_{\delta}, T_{\gamma}) - (D_1 + D_2 \exp(D_3 \sigma_{\beta}^*)) (1 + \dot{p}_{\delta}^*)^{D_4} (1 + D_5 T_{\gamma}^*) \right\}^2 \quad (26)$$

where $\mathfrak{R}(\sigma_{eq})$ and $\mathfrak{R}(p_f)$ refer to the residuals of the constitutive model and the fracture strain model, respectively. Furthermore, p_{α} and r_{α} are discrete values of the strains p and r , σ_{β}^* is a discrete value of the stress triaxiality ratio σ^* , \dot{p}_{δ} , \dot{p}_{δ}^* , and i_{δ}^* are discrete values of the strain-rates \dot{p} , \dot{p}^* and i^* , and T_{γ} is a discrete value of the temperature T . Eqns. (25) and (26) can be calibrated independently of each other. All material constants determined from the identification procedure are given Table 4.

To include the effects of stress triaxiality in the model, expressions for $\sigma^* = \sigma_{II} / \sigma_{eq}$ must be established. Based on the notched specimen tensile tests it is possible to construct the experimental relations $\sigma_{eq} = \sigma_{eq}^{exp}(p, \sigma^*)$ and $p_f = p_f^{exp}(\sigma^*)$. The equivalent stress is obtained from the measured longitudinal true stress $\bar{\sigma}_z^{exp}$, while the stress triaxiality ratio σ^* can be determined using Bridgman (1952). The Bridgman's analysis gives

$$\frac{\sigma_z}{\sigma_{eq}} = 1 + \ln\left(\frac{a^2 + 2aR - r^2}{2aR}\right) \quad (27)$$

$$\frac{\bar{\sigma}_z}{\sigma_{eq}} = \left(1 + \frac{2R}{a}\right) \ln\left(1 + \frac{a}{2R}\right)$$

where a and R are the radius and the radius of the curvature of the neck, respectively, and $\bar{\sigma}_z$ is the mean axial stress. It is assumed that the material is isotropic and that the accumulated plastic strain is uniform over the minimum cross-section area of the specimen. Since the stress distribution in the specimen is axial symmetric, the von Mises yield criterion gives (Hill, 1950)

$$\sigma^* = \frac{\sigma_{fl}}{\sigma_{eq}} = \frac{\sigma_z}{\sigma_{eq}} - \frac{2}{3} \quad \text{or} \quad \sigma_{eq} = \frac{\sigma_z}{2/3 + \sigma^*} \quad (28)$$

Eq. (28) inserted in the Bridgman's analysis can be used to give expressions for the triaxiality ratio in the centre of the notched specimen, i.e. the maximum value when $r = 0$

$$\sigma_{max}^* = \frac{1}{3} + \ln\left(1 + \frac{a}{2R}\right) \quad (29)$$

and the mean value of the triaxiality ratio across the minimum cross-section

$$\bar{\sigma}^* = \left(1 + \frac{2R}{a}\right) \ln\left(1 + \frac{a}{2R}\right) - \frac{2}{3} \quad (30)$$

in the sense that $\sigma_{eq} = \bar{\sigma}_z / (2/3 + \bar{\sigma}^*)$.

Let the longitudinal true stress in a notched specimen be $\bar{\sigma}_z = \bar{\sigma}_z^{exp}(p)$. In a smooth specimen the longitudinal true stress equals the equivalent stress, provided that the strain is uniform. This is the case in a test for strains less than the ultimate strain p_u , i.e. the strain at the onset of diffuse necking. It follows that the equivalent stress is obtained from a smooth specimen test as $\sigma_{eq} = \bar{\sigma}_z^{exp}(p)$ for $p \leq p_u$. An estimate of $\bar{\sigma}^*$ is found either from the Bridgman analysis given above, finite element simulations or directly from the experiments. The last-mentioned approach has been used in this study, but all methods have shown to give

similar results. Fig. 11 shows the development of $\bar{\sigma}^*$ from numerical simulations of the quasi-static notched and smooth specimens. As seen, the assumption that $\bar{\sigma}^*$ does not vary significantly with plastic strain seems to be valid for the notched specimens, while some more deviation is observed for the smooth specimen.

After having established the expressions above, the identification procedure becomes rather straightforward. The introductory quasi-static tensile tests are used to determine the elastic constants E and ν , while the smooth quasi-static tensile tests are used to determine the yield stress A , through standard procedures. The next to determine is the material constants D_1 , D_2 and D_3 , used to define the fracture strain as a function of stress triaxiality. The measured fracture strains for the quasi-static smooth and notched specimens $p_f^{\text{exp}}(\sigma_\beta^*)$ are shown in Fig. 12a) as a function of the calculated triaxiality ratio σ_{max}^* in the centre of the notch as given by Eq.(29). As seen, when fracture is considered the maximum value for the triaxiality ratio is used, because fracture in a tensile specimen is assumed to start in the centre of the necked region (Dieter, 1988). However, it is not certain that the fracture process initiates in the centre region of the notch (i.e. at the minimum cross-section on the axis of the specimen) when the notch radius decreases, but rather at the surface in the notch root (Holland et al, 1990; El-Magd, 1997). Since no material data is available at pure shear ($\sigma^* = 0$) this data point is estimated from a model proposed by Lemaitre (1996)

$$p_f = p_{fs}^{\text{exp}} \left[\frac{2}{3}(1 + \nu) + 3(1 - 2\nu)(\sigma_{\text{max}}^*)^2 \right]^{-1} \quad (31)$$

where p_{fs}^{exp} is the true fracture strain measured from a smooth specimen test. By minimising the residual for the fracture strain model in Eq. (26) at quasi-static strain-rate and room temperature, i.e. $N_\delta = N_\gamma = 1$, the fracture strain constants D_1 , D_2 and D_3 are determined. It is assumed that the stress triaxiality ratio σ_{max}^* is constant for the tensile tests. The model results are compared with the experimental observations in Fig. 12a), while the values for the fracture strain constants are given in Table 4. As seen, an excellent fit is obtained between the model and experimental results. However, material data under hydrostatic compression (i.e. $\sigma_{\text{max}}^* < 0$) is not available. The extension of the curve into the compression region is therefore solely based on the hydrostatic tension test data.

The strain hardening constants, B and n , and the critical damage, D_C , is then determined. These constants can be found by minimising the residual for the constitutive model given by

Eq. (25) at quasi-static strain-rate and room temperature, i.e. $N_\delta = N_\gamma = 1$, using the quasi-static notched specimen tensile tests. In order to take the triaxiality ratio of the different notched specimens into account, each model curve is corrected according to the ratio of the measured triaxiality $\bar{\sigma}_2^{\text{exp}}(p) / \sigma_{\text{eq}}^{\text{exp}}(p)$ at a plastic strain of 5 %. Fig. 12b) shows a comparison between the experimental and model results for a best fit of the material constants. As seen, both the shape of the stress-strain curves and the different strains to fracture seem to be well described. Other and more direct methods may be used to determine the critical damage (Lemaitre, 1996), but the method used gives a reasonable agreement between the experimental observations and the model results with a minimum of effort. Note also that in Eq. (25) the experimental relation for the fracture strain $p_f = p_f^{\text{exp}}(\sigma^*)$ may be substituted by the model relation: $p_f = D_1 + D_2 \exp(D_3 \sigma^*)$. The damage accumulated plastic strain r in the model is calculated, assuming a constant stress triaxiality ratio σ^* , as

$$r = p - \frac{1}{2} \frac{D_c}{p_f(\sigma^*)} p^2 \quad (32)$$

It is further assumed that damage starts to develop immediately when the load is applied for this material, i.e. the damage threshold p_d in Eq. (20) is equal to zero.

The dynamic tensile tests were performed at room temperature and strain-rates ranging from $10^{-4} - 10^3 \text{ s}^{-1}$. Using the measured data, the experimental relations $\sigma_{\text{eq}} = \sigma_{\text{eq}}^{\text{exp}}(p, \dot{p})$ and $p_f = p_f^{\text{exp}}(\dot{p})$ can be found. The former relation is valid for strains to diffuse necking only. The material constants C and D_4 , defining the rate sensitivity on the stress-strain curve and fracture strain, respectively, are found by minimisation of the residuals given in Eq. (25) and Eq. (26). It is here assumed that $\sigma^* = 1/3$ (uniaxial stress, smooth specimen) and $T^* = 0$ (room temperature), i.e. $N_\beta = N_\gamma = 1$. Fig. 12c) shows a comparison between the model results and the obtained stresses at yielding and 12 % plastic strain, respectively, at different strain-rates. Since there is a slight reduction in strain-rate sensitivity of the material with increasing level of plastic strain, a mean value of the strain-rate sensitivity constant C is found. Notice that the calculated stress equals the measured quasi-static stress at low strain rates. A comparison between the measured and calculated fracture strains at different strain-rates are given in Fig. 12d). As seen, the model indicates the general observation of a reduction in fracture strain with an increase in strain-rate.

The results from the quasi-static tensile tests at elevated temperatures using smooth cylindrical specimens were shown in Fig. 8a) and b). The experimental relations $\sigma_{eq} = \sigma_{eq}^{exp}(p, T)$ and $p_f = p_f^{exp}(T)$ can now be established, where the former is valid for strains up to diffuse necking only. The material constants m and D_5 , governing the temperature-sensitivity of the stress-strain curve and fracture strain, respectively, are found by minimising the residuals given in Eq. (25) and Eq. (26) when $\sigma^* = 1/3$ (uniaxial stress, smooth specimen) and at a quasi-static strain-rate, i.e. $N_\beta = N_\delta = 1$. The reduction in Young's modulus with increasing temperature is taken into account by the expression

$$E_T = E(1 - KT^*) \quad (33)$$

where E_T is Young's modulus at the actual temperature, E is Young's modulus at room temperature and K is a material parameter. A comparison between the model results and experimental observations is given in Fig. 12e) and f). The previously described blue brittle region seems to influence the material response at the highest levels of plastic strain at temperatures between 200-400 °C. The present version of the material model can not be used to describe the blue brittle region. On the other hand, the reduction in yield stress seems to be unaffected by this phenomenon. Therefore, the temperature-sensitivity constant m is fitted against the reduction in yield stress with increasing temperatures. This gives a reasonable agreement also at higher strains. The fracture strain is unaffected by temperature up to 300°C, which seems to be a typical value for penetration of relatively thin plates (Børvik et al, 1999). As a consequence, the temperature-sensitivity on the fracture strain is neglected (i.e. $D_5 = 0$). Both assumptions are believed to give a conservative estimate of the material response under adiabatic conditions. In targets were transformed adiabatic shear bands, giving very high local temperatures, are assumed to appear the latter assumption may be too conservative.

A complete listing of all material constants for the target material is given in Table 4. Inserted in the computational model, analytical stress-strain relationships for the target material can be obtained. This is demonstrated in Fig. 13, where the effect of damage, strain-rate and temperature on the quasi-static response is shown. Note that the curve showing damage on the quasi-static response represents the material behaviour measured in the quasi-static tests. In the calculations it is assumed that $\sigma^* = 1/3$ (uniaxial stress, smooth specimen) and that $\dot{p} = 1000 \text{ s}^{-1}$ (adiabatic conditions) in the dynamic case. As seen, each phenomenon described in the computational model significantly influences the material response.

Finally, only a simple constitutive model for the projectile material behaviour is used. Due to the shape of the stress-strain curve, the projectile was modelled as a bilinear elastic-plastic von Mises material with isotropic hardening, i.e.

$$\sigma = \begin{cases} E \varepsilon & \varepsilon \leq \varepsilon_0 \\ \sigma_0 + E_t(\varepsilon - \varepsilon_0) & \varepsilon > \varepsilon_0 \end{cases} \quad (34)$$

The tangent modulus E_t was found by a best fit to the obtained stress-strain curve. A comparison between the model and the measured stress-strain curve is given in Fig. 10, while the material constants are given in Table 5. It is further assumed that the strain-rate sensitivity of a material is significantly reduced with increased static yield stress (Hosford and Caddell, 1993). Therefore, due to the severe yield stress of the hardened projectile possible strain-rate effects were neglected. Projectile damage and possible fracture were also ignored in the model at this stage, but these effects may have to be taken into account if large plastic deformations in softer projectiles or fracture in brittle projectiles are of importance.

5. Verification of Computational Model

To verify the model implementation and material calibration all material tests were simulated using LS-DYNA to see whether the numerical model could reproduce the material behaviour observed experimentally. However, it is important at this point to notice that these simulations have not been used to adjust the material constants or to tune the numerical model towards the experimental results.

The axisymmetric finite element meshes used to model the quasi-static smooth and notched tensile specimens are shown in Fig. 14, while details of the different notches both before and after fracture can be seen in Fig. 15. Two different mesh densities, giving respectively 10 or 20 elements over the specimen gauge radius, were used to reveal any mesh sensitivity. The effect on the flow stress when using different mesh densities was found small, but a reduction in fracture strain was obtained for the finest mesh. In the simulations, the specimen was fixed at the gauge centre, while the load was applied as a displacement at the free end giving a constant strain-rate in the specimen of $5 \cdot 10^{-4} \text{ s}^{-1}$. In order to reduce the computational time, the mass of the material was scaled to increase the stable time step in the

explicit formulation. All material constants were as given in Table 4, except for the Taylor-Quinney coefficient χ that was set equal to zero to avoid any thermal effects (i.e. isothermal conditions). A comparison between the numerical results and the experimental observations are given in Fig. 16, showing reasonable good agreement.

A plot of the coarse element mesh used to simulate the dynamic tensile tests is shown in Fig. 17. At first, the load was applied to the specimen's free end as a linear increasing deformation with time to give the experimentally obtained strain-rate. This resulted in severe oscillations due to stress wave propagation. In order to reduce this effect, the load was given a moderate rise time. Results from simulations carried out at a strain-rate of 1500 s^{-1} are compared with the experimentally obtained engineering stress-strain curve in Fig. 18. As seen, the agreement is quite good. Fig. 19 shows the computed geometry of the specimen at different points of time to complete fracture. According to Lindholm and Johnson (1982), the transition from isothermal to fully adiabatic conditions in steel occurs at a shear strain-rate between 10 and 100 s^{-1} . This indicates that only the Hopkinson bar tests should be considered as truly adiabatic. Therefore, at lower strain-rates simulations were carried out both with $\chi=0$ (isothermal) and $\chi=0.9$ (adiabatic). Fig. 20 gives a comparison between numerical simulations and experimental results at a strain-rate of 2.2 s^{-1} . When $\chi=0$ the agreement between the simulation and the test until diffuse necking occurs is good. However, after diffuse necking severe deviations are observed, and the simulation assuming adiabatic condition is closer to the test results. The reason may be that the strain-rate in the localised neck during testing is significantly higher than the measured average strain-rate. This may result in adiabatic conditions in the necked area of the specimen after localisation.

The numerical model used to simulate the tensile tests at elevated temperatures was identical to the one used in the smooth quasi-static tensile tests, except that the homologous temperature T^* was kept constant and equal to the homologous temperature applied in the experiments. A comparison between the experimentally and numerically obtained engineering stress-strain curves is given in Fig. 21a), and significant deviations are seen. This is partly due to the blue brittle region at a temperature between $200 \text{ }^\circ\text{C}$ and $400 \text{ }^\circ\text{C}$, which is not accounted for in the material model. However, as seen in Fig. 21b) the distinct softening effect on the strength of the material seems to be predicted in the numerical simulations.

6. Validation of constitutive model

Numerical simulations using the calibrated and verified constitutive model have also been validated against ballistic penetration tests on Weldox 460 E steel plates impacted by hardened cylindrical projectiles with a blunt nose at sub-ordnance velocities. In the ballistic penetration tests, a compressed gas gun was used to launch the sabot-mounted projectile at impact velocities just below and well above the ballistic limit, i.e. the perforation velocity of the target. Nominal hardness (HRC 53), diameter (20 mm), length (80 mm) and mass (0.197 kg) of the projectile were kept constant in all tests. The circular targets, having different thicknesses and a constant diameter of 500 mm, were clamped in a rigid frame. Initial and residual velocities were measured, and a digital high-speed camera system was used for visualisation and measurements of the penetration process. Based on the measured velocities, the ballistic limit curve was constructed for each target thickness tested. The experimental set-up and instrumentation used in the tests are described in Børvik et al (1998a), while parts of the experimental programme and some results can be found in Børvik et al (1998b, 1999).

Numerical simulations were carried out to determine the ballistic limit curves, and the results have been compared with the experimental observations (Hopperstad et al, 1998b). Details from one simulation of the perforation of a 12 mm thick Weldox 460 E steel plate are plotted and compared with high-speed camera images from the corresponding test at identical times in Fig. 22. In the finite element model, a total number of 10820 4-node axisymmetric elements with one-point integration were used. The element size in the impacted region of the target was equal to $0.25 \times 0.2 \text{ mm}^2$, giving 60 elements through the plate thickness. The target was modelled as elastic-viscoplastic coupled with ductile damage using the material constants given in Table 4, while the projectile was modelled as elastoplastic using the material constants given in Table 5. In the simulation, the plate was fully clamped at the support, while the projectile was given an initial velocity of 303.5 m/s as in the experiment. Contact between the projectile and target was modelled using a penalty formulation without friction. As seen from Fig. 22, the numerical model seems to capture the overall physical behaviour of the perforation process. Due to the element kill algorithm, used to remove the element when the critical damage is reached, a crack is allowed to propagate in front of the projectile. After severe indentation, a plug is formed and complete perforation of the target plate occurs. The residual projectile velocity was in the simulation found to be 193 m/s, which is close to the experimental observation of 200 m/s.

A comparison between the ballistic limit curves obtained experimentally and in the numerical simulations using a reference mesh of 30 elements and the finer mesh of 60 elements over the target thickness is shown in Fig. 23. The experimental ballistic limit velocity for the 12 mm thick target was 185 m/s, while the predictions were approximately 220 m/s and 193 m/s when using the reference mesh and the fine mesh, respectively. It is seen that the predictions using the fine mesh are very good, whereas significant deviations are seen for the reference mesh. As expected, the numerical solution is found to be mesh sensitive. However, as shown in Fig. 24 the mesh dependence does not seem to be pathological since the strain-rate effect of the material is accounted for in the model (Needleman, 1988). Thus, the simulations converged monotonically towards a limit solution when the element size was sufficiently reduced.

7. Concluding Remarks

This paper describes a coupled computational model of viscoplasticity and damage capable of predicting deformation and fracture in ductile materials during penetration and impact. The complexity of most impact events enforces the use of highly sophisticated material models. Such models involve a large number of material constants to be determined from material tests. The described model can be completely calibrated from relatively simple uniaxial tensile tests, without the use of numerical simulations. All material tests carried out in order to determine the material constants are presented and discussed. It is, however, important to notice that even if the total number of material constants may seem large, the number of necessary material tests is limited since several material constants are determined from each set of experiments. Due to the formulation of the computational model, also the identification procedure becomes straightforward. By establishing two residuals, one for the constitutive model and one for the fracture strain model, the method of least squares can be used to fit the material constants to the experimental data. The calibrated computational model has been used in numerical simulations of both material tests and plate penetration tests, and the agreement with the experimental observations is in general good.

Acknowledgement

The financial support of this study by the Norwegian Defence Construction Service, Central Staff/Technical Division, Oslo, Norway, is gratefully acknowledged.

References

- Bai, Y. and Dodd, B., 1992. *Adiabatic Shear Localization: Occurrence, Theories and Applications*, Pergamon Press.
- Bammann, D.J., Chiesa, M.L., Horstemeyer, M.F. and Weingarten, L.I., 1993. Failure in Ductile Materials using Finite Element Simulations, In: *Structural Crashworthiness and Failure*, N. Jones and T. Wierzbicki (Editors), Elsevier Applied Science, pp. 1-54.
- Barlat, F. and Richmond, O., 1987. Prediction of Tricomponent Plane Stress Yield Surface and Associated Flow and Failure Behaviour of Strongly Textured Polycrystalline Sheets, *Int. J. Mat. Sci. Eng.* 95, pp. 15-29.
- Berstad, T., Hopperstad, O.S. and Langseth, M., 1994. Elasto-Viscoplastic Constitutive Models in the Explicit Finite Element Code LS-DYNA3D, In: *Proceedings of the Second International LS-DYNA3D Conference*, San Francisco, USA, September 20-21.
- Bridgman, P.W., 1952. *Studies in Large Plastic Flow and Fracture*, McGraw-Hill.
- Børvik, T., Holen, K., Langseth, M. and Malo, K.A., 1998a. An Experimental set-up used in Ballistic Penetration, In: *Proceedings of Fifth International Symposium on Structures under Shock and Impact*, pp. 683-692, Thessaloniki, Greece, June 24-26.
- Børvik, T., Langseth, M., Hopperstad, O.S. and Malo, K.A., 1998b. Penetration of Steel Plates - I. Experimental Study, In: *Proceedings of Third International Symposium on Impact Engineering*, Singapore, December 7-9.
- Børvik, T., Langseth, M., Hopperstad, O.S. and Malo, K.A., 1999. Ballistic Penetration of Steel Plates, *International Journal of Impact Engineering* 22, pp. 855 - 886.
- Camacho G.T. and Ortiz, M., 1997. Adaptive Lagrangian Modelling of Ballistic Penetration of Metallic Targets, *Int. J. Comp. Meth. Appl. Mech. Engng.* 142, pp. 269-301.
- Dieter, G.E., 1988. *Mechanical Metallurgy*, McGraw-Hill Book Company.
- El-Magd, E., 1997. Influence of strain-rate on ductility of metallic materials, *Steel Research* 68, pp. 67 - 71.
- Hancock, J.W. and Mackenzie, A.C., 1976. On the Mechanism of Ductile Failure in High-Strength Steels subjected to Multi-Axial Stress-States, *Int. J. Mech. Phys. Sol.*, pp. 147-175.
- Hill, R., 1950. *The Mathematical Theory of Plasticity*, Oxford University Press.
- Holland, D., Halim, A. and Dahl W., 1990. Influence of stress triaxiality upon ductile crack propagation, *Steel Research* 61, pp. 504 - 506.
- Hopperstad, O.S., Berstad, T., Børvik, T. and Langseth, M., 1998a. A Computational Model of Viscoplasticity and Ductile Damage, In: *Proceedings of Fifth International LS-DYNA users Conference*, Michigan, USA, September 21-22.

- Hopperstad, O.S., Børvik, T., Berstad, T., Aas-Jakobsen, K. and Langseth, M., 1998b. Penetration of Steel Plates - II. Numerical Simulations, In: Proceedings of Third International Symposium on Impact Engineering, Singapore, December 7-9.
- Hosford, W.F. and Caddell, R.M., 1993. Metal Forming: Mechanics and Metallurgy, Prentice Hall, New Jersey.
- Johnson, G.R. and Cook, W.H., 1983. A Constitutive Model and Data for Metals Subjected to Large Strains, High Strain Rates and High Temperatures, In: Proceedings of Seventh International Symposium on Ballistics, The Hague.
- Johnson, G.R. and Cook, W.H., 1985. Fracture Characteristics of Three Metals Subjected to Various Strains, Strain Rates, Temperatures, and Pressures, *Int. J. Engineering Fracture Mechanics* 21, pp. 31-48.
- Jones, N., 1997. Dynamic Inelastic Failure of Structures, *Trans. Japan Soc. Mech. Eng.* 12, pp. 21-31.
- Khan, A.S. and Huang, S., 1995. Continuum Theory of Plasticity, Wiley-Interscience.
- Lemaitre, J. and Chaboche, J.-L., 1990. Mechanics of solid materials, Cambridge University Press.
- Lemaitre, J., 1992. A Short Course in Damage Mechanics, Springer-Verlag.
- Lindholm, U.S. and Johnson, G.R., 1982. Strain-Rate Effects in Metals at Large Shear Strains, In: 29th Army Materials Conference on Material Behaviour under High Stress and Ultrahigh Loading Rates, New York.
- LS-DYNA, 1997. User's Manuals, Livermore Software Technology Corporation, V. 940.
- McClintock, F.A., 1968. A Criterion for Ductile Fracture by Growth of Holes, *Int. J. Appl. Mech., Trans. ASME* 35, pp. 363-371.
- Miller, L.E. and Smith, J., 1970. *J. Iron Steel Inst. London* 208, pp. 998-1005.
- Needleman, A., 1988. Material Rate Dependence and Mesh Sensitivity in Localisation Problems, *Int. J. Comp. Meth. Appl. Mech. Engng.* 67, pp. 69-85.
- Quick, M., Del Grande A., Spinelli, R., Albertini, C., Børvik, T., Langseth M. and Hopperstad, O.S., 1997. Tensile Tests at Low, Medium and High Strain-Rate of Weldox 460 E, Norwegian Defence Construction Service, Technical Note No. 251/97.
- Rice, J.R. and Tracey, D.M., 1978. On the Ductile Enlargement of Voids in Triaxial Stress Fields, *Int. J. Mech. Phys. Sol.* 17, pp. 201-217.
- Søvik, O.P., 1996. Numerical Modelling of Ductile Fracture – A Damage Mechanical Approach, Ph.D.-Thesis, Department of Machine Design and Materials Technology, Norwegian University of Science and Technology, Trondheim, Norway.
- Tvergaard, V. and Needleman, A., 1992. Effect of Crack Meandering on Dynamic, Ductile Fracture, *Int. J. Mech. Phys. Solids* 40, pp. 447-471.
- Zukas, J. A. et al, 1990. High Velocity Impact Dynamics, John Wiley & Sons.

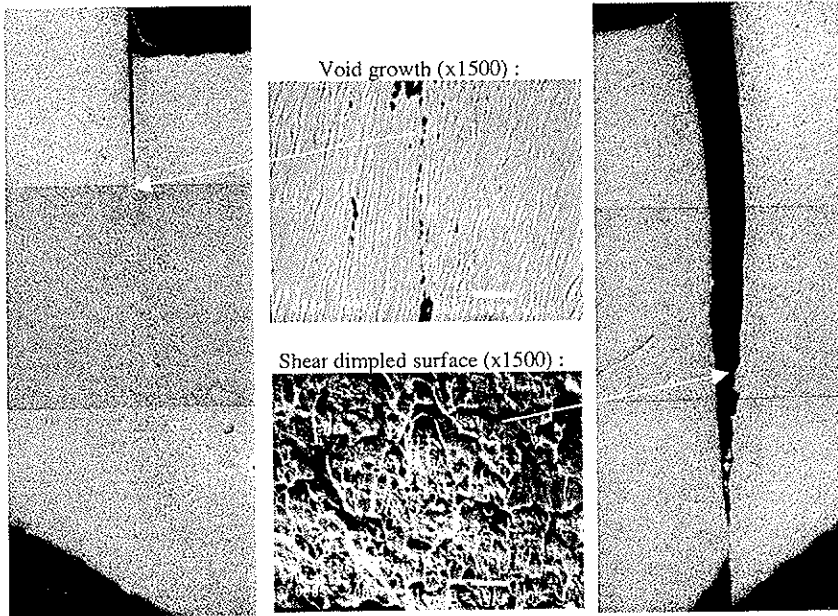
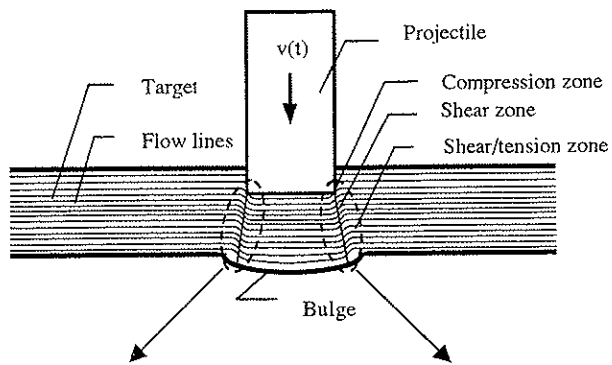


Fig. 1: Metallographic examination of the localised shear zones in a penetrated target. The pictures in the shear zones are constructed based on several images (Børvik et al, 1999).

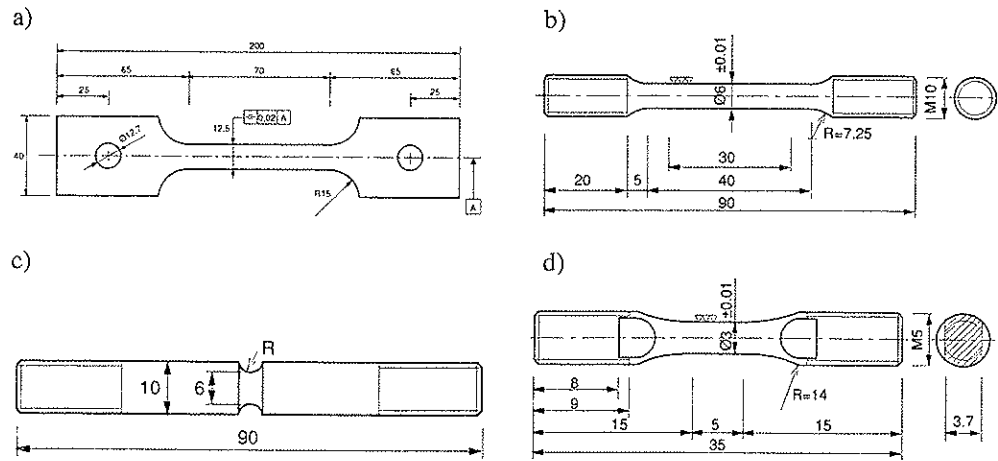


Fig. 2: Geometry of tensile test specimens used for the target material (not in scale - in mm).

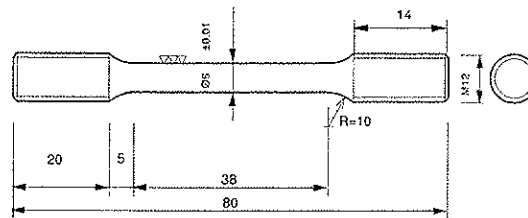


Fig. 3: Geometry of tensile test specimen used for the projectile material (in mm).

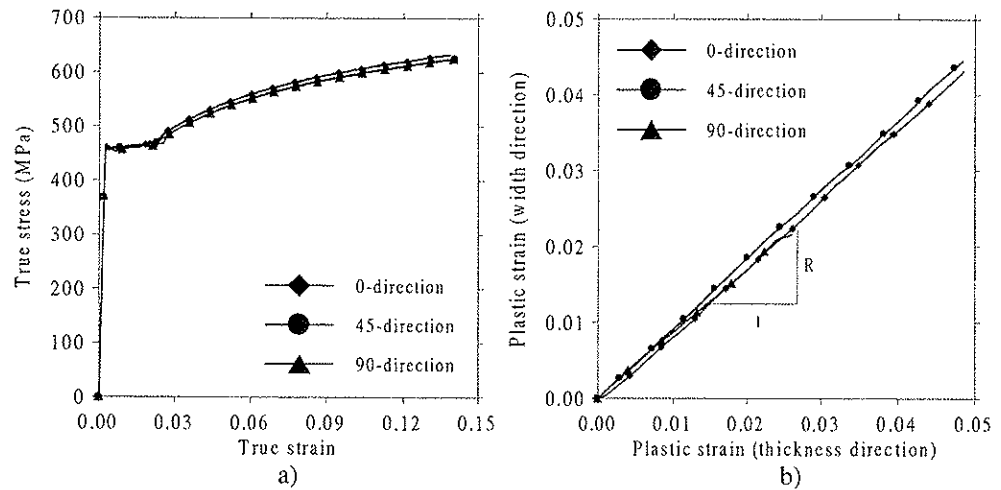


Fig. 4: Comparison between a) mean true stress- strain curves and b) mean R-ratios for different directions to the rolling direction of the target material.

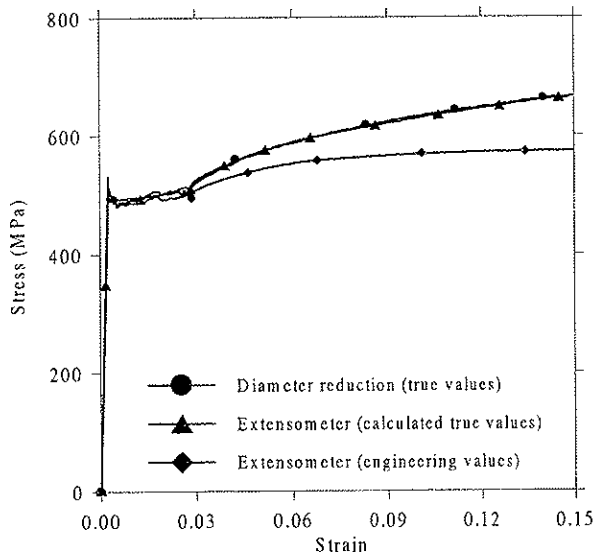


Fig. 5: Comparison between extensometer and diameter reduction measurements for a typical quasi-static tensile test on a smooth specimen.

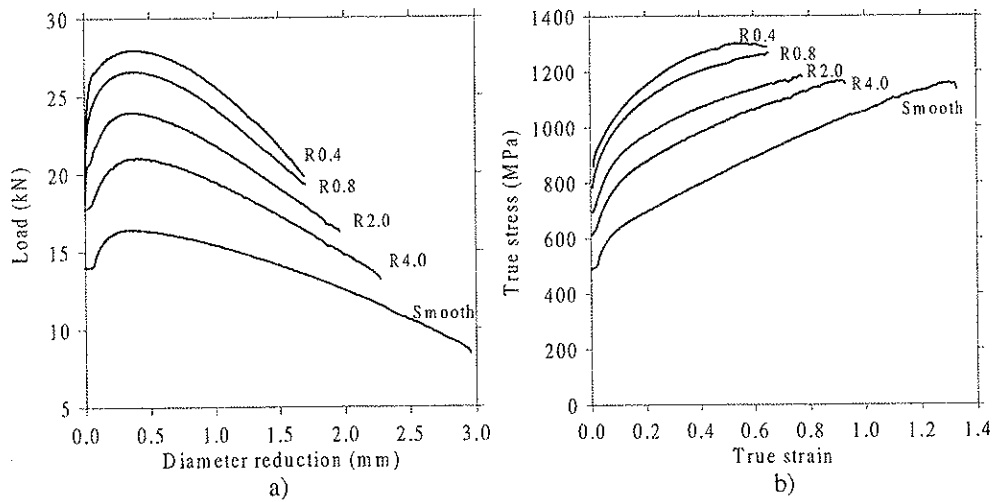


Fig. 6: a) Measured load – diameter reduction curves, b) Calculated true stress – strain curves from quasi-static tensile tests on smooth and notched specimen.

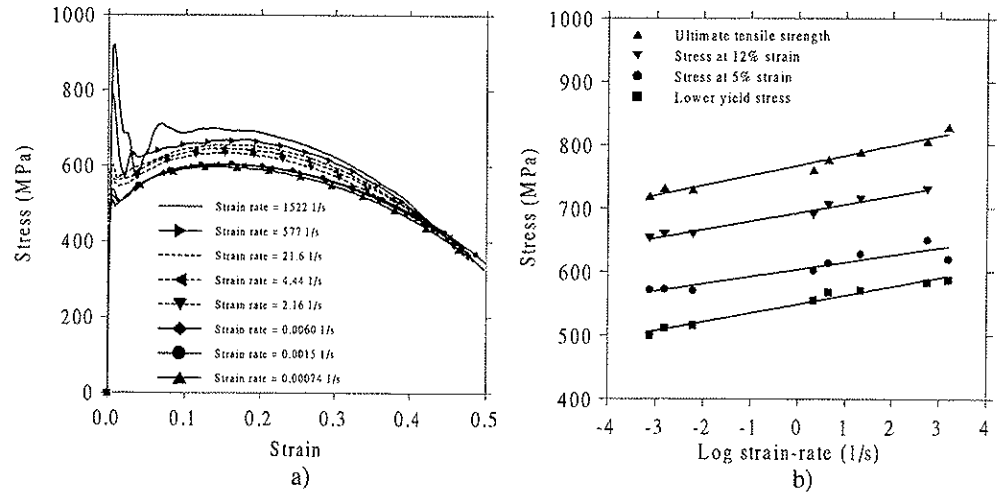


Fig. 7: a) Mean stress – strain curves at different strain rates, b) Stress versus log strain-rate at different levels of strain.

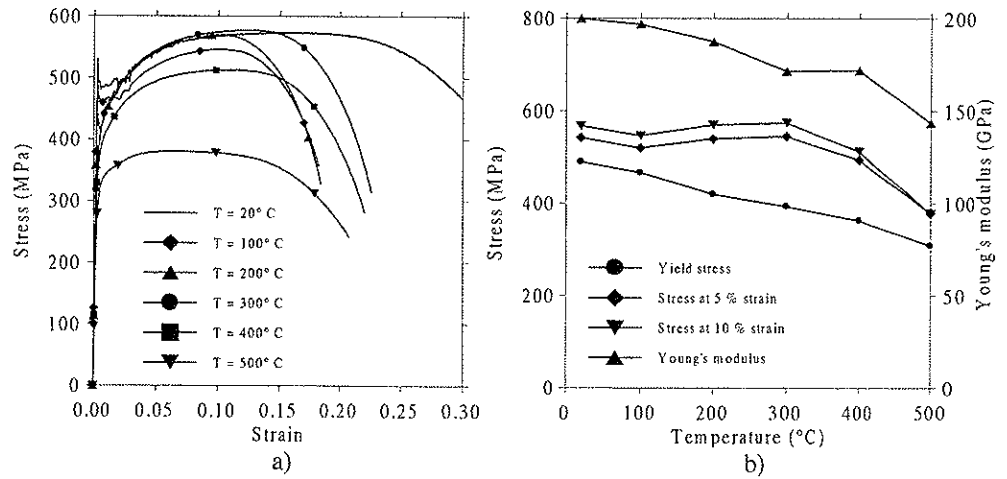


Fig. 8: a) Mean stress – strain curves at elevated temperatures, b) Effect of temperature on the flow properties and stiffness.

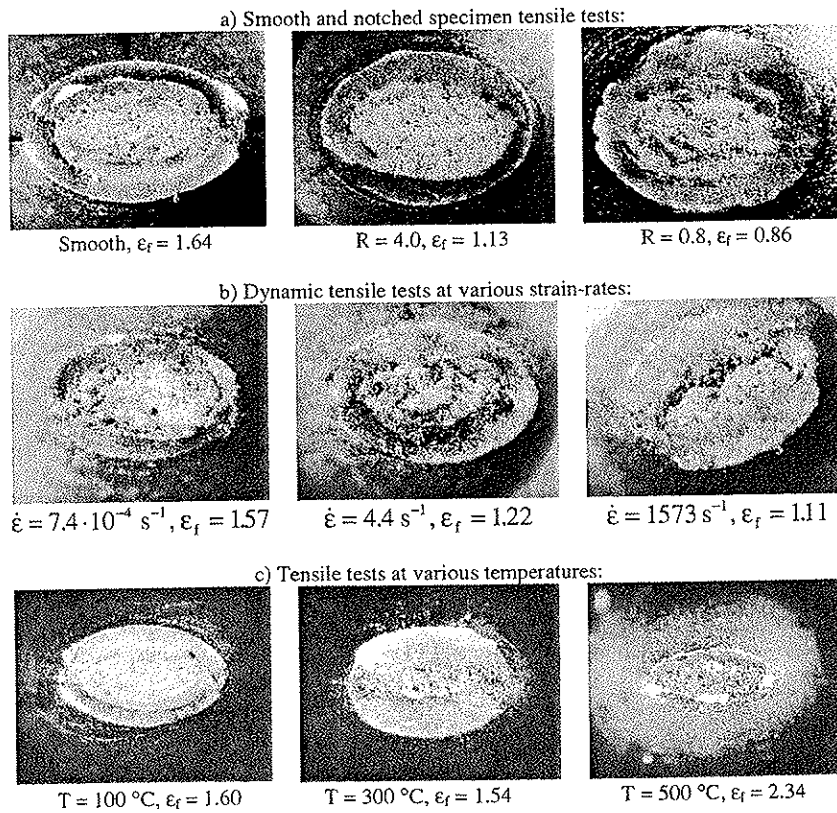


Fig. 9: Fracture surfaces of some tensile test specimens as a function of a) triaxiality, b) strain-rate and c) temperature (Børvik et al, 1999).

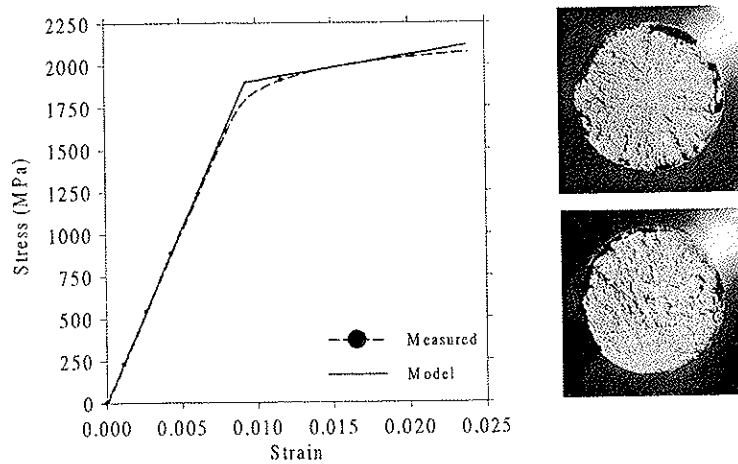


Fig. 10: Comparison between experimental data (dotted line) and model result (solid line), together with typical fracture surfaces of tensile specimens from projectiles of Arne tool steel.

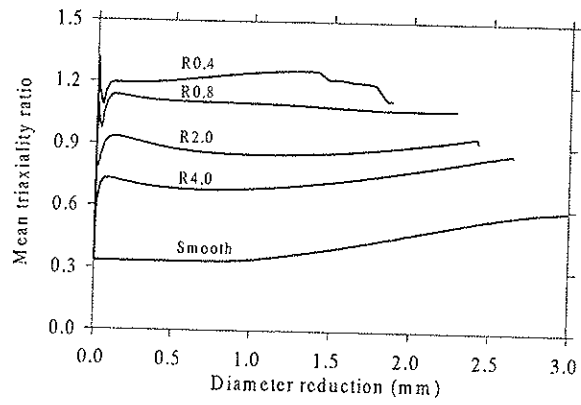
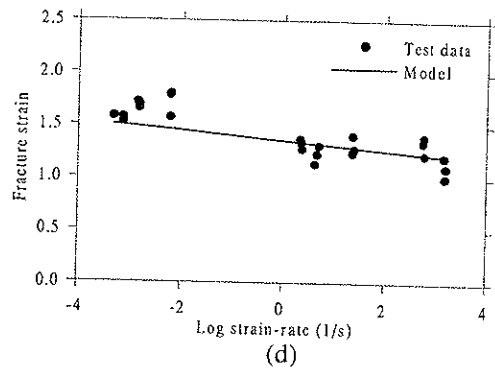
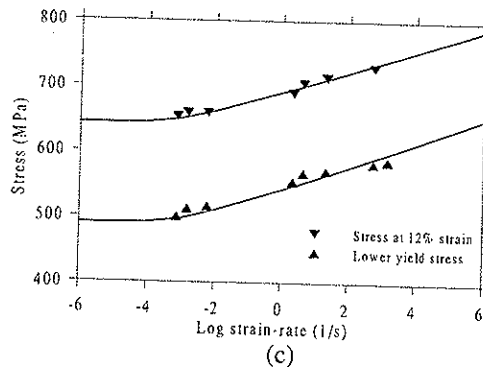
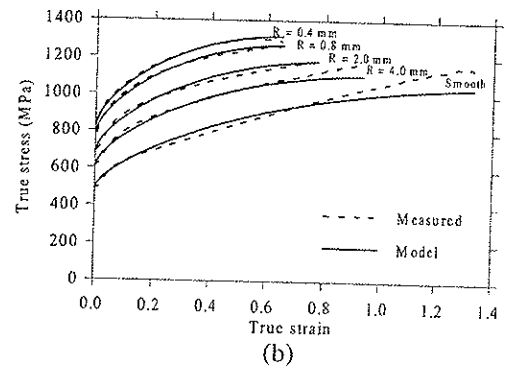
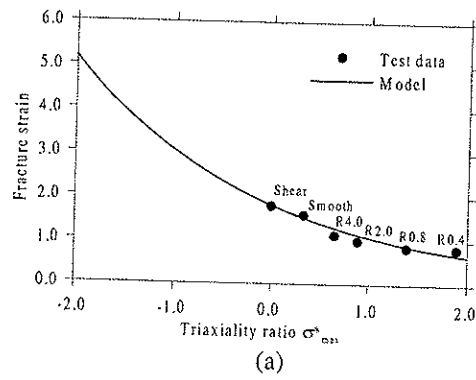


Fig. 11: Mean triaxiality ratio versus diameter reduction from numerical simulations of quasi-static smooth and notched tensile tests.



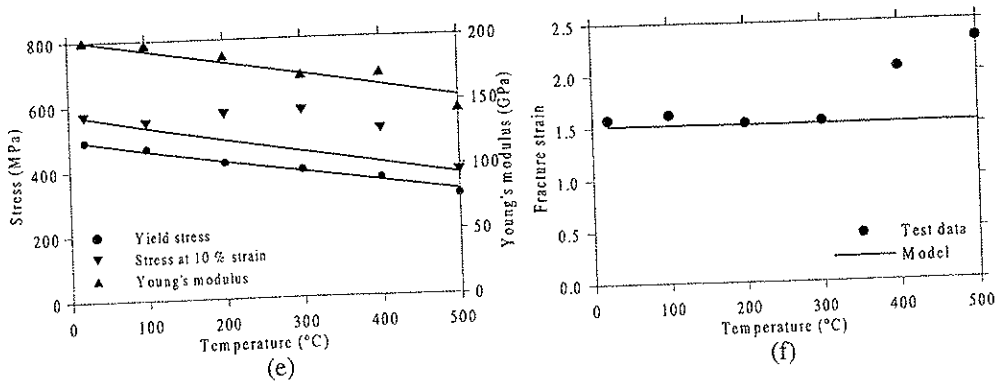


Fig. 12: Comparison between experimental data (symbols or dotted lines) and model results (solid lines) for the target material of Weldox 460 E steel.

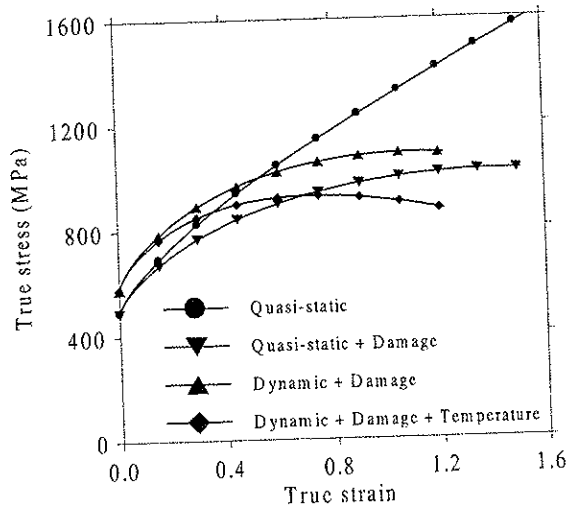


Fig. 13: Effects of the different phenomena included in the computational model on the assumed target stress-strain behaviour.

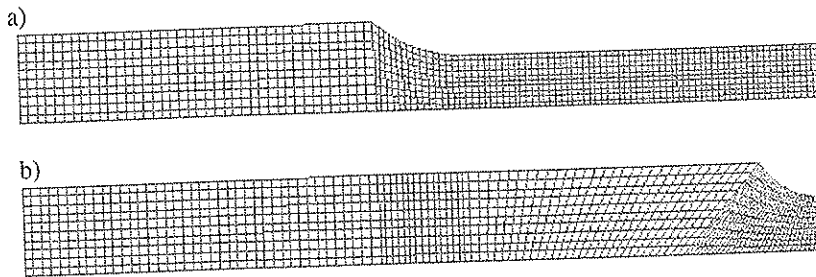


Fig. 14: Plots of course axisymmetric element meshes used to model a) smooth and b) notched specimen tensile tests, respectively.

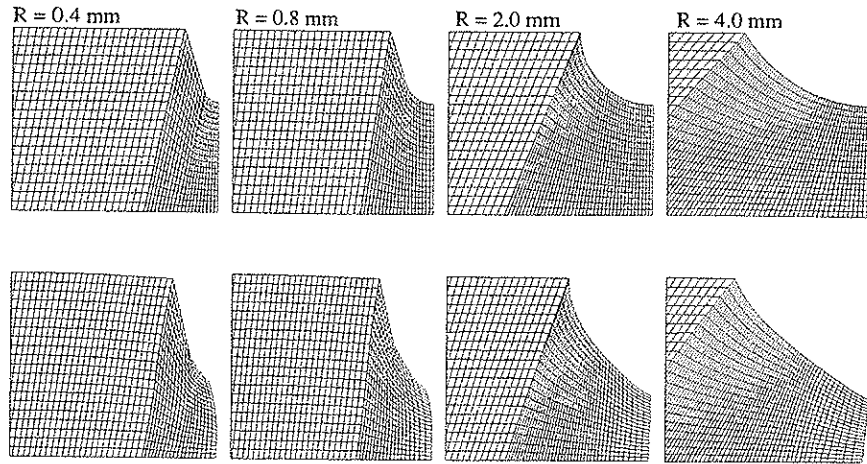


Fig. 15: Details of initial and final element meshes of the four different notches used in the numerical simulations, respectively.

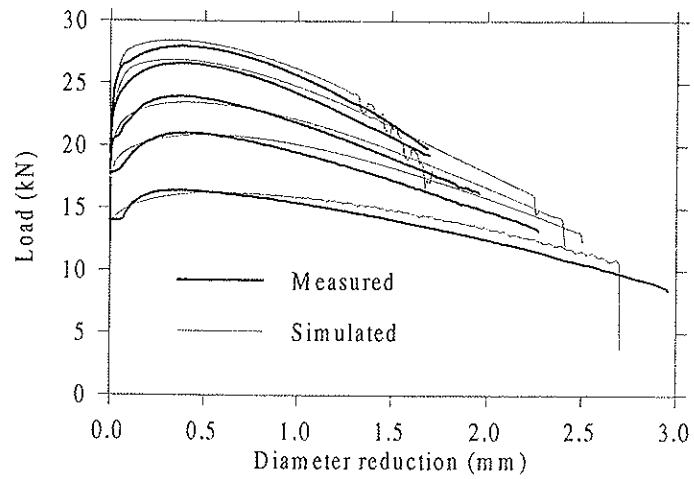


Fig. 16: Comparison between measured and simulated load-diameter reduction curves of quasi-static smooth and notched tensile specimen tests.

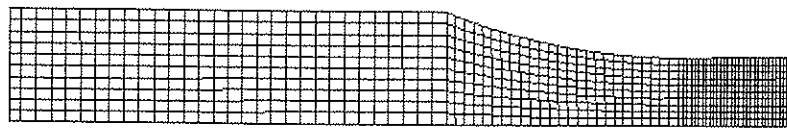


Fig. 17: Plot of coarse element mesh used to model the dynamic material tensile tests.

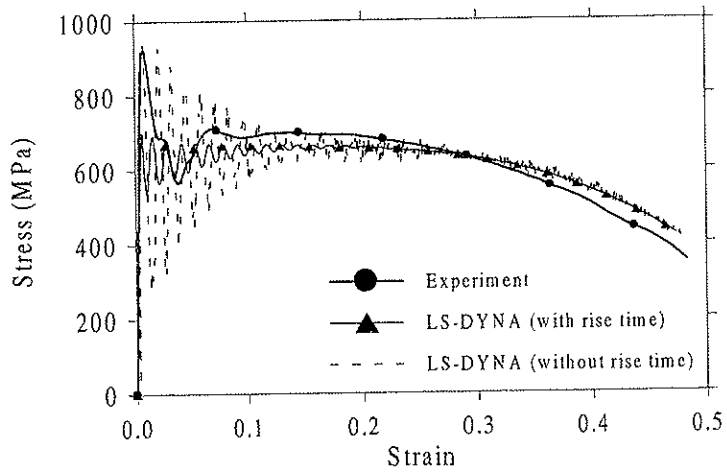


Fig. 18: Comparison between experimental and numerical results at a strain-rate of 1500 s^{-1} .

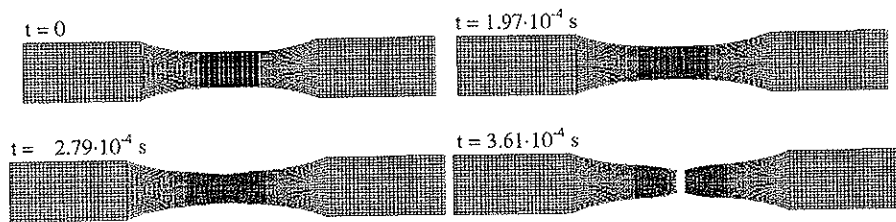


Fig. 19: Plot of deformed element mesh at different time steps to fracture for a dynamic test at a strain-rate of 1500 s^{-1} .

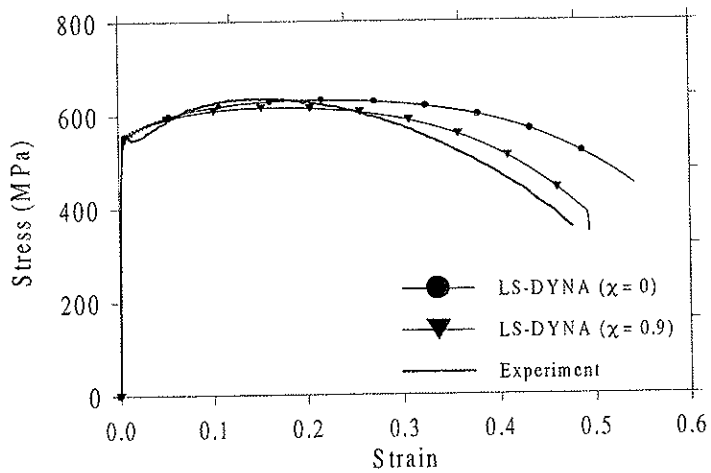


Fig. 20: Comparison between experimental and numerical results at a strain-rate of 2.2 s^{-1} .

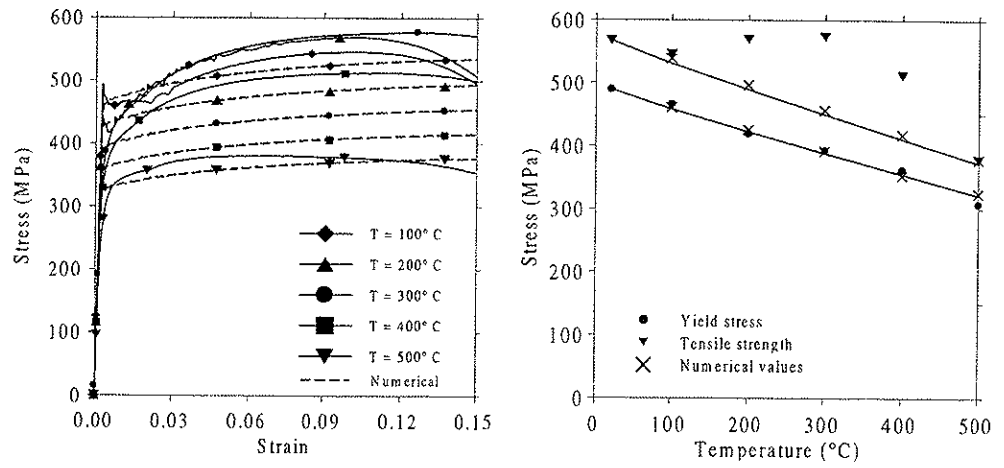


Fig. 21: Comparison between experimental and numerical results at elevated temperatures.

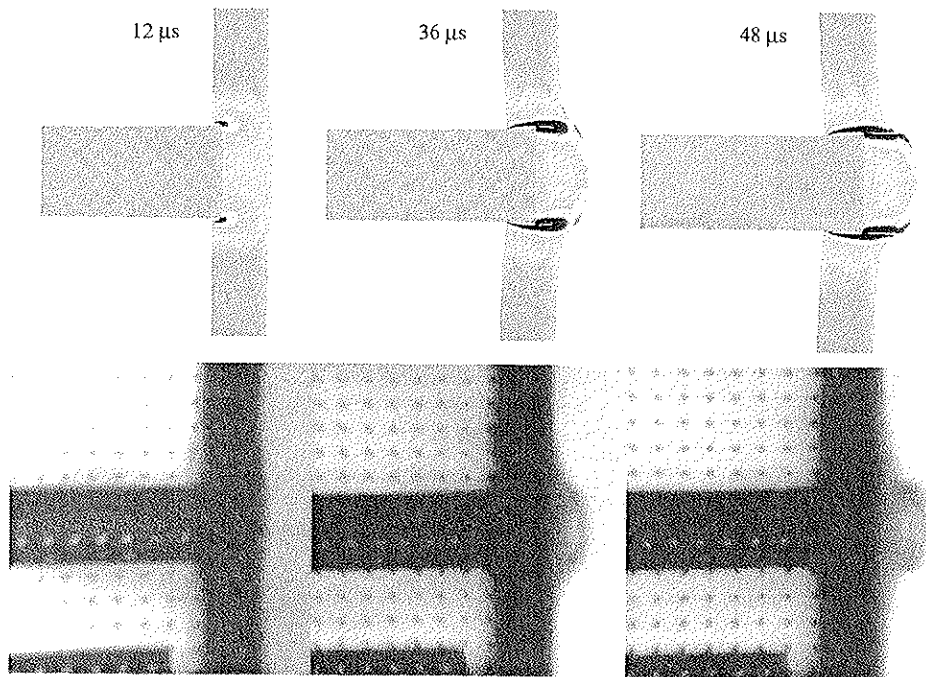


Fig. 22: Comparison between numerical and experimental deformed geometry during perforation of a 12 mm thick Weldox 460 E steel plate at identical times.

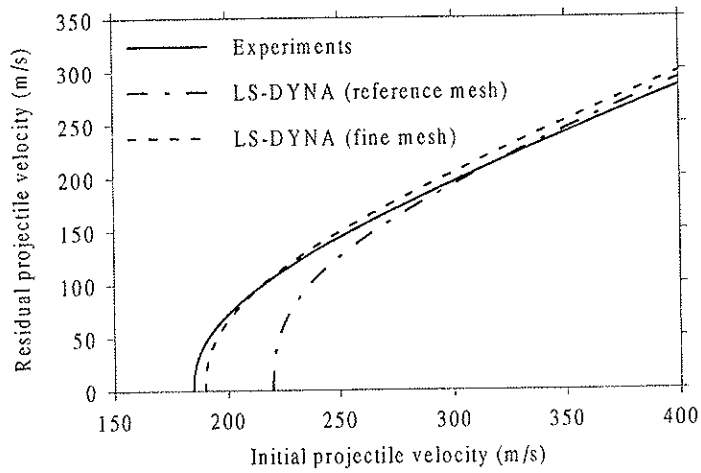


Fig. 23: Experimentally versus numerically obtained ballistic limit curves for 12 mm thick target of Weldox 460 E steel.

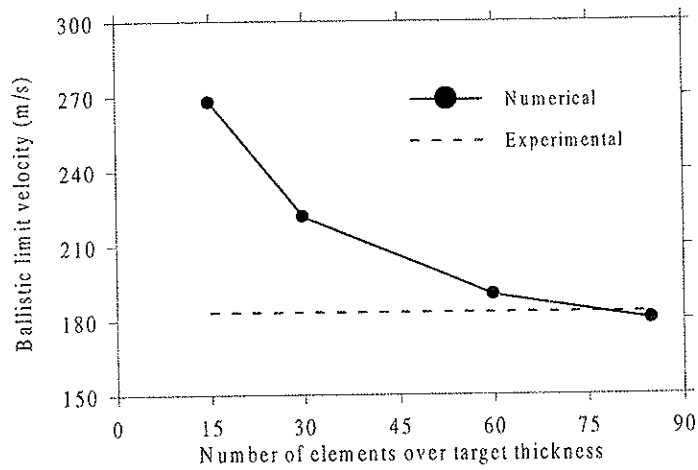


Fig. 24: Mesh sensitivity of numerical simulations for the 12 mm thick target plates.

Table 1: Chemical composition (weight %) of Weldox 460 E steel.

	C	Si	Mn	S	P	Nb	V	Ti	Cr	Ni	Mo	B	N	Al
Nominal	0.09	0.25	1.40	0.003	0.018	0.030	0.04	0.01	-	-	-	-	0.008	0.025
Certificate	0.08	0.26	1.40	0.002	0.008	0.028	0.04	0.01	0.02	0.04	0.007	0.00	0.006	0.032

Table 2: Mechanical properties (typical values) of Weldox 460 E.

	Thickness (mm)	Yield stress, min (MPa)	Tensile strength (MPa)	Elongation, min. A ₅ (%)	Impact property, Charpy-V (J)	Hardness (HB)
Nominal	8 - 40	460	530 - 720	19	40	180
Certificate	6	475	560	26	Not given	Not given
	8	475	575	22		
	10	504	572	22		
	12	507	575	22		
	16	494	569	23		
	20	480	565	26		

Table 3: Thermal properties of Weldox 460 E steel.

Density (kg/m ³)	Grain size (μ m)	Conductivity (W/mK)	Specific heat (J/kgK)	Expansion coeff. (K ⁻¹)	Melting temp. (K)
7850	7-12	47	452	$1.1 \cdot 10^{-5}$	1800

Table 4: Model constants of Weldox 460 E steel.

Elastic constants and density			Yield stress and strain hardening			Strain-rate hardening		Damage evolution			
E (GPa)	ν	ρ (kg/m ³)	A (MPa)	B (MPa)	n	\dot{P}_0, \dot{I}_0 (s ⁻¹)	C	D _c	P _d		
200	0.33	7850	490	807	0.73	$5 \cdot 10^{-14}$	0.0114	0.30	0		
Adiabatic heating and temperature softening						Fracture strain constants					
C _p (J/kgK)	χ	α (K ⁻¹)	T _m (K)	T ₀ (K)	m	K	D ₁	D ₂	D ₃	D ₄	D ₅
452	0.9	$1.1 \cdot 10^{-5}$	1800	293	0.94	0.74	0.0705	1.732	-0.54	-0.015	0

Table 5: Material constants for hardened Arne tool-steel.

E (MPa)	ν	ρ (kg/m ³)	σ_0 (MPa)	E _r (MPa)	Mean ϵ_f (%)
204000	0.33	7850	1900	15000	2.15

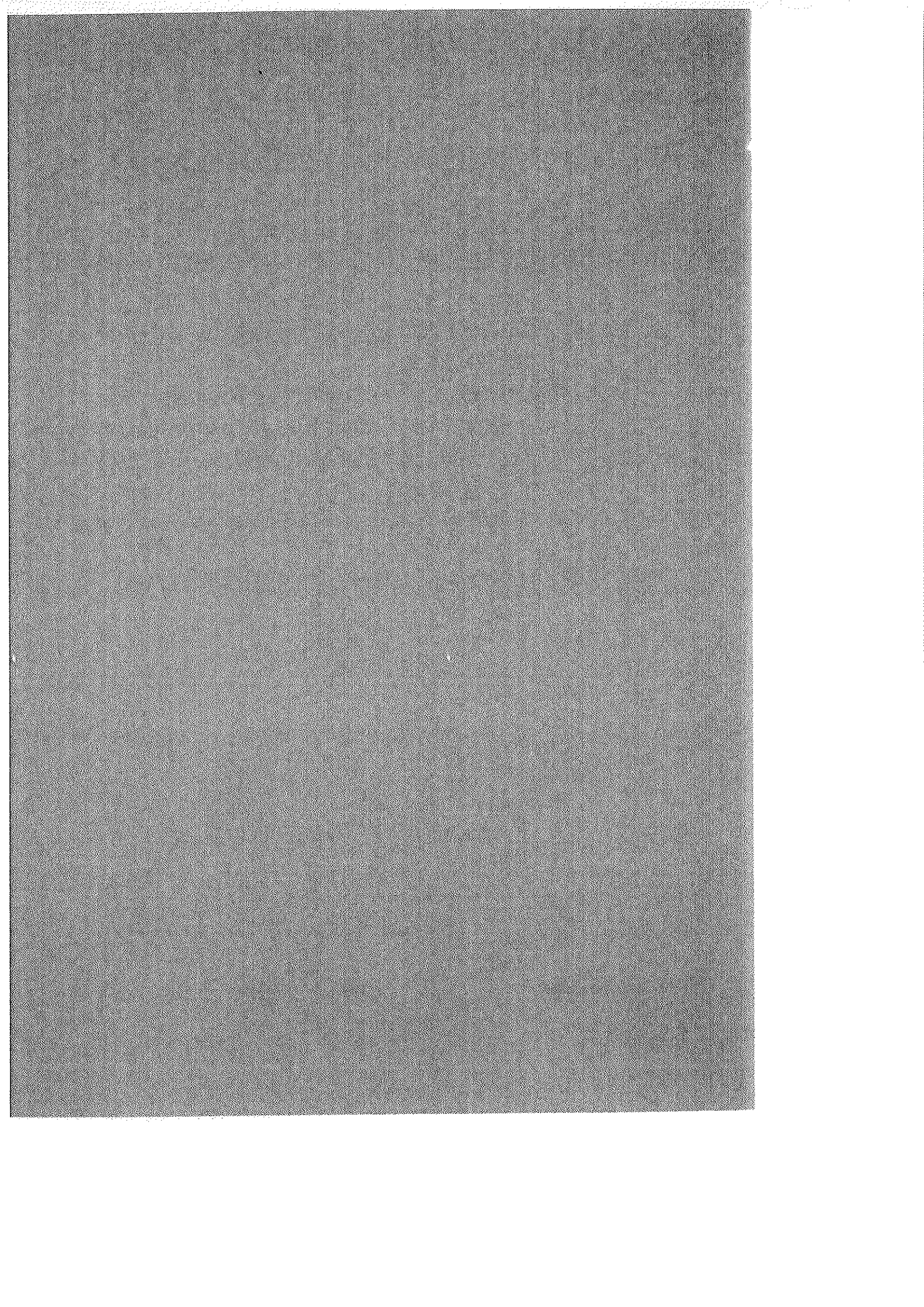


Part IV

T. Børvik, J.R. Leinum, J.K. Solberg, O.S. Hopperstad and M. Langseth

Observations on shear plug formation in Weldox 460 E steel plates impacted by blunt-nosed projectiles.

Accepted for publication in *International Journal of Impact Engineering*.



Observations on shear plug formation in Weldox 460 E steel plates impacted by blunt-nosed projectiles

Tore Børvik^{a,*}, John Rasmus Leinum^b, Jan Ketil Solberg^b,
Odd Sture Hopperstad^a and Magnus Langseth^a

^aStructural Impact Laboratory (SIMLab), Department of Structural Engineering, Norwegian University of Science and Technology, N-7491 Trondheim, Norway

^bDepartment of Materials Technology and Electro Chemistry, Norwegian University of Science and Technology, N-7491 Trondheim, Norway

Abstract

Shear plug formation in circular Weldox 460 E steel plates impacted by blunt-nosed cylindrical projectiles with striking velocities between 100 and 500 m/s has been investigated. Target thickness and projectile impact velocity were the primary variables, and for each target thickness the ballistic limit curve of the material was precisely determined. The test at an impact velocity just below the ballistic limit for each target thickness was selected for a microscopic examination of shear localisation and fracture. In these tests, the plug was pushed only partway through the target, and the localised shear zones outlining the fracture were easily recognised both in the optical and scanning electron microscope. Clear evidence of adiabatic shear bands and material damage due to void growth was found in several of the target plates. Analytical models available in the literature were compared with the results from the experimental and microscopic studies. Reasonable agreement was found between calculations and experiments.

Keywords: ballistic penetration; microscopic examination; shear localisation; fracture; analytical models

1. Introduction

Structural impact problems have become increasingly important for the industry. In design of offshore structures, account is taken for accidental loads such as dropped objects, collisions, explosions and fragment penetration. Some of these accidental loads are also pertinent in design of protective structures in the process industry or fortification installations

* Corresponding author. Tel.: + 47-73-59-46-47; fax: + 47-73-59-47-01

E-mail address: tore.borvik@bygg.ntnu.no (T. Børvik)

for defence purposes. One typical problem is plugging of plates impacted by blunt-nosed projectiles at moderately high velocities. For relatively thin plates a combination of localised shearing, bending and membrane stretching absorbs the kinetic energy of the projectile. However, as the plate thickness or projectile velocity is increased, more and more of the kinetic energy is absorbed in local shear zones along the sharp edges of the impacting projectile. Shear bands usually appear when favourable conditions for localised plastic deformation under high strain rate loading exist. A major part of the plastic work conducted during deformation is converted into heat. When the deformation occurs so rapidly that the heat conduction with the surroundings is constrained, the process becomes adiabatic. If the incremental thermal softening overcomes the incremental strain and strain rate hardening, the deformation will localise in narrow zones of intense shear. Within these shear zones the deformation continues under very high local strain rates and temperatures.

In this paper, only the low alloy steel Weldox 460 E is considered. Low alloy steels are polymorph, i.e. they can exist as three different solid phases with different lattice structure depending on the temperature. The three phases are the cubic body centred δ -ferrite, the cubic body centred α -ferrite and the cubic face centred γ -austenite as shown in the Fe-C phase diagram in Fig. 1 [1]. For the investigated Weldox 460 E material, the transformation from α to γ starts at 723°C and is completed at approximately 850°C. The latter is the minimum temperature required to form a completely transformed shear band in a penetrated plate. If these temperatures are not reached, there will be no phase change, and the adiabatic shear band should be referred to as deformed [2]. The microstructure of the transformed bands is determined by the cooling rate from the austenite temperature and by the size of the austenite grains, that in turn is dependent on the maximum temperature and the time for grain growth. With increasing cooling rate, the microstructure will be ferritic/pearlitic, bainitic or martensitic. The latter is a microstructure with carbon in supersaturated solid solution, which makes its crystal structure slightly tetragonal instead of cubic. The hardness of the microstructures increases with increasing cooling rate and decreasing grain size. Transformed adiabatic shear bands are assumed to consist of a martensitic microstructure [2].

Another important softening mechanism is material degradation or damage due to the nucleation, growth and coalescence of microcracks and microvoids. In dynamic problems, this is assumed to occur independently at various material points in the bulk material caused by the short time duration of the transient stress waves. However, material damage is likely to occur inside the adiabatic shear bands where the deformations are extreme and at some point

the combination of very large strains and thermal and damage softening leads to failure. The deformation and fracture processes during structural impact have been widely studied over the years, and a comprehensive review on the subject can be found in e.g. Zukas et al [3].

Ballistic impact data from tests on 6 to 30 mm thick steel plates of Weldox 460 E using 20 mm diameter hardened steel rod projectiles with a constant mass of 0.197 kg was recently given by Børvik et al [4]. In the present study, a microscopic investigation is carried out to examine the local deformations of impacted plates in an attempt to identify and characterise deformed and transformed adiabatic shear bands and to detect material damage in the form of microvoids and microcracks. The test at an impact velocity just below the ballistic limit for each target thickness was selected for a microscopic examination of shear localisation and fracture. In these tests, the plug was pushed only partway through the target, and the localised shear zone outlining the fracture was easily recognised both in the optical and scanning electron microscope. Also some tests where complete perforation occurred were investigated for comparison.

Bai and Johnson [5] presented a model for plugging based on thermoplastic shear instability. The model is valid for plates in which the energy absorption is dominated by shear deformations, i.e. the part of the kinetic energy absorbed in global deformations is assumed to be negligible. Dodd and Bai [6][7] presented approximate equations for the adiabatic shear bandwidth (see also Bai and Dodd [2] for a comprehensive review on the occurrence and effect of adiabatic shear bands). Data from the impact tests and results from the microscopic investigation are finally discussed in view of these analytical models.

2. Experimental set-up and results

The compressed gas gun shown in Fig. 2 was used to launch the sabot mounted blunt-nosed cylindrical projectiles at impact velocities just below and well above the ballistic limit of the target material. Nominal hardness (HRC 53), diameter (20 mm), length (80 mm) and mass (0.197 kg) of the hardened Arne tool-steel projectiles were kept constant in all tests. The projectile impacted the target plate of Weldox 460 E steel after about 2 meters of free flight. The targets were clamped in a circular frame, having a thickness range from 6 to 30 mm and a constant free span diameter of 500 mm. Thus, the only variables in the tests were the target thickness and the initial projectile velocity. If perforation occurred, the projectile

and plug were soft recovered in a rag-box. Initial and final velocities were obtained by different optical measurement systems, and the ballistic limit curve for each target thickness was constructed based on the measured velocities. A digital high-speed camera system was used to photograph the penetration event. Based on the digital images, impact angles and projectile velocity as a function of penetration time were determined. Target oblique and point of impact were also measured. It is referred to Børvik et al [8][9] for details regarding the experimental set-up and the different measurement techniques used during testing. Projectile and target material data obtained from material tests is presented in [9][10].

In order to investigate the microstructural details associated with the shear localisation and fracture process, the tests at an impact velocity just below the ballistic limit of each target thickness tested were studied. The ballistic limit for the target is defined as the average of the highest projectile velocity giving only partial penetration and the lowest projectile velocity giving complete perforation [11]. The estimated ballistic limit velocity (v_{bl}) for each target thickness is given in Table 1 together with the highest velocity (v_h) only giving partial penetration [4]. The difference between v_{bl} and v_h is as seen very small, indicating a precisely determined ballistic limit. Therefore, the tests selected for the microscopic examination were all close to fracture. Fig. 3 shows the ballistic limit velocity as a function of target thickness [4]. A distinct kink in the fitted response curve occurs at a target thickness of about 10 mm. This transition in target response appears to be related to a change in deformation mode, from typical thin plate membrane stretching and bending to thick plate shear localisation. The maximum permanent target deformation is given in Fig. 4 [4]. While the in-situ measured global deformation is almost twice the target thickness for the 6 mm thick target, it is hardly measurable for 16 and 20 mm thick targets. In thin plates both local and global structural deformations take place. It is here assumed that the global deformation mode absorbs a considerable amount of the projectile kinetic energy during impact. In thick plates, on the other hand, only limited global target deformation can be measured. Hence, most of the kinetic energy has to be absorbed in the highly localised shear zones surrounding the projectile nose. The global target deformation is also a function of the impact velocity, which reaches a maximum at the ballistic limit velocity independent of target thickness. After perforation, the global target deformation for a given thickness decreases with increasing velocity until it stabilises at a velocity well above the ballistic limit [9].

The high-speed camera images in Fig. 5, showing details from some of the tests, support the above assumptions. As shown in Fig. 5a), the global target deformation in a 6 mm thick

target is considerable when the projectile impact velocity is just below the ballistic limit. The actual (i.e. both elastic and plastic) deformation during impact is approximately twice as large as the measured permanent deformation given in Fig. 4. However, this behaviour changes rapidly with target thickness and projectile impact velocity, and for plates in the medium thickness range the deformation becomes more and more localised even if the projectile velocity is close to the ballistic limit. When the target is thick, the deformation becomes extremely localised. This is clearly seen in Fig. 5b), where the projectile penetrates a 20 mm thick target. Owing to an unsymmetrical failure mode, the projectile may rotate somewhat in the cavity during penetration. For the thickest plates, the projectile is defeated. Fig. 5c) shows that a 30 mm thick target shatters the relatively brittle projectile during impact with hardly any visible deformation of the plate. It was not possible to perforate any of the 25 and 30 mm thick targets with the type of projectile used in this study. The projectile also shattered for the highest impact velocities in the tests with 20 mm thick targets. It follows that both impact velocity and target thickness affect the projectile deformation. Projectile shatter was not observed in any of the tests using a target thickness less than 20 mm. It was also found that the projectile indented the front side of the target before any significant deformation could be seen on the rear side. This indentation seemed to increase with target thickness.

3. Microscopic Observations

Based on the experimental observations, it is seen that both the shear localisation and fracture processes during structural impact are highly affected by target thickness and projectile velocity. As the target thickness and/or projectile velocity are/is increased, the deformation process becomes more and more localised, and for thick targets the deformation mainly takes place in narrow shear zones under extreme strains, strain rates and temperatures. It seems reasonable that such structural behaviour facilitates fracture. Also, at some point the capacity of the hardened projectile may be exceeded and shatter occurs. To verify these observations, and to reveal the physical phenomena underlying the structural behaviour, a microscopic examination of the impacted targets was accomplished. It is also known that both the mechanical and thermal properties of the target material itself are important regarding the presence or absence of adiabatic shear bands during structural impact [2], but the effect of varying material properties has not been investigated in this study.

The studies of the cross-sections of penetrated plates were carried out in a Leica MeF4 light microscope equipped with a ProgRes 3008 digital video camera and in a Jeol JSM 840 scanning electron microscope. Hardness measurements were carried out in a Matsuzawa MXT70 digital micro-hardness tester with a Vickers pyramid, applying a load of 50 gram for 15 seconds. Most plates studied were impacted at velocities just below the ballistic limit. The macroscopic images in Fig. 6 clearly illustrate that the intensity of the deformation in the localised shear zone increases with plate thickness. The change in microstructure along the mid-thickness plane of a 10 mm thick plate towards the shear zone is given in Fig. 7. In the centre of the shear zone a strong plastic deformation has taken place, leading to a reduction of the distance between the pearlite bands in the material and consequently a reduced grain diameter. At a position x , a measure of the local dimensionless deformation ε_x of the ferrite grains was defined as (Fig. 8)

$$\varepsilon_x = \ln \frac{d_0}{d_x} \quad (1)$$

where d_0 is the grain diameter as measured normal to the pearlite bands in the undeformed matrix far from the shear zone, and d_x is the value at position x . Fig. 9 shows the measured variation in ε_x as a function of distance from the centre of the shear zone in plates of varying thickness penetrated by projectiles with impact velocities just below the ballistic limit (see Table 1). In the microstructural investigation it was found that the deformation in the pearlite bands far from the middle of the shear zone is too small to be measured. However, the extension of the localised zone with microscopic observable deformation increases with increasing plate thickness, Fig. 9, in contrast to the global target deformation that decreases with increasing plate thickness, Fig. 4.

A large zone of high deformation causes an increased temperature, and transformed shear bands may occur, as in the thickest plates. Fig. 10 gives a comparison of the shear zones in the 16 mm and the 20 mm thick plates, and a transformed adiabatic shear band in the 20 mm plate becomes visible in the lower part of the zone. Fig. 10 also indicates the contour of the sigmoidal shape of the flow lines in the most strained part of the shear zone. The micrographs in Fig. 11 and Fig. 12 are magnifications of a transformed adiabatic shear band in the 20 mm thick plate. Close to the projectile entrance a crack has formed within the band. At 1000x magnification, Fig. 12, it is seen that a new microstructure has formed in the band because the A_3 temperature has been exceeded (see Fig. 1). At this high magnification, the

crack following the centre of the shear band can easily be seen. Vickers hardness measurements of the cross-sections show a strong increase in hardness in the transformed shear band compared to the surroundings both for the 20 mm and 25 mm thick plates, Fig. 13. The hardness of the shear band was compared with that obtained in a thin plate of Weldox 460 E steel homogenised at 930°C and quenched in cold water to obtain a martensitic microstructure. This microstructure is shown in Fig. 14, and differs from the microstructure in the adiabatic shear band in Fig. 12 by its coarse grain size. The hardness of this martensite was 420 HV_{50g}, approximately equal to the hardness measured in the adiabatic shear band in the 20 mm plate, but 30 HV_{50g} lower than the hardness of the shear band in the 25 mm plate. It is reasonable to conclude that the transformation structure in the shear band is martensite, and that the relatively high hardness values are due to an extremely fine-grained structure. It is further assumed that the grain boundaries visible within the adiabatic shear band in Fig. 12 are previous austenite grain boundaries and that the martensite laths are so fine that they are not resolved in the image. The original hardness of the plates was 180-190 HV_{50g}.

A study in the scanning electron microscope (SEM) was done to identify the mechanisms for crack propagation during the penetration process. The cross-section SEM micrographs in Fig. 15 show a crack in the 12 mm thick plate. It is seen that voids are present in front of the crack tip, and that secondary voids have formed in a narrow zone around the crack. Such void growth in front of the crack tip has also been identified in 10 mm thick plates [9]. A special case is the 20 mm thick plate given in Fig. 16a), showing a transformed adiabatic shear band that contains a longitudinal crack. Around this crack is a fully transformed zone where ferrite and pearlite have been transformed into austenite under heating and then into martensite due to the rapid cooling. On both sides of this zone the material is partially transformed and contains both martensite and ferrite. The material has reached the temperature where austenite and ferrite co-exist (Fig. 1), and after rapid cooling austenite has been transformed into martensite. Ferrite has a higher self-diffusivity than austenite and ferrite grain growth in the partially transformed zone can be seen. Secondary microcracks and voids found outside the transformed shear band are shown in Fig. 16b). Probably, this is an example of the simultaneous propagation of two independent cracks. SEM investigations of the fracture surface of a perforated plate confirmed the formation of voids as the main fracture mechanism, Fig. 17b). In this case the projectile has deformed the initial part of the fracture surface, leaving a smooth surface that resembles the surface of an extruded product, Fig.

17a). Investigations of a statically penetrated 10 mm thick plate showed the same type of fracture surfaces as in the dynamically penetrated 10 mm thick plate.

Finally, Fig. 18 shows a macroscopic image of a fractured projectile within the target after impacting a 25 mm thick plate at an initial velocity of approximately 450 m/s. As seen, after the initial indentation the nose part of the projectile is completely shattered, and the penetration process terminates. Only a limited amount of shear localisation seems to have occurred before projectile breakdown, and no proof of transformed adiabatic shear bands propagating towards the rear side of the target was found. However, a closer examination revealed incipient shear bands inclined to the impact direction, similar to the theoretical slip-line field solution for indentation [2]. Shear bands propagating perpendicular to the impact direction can give fragmentation of the target, but no plugging. Woodward et al [12] reported similar behaviour in the penetration of thick aluminium targets by blunt-nosed projectiles.

4. Discussion

An experimental study on the ballistic penetration of circular Weldox 460 E steel plates impacted by blunt-nosed cylindrical projectiles has been carried out. The experimental details from the component tests are presented in [4], but one major observation quoted here is the distinct kink in the ballistic response curve at a target thickness of about 10 mm (Fig. 3). This transition in target response appears to be related to the change in deformation mode with target thickness, from typically thin plate global deformation to thick plate shear localisation. When the target thickness is sufficiently increased the hardened projectile fractures at impact and shear plugging is prevented (see Fig. 5c)). The subsequent metallographic examination of the impacted targets confirmed that for plates of thickness about equal to or larger than the projectile radius (i.e. $b \geq 10$ mm, where b is the target thickness), the plugging process was dominated by adiabatic shear deformation in localised bands. For thinner plates, i.e. $b < 10$ mm, the plugging process seemed to be controlled by a combination of localised shear, bending and tension. For plates of thickness between 10 and 16 mm, the adiabatic shear bands were only deformed, which means that no phase transformed material was found in the zones of intense plastic strain. However, clear evidence of transformed adiabatic shear bands causing extreme strains, strain rates and temperatures was found in plates equal to or

thicker than 20 mm. In other words, the local plugging process seems to be controlled by at least three distinctly different deformation modes depending on the target thickness.

It is very difficult to quantify parameters such as the shear bandwidth, temperature rise, critical strain and strain rate in the localised zones due to a diffuse and complex microstructure within the deformed area. However, in the deformed adiabatic shear bands the bandwidth seemed to be more than 100 μm (typically 200-300 μm). The intensity of the band was found to increase almost exponentially towards the centre, while the width of the band increased linearly throughout the thickness of the plate and became very diffuse due to the influence of tensile forces at the rear side. No transformed shear bands were found in target plates having a thickness less than 20 mm. This indicates that the phase transformation temperature of 723°C was not reached in any of these tests. The transformed adiabatic shear bands in the thickest plates were easier to identify, but also these bands showed a somewhat diffuse microstructure. The width of the band in the most intense zone was about 10-20 μm . Here, a complete phase transformation took place, indicating a temperature above 850°C. However, the width of the entire shear band was measured to be between 40 and 100 μm . In the outer area, the material was only partially transformed, and the temperature is assumed to have been between 723°C and 850°C (see Fig. 1). The width of the transformed band was almost constant throughout its length, while the width was found to increase with increasing target thickness (Fig. 9).

Accordingly, shear instability and localisation play a major role in plugging of steel plates impacted by blunt projectiles. It is therefore of interest to compare the results with available analytical models for plugging based on such behaviour. A large literature exists on the subject concerning the occurrence, formation and evolution of adiabatic shear bands, and much of this work has been gathered in Bai and Dodd [2]. However, fewer publications have considered the plugging process followed by adiabatic shear banding. Bai and Johnson [5] developed a simple mechanical model for plugging based on adiabatic shear instability. The model consists of three major elements: the kinetic energy equation connecting the projectile and the plug, the constitutive equation, and the relationship between the displacement of the plug and the shear strain. It is assumed that only simple shear deformation occurs in the direction of the projectile when in the plate. A necessary criterion for shear instability is that temperature softening outbalance the strain and strain rate hardening, i.e. that the increment in shear stress is equal to or less than zero in a loading process

$$\delta\tau = \frac{\partial f}{\partial \gamma} \delta\gamma + \frac{\partial f}{\partial \dot{\gamma}} \delta\dot{\gamma} + \frac{\partial f}{\partial \theta} \delta\theta \leq 0 \quad (2)$$

where $\tau = f(\gamma, \dot{\gamma}, \theta)$, i.e. that the shear stress τ is a function of shear strain γ , shear strain rate $\dot{\gamma}$ and temperature θ . Bai and Johnson [5] assumed that the effect of strain rate variation is negligible at high strain rates and that the effect of temperature softening caused by adiabatic heating could be implicitly accounted for. Thus, a constitutive relation on the form $\tau = f(\gamma)$ was adopted, and the shear instability criterion from Eq. (2) is simplified to

$$\delta\tau = \frac{d\tau}{d\gamma} \delta\gamma \leq 0 \quad (3)$$

The particular adiabatic constitutive equation used by Bai and Johnson in their model was expressed in terms of the shear strain as

$$\tau = \tau_M \left(\frac{\gamma}{\gamma_i} \right)^n \exp \left\{ \frac{n}{1+n} \left[1 - \left(\frac{\gamma}{\gamma_i} \right)^{n+1} \right] \right\} \quad (4)$$

where the maximum shear stress, τ_M , and the critical value of the shear strain, γ_i , at which $\delta\tau = 0$, were found as

$$\tau_M = \tau_0 (1 + \alpha\theta_0) \gamma_i^n \exp \left(-\frac{n}{1+n} \right) \quad \text{and} \quad \gamma_i = \left(-n \frac{\rho C_v}{\alpha \tau_0} \right)^{1/(1+n)} \quad (5)$$

Here, τ_0 and α are material constants, θ_0 is the initial temperature, C_v is the specific heat, ρ is the density and n is the strain hardening index of the material. Thus, it is seen that the shear localisation depends on the strength and strain hardening characteristics of the material, the material density and the thermal properties. More details regarding the model and all the essential equations can be found in the original paper by Bai and Johnson [5].

The material properties of Weldox 460 E steel have been identified by Børvik et al [9][10] through a test programme including tensile tests in different material directions, at high strain rates, at high temperatures and with different levels of hydrostatic tension. The

material constants required in Eq. (4) for Weldox 460 E have been determined from the experimental data as $\gamma_s = 1.4$, $\tau_M = 570$ MPa and $n = 0.25$. It is here assumed that the shear stress and shear strain can be calculated based on the von Mises relations as $\tau = \sigma_{eq} / \sqrt{3}$ and $\gamma = \sqrt{3} \cdot \varepsilon_{eq}$, where σ_{eq} and ε_{eq} are the von Mises equivalent stress and strain, respectively. The assumed adiabatic shear stress-strain curve from Eq. (4) is shown in Fig. 19.

Instead of modelling the fracture process, involving nucleation, growth and coalescence of microcracks and voids, Bai and Johnson [5] assumed that the penetration process terminates at a penetration depth $p_U = b$, i.e. at a penetration depth equal to the target thickness. It was argued that for metals considerable amounts of energy can be absorbed in post-instability deformation, and in this sense the assumption is reasonable. The approach is assumed to give an upper limit to the energy absorption in plugging. However, some experimental results indicate that fracture occurs when the projectile is approximately halfway through the target (see e.g. [9]). Thus, the termination of the penetration process can also be defined by $p_U = b / 2$.

The ballistic limit velocity $v_{bl} = v_{oc}$ obtained with the Bai-Johnson model for plugging is plotted in Fig. 20a) against target thickness b both for $p_U = b$ and $p_U = b/2$. The penetration time $t(p_U)$ and the ultimate temperature $\theta_a(p_U)$ as functions of target thickness for a striking velocity v_{oc} are presented in Fig. 20b) and Fig. 20c). The nominal values of density and specific heat for steel are adopted as $\rho = 7850$ kg/m³ and $C_v = 452$ J/kgK [9]. It is seen in Fig. 20a) that $p_U = b$ overestimates the plugging capacity of the target plates, while $p_U = b/2$ is in good agreement with the experiments for $b \geq 12$ mm, which corresponds well with the assumed domain of validity for the Bai-Johnson model. For thinner plates the contribution from global deformations is considerable. The perforation time is given in Fig. 20b). The model predicts perforation times between 120 and 140 μ s for plates with thickness from 12 to 20 mm when $p_U = b$, while for $p_U = b/2$ the perforation time is constant about 80 μ s. These values are reasonably close to the experimentally measured perforation times of about 100 μ s independent of target thickness [4]. Based on the microscopic study, it is assumed that the temperature in the adiabatic shear band in the 20 mm thick target plates was slightly above 850°C. The Bai-Johnson model with $p_U = b$ predicts a maximum temperature

of about 800°C for the 20 mm thick plate, while for $p_U = b/2$ the temperature is only slightly above 450°C, see Fig. 20c).

In order to estimate the width of the adiabatic shear band, a model that takes into account both heat generation from plastic work and thermal conductivity is needed. Dodd and Bai [6] derived an equation for the half-width δ of an adiabatic shear band based on Bai's approximate model for simple shear [13], while combined stresses were considered in [7]. The equation shows, in accordance with a number of separate experimental observations, that the bandwidth depends on the thermal properties of the material and the rate of dissipated work, but is independent of the details of the combined stress state [7]. For simple shear, the equation for the half-width of the adiabatic shear band reads [6]

$$\delta \approx \left(\frac{\lambda \Delta\theta_*}{K \tau_* \dot{\gamma}_*} \right)^{1/2} \quad (6)$$

where the subscript * denotes characteristic quantities within the band. The quantities τ_* , $\dot{\gamma}_*$ and $\Delta\theta_* = \theta_* - \theta_0$ are not easily found experimentally, and some approximations have to be adopted. Here the Bai-Johnson model is used to obtain approximations for the quantities within the shear band. τ_* and $\Delta\theta_*$ are approximated by the predicted values of shear stress and temperature increase at termination of the plugging process, while $\dot{\gamma}_*$ is the average strain rate (i.e. shear strain divided by time at $p = p_U$). K is the fraction of plastic work converted into heat. Here, K is chosen equal to 1 for simplicity. The thermal conductivity for Weldox 460 E steel is taken as $\lambda = 50$ W/mK [6]. The adiabatic shear bandwidth 2δ is plotted in Fig. 20d) against target thickness b for $p_U = b$ and $p_U = b/2$. It is found that 2δ is in the order of 50-100 μm , which is in reasonable agreement with the experimental observations.

5. Conclusions

Shear plug formation in Weldox 460 E steel plates impacted by blunt-nosed steel rod projectiles was studied. Plates from impact tests with striking velocity just below the ballistic limit for 6 to 30 mm thick targets were selected for a microscopic investigation of the shear

localisation and fracture. In these tests, the plug was pushed only partway through the target, and the localised shear zones outlining the fracture was easily recognised in the microscope.

Both from post-impact measurements and high-speed camera images of the penetration process it was found that the global deformations decreased rapidly with increasing target thickness, and for targets of 16 mm thickness or more the global deformation was almost negligible. This indicates that the kinetic energy of the impacting object is mainly absorbed as local deformations in narrow shear zones around the periphery of the projectile. The microscopic study showed clear evidence of adiabatic shear bands; deformed shear bands in 10 to 16 mm thick targets, transformed shear bands in thicker targets. The width of the shear bands ranged from 100-300 μm in deformed bands and from 10-100 μm in transformed bands. Microcracks and microvoids were found inside the shear bands, and in front of the propagating crack. This indicates a fracture process as follows. The shear deformation is localised in narrow bands because of thermal softening and thermoplastic instability. In the adiabatic shear bands, extreme strains occur, leading to nucleation and growth of microvoids and microcracks. The material damage leads to further softening and an even stronger localisation of the deformation. Fracture occurs when the voids and cracks coalesce into a macrocrack by necking down of the matrix material between them.

The analytical model of Bai and Johnson was used to predict the plugging process, and reasonable results were obtained, taking into account the simplicity of the model. The model proposed by Dodd and Bai predicted the width of the adiabatic shear bands with reasonable accuracy.

Acknowledgements

The financial support of this study by the Norwegian Defence Construction Service, Central Staff/Technical Division, Oslo, Norway, is gratefully acknowledged.

References

- [1] Solberg, J.K., 1999. Teknologiske Metaller og Legeringer (in Norwegian), Department of Material Science and Electro Chemistry, Norwegian University of Science and Technology (NTNU).
- [2] Bai, Y., Dodd, B., 1992. Adiabatic shear localization. Occurrence, theories and applications, Pergamon Press.
- [3] Zukas, J.A. (Ed.), 1990. High Velocity Impact Dynamics, John Wiley & Sons.
- [4] Børvik, T., Hopperstad, O.S., Langseth, M., Malo, K.A., 2000. Effect of Target Thickness in Blunt Projectile Penetration of Weldox 460 E Steel Plates, submitted for publication.
- [5] Bai, Y.L., Johnson, W., 1982. Plugging: physical understanding and energy absorption, Metals Technology, Vol. 9, pp. 182-190.
- [6] Dodd, B., Bai, Y., 1985. Width of adiabatic shear bands, Materials Science and Technology, Vol. 1, pp. 38-40.
- [7] Dodd, B., Bai, Y., 1989. Width of adiabatic shear bands formed under combined stresses, Materials Science and Technology, Vol. 5, pp. 557-559.
- [8] Børvik, T., Holen, K., Langseth, M., Malo, K.A., 1998. An Experimental set-up used in Ballistic Penetration, Proceedings of Fifth International Symposium on Structures under Shock and Impact, pp. 683-692, Thessaloniki, Greece, 24-26 June.
- [9] Børvik, T., Langseth, M., Hopperstad, O.S., Malo, K.A., 1999. Ballistic Penetration of Steel Plates, International Journal of Impact Engineering, Vol. 22, pp. 855-886.
- [10] Børvik, T., Hopperstad, O.S., Berstad, T., Langseth, M., 2000. Computational Model of Viscoplasticity and Ductile Damage for Projectile Impact, submitted for publication.
- [11] Backman, M.E., Goldsmith, W., 1978. The Mechanics of Penetration of Projectiles into Targets, International Journal of Engineering Science, Vol. 16, pp. 1-99.
- [12] Woodward, R.L., Baxter, B.J., Scarlett, N.V.Y., 1984. In Mechanical Properties of Materials at High Rates of Strain (ed. Harding, J.), Inst. of Physics Conf. Series No. 70, Bristol, U.K.
- [13] Bai, Y.F., 1982. Thermo-Plastic Instability in Simple Shear, J. Mech. Phys. Solids, Vol. 30, No. 4, pp. 195-207.

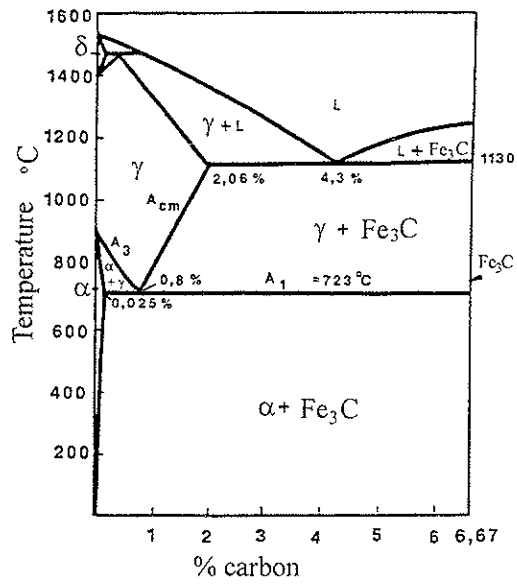


Fig. 1: Part of the Fe-C phase diagram, illustrating the polymorph transformation in Weldox 460 E steel [1].

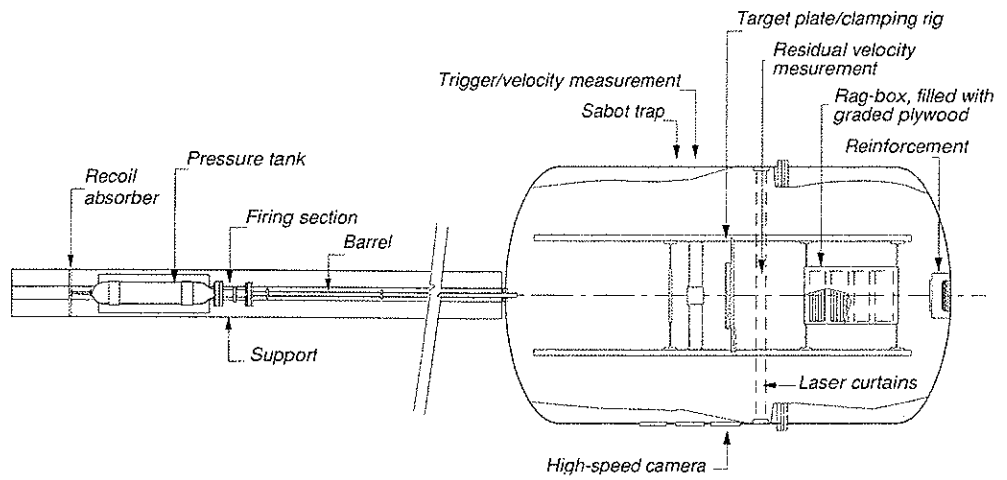


Fig. 2: Sketch of compressed gas gun used in the experiments [9].

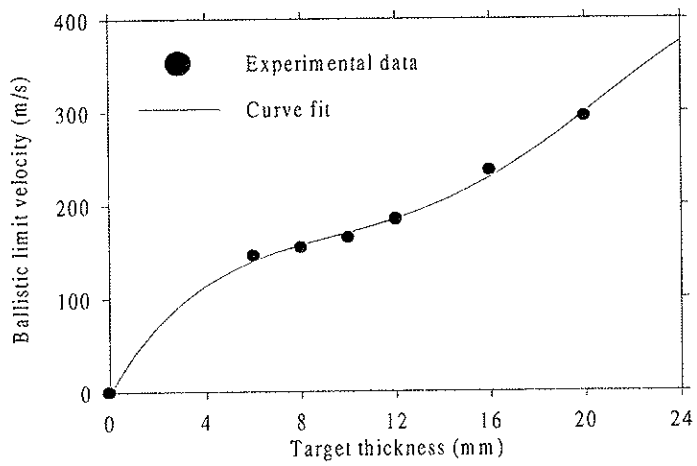


Fig. 3: Ballistic limit velocity versus target thickness [4].

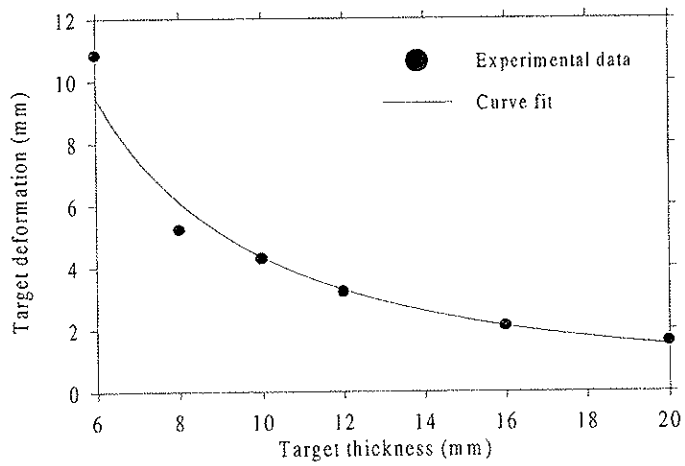
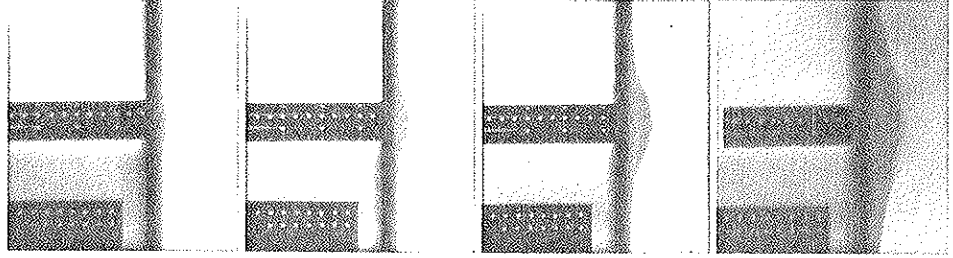
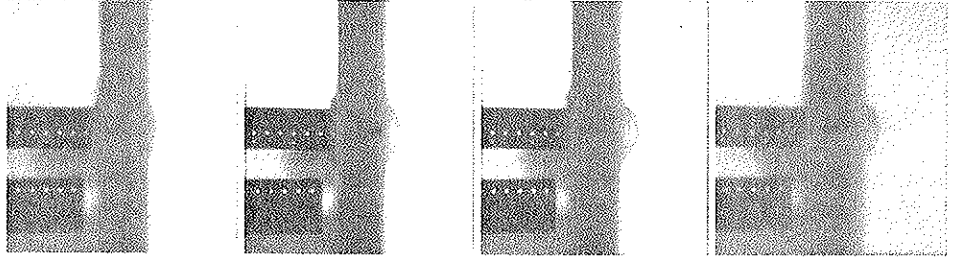


Fig. 4: Target maximum deformation versus target thickness [4].

a) 6 mm thick target impacted at 145.3 m/s (no perforation).



b) 20 mm thick target impacted at 292.5 m/s (no perforation).



c) 30 mm thick target impacted at 450.2 m/s (no perforation – projectile fracture).

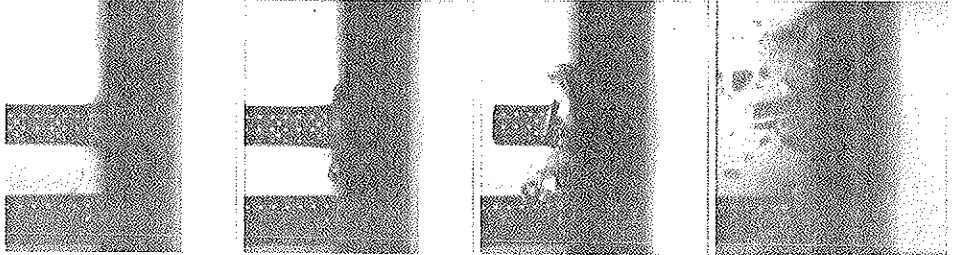


Fig. 5: High-speed camera images from some of the experiments showing penetration of the target without perforation.

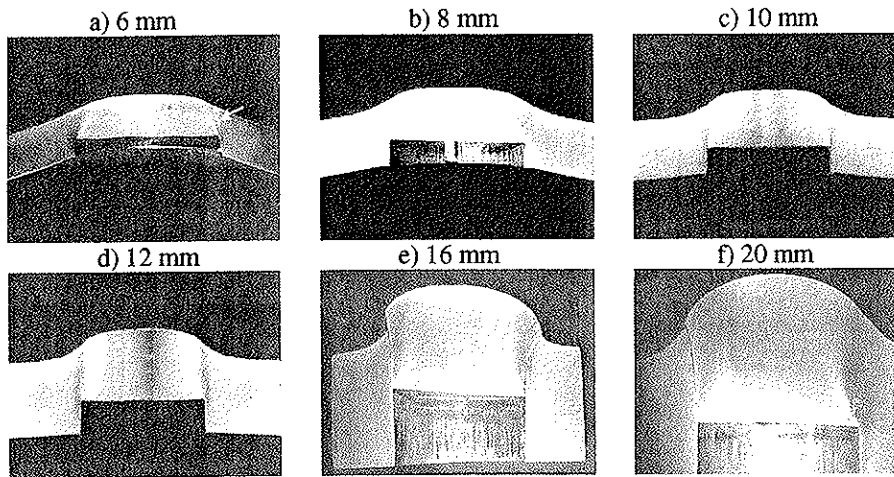


Fig. 6: Macrographs of the cross-section of 6, 8, 10, 12, 16 and 20 mm thick plates penetrated by projectiles with impact velocities just below the ballistic limit. The arrow in Fig. 6a) indicates the zone where cracking has started.



Fig. 7: Micrography of the 10 mm thick plate that shows the change in microstructure towards the shear zone. The crack inside the shear zone can be seen to the left.

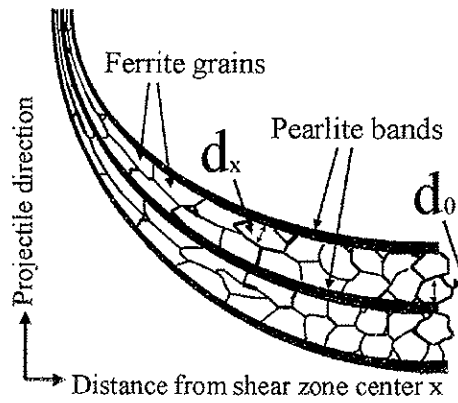


Fig. 8: Sketch of the ferritic/pearlitic microstructure used in the measurements of the local deformation, showing ferrite grains between pearlite bands analogue to Fig. 7. For simplicity the pearlite bands are drawn as continuous bands.

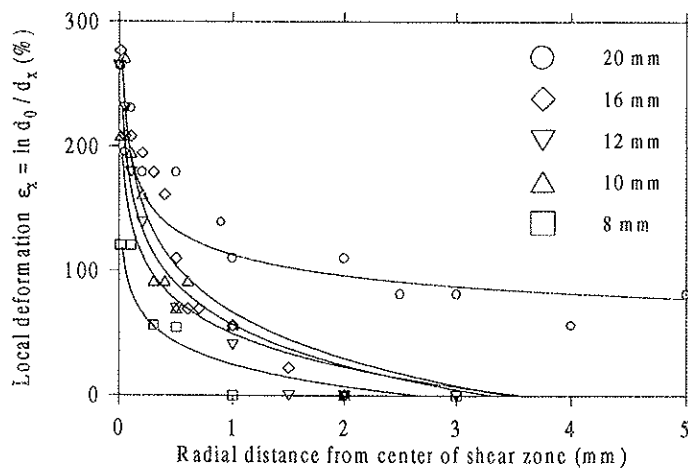


Fig. 9: Microscopic measurable deformation as a function of distance from the shear zone in plates of varying thickness penetrated at impact velocities just below the ballistic limit.

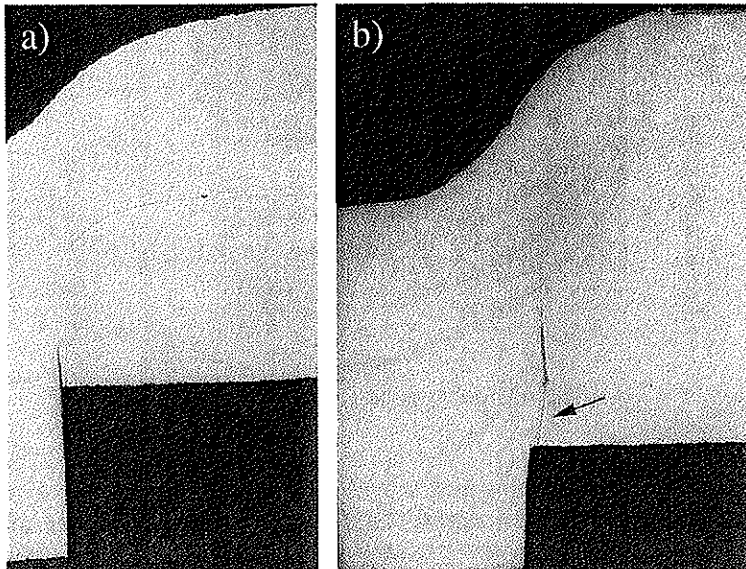


Fig. 10: a) Micrography of penetrated 16 mm thick plate and b) micrography of penetrated 20 mm thick plate. The arrow points at a transformed adiabatic shear band in the 20 mm thick plate.

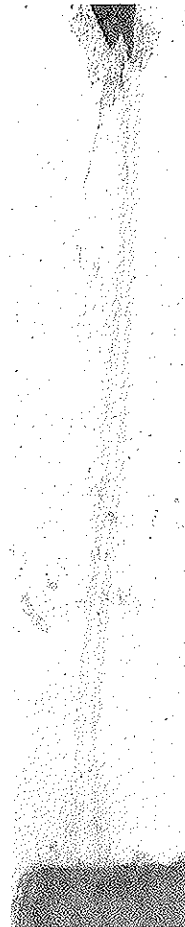


Fig. 11: Transformed adiabatic shear band in the 20 mm thick plate penetrated at an impact velocity just below the ballistic limit.

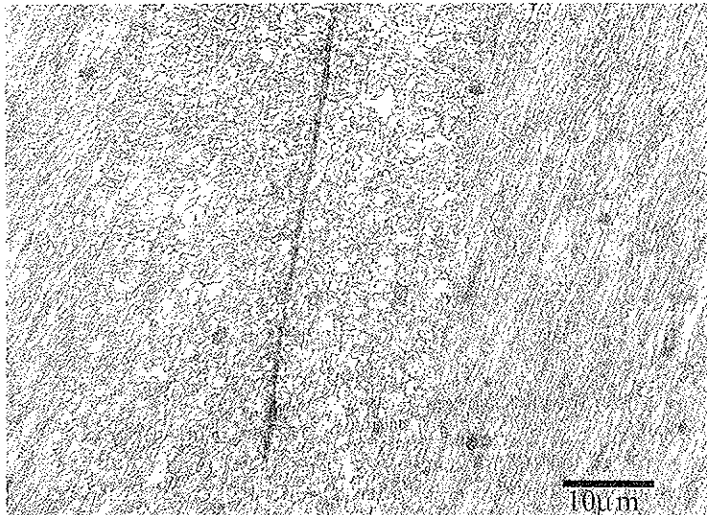


Fig. 12: A 1000x magnification of the adiabatic shear band in the 20 mm thick plate shows a new microstructure as a result of the polymorph phase-transformation in low alloy steels when the temperature crosses the A_3 transformation temperature.

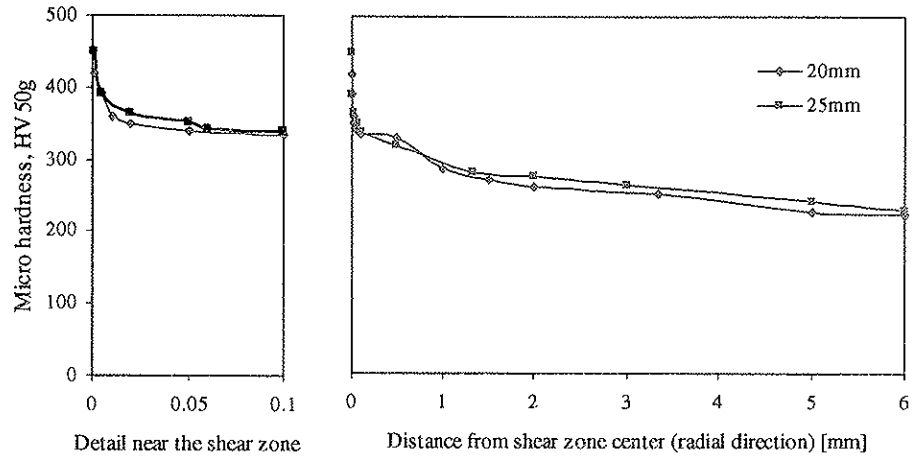


Fig. 13: Vickers hardness measurements of cross-sections show a considerable increase in hardness in the transformed shear-bands that correspond to the martensite hardness of Weldox 460 E steel, $HV_{50g} = 420$.

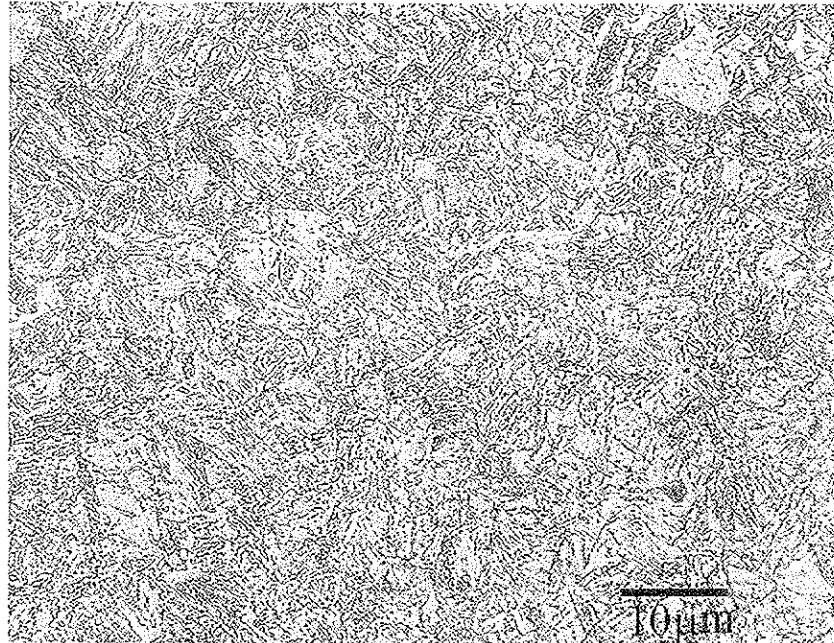


Fig. 14: Martensitic grain structure in a 2 mm thick sample of Weldox 460 E steel heat treated at 930°C and quenched in cold water. The previous austenite grain size is approximately 10 μm.

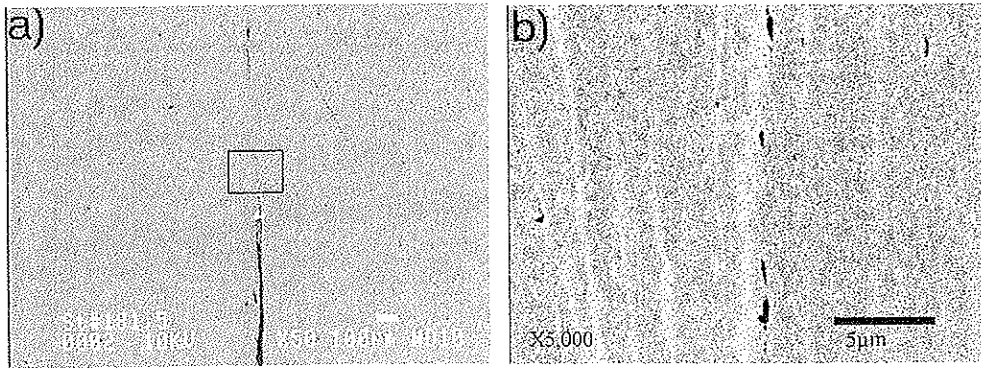


Fig. 15: a) Scanning electron micrography at 50x magnification shows the cross-section of a 12 mm plate in an area around the crack and the formation of voids in front of the crack-tip with secondary voids in a narrow area around the crack-tip. b) At 5000x magnification of the frame in a) small voids in front of the crack-tip in the 12 mm thick plate can be seen.

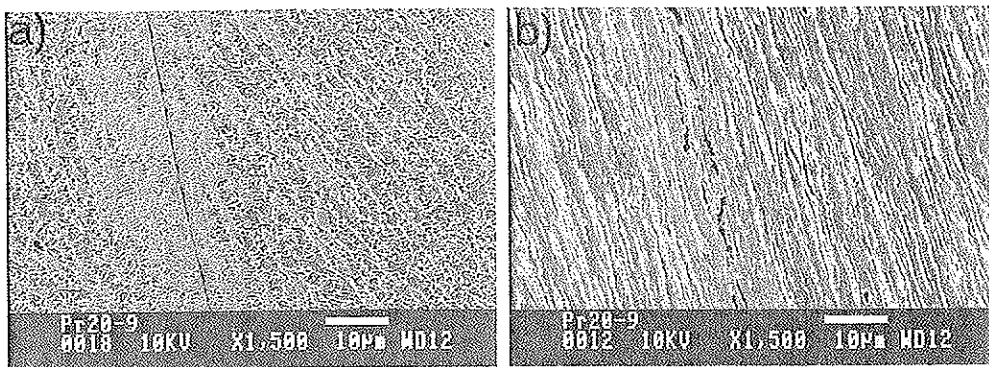


Fig. 16: a) A crack in the transferred adiabatic shear band and b) voids and secondary cracks outside the adiabatic shear band in the 20 mm thick plate.

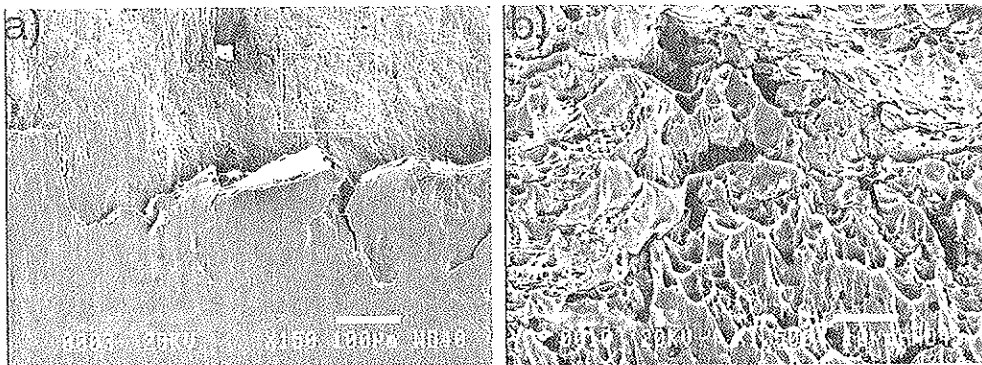


Fig. 17: a) Scanning electron micrography of the fracture surface of the 10 mm thick plate with both a ductile dimple structure and plane areas deformed by the projectile and b) details from the frame in a) of the dimple structure at 1500x magnification.

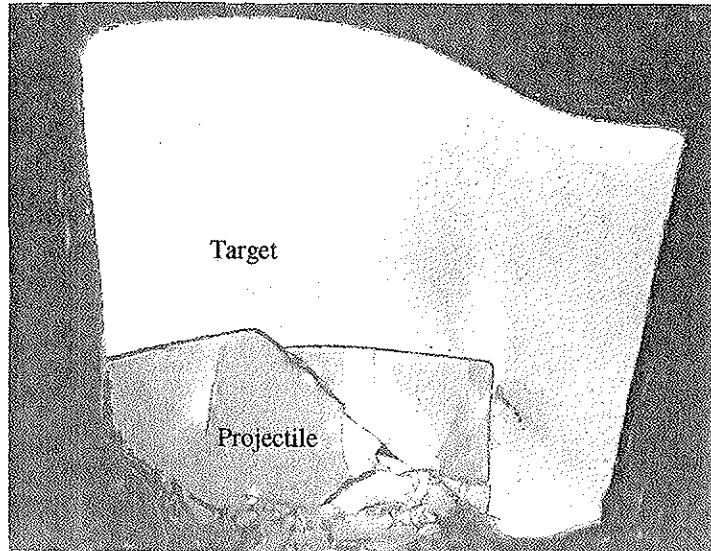


Fig. 18: Fractured projectile in a 25 mm thick target at an impact velocity of 450 m/s.

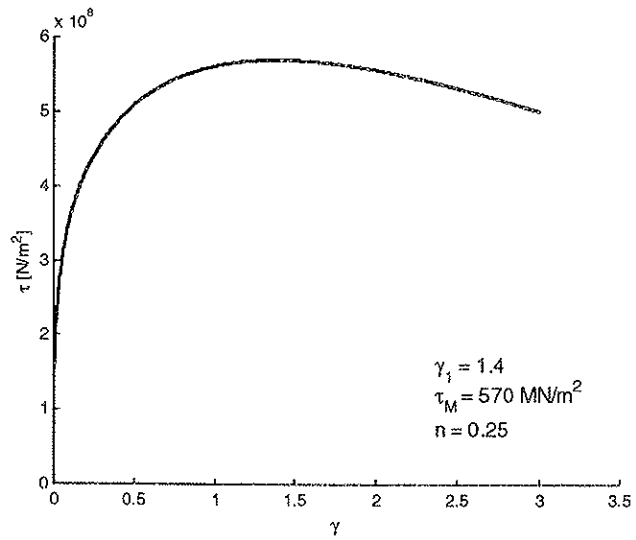


Fig. 19: Adiabatic shear stress-strain curve for Weldox 460 E from the Bai-Johnson model.

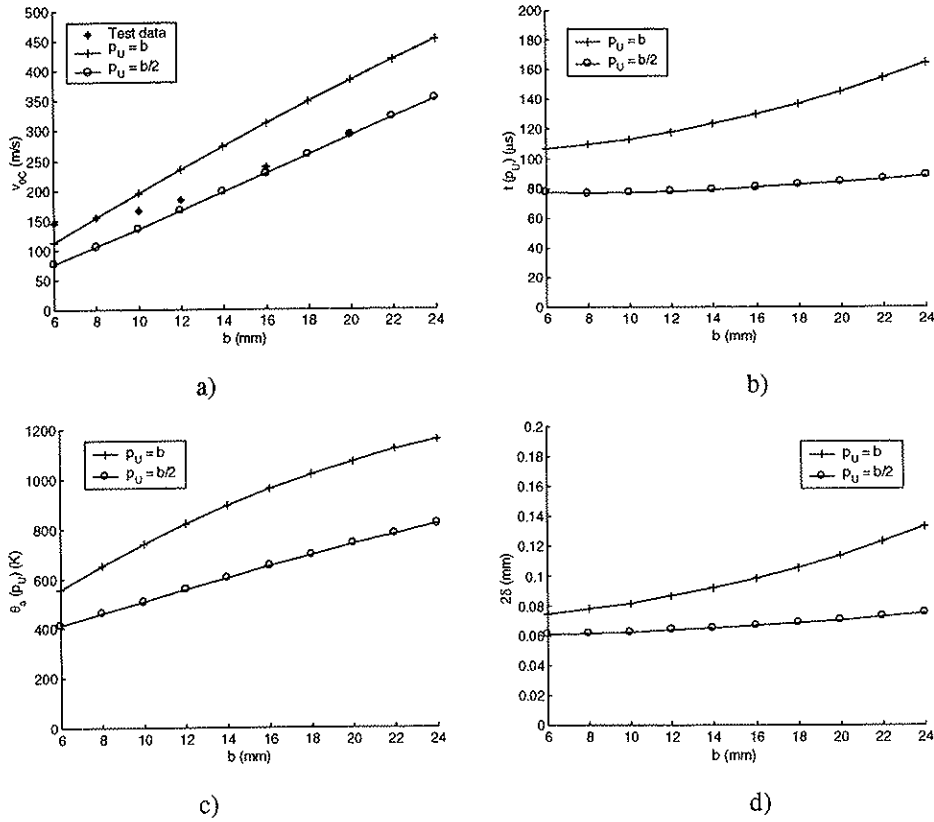


Fig. 20: Results from analytical model of (a-c) Bai and Johnson [5] and (d) Dodd and Bai [6]. The impact velocity in b) – d) is equal to the ballistic limit velocity at the actual target thickness.

Table 1: Estimated ballistic limit velocities (v_{bl}) and highest impact velocities (v_h) not giving complete perforation. The latter tests were used in the microscopic examinations.

	Target thickness (mm)						
	6	8	10	12	16	20	25-30
v_{bl} (m/s)	145.5	154.3	165.3	184.5	236.9	293.9	*
v_h (m/s)	145.3	152.5	161.2	181.5	234.3	292.5	450.2

* Perforation was not obtained in any of these tests due to projectile shattering at impact.

Part V

T. Børvik, O.S. Hopperstad, T. Berstad and M. Langseth

Numerical simulation of plugging failure in ballistic penetration.

Accepted for publication in International Journal of Solids and Structures.

Nomenclature

Unless otherwise stated in the text or references the following notation apply:

ΔD	projectile nose deformation, i.e. $\Delta D = D_f - D_i$
ΔL	projectile length reduction, i.e. $\Delta L = L_i - L_f$
CPU	computational time
d	diameter
D	projectile nose diameter
EI	number of removed elements
h	thickness or height
HRC	hardness Rockwell C
K	kinetic energy
L	projectile length
t	time
T	temperature
m	mass
v	velocity
W	work
w	deformation

Subscripts

bl	ballistic limit
c	cavity
f	final value or fracture
g	global part of target
i	initial value
l	local part of target
m	maximum value
p	projectile
pe	permanent value
pl	plug
r	residual value
t	target

1. Introduction

The finite element method has been accepted as a general computational tool within most branches of industry and is nowadays used to simulate virtually all kinds of non-linear events. Nevertheless, there are still some classes of problems that are very hard to treat numerically. According to Belytschko (1996), simulations involving material instabilities and response discontinuities are among the most difficult problems to solve. One incident that falls within this class of problems is plugging failure of metal plates impacted by blunt-nosed cylindrical projectiles in the sub-ordnance velocity regime. Here, the material in front of the projectile is rapidly accelerated at impact, giving a relative velocity within the target. This gives rise to localised deformation under adiabatic conditions in narrow zones at the well-defined periphery of the projectile. Damage due to growth of microcracks and microvoids and heat generated by plastic work develop in the shear bands. Material instability is assumed to appear if the temperature and damage softening overcome the strain and strain-rate hardening (Bai and Dodd, 1992). When the strain reaches a critical value, a discontinuous crack starts to grow towards the rear side of the target. A plug of material is finally punched out, leaving an almost circular hole in the target. The complexity of this fracture process has limited the use of both analytical and numerical solutions, and the problem has mostly been treated experimentally.

The first attempts of solving plugging failure numerically used simplified constitutive models together with erosion algorithms or element-kill techniques. Chen (1992) gave an example where such a method was used successfully, but the result depended on a user defined failure strain that is hard to determine through material tests. Bammann et al. (1993) pointed out that a plastic strain or similar is inadequate as a fracture criterion since the failure is highly dependent on many factors such as strain path, strain-rate, temperature and stress state. They found that only models in which all these phenomena were included could be used to predict failure when complex stress states were present. Nicholas and Rajendran in Zukas et al. (1990) came to a similar conclusion in their extensive review on the behaviour of materials under impact-generated high strain-rate loading conditions. Due to observations like these, Bammann presented a constitutive model based on internal state variables that described deviatoric plasticity independent of void growth. The effect of void growth was then coupled to the plastic flow using a model based on micro-mechanics. Using this model, close agreement was obtained between simulations and experimental results of plugging failure in aluminium plates impacted by hardened steel projectiles.

In the present work, a somewhat similar approach is used. Here, a computational model based on the constitutive model and fracture strain model by Johnson and Cook (1983,1985) is used to simulate plugging failure during ballistic penetration. In order to include material degradation due to damage, the constitutive model is coupled with ductile damage mechanics as proposed by Lemaitre (1992). That the Johnson-Cook model is able to describe material instability was demonstrated in a paper by Chou et al. (1991). They carried out controlled penetration experiments to produce adiabatic shear bands in steel plates. Simulations showed that shear bands could form without initial disturbances or defects if thermal softening in the material was accounted for. The calculated shear band lengths were in good agreement with those measured experimentally. A similar problem was investigated numerically by Batra and Peng (1996), showing similar results. Chou also discussed the importance of using a refined element mesh since the width of a shear band in steel typically is at the order of 10-100 μm (Bai and Dodd, 1992). In the bands, very large thermal and deformation gradients will be present. No mesh sensitivity on the general shape of the shear band was observed as long as the elements were sufficiently small, but an adaptive meshing technique was found favourable in order to maintain a fine mesh in the area where shear bands were formed. This is in accordance with Needleman (1988), who found that pathological mesh size effects do not occur in simulations if material rate dependency is accounted for. The possibility and effects of adiabatic shear localisation in dynamic punching tests of steel, aluminium and titanium were studied both experimentally and numerically by Roessig and Mason (1999). Experimentally they observed that in the titanium alloy, having a high strength and a low strain hardening, shear localised readily. In 1018 steel with moderate strength and strain hardening, some evidence of shear localisation was found at the highest loading rates. The deformation in the aluminium alloy did not localise in any of the tests carried out. In the numerical simulations, they used a maximum stress criterion and the Johnson-Cook model to determine the occurrence of shear localisation. It was found that the criterion for adiabatic shear localisation was satisfied in the simulation of the titanium alloy, giving a distinct drop in the equivalent stress and high local strains. The strain was more widely distributed in the other two materials, where the same criterion was not satisfied. Camacho and Ortiz (1997) modified the Johnson-Cook model slightly. They also used an adaptive meshing technique to avoid deformation-induced mesh distortions and contact problems during penetration. Simulations showed to be in good agreement with perforation tests of aluminium plates by conical-nosed projectiles if a pilot hole throughout the target thickness was modelled.

The computational material model used in this study does not need predefined defects in order to describe failure, and all material parameters can be identified from standard material tests (Børvik et al., 1999b). No inverse modelling or model tuning is necessary in order to obtain good agreement with experimental results of plugging failure in metal plates. Due to the model formulation, i.e. no coupling between the different physical effects, it is possible to investigate the influence on the final results by including or omitting parameters such as damage, temperature and strain-rate in the model. First in this paper, experimental data from gas-gun penetration tests on 8 mm thick Weldox 460 E steel plates impacted by blunt-nosed projectiles is given. This data will be used to validate the numerical results. Then the main content of the computational material model is given, together with model constants as obtained from material tests. Numerical simulations are carried out, and in the first set of simulations the fully coupled computational model is used. The model is then simplified by omitting the different physical effects, one by one, until a quasi-static material model with a user defined failure strain remains. The differences between the numerical results will be pointed out and discussed, and references will be made to the experimental data. Details from simulations using the fully coupled material model of viscoplasticity and ductile damage are shown to demonstrate the capability and accuracy of the model. In this paper, only fixed element meshes are used. Simulations using adaptive meshing in order to solve the penetration problem is treated in a following paper (Børvik et al., 2000).

2. Experimental set-up and test results

An experimental study on the ballistic penetration of 8 mm thick Weldox 460 E steel plates has been carried out. In the tests, a compressed gas-gun (Børvik et al., 1998a) was used to launch the sabot mounted blunt-nosed projectiles at impact velocities just below and well above the ballistic limit, i.e. the critical plugging velocity, of the target plates. The different sabot pieces were stopped in a sabot trap prior to impact. Nominal hardness (HRC 53), diameter (20 mm), length (80 mm) and mass (0.197 kg) of the cylindrical projectiles were kept constant in all tests. The targets, having a free span diameter of 500 mm, were clamped in a circular frame. Initial and final velocities were optically measured, and the ballistic limit curve of the target was constructed. In addition, a digital high-speed camera system was used to photograph the penetration event. Based on the digital images, impact angles, perforation time and projectile velocity-time curves during penetration were determined. It is referred to

Børvik et al. (1998a,b) for more details regarding the experimental set-up and measurement techniques used in the tests.

Some data from the experimental tests is given in Table 1. The difference in nominal and initial measured values was negligible. Projectile pitch and target oblique were also obtained and found to be small. From the measured initial velocities the ballistic limit of the target was estimated to 154.3 m/s, given as the average between the highest projectile velocity not giving perforation and the lowest projectile velocity giving complete perforation of the target. In test 8-7 perforation did not occur, and this test was assigned for a microscopic investigation. An image of the sectioned and etched cross section is shown in Fig. 1. Here, the projectile indentation and localised areas are clearly seen. The ballistic limit curve of the target material is given in Fig. 2a), while Fig. 2b) shows measured permanent deformation profiles as function of projectile impact velocity. The actual maximum deformation during penetration is found from the high-speed camera images to be about twice as large as the permanent one given in Fig. 2b) and Table 1. As seen, considerable global target deformation occurs close to the ballistic limit, while the deformation is much more localised at the highest impact velocities. Fig. 3 gives measured projectile distance-time curves and calculated velocity-time curves during penetration, while some of the high-speed camera images from test 8-8 and 8-13 are shown in Fig. 9. A typical projectile and plug after the test can be seen in Fig. 11.

3. Computational material model

Only the main content of the computational model of viscoplasticity and ductile damage used in the simulations is given in the following. A more detailed description can be found in Børvik et al. (1999b). The model is based on the work by Johnson and Cook (1983,1985), Camacho and Ortiz (1997) and Lemaitre (1992), and includes linear thermoelasticity, the von Mises yield criterion, the associated flow rule, isotropic strain hardening, strain-rate hardening, softening due to adiabatic heating, softening due to isotropic damage evolution and a fracture criterion. The equivalent von Mises stress σ_{eq} is given as

$$\sigma_{eq} = [1 - \beta D] [A + Br^n] [1 + \dot{\epsilon}^*]^c [1 - T^{*m}] \quad (1)$$

where D is the damage variable, and β reads 0 (no damage coupling) or 1 (damage coupling); A , B , C , n and m are material constants; r is the damage accumulated plastic strain given as $\dot{r} = (1 - \beta D)\dot{p}$, where p is the accumulated plastic strain (Lemaitre, 1992); $\dot{r}^* = \dot{r}/\dot{r}_0$ is a dimensionless strain-rate, and \dot{r}_0 is a reference strain-rate; $T^* = (T - T_0)/(T_m - T_0)$ is the homologous temperature, where T is the actual temperature, T_0 is the room temperature and T_m is the melting temperature of the target material, respectively. The damage variable takes values between 0 (undamaged) and 1 (fully broken). However, the critical value of damage is found to be less than 1. Hence, fracture occurs when

$$D = D_c \leq 1 \quad (2)$$

A damage evolution rule is proposed as

$$\dot{D} = \begin{cases} 0 & \text{when } p < p_d \\ \frac{D_c}{p_f - p_d} \dot{p} & \text{when } p \geq p_d \end{cases} \quad (3)$$

where D_c is the critical damage, \dot{p} is the plastic strain-rate, p_d is the damage threshold and p_f is a fracture strain depending on stress triaxiality, strain-rate and temperature given as

$$p_f = [D_1 + D_2 \exp(D_3 \sigma^*)] [1 + \dot{p}^*]^{D_4} [1 + D_5 T^*] \quad (4)$$

where D_1 to D_5 are material constants, $\sigma^* = \sigma_m/\sigma_{eq}$ is the stress triaxiality ratio and σ_m is the mean stress. The first bracket in Eq. (1) describes material degradation due to damage. The irreversible damage evolution is related to the accumulated plastic strain through Eq. (3). In the implementation, a constant β is connected to the damage variable. When β equals 1, damage is coupled to the constitutive equation. Otherwise, if β equals 0 there is no coupling with damage. The second bracket in Eq. (1) gives the strain hardening, while the effect of strain-rate hardening based on the work by Camacho and Ortiz (1997) is described in the third bracket. The last bracket in Eq. (1) gives the effect of temperature softening on the equivalent stress. The temperature increase is based on the empirical assumption that 90 % of the plastic work under adiabatic conditions is dissipated as heat (Bammann et al., 1993). Any heat transfer with the surroundings is neglected in the model. When softening due to damage and

temperature exceeds the strain and strain-rate hardening, localisation is assumed to occur (Bai and Dodd, 1992). The model is implemented in LS-DYNA (1999) using a fully vectorized backward-Euler integration algorithm (Berstad et al., 1994). To allow crack growth during penetration, the model is coupled with an element-kill algorithm available in LS-DYNA that removes the damaged element from the mesh when the damage variable reaches its critical value D_C .

Four types of tensile tests are required to identify the material constants used in the model (Børvik et al., 1999b). Quasi-static tensile tests are used to identify the elastic constants E and ν , and the yield stress A of the material. Notched-specimen tensile tests define the strain hardening constants B and n , the critical damage D_C , and the fracture strain constants D_1 , D_2 and D_3 . Dynamic tensile tests give the viscoplastic constant C and the fracture strain constant D_4 . Tensile tests at elevated temperatures provide the constants m , K and D_5 , defining the temperature effect on the stress-strain curve, elastic modulus and fracture strain, respectively. Quasi-static tensile tests are also carried out in order to identify the material constants for the projectile. Details regarding the material tests and calibration procedure can be found in Børvik et al. (1999b). Here, the model constants used for the target material and projectile are listed in Table 2 and Table 3, respectively.

4. Numerical simulations

4.1 Numerical models

One major scope of the present work was to investigate the importance of the material model in finite element simulations of plugging failure in structural impact. This was found necessary since it is generally assumed that the details in the material relationship are crucial in the problem, especially at impact velocities close to the ballistic limit of the target material (Harding, 1989). Only the material model of the target plate was varied in the simulations, and unless otherwise stated in the text the material input was as given in Table 2 and Table 3 (Børvik et al., 1999b). In order to have reliable results, the numerical simulations were validated against the experimental data given in Table 1. As demonstrated in Fig. 1 and Fig. 2b), the 8 mm thick target plates showed a distinct combination of global deformation and localised shearing. This, together with the demand of a model for material failure as well as

numerical methods for contact, fracture and crack propagation in the element grid, makes this type of simulations rather complex.

The Johnson-Cook formulation has been somewhat criticised in the literature due to its empirical origin and non-coupling between physical effects, in contrast to e.g. the Zerilli-Armstrong (1987) model. However, in practical applications it has many benefits. Due to its simple form it is straightforward both to calibrate and implement the model. Also, the non-coupling between the different physical effects allows the user to add or omit complexity in the simulations using the same material model. In this study, 8 different versions of the material model given by Eqs. (1)–(4) were used. These are presented in Table 4, where “ x ” indicates that the effect is included in the simulation. Note that the model constants B , n and D_c in Table 2 were determined simultaneously from notched specimen tensile tests (Børvik et al., 1999b). If softening due to damage is neglected in the computational model ($\beta=0$), the hardening coefficients B and n becomes 561 MPa and 0.65, respectively, determined from smooth specimen tensile tests. Here, no Bridgman correction to the average axial stress to compensate for the introduction of transversal stresses in the necked region was carried out. A possible method to correct for the triaxial stresses in the neck of a smooth specimen has been given by Le Roy et al. (1981). If this approach is used, B and n becomes 383 MPa and 0.45, respectively.

In Table 4, M1 represents a fully coupled damage model, while M6 describes a simple quasi-static material behaviour with an assumed constant failure strain of 0.8. The other models describe a material behaviour in between these two extremes. The failure strain in M6 is adopted from a paper by Wen and Jones (1996), while the failure strain of 1.6 used in M5 and M7 is close to the true strain at fracture measured in a smooth quasi-static tensile test (Børvik et al., 1999b). M8 is identical to M1, except that M8 includes thermoelasticity. This involves an extra term in the deformation rate tensor, and a linear reduction in elastic stiffness with temperature (Børvik et al., 1999b). Calculated true stress-strain curves for the target using the material input in Table 2 and 4 are shown in Fig. 4. Here, $\dot{\sigma}^*$ is assumed constant and equal to $1/3$ (i.e. smooth specimen), while \dot{p} is constant and equal to 1000 s^{-1} (assumed adiabatic conditions). The differences between the different material models used are as seen found to be considerable.

Earlier simulations have indicated the problem to be mesh size sensitive due to the localisation of deformation (Hopperstad et al., 1998). This effect was however not found pathological since the result converged monotonically towards a limit solution when the

element size was sufficiently reduced (Børvik et al., 1999b). The mesh dependence is in fact expected since the width of the localised shear zone obtained experimentally is much smaller than the element size normally used (see e.g. Fig. 1). In order to check the mesh sensitivity, two different mesh densities were applied in the simulations. The element size in the coarse mesh was $0.5 \times 0.4 \text{ mm}^2$ in the impact region, giving 20 elements over the target thickness. In the refined mesh the smallest elements were $0.125 \times 0.1 \text{ mm}^2$, giving 80 elements over the target thickness. The meshes were somewhat refined towards the centre, but no adaptive remeshing technique has been applied in this study. Therefore, the axisymmetric finite element meshes used in the LS-DYNA (1999) simulations consisted of either 3120 or 20560 4-node 2-D elements with one integration point. The target was modelled using the material model defined by Eqs. (1)-(4) and the material input in Table 2 and 4, while the projectile of hardened tool steel was modelled as elastoplastic with the material constants in Table 3. In the simulations, the plate was fully clamped at the support, while the projectile was given an initial velocity. Contact between the projectile and target was modelled using an automatic 2-D penalty formulation without friction. Frictional effects are assumed of minor importance in this particular problem (Zukas, 1990). Owing to the CPU requirement, the analyses were stopped before the elastic rebound of the target plate was completed. Hence, the final target deformation as given in Fig. 2b) was not obtained. All simulations were carried out on a HP C360 workstation.

4.2 Coarse element mesh

Projectile residual velocities using the coarse element mesh are compared with the experimental data in Fig. 5a), while numerical details from these simulations can be found in Børvik et al. (1999c). The ballistic limits obtained using the different models are given in Table 5. These values and the solid lines through the data points in Fig. 5 were estimated based on an analytical model proposed by Recht and Ipson (1963)

$$v_r = a(v_i^p - v_{bl}^p)^{1/p} \quad (5)$$

The method of least squares was used to fit the model constants a , p and v_{bl} to the simulated residual projectile velocities (see Table 5). This approach has earlier given accurate results (Børvik et al., 1999a). As seen, none of the models were able to predict the experimentally

obtained ballistic limit within 30 %. However, at impact velocities well above the ballistic limit, all models showed reasonable agreement with the experiment results. Thus, the difference between the computational models seems to increase as the impact velocity approaches the experimentally obtained ballistic limit. Keep in mind that the ballistic limit velocity is the parameter searched for in practical application. Strain-rate and temperature were both found to be important parameters. If not included in the model as in M3, M4 and M6, considerable errors appeared. A constant failure strain was also found to be a poor choice for a failure criterion when the details in the simulations were considered. However, the estimated ballistic limits for M5 and M7 were found to be in relatively close agreement with M1 and M2, where the effect of triaxiality on the failure strain was included. M5, which is a simple quasi-static model with a constant failure strain of 1.6, showed a surprisingly close agreement with M2, which can be considered as the original Johnson-Cook fracture model (1985). This accordance is assumed to be a coincidence. The difference between M1 and M8, i.e. the effect of including thermoelasticity in the simulations, was found to be small in all simulations. Thus, the effect of thermoelasticity in the material model is assumed negligible in this velocity regime.

Due to the findings described above, only M1, M2 and M7 were considered in any detail. The coupled computational model of viscoplasticity and ductile damage (M1) showed the closest agreement with the experimental results, but the difference in ballistic limit between M1, M2 and M7 was not significant (see Table 5). However, when the details in the numerical simulations were compared, important and distinct differences were obtained. The details revealed that M1 gave the highest local temperature, the smallest global deformation and a more confined plastic strain distribution, indicating a better description of the localisation. It also gave the lowest perforation time, which made M1 more efficient regarding CPU time than both M2 and M7. Based on the numerical data, a rough energy balance was established. This was possible since the target material was modelled as one local and one global part with identical properties. The border between the two parts was placed 0.5 mm outside the projectile boundary (see Fig. 6). The amount of energy absorbed by the different parts at the computational termination time using the coarse element mesh is shown in Fig. 7a). Close to the ballistic limit, 60 % of the energy was absorbed in the global part, 30 % in the local part and 10 % in projectile deformation. At the highest impact velocities, approximately 45 % of the energy was absorbed globally, 30 % locally and 25 % by the projectile. The target absorbed less energy at all velocities using M1. It was also found that 4-5 % of the total energy was lost in the simulations, mainly due to internal energy in removed elements.

However, in the latest version of LS-DYNA the internal energy of removed elements and the kinetic energy of eroded nodes are stored and may therefore be included in the total energy balance. The effect of energy and mass losses in simulations using an element erosion technique was studied in detail by Børvik et al. (2000). It was found that conservation of both energy and mass was fulfilled if the number of eroded elements and nodes were moderate.

4.3 Fine element mesh

Residual velocities of the projectile using the fine element mesh are compared with the experimental data in Fig. 5b), while numerical details from some of the runs can be found in Table 6. Two major differences arise compared with simulations using the coarse element mesh. First, the computational time is dramatically increased. The critical time step in LS-DYNA (1999) for quadrilateral elements is given as

$$\Delta t_c = \alpha \frac{L_s}{c_c} = \alpha \frac{A_s}{\max(L_i)} \sqrt{\frac{\rho(1+\nu)(1-2\nu)}{E(1-\nu)}} \quad (6)$$

where L_s is a characteristic length, A_s is the elements area, L_i ($i = 1, 2, 3, 4$) is the length of the sides defining the element, c_c is the elastic wave speed in the material and α is a factor used to scale the critical time step for stability reasons in highly non-linear problems. During updating, the code determines the next time step by looping through all elements to determine the minimum value. This indicates that dividing all element sides by a factor 4 increases the computational time by a theoretical factor of $4^3 = 64$. However, since the elements are distorted during straining, this factor varies. The time steps for Run 230-20-M1 and Run 175-80-M1 are shown in Fig. 8. As seen, each time an element is removed from the mesh the time step is somewhat increased. Camacho and Ortiz (1997) discussed the use of eroding elements as opposed to adaptive remeshing. They concluded that both methods eliminate troublesome elements, but adaptive remeshing has the benefit of avoiding deformation-induced mesh disturbances, thus preventing the degradation of the time step required for stability. Similar results were obtained in a study using adaptive meshing by Børvik et al. (2000). Here, due to the steep gradients present in the problem it was found reasonable to scale the critical time step in order to increase the accuracy. Hence, the time steps in Fig. 8 are much smaller than the critical time step given by Eq. (6).

The second effect is that a refined mesh will give a much better description of the localised behaviour. As shown in Fig. 5b), this significantly improved the numerical results. Using the refined mesh, excellent agreement was obtained between the fully coupled damage model (M1) and the experimental data. The difference in ballistic limit was only 2 % (see Table 5), and the ballistic limit curve of the target material was precisely determined. Also the results from the other models were improved. However, except for M5, which again showed a surprisingly close agreement with the experimental data, none of the other models were able to describe the experimentally obtained ballistic limit within 12 %. For M3, M4 and M6 the deviation was more than 25 %. As for the coarse element mesh, all models showed good agreement with the experimental data at the highest impact velocities. This illustrates the incorrectness of validating numerical simulations of plugging failure using experimental data at velocities well above the ballistic limit. When the details from the simulations in Table 6 were considered, similar observations as for the coarse mesh were obtained regarding local temperature, global target deformation, strain distribution, projectile perforation time and model efficiency. Again, M1 showed a better description of the perforation process than the other models.

The energy absorbed during penetration using the fine element mesh and model M1, M2 and M7 are shown in Fig. 7b), and the behaviour was found somewhat different compared to the results using the coarse element mesh. At the highest impact velocities, about 42 % of the energy was absorbed locally, 28 % globally and 30 % by the projectile using M1. As the impact velocity was reduced, more and more energy was absorbed in global target deformation, and at some point more energy was absorbed globally than locally. This distinct increase in global target deformation is as observed experimentally (see e.g. Fig. 2b)). Close to the ballistic limit, approximately 55 % of the energy was absorbed globally, 38 % locally and 7 % in projectile plastic deformation. About 1-3 % of the energy was lost mainly due to removed elements (see Børvik et al., 2000). The energy absorbed by the projectile was found similar for both element meshes and all models, indicating that projectile deformation takes place early in the penetration process and is thus less sensitive to the target material model. However, while the plastic work carried out in the projectile at the lowest impact velocities seems reasonable, the amount of energy absorbed at the highest velocities seems high according to the literature. This is partly based on an analytical model by Johnson (1972) used to calculate the amount of energy necessary to plastically deform a linear strain hardening material from a cylinder into a frustum. Using the material input in Table 1 and 3, the model indicates that less than 20 % of the energy is used in projectile deformation. The reason for

the discrepancy may be due to a too coarse element mesh in the projectile (see Fig. 16a)), the omission of possible frictional effects between the projectile nose and target surface in the contact algorithm, or inaccuracies in the material data, material model or the numerical simulations itself.

In order to check the first two assumptions, some more simulations at the highest impact velocities were carried out. At first, a refined element mesh was used in the nose part of the projectile. A plot showing the deformed mesh 5 μ s after impact in Run 298-80-M1 is given in Fig. 12. Such sudden refinements of the element mesh should be carried out with caution since reflections of stress waves may take place at the transition zone. However, the refined mesh did not affect the energy absorption in the different parts to any extent. Then, friction was added in the contact. According to Ravid and Bodner (1983), a frictional coefficient of 0.10 is usually given in the literature for dynamic metal working operations. This value was adopted in the simulations, even if a lower value was recommended in impact situations due to higher velocities and temperatures. Nor this attempt gave any change in the energy distribution. The plastic deformation of the projectile was also compared with the experimental observations. It was found that the change in projectile nose diameter (ΔD) was 0.7 mm and that the change in projectile length (ΔL) was 0.55 mm. These values are close to the measured values given in Table 1 for test 8-13. Thus, the energy absorbed by the projectile in the simulations seems to be reasonable. Of equal importance, the exercise reveals that projectile plastic deformation is an important parameter during structural impact, and can not be neglected in calculations.

4.4 Details from simulations

As shown, the element size is a vital parameter in numerical simulations involving localisation. Also, the fully coupled damage model (M1) was found superior to the other models in all simulations, even if the differences in ballistic limit velocity were not as distinct as first assumed. In order to demonstrate the features of the model, some details from simulations using M1 and the refined element mesh will be given in the following. Fig. 9 shows high-speed camera images from test 8-13 ($v_i = 298$ m/s) and test 8-8 ($v_i = 173.7$ m/s) compared with numerical results at identical times. The plots are shown as fringes of effective plastic strain, where "red" indicates a plastic strain above 30 %. Not only are the residual velocity of the projectile and plug correctly predicted, but also the overall physical behaviour of the structure seems to be well described. This is further illustrated in Fig. 10, where the

measured projectile velocity-time curves in Fig. 3 are compared with the numerical results. Again, excellent agreement is obtained between the experimental and numerical data. The final shape of the projectile and plug from test 8-8 are compared with the projectile and plug from Run 175-80-M1 in Fig. 11.

Details of the crack propagation and failure during perforation from Run 298-80-M1 is plotted as fringes of accumulated plastic strain in Fig. 13, while the number of failed elements as function of computational time for Run 298-80-M1 and Run 175-80-M1 are shown in Fig. 14. After the first indentation of the projectile, the critical damage is rapidly reached and a crack starts to grow. The crack propagates in front of the projectile towards the rear side of the target, and a plug is formed. If the plots in Fig. 13 are compared with metallurgical images of penetrated plates given in Børvik et al. (1999a), the behaviour is found very similar. As seen in Fig. 14, the number of failed elements is increased towards perforation. Close to fracture severe stretching appears in the localised zone. Since the failure strain is much more sensitive to tensile stresses than compression or shear (Børvik et al., 1999b), the fracture process is accelerated and a second crack starts to propagate from the rear side. When the two cracks meet, complete perforation appears and the plug is just pushed out of the cavity. This observation supports the general experimental assumption that the residual projectile velocity never is small, but a significant percentage of the initial velocity (Awerbuch and Bodner, 1974). Fig. 15a) shows the difference in fracture patterns just above the ballistic limit using M1, M2 and M7, while Fig. 15b) shows the fracture pattern from Run 175-80-M1. At the highest impact velocities, most fracture patterns are similar to the one given in Fig. 15c) from Run 298-80-M1, indicating grossly shear during perforation.

Fig. 16 shows details of the deformed element mesh and the distribution of equivalent von Mises stress, damage, stress triaxiality ratio, temperature and damaged plastic strain-rate in the target 63 μ s after impact in Run 175-80-M1. These plots clearly illustrate that the deformation mainly develops in a narrow and almost vertical zone in the target. Outside the localised area, only small deformations are observed. Some details should be noticed. Due to bending, contact is occasionally reduced between the projectile and plug surface (see Fig. 16a)). As a result, the interface force between the projectile and target is concentrated into a much smaller area near the sharp edge of the projectile. It should also be noticed that the material in front of the crack tip is severely damaged (Fig. 16c)) and heated (Fig. 16e)), causing a degradation of the material strength that facilitates fracture in that area. As indicated in Fig. 16f), this is also the only area where the strain-rate is still high. The maximum damaged plastic strain-rate in the localised zone is found as high as $6 \cdot 10^5 \text{ s}^{-1}$. Finally, Fig.

16d) shows the hydrostatic stress state in the target at this stage, indicating hydrostatic tension at the rear side of the target and in the localised shear zone, while the front is under severe hydrostatic compression. The stress state is found to change continuously during perforation, which again highly affects the fracture process.

The observations from Run 175-80-M1 are further outlined in Fig. 17, where the history variables included in the computational model are plotted for some of the elements. The position of the different elements in the mesh is shown in Fig. 6. All elements except element # 16400 failed during impact. As seen, the behaviour of the elements is rather different and changes continuously depending on their location in the target. Roessig and Mason (1999) discussed the occurrence of adiabatic shear bands in punch test simulations. They concluded that even if some contradictions exist in the literature, a maximum stress criterion could be used as an indicator of whether adiabatic shear bands really occur or not. Roessig and Mason also showed that such a criterion is only valid if the change in strain and strain-rate with time is greater than or equal to zero, i.e. that the strain is a monotonically increasing function of time. Fig. 18a) shows the effect on the equivalent stress in element # 19000 for each of the four different terms in Eq. (1). This element is located inside the proposed shear band. As seen, the strain hardening grows monotonically all the way to failure, while the strain-rate hardening gives a constant and positive contribution to the equivalent stress. On the other side, the effect of material softening due to damage and temperature are found to be of equal importance and size. The effect of softening is moderate at first, but increases when the strain becomes large. When the effect of softening exceeds the effect of hardening, the equivalent stress starts to drop. This appears about 16 μs after impact. Since all criteria are satisfied, and all plots indicate a change in behaviour at this point, a true adiabatic shear localisation is assumed in the element. After localisation, the element is rapidly taken to failure.

Element # 16400, which is located just outside the assumed shear band, shows a rather different behaviour. This is indicated in Fig. 18b). At first, the behaviour is similar to the one observed in element # 19000. After about 30 μs , a maximum is obtained in the stress-time curve, and the stress starts to drop. Simultaneously the effect of strain-rate decreases and approaches zero, while the accumulation of strain, damage and temperature stops. Thus, the drop in stress is not due to localisation, but is caused by unloading due to a loss in contact between the projectile and target. About 10 μs later contact is re-established and the history variables continue to grow toward a second maximum in the stress-time curve. Neither this point is due to localisation. Since the elements inside the proposed shear band now is

localising, the area just outside the shear band is unloading. This can be seen since the strain-rate starts to decrease monotonically after about 45 μs , and that no more plastic strain is accumulated in the element. Since the accumulation of damage stops before the critical damage is reached, the element is not removed. All failed elements in this simulation are shown in the fracture pattern given in Fig. 15b).

As just indicated the drop in equivalent stress observed in several of the elements after about 30 μs is not caused by localisation, but is due to unloading. At impact, the material in the plug is accelerated to a higher velocity than that of the projectile. Thus, contact between the projectile and plug is gradually lost and unloading occurs. However, due to restraining of the shear zone, the plug is prevented from leaving the target. The projectile catches up with the plug and full contact is re-established. This loss of contact during impact is seen both experimentally and numerically in the velocity-time plot in Fig. 10, and from the interface force-time plot in Fig. 19a). As also shown in Fig. 19b), this complete loss of contact is not seen in Run 298-80-M1. Several such impacts may take place during penetration. Close to or at perforation, this becomes an impact between two free bodies. This is believed responsible for the obtained difference in residual velocity between the projectile and plug.

5. Concluding remarks

A coupled computational material model of viscoplasticity and ductile damage for projectile penetration has been developed and implemented in LS-DYNA (1999). In the present study, 8 different complexity levels of the material model have been used in numerical simulations of plugging failure during ballistic penetration in order to investigate the importance of the constitutive relationship in the problem. The numerical results have been compared with observations from gas-gun experiments where blunt-nosed projectiles were launched against 8 mm thick Weldox 460 E steel plates. From the study, the following main conclusions can be drawn:

- The element size is found to be a vital parameter in numerical simulations involving adiabatic shear localisation. Since the width of the experimentally obtained shear zone is much smaller than the element size normally used, this is as expected. When a coarse element mesh was used, none of the models were able to predict the experimentally

obtained ballistic limit within 30 %. However, when the mesh was sufficiently refined the agreement was significantly improved.

- All models showed reasonable agreement with the experimental observations at impact velocities well above the ballistic limit. However, as the impact velocity approached the ballistic limit, the difference between the models was increased.
- Strain-rate, temperature and stress-state were all found to be important parameters. If not included in the model, considerable errors could appear. Also, a constant failure strain was found to be a poor choice for a failure criterion.
- The fully coupled computational model of viscoplasticity and ductile damage showed the best agreement with the experimental results in all simulations, but the difference in ballistic limit between M1, M2 and M7 was not significant. However, when details from the numerical simulations were compared, important and distinct differences were obtained.
- Examples from simulations using M1 showed that details like energy absorption, crack propagation, fracture patterns, strain localisation and overall physical behaviour were well predicted by the model.
- The detailed insight into the behaviour of penetrated steel plates obtained using the computational model of viscoplasticity and ductile damage is hard, if possible at all, to get from experimental tests or analytical calculations. Thus, numerical simulations using a verified and validated material model seem to be an essential tool in order to increase the physical understanding of the different processes in structural impact.
- Finally, an important issue in numerical simulations of structural impact that has not been discussed in this paper is related to contact algorithms and adaptive meshing. Even if the methods used in this study seems to work satisfactory in plugging failure, this may not be the case in e.g. ductile hole enlargement using conical projectiles. Here, adaptive meshing may become necessary. However, adaptivity introduces new challenges and variables not present when a fixed element mesh is used.

Acknowledgements

The authors would like to acknowledge the Norwegian Defence Construction Service, Central Staff/Technical Division, Oslo, Norway, for their support of this work.

References

- Awerbuch, J. and Bodner, S.R., 1974. Experimental Investigation of Normal Perforation of Projectiles in Metallic Plates, *Int. J. Solids Structures* 10, pp. 685-699.
- Bai, Y. and Dodd, B., 1992. *Adiabatic Shear Localisation*, Pergamon Press.
- Bammann, D.J., Chiesa, M.L., Horstemeyer, M.F. and Weingarten, L.I., 1993. Failure in Ductile Materials using Finite Element Simulations, In *Structural Crashworthiness and Failure*, edited by N. Jones and T. Wierzbicki, Elsevier Applied Science, pp. 1-54.
- Batra, R.C. and Peng, Z., 1996. Development of Shear Bands during the Perforation of a Steel Plate, *Computational Mechanics* 17, pp. 326-334.
- Belytschko, T., 1996. On Difficulty Levels in Non Linear Finite Element Analysis of Solids, *Bulletin Int. Assoc. Comp. Mech.* 2, pp. 6-8.
- Berstad, T., Hopperstad, O.S. and Langseth, M., 1994. Elasto-Viscoplastic Constitutive Models in the Explicit Finite Element Code LS-DYNA3D, *Proceedings of the 2nd Int. LS-DYNA3D Conference*, San Francisco, 20-21 September.
- Børvik, T., Holen, K., Langseth, M. and Malo, K.A., 1998a. An Experimental set-up used in Ballistic Penetration, *Proceedings of Fifth International Symposium on Structures under Shock and Impact*, pp. 683 - 692, Thessaloniki, Greece, 24-26 June.
- Børvik, T., Langseth, M., Hopperstad, O.S. and Malo, K.A., 1998b. Penetration of Steel Plates - I. Experimental Study, *Proceedings of Third International Symposium on Impact Engineering*, Oxford University Press, Singapore, 7-9 December.
- Børvik, T., Langseth, M., Hopperstad, O.S. and Malo, K.A., 1999a. Ballistic Penetration of Steel Plates, *Int. J. Impact Engng.* 22 (9-10), pp. 855-887.
- Børvik, T., Hopperstad, O.S., Berstad, T. and Langseth, M., 1999b. Computational Model of Viscoplasticity and Ductile Damage for Projectile Impact, submitted for publication.
- Børvik, T., Hopperstad, O.S., Berstad, T., Malo, K.A. and Langseth, M., 1999c. Numerical Simulation of Plugging Failure in Ballistic Penetration using LS-DYNA, *Proceedings of Second European LS-DYNA User Conference*, Gothenburg, Sweden, 14-15 June.
- Børvik, T., Hopperstad, O.S., Berstad, T., Langseth, M., 2000. Effect of Projectile Nose Shape in Structural Impact, Part II: Numerical Simulations, submitted for publication.
- Camacho, G.T. and Ortiz, M., 1997. Adaptive Lagrangian Modelling of Ballistic Penetration of Metallic Targets, *Comp. Meth. Appl. Mech. Engng.* 142, pp. 269-301.
- Chen, E.P., 1992. Numerical Simulation of Shear Induced Plugging in HY100 Steel Plates, *Int. J. Damage Mech.* 1, pp. 132-143.
- Chou, P.C., Hashemi, J., Chou, A. and Rogers, H.C., 1991. Experimentation and Finite Element Simulation of Adiabatic Shear Bands in Controlled Penetration Impact, *Int. J. Impact Engng.* 11, pp. 305-321.
- Harding, J., 1989. The Development of Constitutive Relationships for Material Behaviour at High Rates of Strain, *Int. Conf. Mech. Prop. Materials at High Rates of Strain*, Oxford.

- Hopperstad, O.S., Børvik, T., Berstad, T., Aas-Jakobsen, K. and Langseth, M., 1998. Penetration of Steel Plates - II. Numerical Simulations, Proceedings of Third International Symposium on Impact Engineering, Singapore, 7-9 December.
- Johnson, G.R. and Cook, W.H., 1983. A Constitutive Model and Data for Metals Subjected to Large Strains, High Strain Rates and High Temperatures, 7th Int. Symp. Ballistics, The Hague, The Netherlands, pp. 541-547.
- Johnson, G.R. and Cook, W.H., 1985. Fracture Characteristics of Three Metals Subjected to Various Strains, Strain Rates and Temperatures, Engng. Fracture Mechanics 21, pp. 31-48.
- Johnson, W., 1972. Impact Strength of Materials, Edward Arnold Ltd.
- Le Roy, G., Embury, J.D., Edward, G. and Ashby, M.F., 1981. A Model of Ductile Fracture based on the Nucleation and Growth of Voids, Acta Metallurgica 29, pp. 1509-1522.
- Lemaitre, J., 1992. A Course on Damage Mechanics, Springer-Verlag.
- LS-DYNA, 1999. LS-DYNA User's Manual, Version 950.
- Needleman, A., 1988. Material Rate Dependence and Mesh Sensitivity in Localisation Problems, Comp. Meth. Appl. Mech. Engng. 67, pp. 69-85.
- Ravid, M. and Bodner, S.R., 1983. Dynamic Perforation of Viscoplastic Plates by Rigid Projectiles, Int. J. Impact Engng. 21 (6), pp. 577-591.
- Recht, R.F. and Ipson, 1963. T.W., Ballistic Perforation Dynamics, Int. J. Applied Mech. 30 (Trans. ASME), pp. 384-390.
- Roessig, K.M. and Mason, J.J., 1999. Adiabatic Shear Localisation in the Dynamic Punch Test, Part II: Numerical Simulations, Int. J. Plasticity 15, pp. 263-283.
- Wen, H.-M. and Jones, N., 1996. Low-Velocity Perforation of Punch-Impact-Loaded Metal Plates, Trans. ASME, J. Press. Vessel Technol. 118, pp. 181-187.
- Zerilli, F.J. and Armstrong, R.W., 1987. Dislocation-Mechanics-Based Constitutive Relations for Material Dynamic Calculations, J. Appl. Phys. 65 (5), pp. 1816-1825.
- Zukas, J.A. (ed.), 1990. High Velocity Impact Dynamics, John Wiley & Sons.

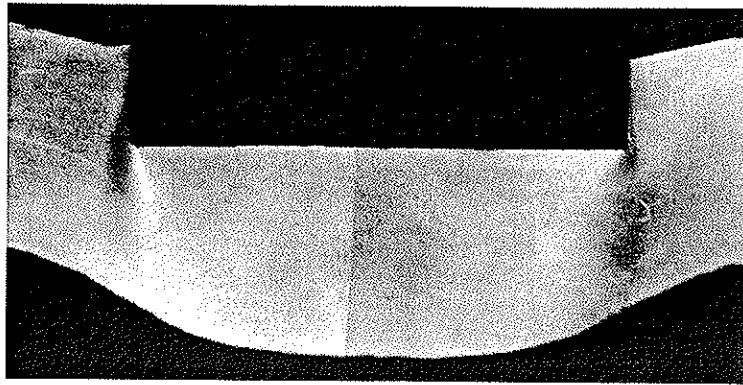


Fig. 1: Macrograph of test 8-7 showing projectile indentation and localisation.

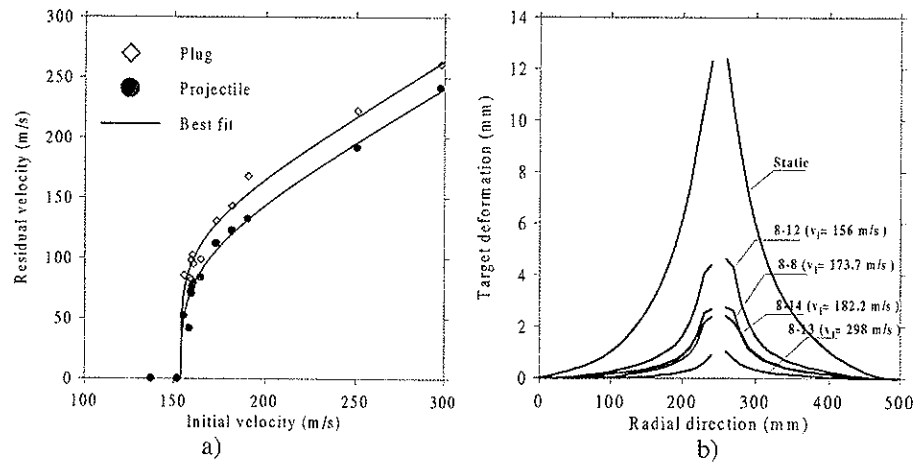


Fig. 2: a) Ballistic limit curves and b) measured permanent deformation profiles.

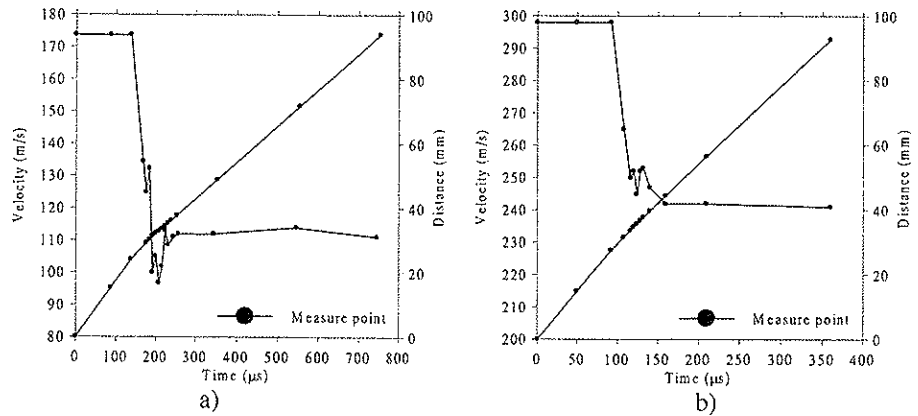


Fig. 3: Measured projectile distance-time curve and calculated velocity-time curve from test a) 8-8 and b) 8-13 based on the high-speed camera images.

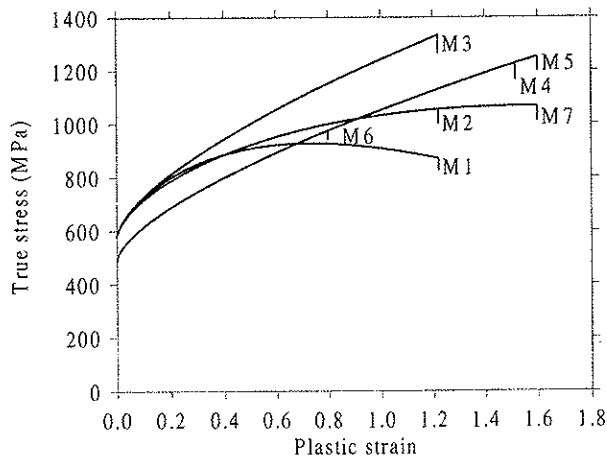


Fig. 4: Calculated stress-strain curves showing the different material models.

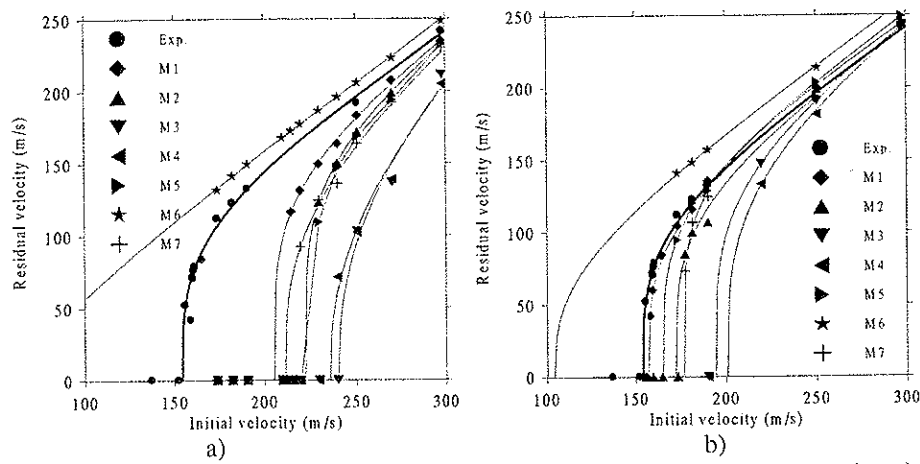


Fig. 5: Comparison between experimental and numerical ballistic limit curves using a) a coarse element mesh and b) a fine element mesh.

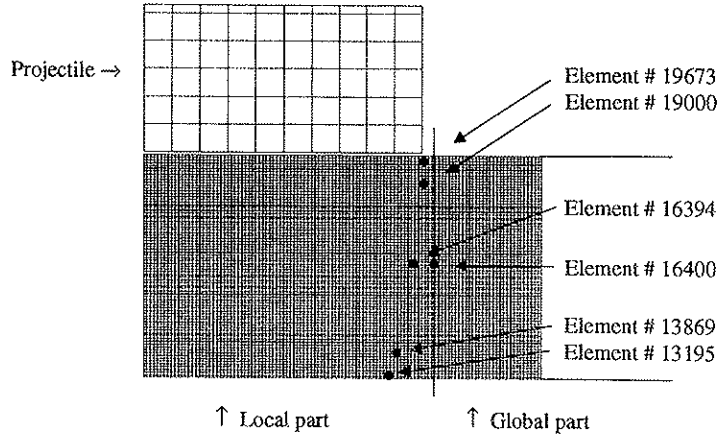


Fig. 6: Details from the element mesh showing the different parts in the simulations.

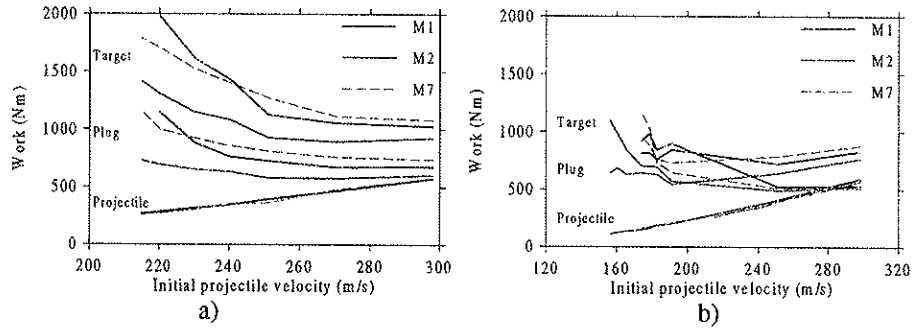


Fig. 7: Energy absorbed in the different parts during impact with a) coarse element mesh and b) fine element mesh.

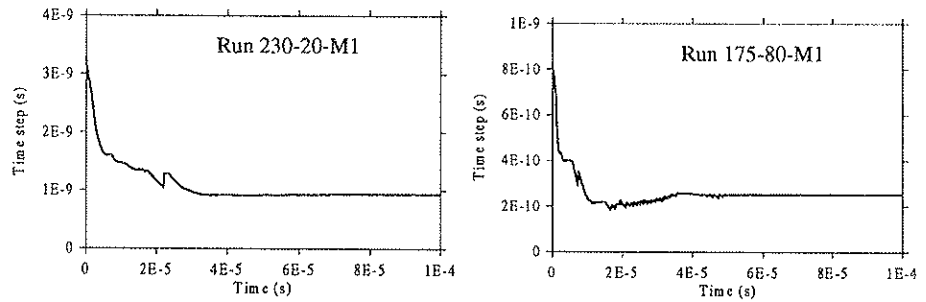
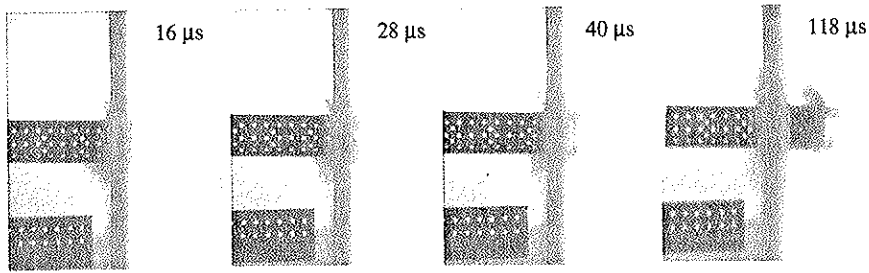
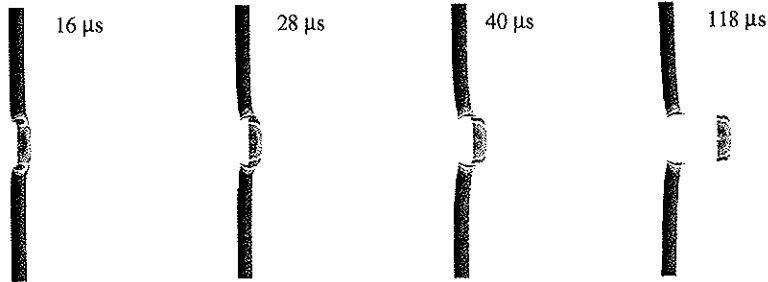


Fig. 8: Computational time step vs. time in Run 230-20-M1 and Run 175-80-M1.

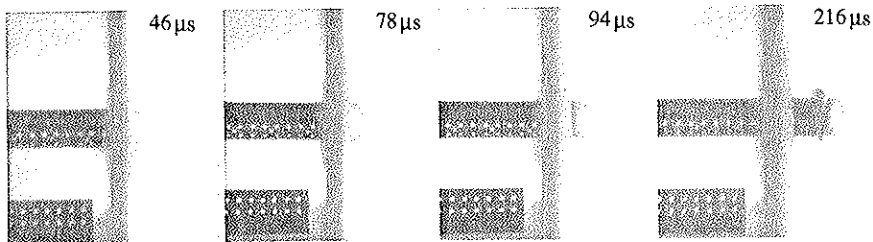
a) Test 8-13 ($v_i = 298$ m/s)



Run 298-80-M1 ($v_i = 298$ m/s)



b) Test 8-8 ($v_i = 173.7$ m/s)



Run 175-80-M1 ($v_i = 173.7$ m/s)

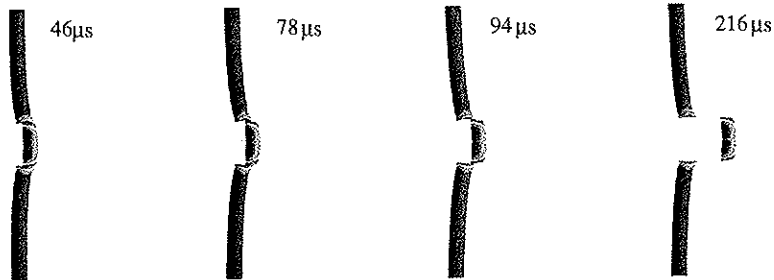


Fig. 9: High-speed camera images from test a) 8-13 and b) 8-8 compared to numerical simulations using model M1 with a) coarse element mesh and b) fine element mesh.

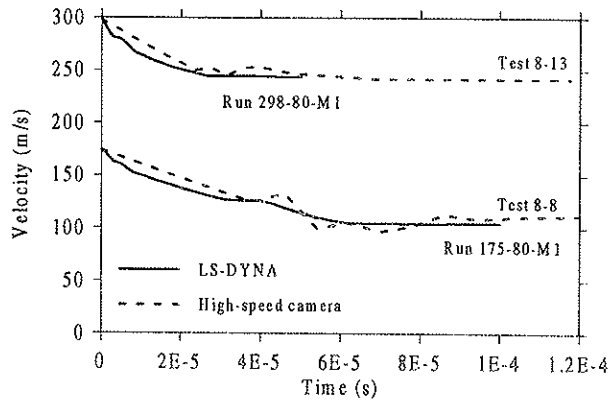


Fig. 10: Comparison between experimental and numerical velocity-time curves.

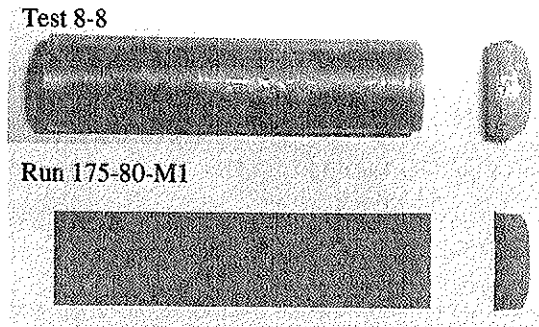


Fig. 11: Projectile and plug after perforation (test 8-8 and Run 175-80-M1).

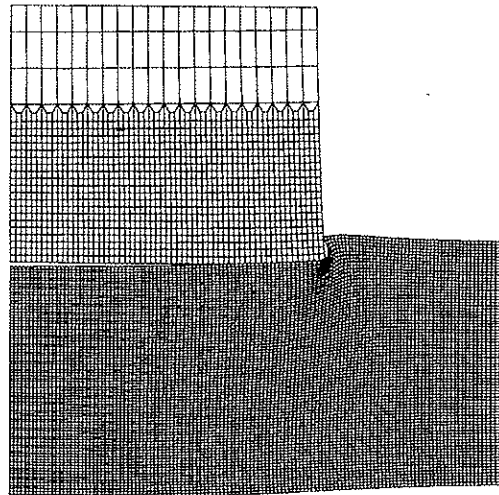


Fig. 12: Refined element mesh in the projectile 5 μ s after impact in Run 298-80-M1.

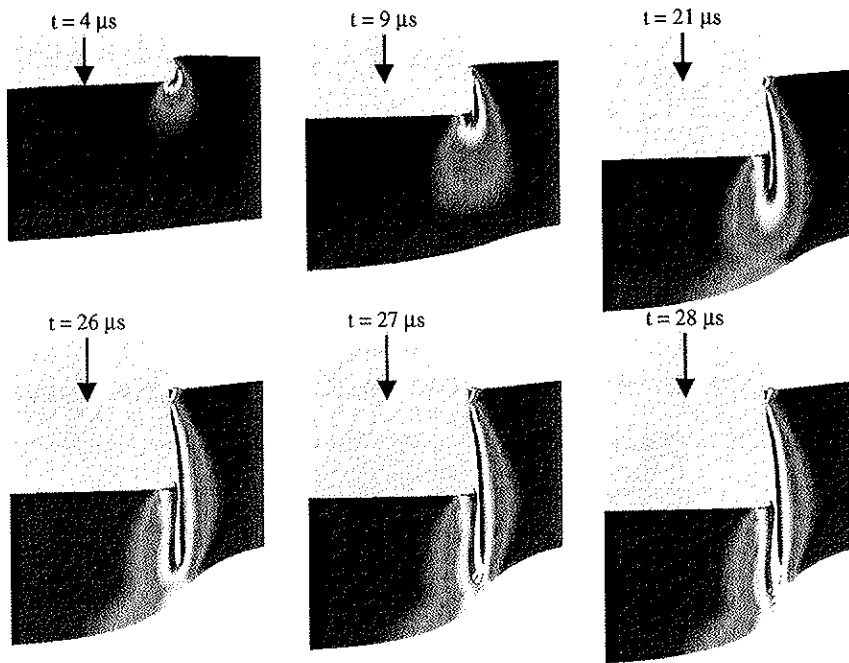


Fig. 13: Details of crack propagation and fracture in the target during penetration for Run 298-80-M1 (plotted as fringes of accumulated plastic strain).

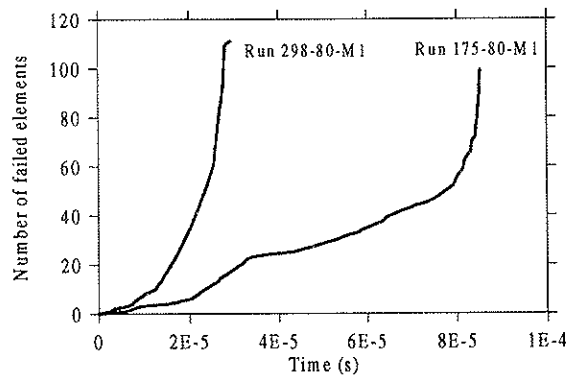
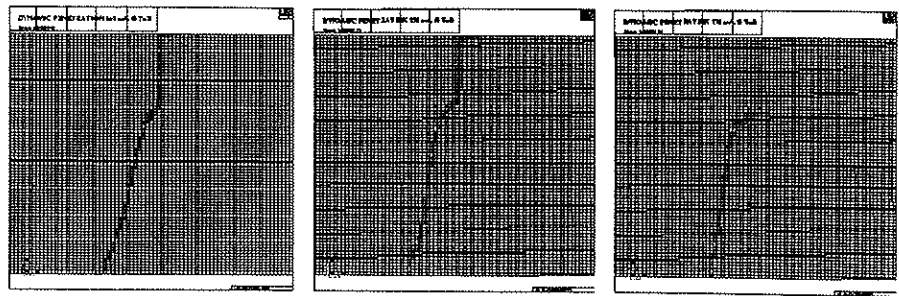
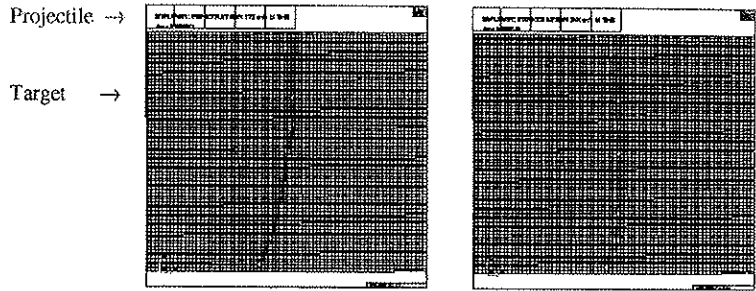


Fig. 14: Number of failed elements vs. time for Run 298-80-M1 and Run 175-80-M1.



a) M1 ($v_1 = 160$ m/s) M2 ($v_1 = 178$ m/s) M7 ($v_1 = 178$ m/s)



b) Run 175-80-M1 c) Run 298-80-M1

Fig. 15: Removed elements giving fracture patterns at a) impact velocities just above the ballistic limit for M1, M2 and M7, b) Run 175-80-M1 and c) Run-298-M1.

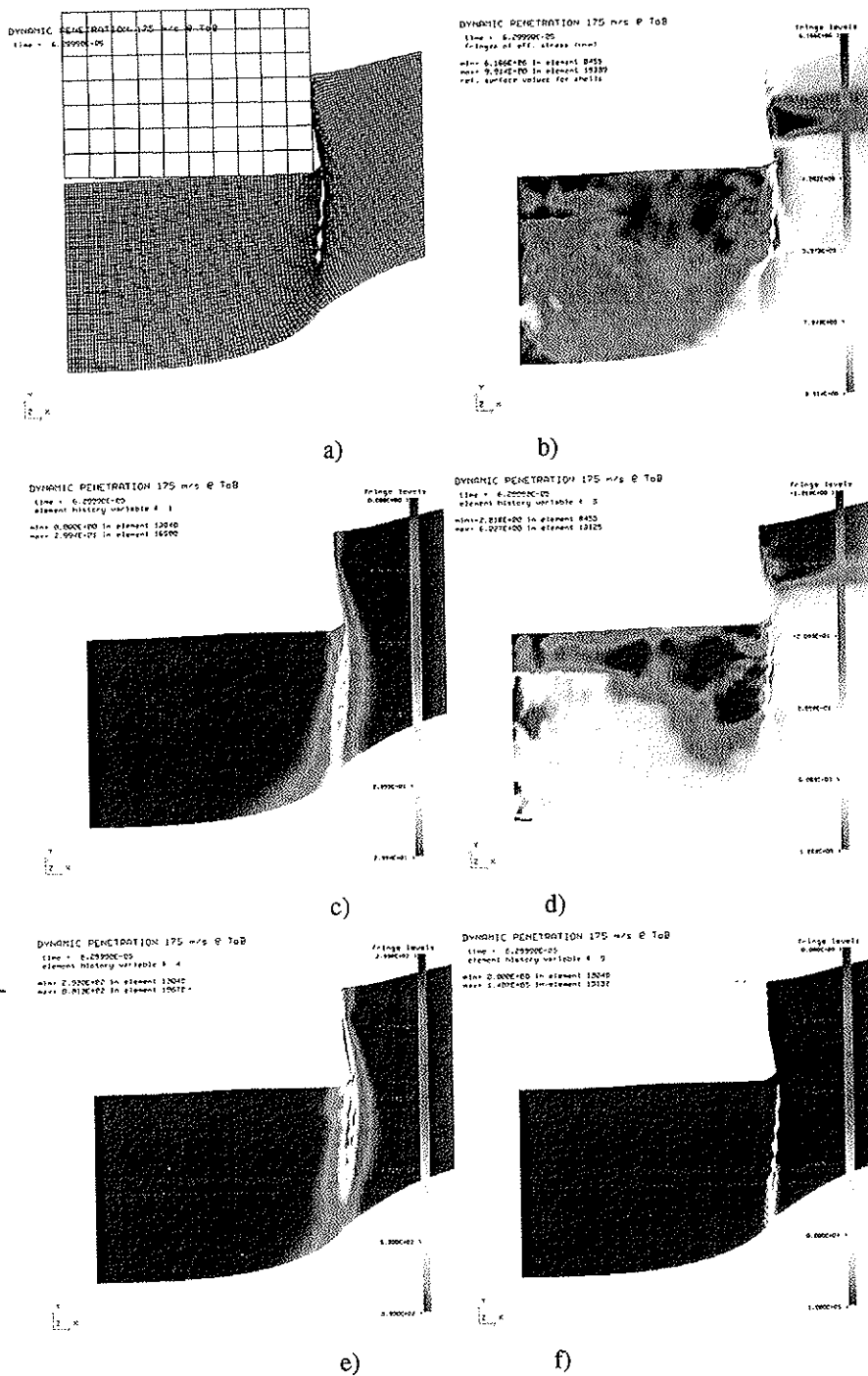


Fig. 16: a) Deformed mesh and distribution of b) equivalent von Mises stress, c) damage, d) stress triaxiality ratio, e) temperature and f) plastic strain-rate in the target 63 μ s after impact in Run 175-80-M1.

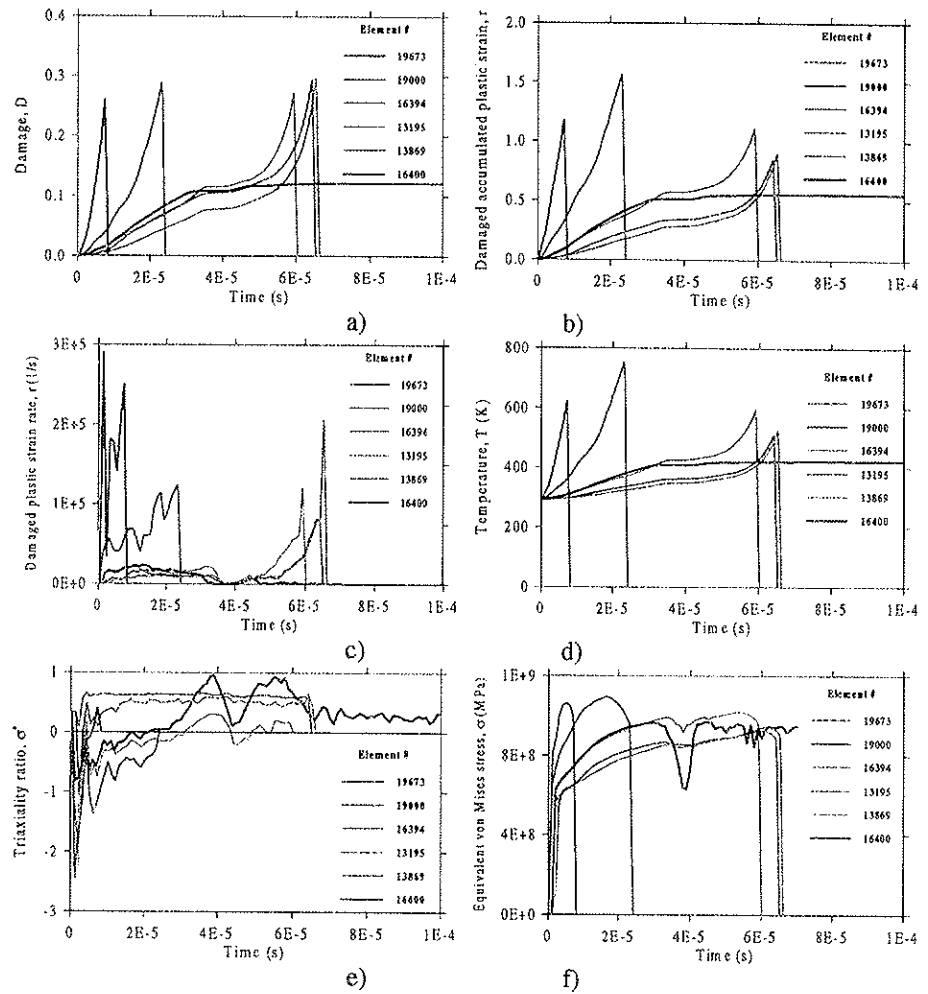


Fig. 17: Plots of some history variables for different elements as function of penetration time.

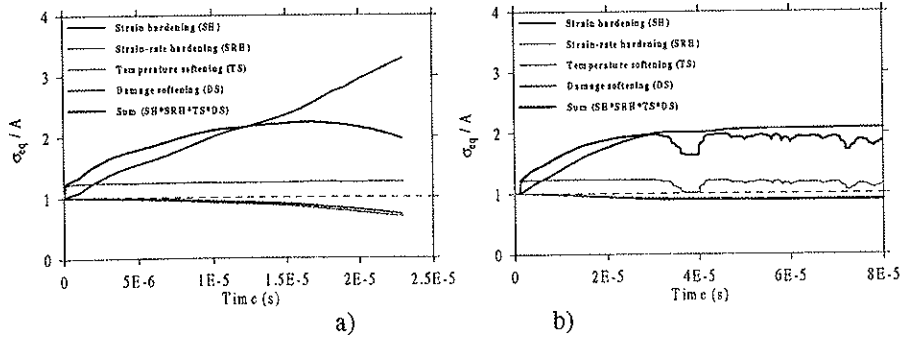


Fig. 18: The effect of strain hardening, strain-rate hardening, damage and temperature softening on the equivalent stress for element a) 19000 and b) 16400 in Run-175-80-M1. For comparison the equivalent stress is divided by the yield stress A of the target.

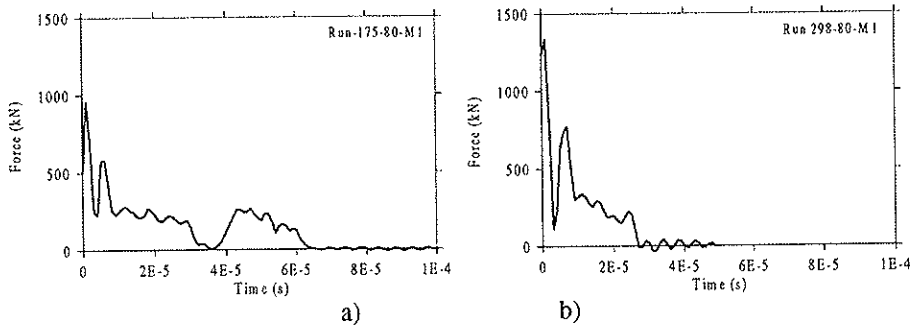


Fig. 19: Projectile force vs. penetration time in a) Run 175-80-M1 and b) Run 298-80-M1.

Table 1: Experimental data for the 8 mm thick Weldox 460 E steel plates.

Test #	v_i (m/s)	v_{rp} (m/s)	v_{rpl} (m/s)	m_{pl} (g)	w_{tm}^1 (mm)	d_{cm} / d_{plm} (mm)	h_c (mm)	h_{pl} (mm)	ΔD (mm)	ΔL (mm)	t_f^2 (μs)
8-13	298.0	241.4	261.2	18.7	0.98	20.7/21.3	11.1	7.9	0.58	0.47	28
8-1	250.8	191.7	222.7	18.8	1.02	20.4/20.8	10.3	8.0	0.38	0.38	35
8-2	190.7	132.3	168.2	18.6	2.31	20.3/20.8	10.4	8.1	0.15	0.10	51
8-14	182.2	122.6	143.4	18.1	2.40	20.2/20.5	11.2	7.9	0.12	0.14	-
8-8	173.7	112.0	131.0	18.5	2.64	20.2/20.8	10.2	8.0	0.08	0.10	82
8-5	165.2	83.7	99.1	18.5	3.69	20.3/20.6	10.1	8.2	0.07	0.12	107
8-9	161.1	78.7	95.4	18.5	3.05	20.2/20.4	10.0	8.1	0.11	0.09	104
8-3	160.7	76.0	102.8	18.2	3.91	20.2/20.5	10.2	8.2	0.11	0.09	109
8-11	160.2	70.2	82.5	18.2	3.93	20.3/20.4	10.2	8.0	0.09	0.15	104
8-10	160.0	71.6	98.7	18.6	2.96	20.3/20.8	10.0	8.2	0.05	0.07	100
8-6	159.0	41.7	83.6	18.2	5.04	20.6/20.9	9.9	8.1	0.02	0.05	106
8-12	156.0	52.0	86.0	18.3	4.52	20.7/21.1	10.1	8.0	0.06	0.12	108
8-7	152.5	0	0	0	5.02	- / -	3.8 ³	-	0.07	0.05	-
8-4	137.4	0	0	0	4.85	- / -	2.9 ³	-	0.01	0.02	-

¹ $w_{tm} = w_{pc} - w_i$, ² Fracture time estimated from high-speed camera images, ³ Projectile indentation.

Table 2: Model constants for Weldox 460 E steel (see Børvik et al., 1999b, for notation).

Elastic constants and density			Yield stress and strain hardening			Strain-rate hardening		Damage evolution			
E (GPa)	ν	ρ (kg/m ³)	A (MPa)	B (MPa)	n	\dot{P}_0, \dot{t}_0 (s ⁻¹)	C	β	D_c	P_d	
200	0.33	7850	490	807	0.73	$5 \cdot 10^{-4}$	0.0114	1	0.30	0	
Adiabatic heating and temperature softening						Fracture strain constants					
C_p (J/kgK)	α	$\bar{\alpha}$ (K ⁻¹)	T_m (K)	T_0 (K)	m	K	D_1	D_2	D_3	D_4	D_5
452	0.9	$1.1 \cdot 10^{-5}$	1800	293	0.94	0.74	0.0705	1.732	-0.54	-0.015	0

Table 3: Material constants for hardened projectile (see Børvik et al., 1999b, for notation).

E (GPa)	ν	ρ (kg/m ³)	σ_0 (MPa)	E_t (MPa)	Mean ϵ_f (%)
204	0.33	7850	1900	15000	2.15

Table 4: Computational models used in the simulations.

Model #	Constitutive model				Fracture strain model		
	Damage	Temperature	Strain-rate	Hardening	Triaxiality	Strain-rate	Temperature
M1	x	x	x	x	x	x	$D_5=0$
M2	$\beta=0$	x	x	x	x	x	$D_5=0$
M3	$\beta=0$	$\alpha=0$	x	x	x	x	$D_5=0$
M4	$\beta=0$	$\alpha=0$	c=0	x	x	$D_4=0$	$D_5=0$
M5	$\beta=0$	$\alpha=0$	c=0	x	$D_1=1.6^*$	$D_4=0$	$D_5=0$
M6	$\beta=0$	$\alpha=0$	c=0	x	$D_1=0.8^*$	$D_4=0$	$D_5=0$
M7	$\beta=0$	x	x	x	$D_1=1.6^*$	$D_4=0$	$D_5=0$
M8 ²	x	x	x	x	x	x	$D_5=0$

* $D_2 = D_3 = 0$, ² Thermoelasticity included.

Table 5: Estimated ballistic limits using the coarse or refined element mesh.

Coarse mesh		Exp	M1	M2	M3	M4	M5	M6	M7
v_{bl} (m/s)		154.3	205.3	222.4	240	235.5	224.8	64.7	211.2
p		3.59	4.06	4.42	2.45	2.38	4.17	1.56	2.92
a		0.83	0.84	0.84	0.97	0.96	0.85	0.89	0.89
Fine mesh		Exp	M1	M2	M3	M4	M5	M6	M7
v_{bl} (m/s)		154.3	157.4	172.5	194.4	200.9	165.5	104.4	177.1
p		3.59	3.54	3.71	3.92	3.46	3.95	2.90	5.28
a		0.83	0.83	0.84	0.86	0.88	0.86	0.88	0.83

Table 6. Numerical results using 80 elements over the target thickness (refined mesh).

Run #	Run 298-80 ($v_i = 298.0$ m/s)									
	v_r (m/s)	v_{rpt} (m/s)	t_f (μ s)	El_f (-)	CPU (h)	w_m (mm)	T_m (K)	$K_{fp}+W_p$ (Nm)	K_n+W_1 (Nm)	$K_{fg}+W_g$ (Nm)
M1	243.7	270	28.0	96	14.2	1.99	1031	5874+570	792+775	72+527
M2	245.0	291	29.5	109	15.6	2.06	930	5938+587	770+828	79+528
M3	241.8	280	31.0	100	14.6	2.54	293	5783+589	725+916	101+611
M4	243.4	248	35.0	115	10.0	2.76	293	5865+526	575+983	111+634
M5	249.2	279	32.5	113	6.5	1.93	293	6147+526	665+839	70+474
M6	259.2	301	24.5	250	3.6	1.08	293	6659+497	634+588	41+309
M7	245.9	280	32.5	111	12.8	2.17	629	5983+573	688+875	84+507
Run #	Run 250-80 ($v_i = 250.8$ m/s)									
	v_r (m/s)	v_{rpt} (m/s)	t_f (μ s)	El_f (-)	CPU (h)	w_m (mm)	T_m (K)	$K_{fp}+W_p$ (Nm)	K_n+W_1 (Nm)	$K_{fg}+W_g$ (Nm)
M1	199.7	238	30.4	93	17.8	2.54	951	3948+403	547+636	67+484
M2	198.7	226	33.6	96	21.0	2.85	854	3912+391	467+718	76+519
M3	190.8	222	46.8	103	25.2	4.75	293	3606+375	438+848	108+690
M4	181.5	221	60.5	132	17.4	5.18	293	3262+365	415+1022	159+803
M5	203.5	218	42.7	100	11.0	2.36	293	4104+353	418+701	60+437
M6	213.9	252	26.0	140	6.2	1.09	293	4535+352	500+455	34+243
M7	199.4	205	38.4	102	18.4	2.93	630	3942+386	367+781	81+504
Run #	Run 220-80 ($v_i = 220.0$ m/s)									
	v_r (m/s)	v_{rpt} (m/s)	t_f (μ s)	El_f (-)	CPU (h)	w_m (mm)	T_m (K)	$K_{fp}+W_p$ (Nm)	K_n+W_1 (Nm)	$K_{fg}+W_g$ (Nm)
M3	147.4	185	58.0	105	32.1	5.90	293	2154+282	306+878	358+857
M4	133.2	154	76.0	134	23.5	7.96	293	1755+247	170+1041	275+1130
Run #	Run 191-80 ($v_i = 190.7$ m/s)									
	v_r (m/s)	v_{rpt} (m/s)	t_f (μ s)	El_f (-)	CPU (h)	w_m (mm)	T_m (K)	$K_{fp}+W_p$ (Nm)	K_n+W_1 (Nm)	$K_{fg}+W_g$ (Nm)
M1	135.5	165	46.0	95	22.3	4.00	877	1824+197	244+550	100+556
M2	106.9	131	82.0	112	28.5	6.92	974	1121+200	144+839	255+894
M3	81.2 ¹	-	100 ²	23	38.2	8.91	293	659+187	62+887	515+1221
M4	85.6 ¹	-	100 ²	25	21.8	8.54	293	728+178	62+933	507+1133
M5	128.8	160	62.0	109	13.1	4.61	293	1646+177	227+710	119+579
M6	157.1	189	27.0	108	7.5	1.12	293	2452+180	323+334	33+189
M7	124.8	148	64.0	97	24.9	4.82	631	1545+195	208+725	141+641
M8	135.9	165	45.0	97	23.1	3.70	872	1834+197	244+546	110+537

¹ No perforation at $t=t_{term}$, ² Termination time reached.

Run		Run 182-80 ($v_i = 182.2$ m/s)								
#	v_r (m/s)	v_{rpl} (m/s)	t_f (μ s)	El_f (-)	CPU (h)	w_m (mm)	T_m (K)	$K_{fp}+W_p$ (Nm)	$K_{fl}+W_l$ (Nm)	$K_{fg}+W_g$ (Nm)
M1	115.9	146	60.0	99	25.9	4.34	830	1334+183	199+624	143+690
M2	99.9	120	81.0	105	31.5	6.72	729	989+181	136+758	244+841
M3	76.9 ¹	-	100 ²	21	43.2	8.77	293	587+162	53+825	477+1123
M4	81.4 ¹	-	100 ²	25	19.0	8.51	293	660+144	60+824	462+1067
M5	120.4	149	63.0	96	12.1	4.60	293	1438+154	196+672	121+574
M6	148.5	181	27.0	107	6.8	1.19	293	2191+160	299+321	34+190
M7	107.0	128	81.0	103	26.3	7.15	630	1134+176	155+755	196+725

¹ No perforation at $t=t_{term}$, ² Termination time reached.

Run		Run 178-80 ($v_i = 178.0$ m/s)								
#	v_r (m/s)	v_{rpl} (m/s)	t_f (μ s)	El_f (-)	CPU (h)	w_m (mm)	T_m (K)	$K_{fp}+W_p$ (Nm)	$K_{fl}+W_l$ (Nm)	$K_{fg}+W_g$ (Nm)
M2	84.8	98	100	104	34.1	7.09	793	713+154	77+815	275+975
M7	73.3	101	124	112	39.9	8.43	631	533+156	86+878	290+1033

Run		Run 175-80 ($v_i = 173.7$ m/s)								
#	v_r (m/s)	v_{rpl} (m/s)	t_f (μ s)	El_f (-)	CPU (h)	w_m (mm)	T_m (K)	$K_{fp}+W_p$ (Nm)	$K_{fl}+W_l$ (Nm)	$K_{fg}+W_g$ (Nm)
M1	104.4	126	86.0	99	29.9	5.10	881	1082+143	139+639	164+701
M2	77.8 ¹	-	100 ²	43	34.0	7.24	815	600+142	55+813	381+921
M3	70.6 ¹	-	100 ²	16	42.7	8.43	293	494+142	45+739	458+1060
M4	76.2 ¹	-	100 ²	18	19.8	7.81	293	577+128	51+751	431+996
M5	94.7	122	88.0	126	12.2	6.06	293	891+144	124+750	231+712
M6	141.0	175	27.0	99	6.7	1.17	293	1976+145	274+300	34+176
M7	46.9 ¹	-	150 ³	54	46.0	9.55	629	219+158	20+944	416+1151

¹ No perforation at $t=t_{term}$, ² Termination time reached, ³ Restarted with $t_{term}=150$ μ s.

Run		Run 165-80 ($v_i = 165.2$ m/s)								
#	v_r (m/s)	v_{rpl} (m/s)	t_f (μ s)	El_f (-)	CPU (h)	w_m (mm)	T_m (K)	$K_{fp}+W_p$ (Nm)	$K_{fl}+W_l$ (Nm)	$K_{fg}+W_g$ (Nm)
M1	84.2	107	87.0	98	33.9	6.93	770	703+134	107+627	170+839

Run		Run 160-80 ($v_i = 160.0$ m/s)								
#	v_r (m/s)	v_{rpl} (m/s)	t_f (μ s)	El_f (-)	CPU (h)	w_m (mm)	T_m (K)	$K_{fp}+W_p$ (Nm)	$K_{fl}+W_l$ (Nm)	$K_{fg}+W_g$ (Nm)
M1	56.0	70	125	102	40.0	8.35	769	312+119	53+680	277+980

Run		Run 156-80 ($v_i = 156.0$ m/s)								
#	v_r (m/s)	v_{rpl} (m/s)	t_f (μ s)	El_f (-)	CPU (h)	w_m (mm)	T_m (K)	$K_{fp}+W_p$ (Nm)	$K_{fl}+W_l$ (Nm)	$K_{fg}+W_g$ (Nm)
M1	34.1 ¹	-	150 ¹	27	44.8	9.08	781	116+108	11+641	386+1093

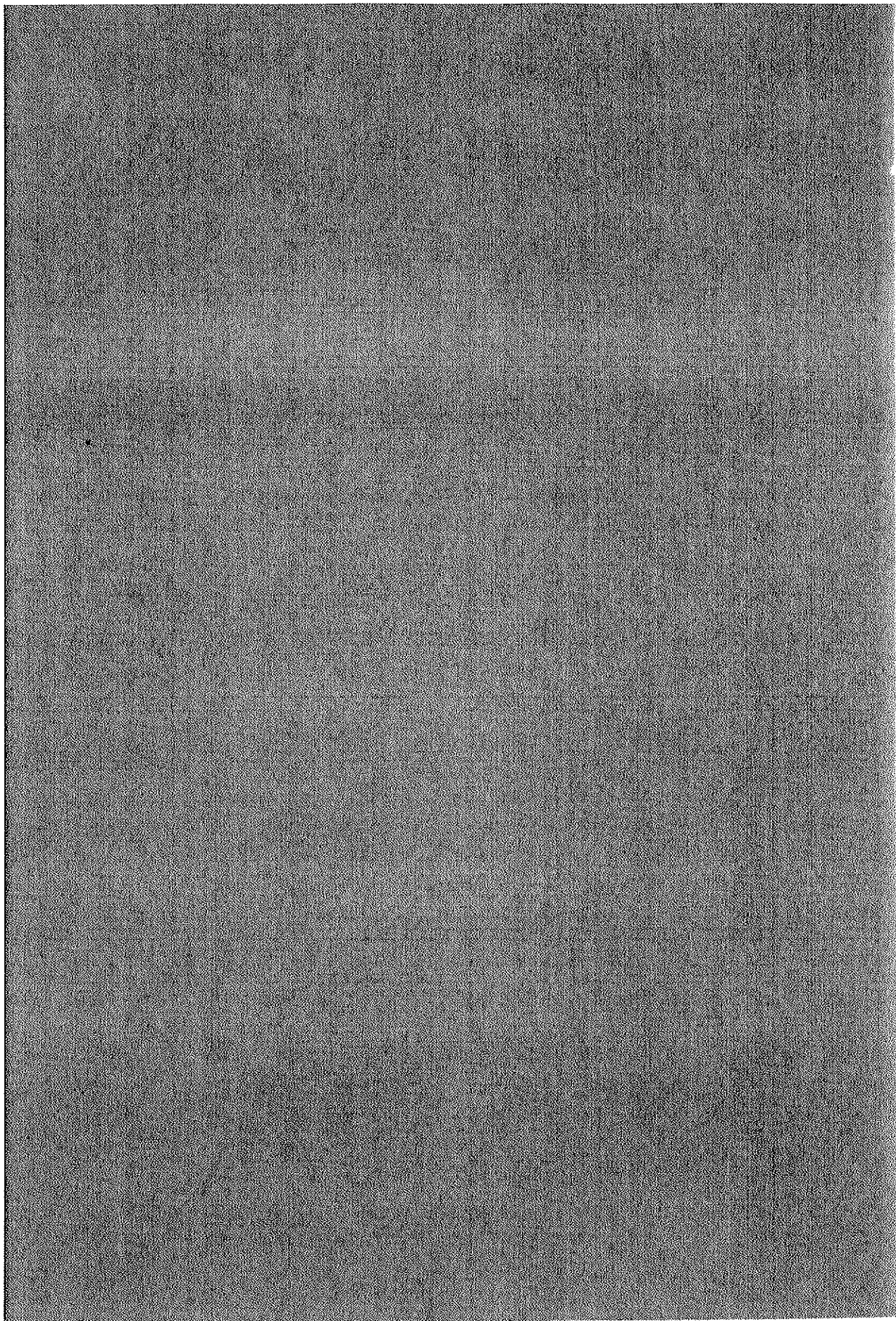
¹ No perforation at $t=t_{term}$, ² Termination time reached.

Part VI

T. Borvik, M. Langseth, O.S. Hopperstad and K.A. Malo

**Effect of Projectile Nose Shape in Structural
Impact, Part I: Experimental Study.**

Submitted for possible journal publication



Effect of projectile nose shape in structural impact, Part I: Experimental study

T. Børvik*, M. Langseth, O.S. Hopperstad and K.A. Malo

*Structural Impact Laboratory (SIMLab), Department of Structural Engineering,
Norwegian University of Science and Technology, N-7491 Trondheim, Norway*

Abstract

Projectiles with three different nose shapes (blunt, hemispherical and conical) have been used in gas gun experiments to penetrate 12 mm thick Weldox 460 E steel plates. Based on the experimental results, the residual velocity curves of the target material were constructed and compared. It was found that the nose shape of the projectile significantly affected both the energy absorption mechanism and the failure mode in the target during penetration. The ballistic limit velocities were about equal and close to 300 m/s for hemispherical and conical projectiles, while it was considerably lower for blunt projectiles. Blunt projectiles caused failure by plugging, which is dominated by shear banding, while hemispherical and conical projectiles penetrated the target mainly by pushing the material in front of the projectile aside. Also the residual velocity curves were influenced by nose shape, partly due to the differences in projectile deformation at impact. The experimental study given in this part of the paper forms the basis for explicit finite element analysis using the commercial code LS-DYNA presented in Part II of the paper.

Keywords: Impact; Experiments; Nose shape; Energy absorption mechanisms; Failure modes; Ballistic limit

* Corresponding author. Tel.: + 47 73 59 46 47; fax: + 47 73 59 47 01.
E-mail address: tore.borvik@bygg.ntnu.no (T. Børvik).

Notation

Unless otherwise stated in the text or references the following notation apply:

ΔD	projectile nose deformation, i.e. $\Delta D = D_f - D_i$
Δh_i	plug thinning, i.e. $\Delta h_i = h_i - h_{pi}$
ΔL	projectile length reduction, i.e. $\Delta L = L_i - L_f$
d	diameter
D	projectile nose diameter
h	thickness
HRC	hardness Rockwell C
K	kinetic energy
L	projectile length
m	mass
T	temperature
t	time
v	velocity
w	deformation
W	work

Subscripts:

bl	ballistic limit
c	cavity
f	final value, fracture or front side
g	global part of target
i	initial value
l	local part of target
m	maximum value
p	projectile
pe	permanent value
pl	plug
r	residual value, rear side
t	target or total

1. Introduction

Structural impact is known as a complex problem, both from an experimental, analytical and numerical point of view (Backman and Goldsmith (1978), Anderson and Bodner (1988), Corbett et al (1996)). One reason is the many physical parameters involved that may cause highly non-linear and sometimes unexpected structural behaviour when varied. As an example, Baker et al (1991) identified nearly 30 possible and relevant input parameters in the general penetration problem of metal plates. However, several of these parameters are problem dependent and can be neglected in certain situations. One typical problem where the number of variables is limited is impact loading of stationary targets by explosion-generated fragments at sub-ordnance velocities. In this problem it is assumed that the nose shape of hard projectiles greatly affects the response of the target structure. Here, blunt projectiles normally cause failure by shear plugging, conical projectiles tend to give petaling in thin plates and ductile hole enlargement in thicker plates, while hemispherical projectiles seem to give failure by tensile stretching after severe indentation and thinning of the target plate. However, as pointed out by Woodward (1990), in many cases mixed modes of failure appear as a result of anisotropy in the target material at fracture.

Some investigations have study in what way different nose shapes affect the ballistic behaviour of the target material, but the results are to some extent incompatible. Experimental results by Grabarek presented in Zukas et al (1992) indicate that the more blunt the nose shape, the higher is the ballistic limit velocity. This is in some conflict with results by Corran et al (1983), which show that the critical impact energy depends on the projectile nose radius. They found that the energy reached a maximum when there was a change in failure mode from shear plugging to tensile stretching. Johnson et al (1980) reported similar results in quasi-static punching tests of metal plates. Ipson and Recht (1977) found that sharp projectiles penetrated the target in a less efficient way than blunt projectiles, giving a higher ballistic limit for conical projectiles as long as the target thickness was moderate. However, for thin and thick targets conical projectiles were found superior. Wingrove (1973) observed similar behaviour in perforation tests of 2014-T6 aluminium alloy targets. He showed that blunt projectiles penetrated the target with the least resistance, followed by hemispherical and ogive penetrators in that order, as long as the target thickness to projectile diameter ratio was less than one. Othe et al (1982) found that the critical perforation energies for blunt and hemispherical projectiles were similar, while less energy was required for conical projectiles. They also found a distinct drop in the perforation resistance of the target as the nose angle of

the sharp projectile was decreased. This decrease in critical energy was attributed to the decrease in effective contact area for the projectiles. Wilkins (1978) found that sharp projectiles gave lower ballistic limits than blunt projectiles when fired into thick metal plates, while the opposite was found for thin targets.

The above and similar contradictions found in the literature indicate that the influence of projectile nose shape in structural impact is controlled by parameters varying from one investigation to the other. It follows that the problem is not yet fully solved, and more work is necessary in order to determine the governing variables of the problem. To this end, a study on the penetration of steel plates by projectiles with different nose shapes has been completed. The investigation is divided into two parts. In Part I, presented in this paper, three different projectile nose shapes (blunt, hemispherical and conical) are used in compressed gas gun experiments to penetrate 12 mm thick Weldox 460 E steel plates. The tests are carried out in order to study the importance of projectile nose shape in structural impact at sub-ordnance velocities, and to provide high-precision experimental data for validation of numerical computations. Based on the experimental results, the residual velocity curves of the target plates are constructed and compared, and the obtained differences in energy absorption and failure mode caused by varying the projectile nose shape are discussed in some detail. Numerical results from explicit finite element analysis of the problem are presented in Part II of the paper, see Børvik et al (2000c).

2. Experimental set-up and programme

The experimental programme on the ballistic penetration of 12 mm thick Weldox 460 E steel plates by projectiles with different nose shapes was carried out in the compressed gas gun shown in Fig. 1 (Børvik et al, 1998). In the tests, the sabot-mounted projectiles were fired at impact velocities just below and well above the ballistic limit of the target plate. The serrated sabot separated immediately after leaving the muzzle due to aerodynamic forces, and the sabot pieces were stopped in a sabot trap prior to impact.

Projectiles were manufactured from Arne tool steel. After machining, they were oil hardened to a maximum Rockwell C value of 53 in order to minimise the plastic deformation during impact. Nominal hardness (HRC 53), diameter (20 mm) and mass (0.197 kg) of the cylindrical projectiles were constant in all tests. The L/D-ratio of the projectiles varied somewhat because of the constant mass. The geometry of the different projectiles used in the

tests is defined in Fig. 2. Note that the tip of the conical projectile was removed, giving it a truncated cylindro-conical shape. Before testing, the projectiles were painted dead black and equipped with fiducial marks for high-speed camera measurements.

The target plates, having a free span diameter of 500 mm and a constant nominal thickness of 12 mm, were clamped in a circular frame approximately 2 metres behind the muzzle by 21 prestressed M16 bolts. In order to allow high-speed photography during penetration, the frame was equipped with a 150 mm framing window. All target plates were carefully sandblasted on both sides prior to testing. Target thickness, oblique, initial imperfections and final deformations were measured *in situ*. If perforation occurred, the projectile and possible plug were soft recovered in a rag-box filled with graded plywood.

Initial and final velocities were measured using different laser-based optical devices, and a digital high-speed camera system was used in all tests to photograph the penetration event. From the digital images, impact angles and projectile velocities during penetration were determined using image processing. It is referred to Børvik et al (1998, 1999) for further details regarding the experimental set-up and measurement techniques used in the penetration tests. Tensile material test results for the projectile and target have been presented elsewhere (Børvik et al, 1999), but are also given in Part II of this paper (Børvik et al, 2000c).

3. Experimental results and discussion

Experimental results for blunt, hemispherical and conical projectiles are given in Table 1, Table 2 and Table 3, respectively. The experimental data for blunt projectiles has partly been presented before (Børvik et al, 1999), and is therefore mainly given for comparison. Based on the measured initial and residual velocities of the free flying projectiles, the residual velocity curves in Fig. 3 were constructed. The ballistic limit velocities were calculated as the average between the highest impact velocity not giving perforation and the lowest impact velocity giving complete perforation of the target. The solid lines through the data points shown in Fig. 3 were fitted to an analytical model originally proposed by Recht and Ipson (1963)

$$v_r = a(v_i^p - v_{bl}^p)^{1/p} \quad , \quad a = \frac{m_p}{m_{pl} + m_p} \quad , \quad p = 2 \quad (1)$$

Here, the method of least squares was used to find a best fit of the model constants a and p to the experimental values. The ballistic limit velocities obtained experimentally and the fitted values of a and p are given in Table 4.

From the residual velocity curves in Fig. 3 some immediate conclusions can be drawn. First, it is seen that the nose shape of the projectile significantly affects the ballistic resistance of the target plate. The ballistic limit velocity for hemispherical and conical projectiles are about equal and close to 300 m/s, while the ballistic limit velocity is as low as 185 m/s for blunt projectiles. The residual velocity curves for blunt and hemispherical projectiles seem to coincide as the impact velocity becomes high compared to the respective ballistic limits. The residual velocity curve for conical projectiles exceeds the other two at the highest impact velocities, and becomes almost parallel to the residual velocity line, i.e. the asymptotic response to a target of zero thickness. The residual velocity line is given as the dashed line in Fig. 3. It should be noticed from Table 2 that the projectile deformation in test H7 is high. Post measurements of the hardness profile of this particular projectile revealed that the core was not as hard as initially specified. Therefore, it might be that the residual velocity curve in Fig. 3 for hemispherical projectiles is somewhat low at the highest impact velocities.

The observed differences in ballistic limit velocity are mainly attributed to the change in failure mode with projectile nose shape. High-speed camera images from typical perforation tests for blunt, hemispherical and conical projectiles are given in Fig. 4. Note that the given times refer to the image taken closest to the assumed time of impact. All images are from tests at an impact velocity close to the ballistic capacity of the target, i.e. approximately 3 % above the respective ballistic limits. The figure shows that blunt projectiles cause failure by plugging, and an almost circular plug is ejected from the target. This failure mode is dominated by shear banding. Hemispherical and conical projectiles seem to penetrate the target mainly by ductile hole enlargement, pushing the material in front of the projectile aside. After severe localised bulging, a cup-shaped plug is ejected from the target for hemispherical projectiles. No plug is seen in any of the tests for conical projectiles, but petals are formed on both sides of the cavity. It should be noted that in some of the tests, the projectile rotated during perforation because of an unsymmetrical fracture process, even though the pitch angle prior to impact was measured to be small.

Fig. 5 gives measured distance-time and velocity-time curves to the projectile based on the digital high-speed camera images from the tests shown in Fig. 4. Significant differences in behaviour during perforation are detected. The blunt projectile shows a sharp drop in velocity after impact, indicating a high interface force between the projectile and target. The slope is

far less steep for the other two nose shapes and in particular for the conical projectile. Thus, the interface force at impact is reduced accordingly. The perforation time is also seen to increase somewhat both for the hemispherical and conical projectile.

Photographs of the target plates perforated in Fig. 4 are given in Fig. 6a)-f). Front surfaces of the targets are shown in Fig. 6a)-c), while rear surfaces together with the corresponding projectiles and plugs are shown in Fig. 6d)-f). Blunt projectiles cause clean cuts, giving a sharp indentation of the target without any frontal bulge. A modest frontal bulge appears when hemispherical projectiles are used, while a distinct bulge is seen for conical projectiles. In the latter, petals are formed because of high circumferential tensile stresses in the bulge. The corresponding rear sides exhibit a somewhat similar behaviour. A modest and smooth bulge is obtained for blunt projectiles, and the punched plug is almost cylindrical with a diameter equal to the nose diameter of the deformed projectile. The bulge for hemispherical projectiles is more irregular and unsymmetrical. The plug is ripped out of the target after severe thinning, indicating large tensile forces in the bulge at fracture. As for the frontal side, distinct bulging and petals are obtained for conical projectiles. All cavities in the targets are smooth and uniform, independently of projectile nose shape. As indicated in Tables 1-3, the diameter of the cavity for blunt projectiles is increasing towards the rear side, while for hemispherical and conical projectiles the diameter is reduced. Note also that the rear side diameter of the cavity for hemispherical and conical projectiles is smaller than the initial diameter of the projectile. This indicates considerable elastic deformation and rebound of the target after perforation. Elastic deformations and rebound were also obtained for blunt projectiles, but the effect of these phenomena in the penetration problem is assumed small.

Fig. 6g)-i) show some target rear surfaces where complete perforation did not occur. In test H2, a through-thickness-crack was found almost completely around the circumference of the bulge. Test H4 was rather special. Here, the projectile was contained at the tail just before leaving the target, while the plug was fully ejected. This was probably caused by elastic rebound of the target plate, sliding friction between the projectile and target, or a combination of both. Owing to this behaviour, the impact velocity in test H4 was taken as the ballistic limit of the target for hemispherical projectiles. Conical projectiles easily pierced the target plates, and such failure occurred in all tests reported in Table 3. However, the lowest impact velocities only giving piercing was not taken as the ballistic limit. One example of piercing is shown in Fig. 6i). Here, only a part of the nose perforated the target, and the projectile was stopped before complete perforation occurred.

Cross-sections of the target plates perforated in Fig. 4 are shown in Fig. 7. These pictures reveal the differences in plastic flow around the projectile nose during impact. Limited plastic deformation of the target plate seems to appear outside the localised shear zone for blunt projectiles, while the plastic deformation in the vicinity of the penetrating projectile using a conical nose is considerable. In the latter, the moving projectile pushes the material aside radially. This results in a plastic flow field where the material flows either upwards into a frontal bulge or downwards into a rear side bulge, instead of forming a plug. It seems reasonable that more plastic work is needed for this operation than to just shear a plug out of the target. The behaviour of hemispherical projectiles seems to be somewhere in between these two extremes.

The plastic flow during the penetration process is further illustrated in the macrographs in Fig. 8 of sectioned and etched cross-sections of target plates close to perforation. When blunt projectiles are used, a sharp and distinct indentation is seen. Because of the high relative velocity between the accelerated material in front of the projectile and the rest of the target, the deformation localises in narrow shear bands. In these localised zones, very large strains, strain rates and temperatures appear, causing material damage. In the present case, the localised deformation is assumed to take place in the transition region between an isothermal and an adiabatic process (see also Børvik et al, 2000b). Thus, both temperature and damage affect the material softening. When the strain reaches a critical value, a crack starts to grow towards the rear side of the target, and a plug is finally formed. For hemispherical and conical projectiles the behaviour is different. For the former, the projectile indents the target, giving a very localised bulge and target thinning. The result is regions of intense tensile strain, but no shear localisation. However, as the deformation continues, the material in the intense tensile zone starts to neck. When the tensile strain exceeds the capacity of the target material, a plug with reduced thickness and diameter is ejected. Conical projectiles displace a significant amount of target material radially. The internal separation required for perforation initiates at the tip, and the hole is enlarged along the trajectory of the projectile. Note also that the target deforms almost perfectly to the shape of the conical nose as the projectile indents.

The flow lines of dark pearlite running parallel to the surface of the target as a result of the manufacturing process reveals the plastic flow in the material during penetration. For blunt projectiles these lines are cut straight off and hardly distorted near the impact surface. As the material in front of the projectile starts to move, the flow lines indicate intense shear inside localised bands, while limited bending is seen outside the bands. Once the deformation localises, the material is constrained to flow in the direction of the moving projectile.

Towards the rear side the flow lines are severely stretched, indicating tensile stresses in the bulge. When a hemispherical projectile impacts the target, the flow lines deflect and the material flows up to form a frontal bulge. However, this stage is rapidly overcome and the flow changes direction towards the rear side as the projectile indents the target. The region where the flow lines change direction is indicated in Fig. 8b). As the indentation continues, the material in front of the projectile stretches and bends, giving parallel and dense flow lines. This results in a region of intense tensile strain, where failure finally is initiated due to necking. In Fig. 8c), the flow lines indicate that a considerable amount of material flows up and out into a frontal bulge when a conical projectile indents the target, while the material in front and close to the truncated tip flows down and aside. When the nose is completely embedded, the material is just pushed aside by the moving projectile. In the present investigation, the region where the flow lines change direction seems to be close to the middle plane of the target plate. Once this area is passed, the flow lines indicate a downstream movement towards the rear side bulge. The flow pattern is much more complex for conical projectiles than for blunt and hemispherical projectiles.

Fig. 9 gives measured permanent deformations in projectiles, targets and plugs. As shown in Fig. 9a), blunt projectiles are rapidly deformed with increasing impact velocity, and at the highest impact velocity a part of the nose of the blunt projectile broke off. The plug thinning is small, again indicating a modest lateral flow of material during plugging. Hemispherical projectiles show limited plastic deformations when the impact velocity is high. The plug thinning is extensive, in agreement with the considerable lateral movement of material during penetration. Conical projectiles hardly deform at all in this velocity regime. Since no plug is formed, the material in front of the projectile is pushed away laterally. The differences in measured projectile deformation is probably due to the differences in interface force between the projectile and target, as illustrated in Fig. 5.

The effect on the global target deformation (dishing) for different projectile nose shapes is illustrated in Fig. 9b)-d). From Fig. 9b) the maximum target deformation is seen to decrease from a maximum value at the ballistic limit to a limit value when the impact velocity becomes high. Conical projectiles are found to give the largest global target deformation at all velocities. At an impact velocity of 300 m/s, the maximum deformation in the target is more than three times larger for hemispherical and conical projectiles than for blunt projectiles. Note that these measurements do not include the localised bulge. Fig. 9c) and d) show comparisons between measured permanent deformation profiles at impact velocities close to and well above the respective ballistic limits. The global target deformation is much

more distinct for conical than for blunt projectiles. This is valid also at higher velocities, even if the differences between the deformation profiles are reduced. These measurements also indicate that a larger part of the target plate is activated for conical projectiles than for the other two nose shapes under the given impact conditions.

At impact, the very complex process of transforming projectile kinetic energy into work through a diffuse stress wave transfer begins. In the problem under consideration, it is reasonable to assume that one part of the energy is absorbed in global target deformation (W_g), another part is absorbed in localised plastic flow and failure (W_l), while the rest is absorbed in projectile deformation (W_p). Even if both elastic and frictional work will be done, these are assumed to be of minor importance in the total energy balance during ballistic penetration, and are therefore often neglected (Woodward, 1984). A simple energy balance can then be established as

$$\Delta K = \frac{1}{2} m_p v_i^2 - \frac{1}{2} m_p v_r^2 - \frac{1}{2} m_{pl} v_{rpl}^2 = W_g + W_l + W_p = W_t \quad (2)$$

The total amount of projectile kinetic energy converted into projectile and target work during impact is easily calculated from the measured values in Table 1-3, and this is shown in Fig. 10. For blunt projectiles ΔK seems to increase continuously with increasing initial projectile velocity. For conical and hemispherical projectiles ΔK decreases from a local maximum at the ballistic limit to a local minimum, before it again increases monotonically with initial projectile velocity. The drop in ΔK is far less distinct for hemispherical projectiles than for conical projectiles. Blunt projectiles are found to perforate the 12 mm thick Weldox 460 E steel targets with least energy consumption up to a velocity of approximately 440 m/s. For higher impact velocities, conical projectiles are more efficient. This is partly caused by the difference in projectile plastic deformation (see Tables 1-3) due to the change in interface force and contact surface when the nose shape is varied, as indicated in Fig. 4 and Fig. 5. Hemispherical projectiles are found to be the least efficient penetrator in all tests carried out in this particular study.

It is very difficult to quantify the different terms in Eq.(2) using simplified computational methods, as also indicated in the literature (Backman and Goldsmith, 1978, Corbett et al, 1996). Woodward (1984) showed analytically that for a rigid-plastic material plugging is more favourable than ductile hole enlargement when the target thickness h_t is less than $\sqrt{3}D/2$, which in this study gives a target thickness of about 17 mm. In the study by

Woodward, only the local area around the projectile nose was considered and the possible effect of adiabatic shear banding was neglected. Bai and Dodd (1992) have discussed the mechanisms governing the occurrence and formulation of adiabatic shear bands in detail.

Frictional effects are frequently neglected in impact problems. According to Ravid and Bodner (1983) a dynamic friction coefficient of 0.1 is proposed in the literature for metal working operations. A lower value of 0.05 should be used for the lateral surfaces in impact situations due to the higher velocities and temperatures. Recht in Zukas et al (1990) indicated an even lower value. He suggested a dynamic friction coefficient of 0.01 for ballistic impact involving metal to metal surfaces. Fig. 11 shows images of the sliding contact area between the projectile and target for a blunt and conical nose shape during perforation. For blunt projectiles the nose is plastically deformed at impact, giving it a mushroomed shape, and a plug with front side diameter almost equal to the deformed nose is ejected. The result is a cavity of larger diameter than the initial diameter of the projectile. Thus, after passage of the initial nose the rest of the projectile is hardly in contact with the target (see Fig. 11a) and no sliding friction is expected. This is not the case for conical projectiles, where the projectile is in full contact with the target material during the entire perforation process. Consequently, it seems reasonable to neglect frictional effects for blunt projectiles, while a small frictional coefficient should be used for conical (and hemispherical) projectiles. The minor importance of friction in plate impact with blunt projectiles has previously been validated through numerical simulations (Børvik et al, 2000a).

4. Conclusions

This paper presents gas gun experiments in which projectiles with three different nose shapes (blunt, hemispherical and conical) were used to penetrate 12 mm thick Wieldox 460 E steel plates. Based on the experimental observations, the following conclusions are drawn:

- The ballistic limit velocity of the target plate is severely affected by the nose shape of the projectile under the given impact conditions. Hemispherical and conical projectiles give a ballistic limit velocity close to 300 m/s, while the ballistic limit velocity is only about 185 m/s for blunt projectiles.

- Also the residual velocity curves are influenced by projectile nose shape. For blunt and hemispherical projectiles the residual velocity curves seem to coincide as the impact velocity becomes high compared to the ballistic limit. The residual velocity curve for conical projectiles, on the other hand, exceeds the other two at the highest impact velocities and becomes almost parallel to the residual velocity line.
- The differences in ballistic limit velocities are attributed to the change in energy absorption and failure mode of the target with projectile nose shape. It appears that both local and global deformations in the target are largest for conical projectiles, followed by hemispherical and blunt projectiles in that order.
- The variation in the residual velocity curves is partly caused by projectile deformation. Blunt projectiles deform almost linearly with impact velocity in the actual velocity regime, while conical projectiles hardly deform at all. Conical projectiles require less energy to perforate the target plate than the other projectiles when the impact velocity is above 440 m/s. For lower impact velocities, the energy consumption is least for blunt projectiles. Plastic deformations also occur in hemispherical projectiles, but not to the same extent as for the blunt ones.
- From sectioned target plates, it is revealed that sliding frictional effects can be neglected for blunt projectiles. However, small frictional effects seem to be present for conical and hemispherical projectiles, and should be accounted for in finite element simulations.

Acknowledgements

The authors would like to express their gratitude to the Norwegian Defence Construction Service, Central Staff/Technical Division, for their generous financial support of this study.

References

- Anderson Jr., C. E. and Bodner, S. R., 1988. Ballistic Impact: The Status of Analytical and Numerical Modeling, *International Journal of Impact Engineering*, Vol. 7 (1), pp. 9 - 35.
- Backman, M.E. and Goldsmith, W., 1978. The Mechanics of Penetration of Projectiles into Targets, *International Journal of Engineering Science*, Vol. 16, pp. 1 - 99.

- Bai, Y. and Dodd, B., 1992. *Adiabatic Shear Localization: Occurrence, Theories and Applications*, Pergamon Press, Oxford.
- Baker, W.E., Westine, P.S. and Dodge, F.T., 1991. *Similarity Methods in Engineering Dynamics; Theory and Practice of Scaling Modeling*, revised edition, Elsevier.
- Børvik, T., Holen, K., Langseth, M. and Malo, K.A., 1998. An Experimental set-up used in Ballistic Penetration, *Proceedings of Fifth International Symposium on Structures under Shock and Impact*, pp. 683 - 692, Thessaloniki, Greece, 24-26 June.
- Børvik, T., Langseth, M., Hopperstad, O.S. and Malo, K.A., 1999. Ballistic penetration of steel plates, *International Journal of Impact Engineering*, Vol. 22 (9-10), pp. 855-887.
- Børvik, T., Hopperstad, O.S., Berstad, T. and Langseth, M., 2000a. Numerical Simulation of Plugging Failure in Ballistic Penetration, accepted for publication in *International Journal of Solids and Structures*.
- Børvik, T., Leinum J.R., Solberg, J.K., Hopperstad, O.S., and Langseth M., 2000b. Observations on shear plug formation in Weldox 460 E steel plates impacted by blunt-nosed projectiles, accepted for publication in *International Journal of Impact Engineering*.
- Børvik, T., Langseth, M., Hopperstad, O.S. and Malo, K.A., 2000c. Effect of projectile nose shape in structural impact, Part II: Numerical simulations, submitted for publication.
- Corbett, G.G., Reid, S.R. and Johnson, W., 1996. Impact Loading of Plates and Shells by Free-Flying Projectile, *International Journal of Impact Engineering*, Vol. 18 (2), pp. 141 - 230.
- Corran, R.S.J., Shadbolt, P.J. and Ruiz, C., 1983. Impact Loading of Plates - An Experimental Investigation, *International Journal of Impact Engineering* 1 (1), pp. 3 - 22.
- Ipson, T.W. and Recht, R.F., 1977. *Ballistic Perforation by Fragments of Arbitrary Shape*, NWC TP 5927, Denver Research Institute, Naval Weapons Center, China Lake, CA, USA.
- Johnson, W., 1972. *Impact Strength of Materials*, Edward Arnold Ltd.
- Johnson, W., Ghosh S.K. and Reid, S., 1980. Piercing and Hole-Flanging of Sheet Metals: A Survey, *Aluminium* 56, pp. 142 - 146.
- Jones, N., 1989. *Structural Impact*, Cambridge University Press.
- Othe, S., Yoshizawa, H., Chiba, N. and Shida, S., 1982. Impact Strength of Steel Plates Struck by Projectiles, *Bulletin JSME* 25 (205), pp. 1226-1231.
- Ravid, M. and Bodner, S.R., 1983. Dynamic Perforation of Viscoplastic Plates by Rigid Projectiles, *Int. J. Engng. Sci.* 21 (6), pp. 577 - 591.
- Wilkins, M.L., 1978. Mechanics of Penetration and Perforation, *Int. J. Engng. Sci.* 16, pp. 793 - 807.
- Wingrove, A.L., 1973. The Influence of Projectile Geometry on Adiabatic Shear and Target Failure, *Metall. Trans. A.*, Vol. 4, pp. 1829 - 1833.
- Woodward, R.L., 1984. The Interrelation of Failure Modes Observed in the Penetration of metallic Targets, *International Journal of Impact Engineering* 2 (2), pp. 121 - 129.
- Zukas, J.A. et al., 1992. *Impact Dynamics*, Krieger Publishing Company.

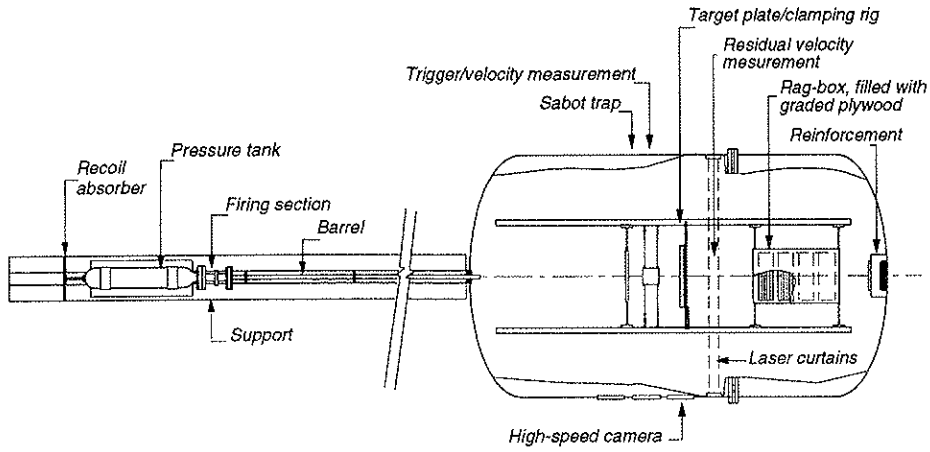


Fig. 1: Sketch of compressed gas gun used in the tests (Børvik et al, 1998).

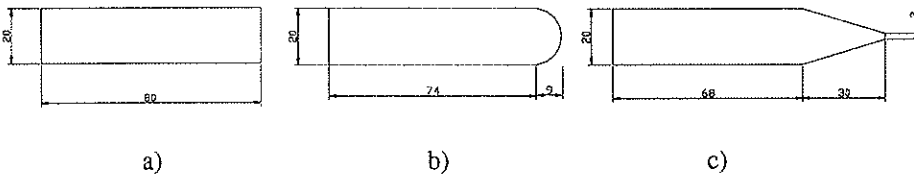


Fig. 2: The different projectiles used in the tests; a) blunt, b) hemispherical, c) conical.

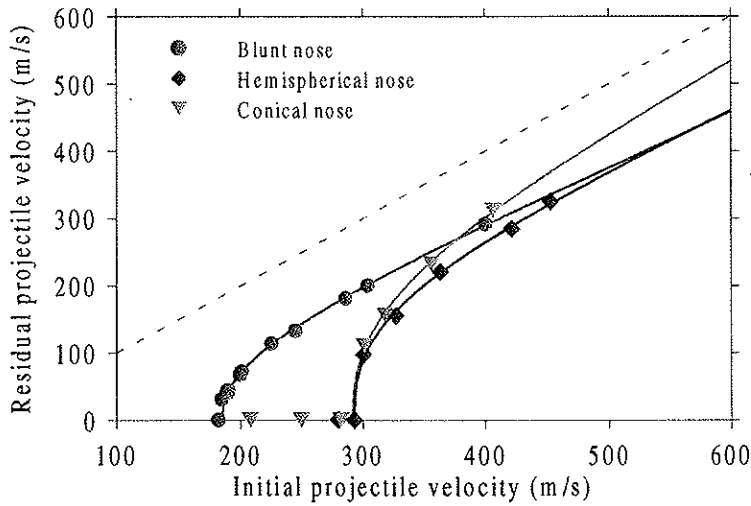


Fig. 3: Residual velocity curves for the different projectile nose shapes.

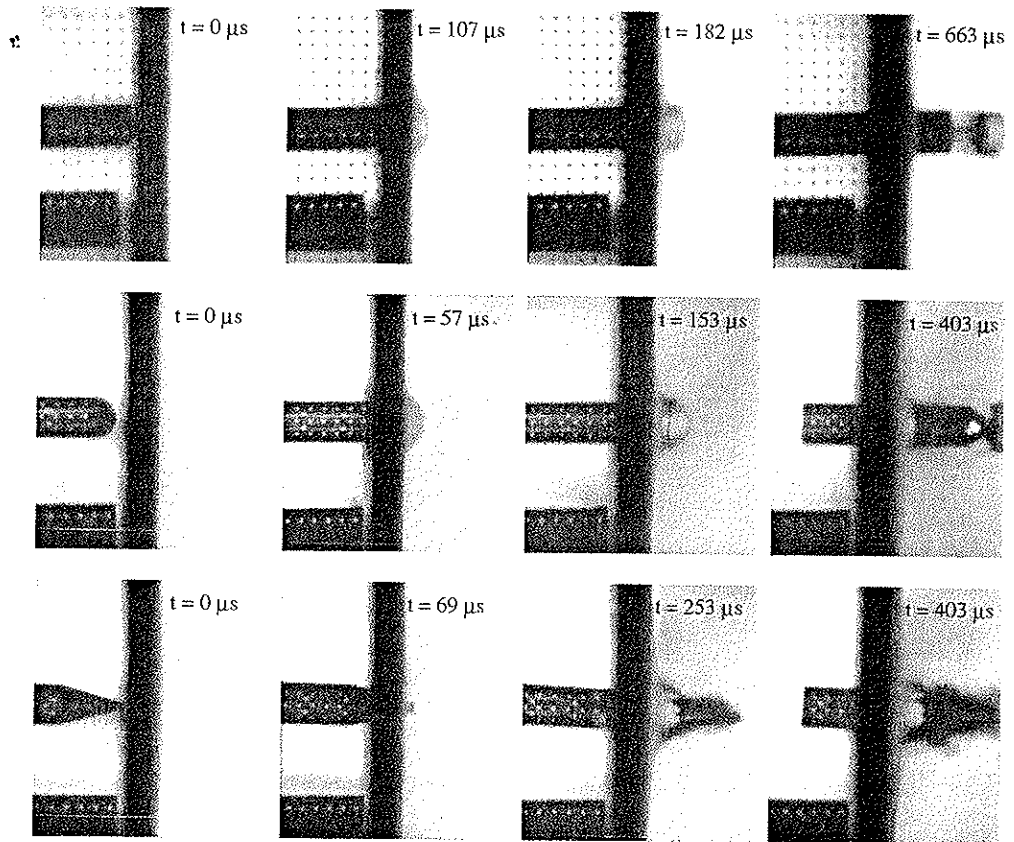


Fig. 4: A selection of high-speed camera images showing perforation of the target plate at impact velocities close to the respective ballistic limits with blunt (Test B15), hemispherical (Test H1) and conical (Test C6) projectiles.

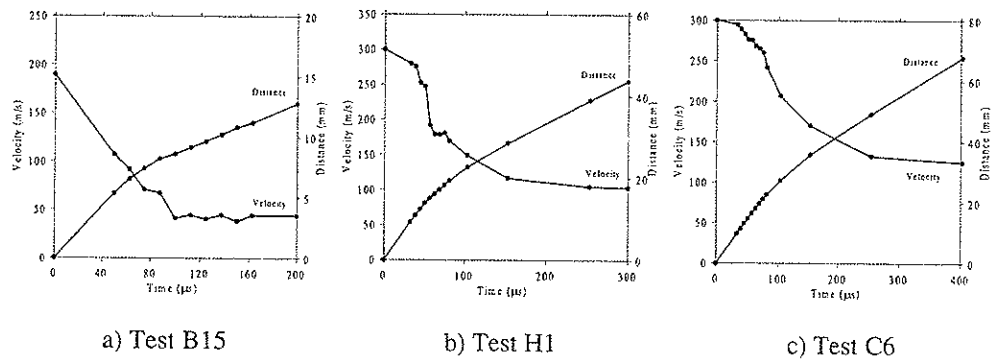
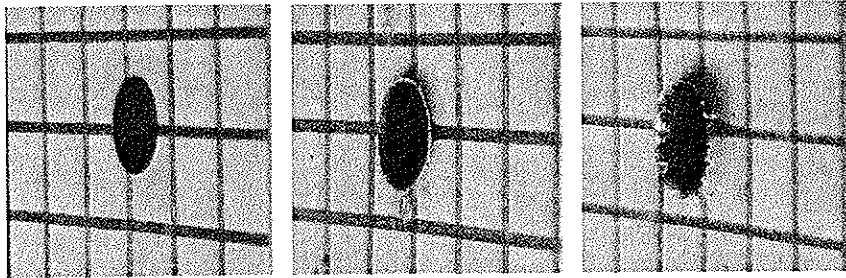


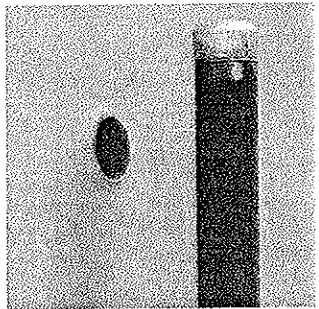
Fig. 5: Measured distance-time and velocity-time curves to the projectile based on the high-speed camera images (some of them are shown in Fig. 4).



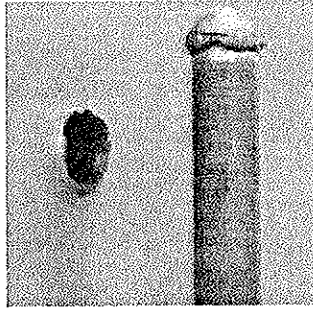
a) Test B15

b) Test H1

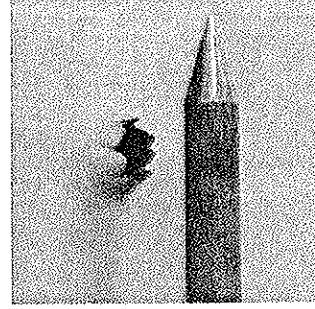
c) Test C6



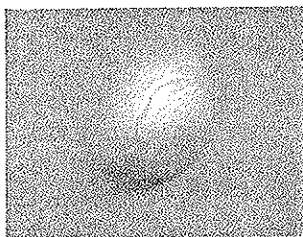
d) Test B15



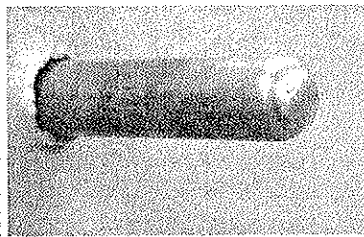
e) Test H1



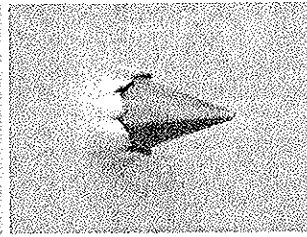
f) Test C6



g) Test H2

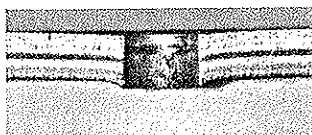


h) Test H4

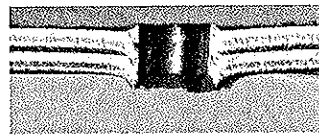


i) Test C5

Fig. 6: Details of some targets, projectiles and plugs after the test.



a) Test B15

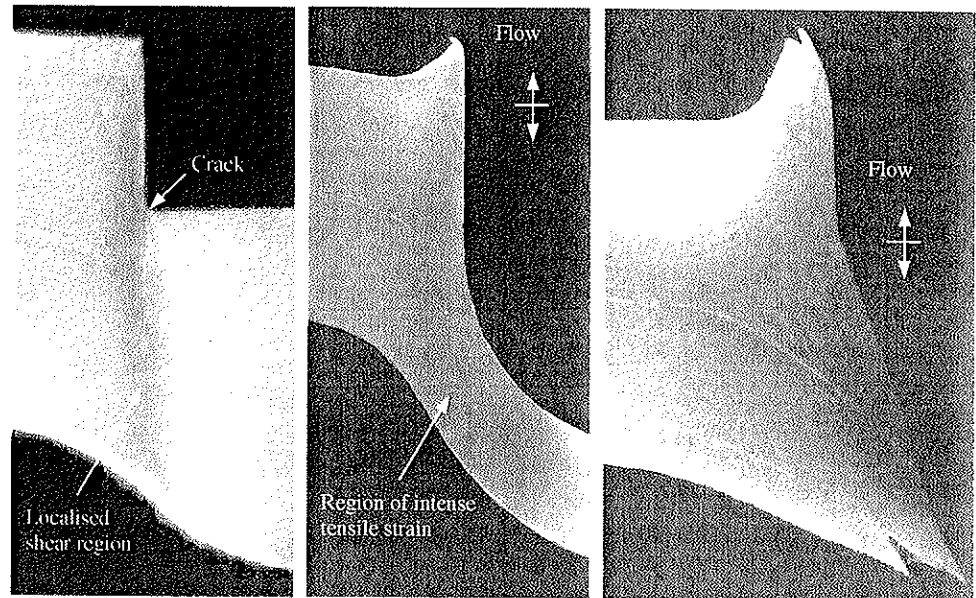


b) Test H1



c) Test C6

Fig. 7: Cross-sections of target plates perforated by a) blunt, b) hemispherical and c) conical projectiles.



a) Test B8

b) Test H2

c) Test C5

Fig. 8: Macrographs of sectioned and etched penetrated plates (not in scale).

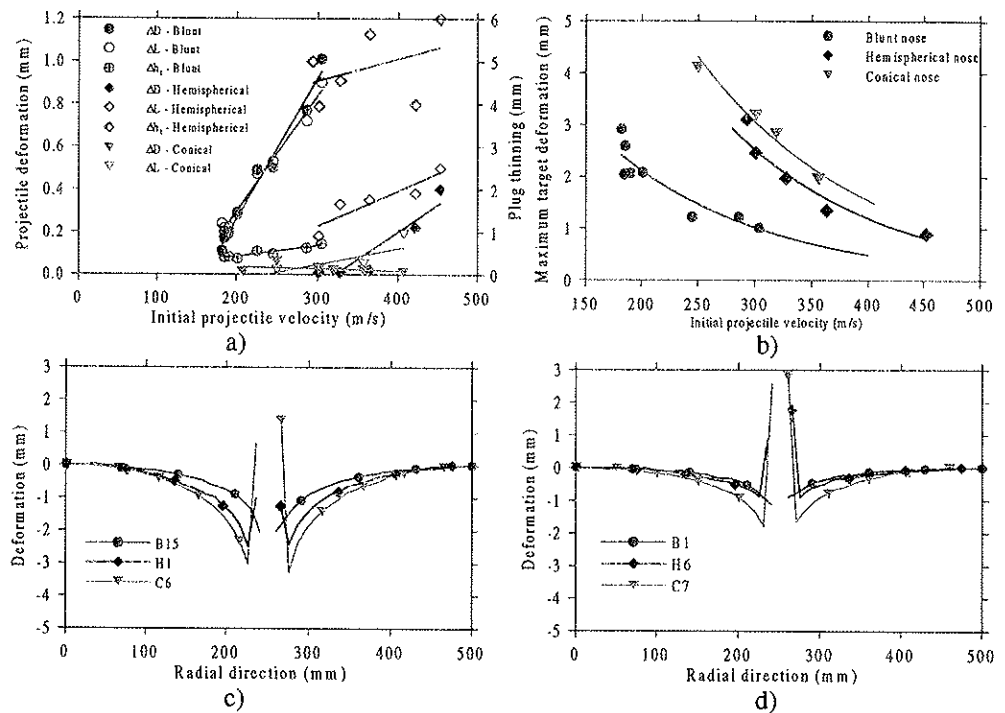


Fig. 9: a) Projectile deformation and plug thinning versus impact velocity, b) maximum target deformation versus impact velocity and c) measured permanent deformation profiles close to the ballistic limit and d) at the highest impact velocities.

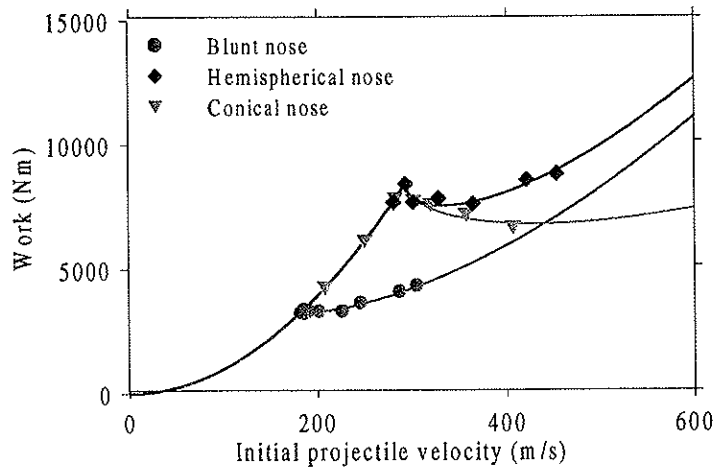


Fig. 10: Measured change in projectile kinetic energy ($\Delta K = W$) during testing.

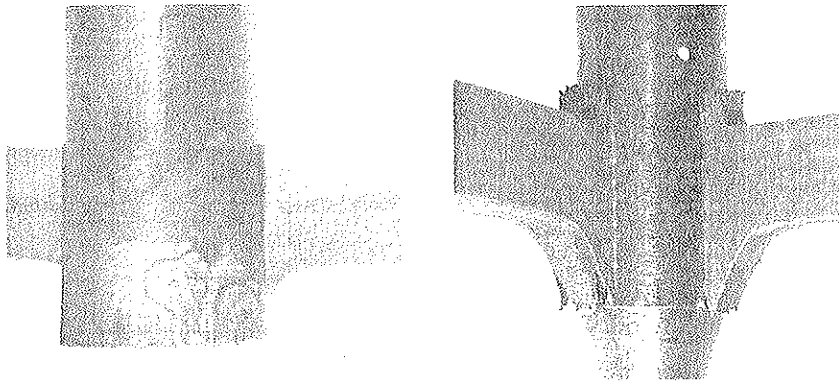


Fig. 11: Sliding contact between projectile and target with a) blunt (Test B5) and b) conical (Test C5) nose shape.

Table 1: Experimental results with blunt projectiles.

Test #	v_i (m/s)	v_r (m/s)	v_{rpl} (m/s)	m_{pl} (gram)	w_{max} (mm)	d_{ef} (mm)	d_{cr} (mm)	ΔD (mm)	ΔL (mm)	t_r^{**} (μs)
B20*	399.6	291.3	-	36.0	0.62	22.69	23.82	-	-	-
B1	303.5	199.7	242.3	27.6	1.01	20.65	20.93	1.01	0.90	60
B3	285.4	181.1	224.7	27.6	1.22	20.59	20.75	0.77	0.72	65
B2	244.2	132.6	187.7	28.1	1.22	20.42	21.18	0.50	0.53	69
B9	224.7	113.7	169.0	27.3	1.72	20.56	20.72	0.49	0.47	100
B4	200.4	71.4	103.7	27.8	2.08	20.35	20.88	0.29	0.28	104
B15	189.6	42.0	64.0	27.7	2.06	20.34	20.63	0.19	0.22	106
B14	184.3	30.8	45.3	27.8	2.04	20.35	20.64	0.17	0.20	110
B16	184.8	0	0	-	2.59	20.20	-	0.17	0.22	-
B8	181.5	0	0	-	2.92	20.21	-	0.11	0.24	-

* Projectile nose broke at impact. ** Estimated from the high-speed camera images.

Table 2: Experimental results with hemispherical projectiles.

Test #	v_i (m/s)	v_r (m/s)	v_{rpl} (m/s)	m_{pl} (gram)	w_{max} (mm)	d_{ef} (mm)	d_{cr} (mm)	ΔD (mm)	ΔL (mm)	t_r (μs)
H6	452.0	325.1	348.0	15.12	0.89	20.03	19.65	0.40	0.50	62
H7	420.6	284.3	301.8	19.80	1.43	21.16	20.17	0.22	2.38	84
H3	362.9	220.2	265.1	16.72	1.35	20.14	19.76	0.02	0.35	90
H5	326.7	154.8	189.4	18.08	1.97	20.1	19.68	0.01	0.33	102
H1	300.0	97.2	159.5	20.30	2.46	20.28	19.85	0.01	0.18	135
H4	292.1*	0	-	18.58	3.10	20.13	-	-	-	143
H2	278.9	0	-	-	-	-	-	-	-	-

* Assumed ballistic limit, see Fig. 6h.

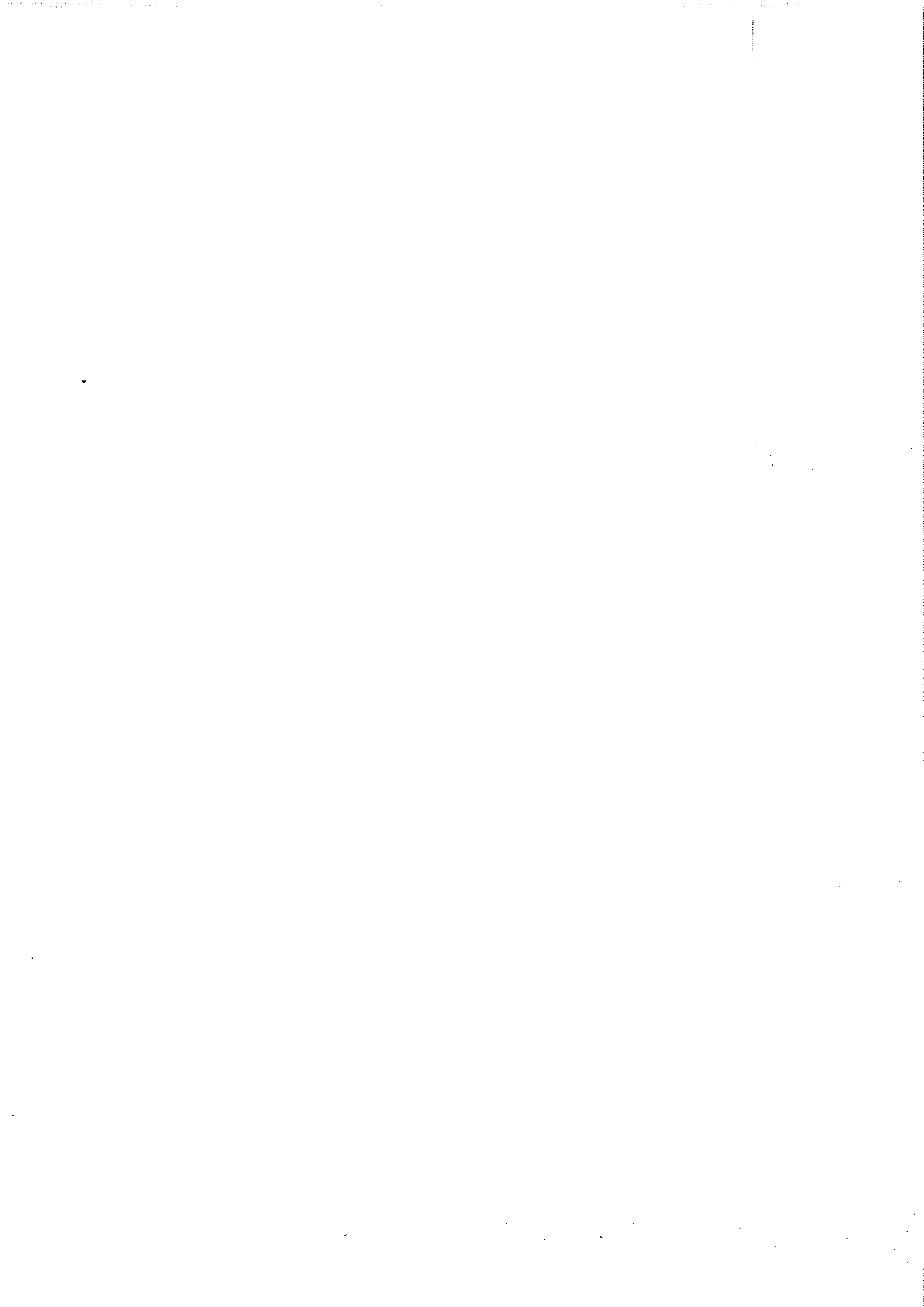
Table 3: Experimental results with conical projectiles.

Test #	v_i (m/s)	v_r (m/s)	v_{rpl} (m/s)	m_{pl} (gram)	w_{max} (mm)	d_{ef} (mm)	d_{cr} (mm)	ΔD (mm)	ΔL (mm)	t_r (μs)
C7	405.7	312.0	-	-	1.73	20.82	19.61	0.01	0.19	46
C4	355.6	232.3	-	-	1.95	20.58	19.59	0.02	0.05	52
C2	317.9	155.8	-	-	2.83	20.19	19.76	0.02	0.01	54
C6	300.3	110.3	-	-	3.18	21.40	19.76	0.03	0.02	62
C5	280.9	0	-	-	-	20.61	20.26	0.02	0.04	62
C1	248.7	0	-	-	4.10	20.24	11.56	0.06	0.02	68
C3	206.9	0	-	-	2.73	19.26	8.11	0.01	0.01	103

* Refer to the time for the projectile to pierce the target, and not to complete perforation (see e.g. Fig. 6i).

Table 4: Experimentally obtained ballistic limit velocities and curves.

v_{bl} (m/s)	Blunt			Hemispherical			Conical		
	a	p		v_{bl} (m/s)	a	p	v_{bl} (m/s)	a	p
184.5	0.79	2.24		292.1	0.81	2.71	290.6	0.95	2.52

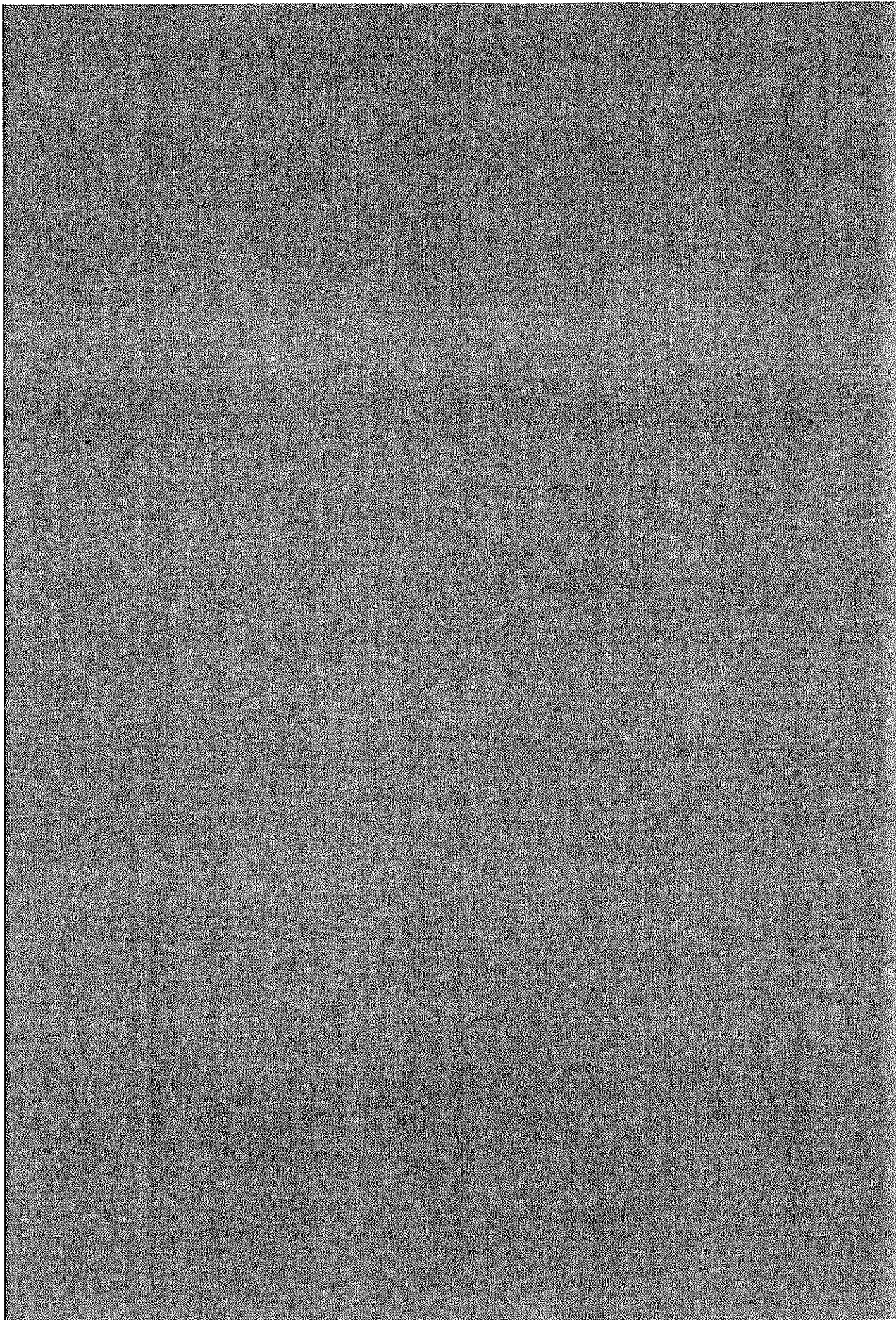


Part VII

T. Børvik, O.S. Hopperstad, T. Berstad and M. Langseth

Effect of Projectile Nose Shape in Structural Impact, Part II: Numerical Simulations.

Submitted for possible journal publication.



Effect of projectile nose shape in structural impact, Part II: Numerical simulations

T. Børvik^{*1}, O.S. Hopperstad¹, T. Berstad² and M. Langseth¹

¹*Structural Impact Laboratory (SIMLab), Department of Structural Engineering,
Norwegian University of Science and Technology, N-7491 Trondheim, Norway.*

²*Livermore Software Technology Corporation (LSTC), Livermore, CA 94550, U.S.A.*

Abstract

In Part I of this paper, projectiles with three different nose shapes (blunt, hemispherical and conical) were used in gas gun experiments to penetrate 12 mm thick Weldox 460 E steel plates. It was found that the nose shape of the projectile severely affected both the energy absorption and failure mode of the target structure during penetration. This part of the paper describes numerical simulations of the problem investigated experimentally. A constitutive model of viscoplasticity and ductile damage for projectile impact has earlier been developed and implemented in the explicit finite element code LS-DYNA. Numerical simulations involving the model have been carried out, and the results are compared with the experimental data. However, several numerical problems associated with the element mesh were detected, and adaptive meshing was found necessary in order to obtain reliable results for conical projectiles. From the numerical simulations it is seen that the LS-DYNA code is able to describe the different failure modes without any predefined defects in the element mesh if special care is taken, and good agreement is in general obtained between the numerical simulations and experimental results.

Keywords: Impact; Numerical simulations; Nose shape; Failure mode; Ballistic limit; Adaptive meshing

* Corresponding author. Tel.: + 47 73 59 46 47; fax: + 47 73 59 47 01.
E-mail address: tore.borvik@bygg.ntnu.no (T. Børvik).

Notation

Unless otherwise stated in the text or references the following notation apply:

ΔD	projectile nose deformation, i.e. $\Delta D = D_f - D_i$
ΔL	projectile length reduction, i.e. $\Delta L = L_i - L_f$
ϵ	strain
CPU	computational time
d	diameter
D	projectile nose diameter
El	number of removed elements
h	thickness or height
HRC	hardness Rockwell C
K	kinetic energy
L	projectile length
m	mass
T	temperature
t	time
v	velocity
w	deformation
W	work

Subscripts:

bl	ballistic limit
c	cavity
ee	eroded elements
f	final value or fracture
g	global part of target
i	initial value
l	local part of target
m	maximum value
p	projectile
pe	permanent value
pl	plug
r	residual value
t	target

1. Introduction

In Part I of this paper (Børvik et al, 2000c), projectiles with three different nose shapes (blunt, hemispherical and conical) were used in gas gun experiments to penetrate 12 mm thick Weldox 460 E steel plates. From the experimental study it was found that the nose shape of the projectile severely affected both the energy absorption and the failure mode of the target plate during penetration. Hemispherical and conical projectiles penetrated the target mainly by indentation and ductile hole enlargement. In this failure mode the material in front of the moving projectile is pushed aside. The ballistic limit velocity was almost identical for these two nose shapes and close to 300 m/s. Blunt projectiles, on the other hand, caused failure by plugging and the ballistic limit velocity was reduced to about 185 m/s. This failure mode is dominated by shear banding. However, at impact velocities above 440 m/s conical projectiles were found to be the most effective penetrator. From a qualitative estimate of the energy dissipation, it was observed that both the local plastic flow around the projectile nose and the global target deformation were most severe for conical projectiles, followed by hemispherical and blunt projectiles in that order. The opposite was observed regarding projectile plastic deformation.

As seen, depending on the specific penetration configuration, there may be various modes of failure and energy absorbing mechanisms. Thus, it is utmost important that numerical models used in structural impact problems are able to take these effects into account since the loading situation is never known in advance. A computational model of viscoplasticity and ductile damage for projectile impact has been developed and implemented in LS-DYNA (LSTC, 1999) by Børvik et al (1999). Numerical simulations using this model give results in close agreement with experimental data for plugging failure caused by blunt projectiles (Børvik et al, 1999, 2000a). The scope of the numerical study presented in this paper is to investigate if the code is able to describe the structural response to projectile impact when different failure modes are expected to occur. This is done by conducting numerical simulations of the experimental tests presented in Part I of the paper. However, it is important to realise that in these highly complex non-linear finite element simulations the material behaviour is not the only matter causing problems. As will be shown, several challenges are associated with the numerical approach itself and special care must be taken in order to avoid errors and premature termination of the analysis. LS-DYNA is a commercial general-purpose finite element code for analysis of large deformation dynamic response of structures based on explicit time integration, and is therefore suitable for the type of problem under investigation.

No attempts are here made in order to describe the many different algorithms involved in the numerical simulations. It is referred to the manuals of LS-DYNA (1998, 1999) for more detailed information regarding the numerical scheme, such as the contact-impact algorithm, the automatic mesh generator, the transfer operator and similar.

A limited review on recent papers in the area of numerical modelling of ballistic penetration and perforation was presented by Børvik et al (2000a), but surprisingly few papers dealing with such problems have appeared in the open literature. From the literature review it was, however, noticed that adaptive meshing is frequently used in simulations involving penetration. As will be demonstrated in the following, continuous remeshing provides an alternative to the common practice of elements erosion in Lagrangian codes. In some situations, such as in conical projectile penetration, adaptive meshing was found necessary in order to have reliable results.

2. Constitutive relation

The coupled computational model of viscoplasticity and ductile damage used to predict material behaviour under projectile impact loading has earlier been presented by Børvik et al (1999). Thus, only the main equations will be given in the following. The model is based on work by Johnson and Cook (1983,1985), Camacho and Ortiz (1997) and Lemaitre (1992). It includes linear thermoelasticity, the von Mises yield criterion, the associated flow rule, isotropic strain hardening, strain-rate hardening, softening due to adiabatic heating, softening due to isotropic damage evolution, and finally a failure criterion. The equivalent von Mises stress σ_{eq} is given as

$$\sigma_{eq} = [1-D][A + Br^n][1 + \dot{\epsilon}^*]^C [1 - T^{*m}] \quad (1)$$

where D is the damage variable; A , B , C , n and m are material constants; r is the damage accumulated plastic strain given as $\dot{\epsilon} = (1-D)\dot{p}$, where p is the accumulated plastic strain (Lemaitre, 1992); $\dot{\epsilon}^* = \dot{\epsilon} / \dot{\epsilon}_0$ is a dimensionless strain-rate, and $\dot{\epsilon}_0$ is a reference strain-rate; $T^* = (T - T_0) / (T_m - T_0)$ is the homologous temperature, where T is the absolute temperature, T_0 is the room temperature and T_m is the melting temperature of the target material, respectively. The damage variable D takes values between 0 (undamaged) and 1 (fully

broken). However, the critical value of damage is found to be less than 1. Hence, fracture occurs when

$$D = D_c \leq 1 \quad (2)$$

A damage evolution rule is proposed as

$$\dot{D} = \begin{cases} 0 & \text{when } p < p_d \\ \frac{D_c}{p_f - p_d} \dot{p} & \text{when } p \geq p_d \end{cases} \quad (3)$$

where D_c is the critical damage, \dot{p} is the plastic strain rate, p_d is the damage threshold and p_f is a fracture strain depending on stress triaxiality, strain rate and temperature given as

$$p_f = [D_1 + D_2 \exp(D_3 \sigma^*)] [1 + \dot{p}^*]^{D_4} [1 + D_5 T^*] \quad (4)$$

Here, D_1 to D_5 are material constants, $\sigma^* = \sigma_m / \sigma_{eq}$ is the stress triaxiality ratio and σ_m is the mean stress. The first bracket in Eq. (1) describes material degradation due to damage, and the irreversible damage evolution is related to the accumulated plastic strain through Eq. (3). The second bracket in Eq. (1) gives the yield and strain hardening, while the effect of strain-rate hardening as proposed by Camacho and Ortiz (1997) is expressed in the third bracket. The last bracket in Eq. (1) gives the effect of temperature softening on the equivalent stress. The temperature increase is based on the empirical assumption that 90 % of the plastic work under adiabatic conditions is dissipated as heat (Bammann, 1993). Any heat transfer with the surroundings is neglected in this model. When the softening due to damage and temperature exceeds the strain and strain rate hardening, localisation is expected to occur (Bai and Dodd, 1992). The model is implemented in LS-DYNA (1999) using a fully vectorised backward-Euler integration algorithm (Berstad, 1994). To allow crack growth during penetration, the model is coupled with an element-kill algorithm available in LS-DYNA that removes the damaged element from the mesh when the damage variable reaches the critical value D_c .

Four different types of tensile tests are required to identify the material constants used in the model (Børvik et al, 1999, 2000b). Quasi-static tensile tests are used to identify the elastic constants E and ν , and the yield stress A of the material. Notched-specimen tensile tests are

used to define the strain hardening constants B and n , the critical damage D_C , and the fracture strain constants D_1 , D_2 and D_3 . Dynamic tensile tests give the viscoplastic constant C and the fracture strain constant D_4 . Tensile tests at elevated temperatures provide the constants m and D_5 , defining the temperature effect on the stress-strain curve and on the fracture strain, respectively. Thermoelasticity is not included in these simulations (see Børvik et al, 2000a). For simplicity, the projectile is modelled as a bilinear elastic-plastic strain rate independent von Mises material with isotropic hardening, and quasi-static tensile tests were carried out on specimens machined directly from hardened projectiles in order to identify the material constants. All details regarding the model, material tests and calibration procedure can be found in Børvik et al (1999, 2000b). If not otherwise stated in the text, the tensile test model constants listed in Table 1 for the target material of Weldox 460 E steel and in Table 2 for the projectile material of hardened Arne tool steel are used in all simulations.

3. Simulations with a uniform element mesh

Uniform or fixed element meshes are still the most used discretisation method in finite element simulations, and such meshes are known to be both accurate and robust for problems involving small to moderate deformations (Belytschko, 1996). However, when large deformations and subsequently large plastic strains are present, meshes become progressively more and more distorted as the deformation increases. Distorted meshes are less accurate and may accordingly introduce numerical difficulties. Thus, in some transient dynamic problems, and in particular those dealing with projectile impact, uniform element meshes may give severe numerical inaccuracies and eventually an error termination of the simulation.

Here, in the first set of simulations a fixed mesh of 4-node 2D axisymmetric elements with one-point integration and a stiffness based hourglass control was used. Plots of the initial configurations, showing a part of the target plate and the three different projectile nose shapes just prior to impact, are given in Fig. 1. The target consists of two parts with identical properties in order to study global versus local energy absorption during impact (Børvik et al, 2000a). Recall from the experimental part of the study that the circular target plate has a nominal thickness of 12 mm and a diameter of 500 mm, while the nominal mass and diameter of the hardened projectile was 0.197 kg and 20 mm, respectively, in all tests. The exact geometry of the different projectile nose shapes in Fig. 1 is given in Fig. 2 in Part I of the paper. In each run the target plate was fully clamped at the support, while the projectile was

given an initial velocity similar to the one used in the corresponding experiment. The initial size of the smallest element in the impact region was $0.25 \times 0.2 \text{ mm}^2$ in all simulations, giving a total of 60 elements over the target thickness. In order to reduce the computational time, which is affected both by the element size and number, the mesh was somewhat coarsened towards the boundary. Owing to this coarsening, the total number of elements in the target plate was about 10000 in all simulations. Contact was modelled using an automatic 2D single surface penalty formulation available in LS-DYNA. In accordance with the experimental observations in Part I of the paper, frictional effects were neglected for blunt projectiles, while a small dynamic frictional coefficient of 0.05 was used between all surfaces in contact in simulations for conical and hemispherical projectiles.

Earlier simulations have indicated the problem involving shear localisation and plugging for blunt projectiles to be mesh size sensitive (Børvik et al, 2000a). However, the numerical solution using the present model seems to converge monotonically towards a limit solution when the number of elements over the target thickness becomes sufficiently large, i.e. the mesh size dependency is not pathological. It is therefore assumed that the numerical results will improve as the element size is reduced, until it stabilises at some value. This is as expected, since the width of a deformed or transformed adiabatic shear band is known to be at the order of 10^1 - $10^2 \text{ }\mu\text{m}$ (Bai and Dodd, 1992). From the metallurgical examination carried out in Part I of the paper (see Fig. 8), shear localisation was not found for hemispherical and conical projectiles. Thus, it is likely to assume that the mesh size sensitivity is most distinct in simulations involving blunt projectiles.

Numerical results from simulations with blunt and hemispherical projectiles are given in Table 3. The computed residual projectile velocities were inserted into the Recht-Ipson (1963) model, given in Eq. (1) in Part I of the paper, and the method of least squares was used to estimate the ballistic limit velocities and the model constants a and p given in Table 4. As seen, the agreement with the experimental results presented in Table 4 in Part I of the paper is good. While the experimental ballistic limit velocities are 184.5 and 292.1 m/s for blunt and hemispherical projectiles, respectively, the corresponding numerical values are 196.4 and 297.3 m/s, i.e. a non-conservative deviation of 6 and 2 %. Also the residual velocity curves, represented by a and p in Table 4 and shown as the dotted lines in Fig. 6, are well predicted by the numerical model. A direct comparison between these curves and the residual velocity curves obtained experimentally is given in Fig. 22. At the highest impact velocities, some more plastic deformation of the projectile takes place experimentally than

what is captured in the simulations. This is probably due to the simple constitutive model used for the projectile material (Børvik et al, 2000a). Remember also that the experimentally obtained residual velocity curve for the hemispherical projectile was assumed low at the highest impact velocities due to an abnormal projectile deformation in one of the tests (see Part I of the paper). It follows that the deviation between the experimental and numerical residual velocity curves increases with impact velocity. Plots showing perforation of the target plate by a blunt and a hemispherical projectile at impact velocities close to the respective ballistic limits are given in Fig. 2. Here, fringes of accumulated damage are plotted on the deformed mesh. If these plots are compared to the high-speed camera images in Fig. 4 in Part I of the paper or to micrographs of the crack propagation in a plate impacted by a blunt projectile (Børvik et al, 1999), it is clearly demonstrated that the numerical model also qualitatively captures the overall physical behaviour of the target plate during penetration.

However, numerical problems occurred when conical projectiles were simulated using the fixed element mesh in Fig. 1 and the original material constants from Table 1. Owing to the severe hydrostatic compression in the elements just in front of the nose tip, the actual fracture strain, which is a function of the stress triaxiality ratio, increased dramatically. This delayed the damage evolution process and consequently the erosion of damaged elements. Thus, the elements in the impacted area were significantly distorted, and the time step started to drop. As a final result, the upper nodes in a critical element penetrated the lower nodes, giving a negative element volume and subsequently error termination of the simulation. Even though severe distortions were obtained in some elements also for blunt and hemispherical projectiles during impact, error termination only occurred for conical projectiles. The problem is illustrated in Fig. 3, where the element distortion in the target plate just after impact is shown for the three different projectile nose shapes. In an attempt to avoid this problem, two different approaches were explored.

The first approach involved forcing the elements causing problems to erode at an earlier stage. This can easily be done by altering the material constants D_1 to D_3 used to describe the strain to failure under different stress states. Fig. 4 shows experimentally measured fracture strains ϵ_f as a function of the stress triaxiality ratio σ^* (Børvik et al, 1999). The solid line through the data points is determined from a least square fit of the fracture strain constants D_1 to D_3 in the fracture model given by Eq. (4) to the experimental data from quasi-static tensile tests on smooth and notched specimens at room temperature. The strong effect of stress triaxiality on ductility indicated by the model is generally accepted, and has been confirmed

experimentally by e.g. Bridgman (1952), Hancock and Mackenzie (1976) and others. Nevertheless, in this study no experimental data is available for Weldox 460 E under pure shear ($\sigma^* = 0$) and hydrostatic compression ($\sigma^* < 0$), and the extension of the curve into the compression region is solely based on the hydrostatic tension test data. It is thus possible to recalibrate the fracture strain constants to $D_1 = -5.0388$, $D_2 = 6.6198$ and $D_3 = -0.0774$. This gives the almost linear dependence of the fracture strain on the stress triaxiality ratio as shown by the dotted line in Fig. 4. Lindholm and Johnson (1982) indicated a similar linear trend based on experimental results from the literature. Consequently, a reduced fracture strain under hydrostatic compression is obtained, while still having a very close fit to the experimental data.

Numerical simulations were then carried out with conical projectiles and the new values of the fracture strain constants D_1 to D_3 . Except for these three values, the numerical model was exactly as before. Plots showing perforation of the target plate by a conical projectile at an impact velocity close to the ballistic limit are given in Fig. 5, where fringes of accumulated damage are plotted on the deformed mesh. Here, no numerical problems occurred and qualitatively close agreement is seen between the simulated behaviour and the high-speed camera images in Fig. 4 in Part I of the paper. A negligible plug of 3-4 elements was ejected in some of the simulations. Such plugs were not observed in any of the tests on Weldox 460 E steel, but has been seen in similar experiments on aluminium alloy AA5083. Notice also how well the complex sliding along different contact interfaces are described by the automatic contact-impact algorithm. Accurate comparison of results from simulations with different projectile nose shapes requires that all simulations are performed using the same material constants. Therefore, the penetration tests with blunt and hemispherical projectiles were also re-analysed with the new fracture strain constants.

Numerical results from all simulations with blunt, hemispherical and conical projectiles, a uniform element mesh and the new values of the fracture strain constants D_1 to D_3 are given in Table 5. In a similar way as before, the computed residual projectile velocities were used together with the Recht-Ipson model to estimate the ballistic limit velocities given in Table 6. As seen, the ballistic limits are somewhat reduced due to the reduced fracture strain under hydrostatic compression, while the shape of the residual velocity curves, represented by a and p in Table 6, are less affected by this reduction. If the new ballistic limit velocities are compared to the experimental results presented in Table 4 in Part I of the paper, a conservative deviation of about 8 % for all nose shapes are obtained. The different residual

velocity curves are plotted and compared with results from simulations using the original fracture strain constants in Fig. 6. In an exactly similar manner as found experimentally, the ballistic limit velocity for hemispherical and conical projectiles are about equal, while it is considerably lower for blunt projectiles. Also the residual velocity curves are similar, but one major difference is observed. While the residual velocity curve for hemispherical projectiles merges into the curve for blunt projectiles at high impact velocities in the experiments, the same curve is almost parallel and relatively close to the curve for conical projectiles in the numerical simulations (see also Fig. 22). Except for this difference, the overall agreement between numerical simulations and experimental results is in general very good. Notice also that the values of a and p in the best fit using conical projectiles are equal to 1.0 and 2.05, respectively. Recht and Ipson showed theoretically that $a = m_p / (m_{pl} + m_p)$, where m_p and m_{pl} are the mass of the projectile and plug, respectively, and $p = 2$. For conical projectiles, no plug is ejected and m_{pl} is zero. Thus, a is also theoretically equal to 1. A similar behaviour for the model constant a can be seen both for blunt and hemispherical projectiles.

As clearly demonstrated in Fig. 6, the main trends in the simulations are similar when the original and the new fracture strain constants are used, and the effect of reducing the fracture strain is most distinct on the ballistic limit velocity. Thus, it seems safe to compare numerical results and to draw qualitative conclusions based on the simulations with the new fracture strain constants. Fig. 7 compares velocity-time curves and Fig. 8 compares force-time curves from simulations close to the respective ballistic limits for blunt, hemispherical and conical projectiles. Here, the plots for blunt and hemispherical projectiles are from simulations using the original fracture strain values, while plots for conical projectiles are obtained using the new fracture strain constants. A similar behaviour as the one measured based on the digital high-speed camera images is obtained (see Fig. 5 in Part I of the paper). This can be used to explain the distinct difference in projectile plastic deformation observed both experimentally and numerically. Even though the impact velocity for a blunt projectile is almost 50 % less than the impact velocity using a conical projectile, the maximum interface force is about 5 times higher and occurs immediately after impact. Cross-sections of the same target plates after perforation are presented in Fig. 9, where fringes of accumulated plastic strain are plotted on the deformed mesh. Here, the fringe colour red indicates a plastic strain above 120 %. While only limited plastic deformations occur outside the localised shear zone for blunt projectiles, the plastic zone is far more extensive for hemispherical and conical projectiles. However, the difference in cross-section between hemispherical and conical projectiles is

small. This difference was much more distinct in the experimental study, as shown in e.g. Fig. 7 in Part I of the paper. Maximum target deformations from numerical simulations are shown in Fig. 18. In close agreement with the experimental observations, the deformation is found to decrease from a maximum value at the ballistic limit towards a value less than 1 mm as the impact velocity becomes high. Conical projectiles are also numerically found to give the largest target deformation, followed by hemispherical and blunt projectiles. As expected, the maximum deformation is higher both for blunt and hemispherical projectiles using the original model (thick solid lines) than the model with new fracture strain constants (dotted lines). The maximum deformation is also found to be much higher numerically than experimentally at identical impact velocities. This is mainly due to that the numerical values are measured immediately after fracture, while the corresponding experimental values are measured after elastic rebound.

The amount of energy absorbed during penetration using a fixed element mesh and different projectile nose shapes is finally considered. The total energy balance, given by Eq.(2) in Part I of the paper, indicates that some of the energy is lost in the analyses. A small amount is used in sliding and hourglass energy, but this is found to be negligible in these simulations. However, more severe losses of both energy and mass may take place due to element erosion. This is important in simulations where a large number of elements are eroded at impact velocities close to the ballistic limit (see Table 5). In the worst case, run 272-60, where a conical projectile and the new fracture strain constants were used, more than 10 % of the total energy was lost. For most other cases the loss in total energy is much smaller, typically 1-3 % (see Fig. 20). The target is modelled as one local and one global part with identical properties, as shown in Fig. 1. The border between the parts is placed two element columns, i.e. 0.5 mm, outside the projectile boundary. An examination of the target during perforation shows that all eroded elements are situated within the local part of the plate (see e.g. Fig. 12). Thus, it is reasonable to assume that the total energy loss is due to the loss of internal energy in eroded elements in the local part of the target. In other words, a perfect energy balance is obtained if the total energy loss is added to the local work W_1 .

The total amount of projectile kinetic energy converted into target and projectile work during impact is given in Table 3 for the original model and in Table 5 for the new fracture strain constants, and this is plotted in Fig. 10. As also observed experimentally (see Fig. 10 in Part I of the paper), the amount of work carried out by the system drops from a local maximum at the ballistic limit to a local minimum just after perforation. Then it starts to increase monotonically with impact velocity for blunt and hemispherical projectiles, while

the conducted work is almost constant for conical projectiles. Also numerically blunt projectiles are found to be the most efficient penetrator to a velocity of about 440 m/s. At higher impact velocities, both hemispherical and conical projectiles are more efficient using the new fracture strain constants, while hemispherical projectiles becomes more efficient than blunt projectiles at an impact velocity above 530 m/s using the original fracture strain constants. This is in contradiction with the experimental results in Part I of the paper, where hemispherical projectiles were found to be the least efficient penetrator in all tests.

Details from the energy calculations are plotted in Fig. 11 for simulations using the new fracture strain constants. As seen, the energy absorption for hemispherical and conical projectiles is very similar, while blunt projectiles show a somewhat different behaviour. First, the amount of energy absorbed by the blunt projectile is considerable and increases with impact velocity, while the local work is moderate due to the localised plugging failure. Second, the amount of global target work increases with velocity for blunt projectiles. In contrast, for hemispherical and conical projectiles the global work decreases with impact velocity, at least within the stated velocity range. These results may have been affected by the chosen location of the border between the local and global parts in the model, especially for blunt projectiles.

As illustrated in Fig. 12, many elements are eroded in simulations with hemispherical and conical projectiles. Severe erosion of elements also appears for blunt projectiles at the highest impact velocities, but in these simulations the effect is of minor importance in the energy balance. Furthermore, the lower the fracture strain becomes, the more elements are eroded. Consequently, hemispherical and conical projectiles erode the material in front of the nose instead of pushing it out laterally as obtained experimentally. Thus, neither conservation of mass nor energy is achieved in these analyses. However, in the newest version of LS-DYNA, it is possible to store both the energy and mass of removed elements in the history variable output to satisfy the conservation laws. Even though fixed element meshes give good results, particularly in plugging failure close to the ballistic limit, there is a need for a more physically correct method, especially for conical projectiles. Thus, the second and physically more correct approach used in this study is adaptive meshing without altering the material constants in the constitutive model.

4. Simulations with adaptive meshing

Lagrangian solution techniques based on a fixed element mesh generally works well as long as the element distortion is moderate. But, in the presence of large deformations such as in ballistic penetration, finite elements may become severely distorted (see Fig. 3). This in turn may cause premature termination of the analysis, or give unacceptably small time steps. Therefore, in some situations an Eulerian approach that is not affected by deformation-induced mesh distortions may seem necessary. However, as pointed out by Camacho and Ortiz (1997), Eulerian formulations of ballistic penetration suffer from several shortcomings. This has enforced the development of alternative methods to avoid numerical problems due to mesh disturbances. The simplest approach is to use an erosion or element kill technique as in the previous chapter, where troublesome elements simply are removed from the mesh in accordance with a failure criterion. However, this technique is as just demonstrated not always adequate (see Fig. 12). Other techniques, such as the coupled ALE (Arbitrary-Lagrangian-Eulerian) formulation or the more recent "meshless methods" (Belytschko et al, 1996), have been developed to solve problems involving large plastic flow in localised areas. The latter method also seems to have a great potential in describing propagating discontinuities, such as arbitrary crack growth in brittle materials.

However, the approach that has received most attention during the last decade is probably the adaptive meshing method. This method is used to extend the domain of application in Lagrangian codes. Adaptive meshing is generally classified into several groups. In the present version of LS-DYNA (LSTC, 1999) only two of these are available. The first method is often referred to as r-adaptivity, moving grid adaptivity or rezoning. Here, the number of elements and nodes are tried fixed, while the nodal positions are relocated to achieve optimal aspect ratios of the elements within a part at predefined time intervals. The second available method, called fission h-adaptivity, subdivides the elements into smaller elements whenever an error indicator shows that subdivision of these elements is necessary for improved accuracy. Unfortunately, the fission process can only be applied to specific groups of shell elements, and r- and h-adaptivity can not be combined in the present version of LS-DYNA.

The advantages of using adaptive meshing in ballistic penetration are undoubtedly many (Camacho and Ortiz, 1997). It enables the simulation of large plastic flow in a Lagrangian framework. It may also include the possibility to obtain a solution of comparable accuracy using much fewer elements, and hence less computational resources than with a fixed mesh. Rezoning ensures good element aspect ratio, thus preventing severe mesh distortions and

unacceptable small time steps in the simulations. The major disadvantages with the method are the possible introduction of inaccuracies and smoothing of the results during mapping of the history variables. In this study, 2D r-adaptivity is used in combination with a simplified approach to imitate the advantages of h-adaptivity in the penetration problem. Since the simulations with blunt and hemispherical projectiles worked satisfactory using a fixed element mesh, rezoning was only crucial for the conical projectiles. However, in order to be able to compare the results, all test configurations were re-analysed using adaptive meshing.

The adaptive method available in the commercial version of LS-DYNA was originally intended for forging operations, and not for ballistic penetration involving failure. Thus, in order to carry out simulations some new features had to be implemented in the code. First, it was not possible to rezone only the local part of the target plate, while keeping the global part fixed. This resulted in a complete relocation of the entire element mesh at each rezoning, also in the relatively inactive parts at the boundary, causing an increase in both computer time and data storage requirements. In order to solve this problem a subroutine that refines the element mesh from the boundary towards the centre by a predefined factor was implemented. This could be done since the zone of large deformation gradients, giving severe mesh distortions, always is at the centre of the target in these particular tests. Thus, the method imitates the advantage of h-adaptivity, which keeps the order of the elements unchanged while seeking to improve the solution by adaptive mesh refinement and coarsening in active and inactive areas, respectively. In this study a scale factor of 10 was used in the radial direction in all simulations, which means that there are 10 times more elements over the thickness in the impacted region than at the boundary. One disadvantage with this approach is that only a single part is modelled, so that there is not longer possible to study local versus global energy absorption in the target during penetration. Secondly, there was a need to modify the automatic mesh generator in LS-DYNA so to construct a new mesh from the contour of the previous mesh when propagating cracks due to eroded elements formed new parts such as a plug or fragment. Since the mesh generator required uniquely defined closed contours in order to work, it was necessary to automatically divide the original part into two or several closed parts at failure. If not, error occurred in the simulations when the lines defining the contour overlaid each other. Nodal values for all variables to be remapped are generated using a least square best fit. A completely new mesh is then generated from the old mesh at each remeshing interval. In the new mesh, the elements are adjusted towards a given characteristic element size. Finally, the remeshed regions are initialised by interpolation from nodal point values in the old mesh to the corresponding new nodal positions.

In fact, only one additional parameter (and some default values) is needed in the input file in order to run adaptive simulations. This parameter, ADPFREQ, defines the time interval between adaptive refinements. For blunt projectiles, ADPFREQ was adjusted to give approximately 10 adaptive refinements in each run. For hemispherical and conical projectiles, many more refinements were required, and as many as 100 were used in some of the simulations. As pointed out by Scheffler and Zukas (2000), such frequent rezoning may render the computational mesh semi-Eulerian and give the results a smoothness characteristic of Eulerian calculations. A second input is also demanded, ADPTOL, but this is just the characteristic element size, equal to the smallest element in the impact region. However, the automatic mesh generator available in LS-DYNA was rather unstable, and caused error if the lines defining the contour overlaid each other or if internal eroded elements were present at rezoning. The instability problems increased with number of elements, and it was for that reason decided to run all adaptive simulations with a characteristic element size of $0.3 \times 0.375 \text{ mm}^2$, giving only 40 elements over the target thickness. The potential effect of mesh size sensitivity in adaptive simulations will not be discussed in this paper. Except for these parameters, the numerical model with the adaptive mesh was exactly the same as the model with the fixed mesh, using the original material constants as given in Table 1 and Table 2.

Numerical results from adaptive simulations are given in Table 7, while ballistic limit velocities and curves, estimated from the Recht-Ipson model, are given in Table 8. Since the results from adaptive simulations are not as easily available as in fixed mesh simulations the content in Table 7 is somewhat reduced compared to Table 3 and Table 5. The very good aspect ratio of the elements just in front of the projectile after rezoning is clearly seen in Fig. 13. These plots should be compared with Fig. 3 where the fixed element meshes are shown just after impact. Notice also from Fig. 13 how the element mesh shapes and forms around the nose of the projectile as it slides into the target. No numerical problems appeared when using conical projectiles and the original fracture strain values when rezoning was allowed. Fig. 14 shows some detailed plots from the perforation process using different projectile nose shapes and adaptive meshing. Again, qualitatively good agreement is obtained between simulations and experiments. Note also that the remeshing continues after complete fracture. This is important, especially for conical projectiles, since the perforation process continues even though the target has been pierced. The final cross-section of a target plate perforated by a conical projectile at an impact velocity close to the ballistic limit is shown in Fig. 15. As seen, the cross-section is more similar to the experimental cross-section (see Fig. 7 in Part I of the paper) than the corresponding cross-section shown in Fig. 9 using a fixed mesh. Thus,

when rezoning is allowed the material in front of the projectile nose is pushed out laterally instead of being eroded. This is also clearly seen from the number of eroded elements (E_1) in the simulations given in Table 3, Table 5 and Table 7. While approximately 1500 elements were eroded in the simulation using a fixed element mesh and the new fracture strain constants, only about 60 elements were eroded in the corresponding simulation using rezoning. Vector plots of the nodal displacements can be used to study material flow in the target after impact. The direction of the flow is found very similar to the one obtained microscopically and presented in Fig. 8 in Part I of the paper, i.e. a lateral flow of the material in front of the projectile. This was not the case using a fixed element mesh, where the material flow essentially was parallel to the direction of the moving projectile. Finally, Fig. 16 illustrates the coarsening of the element mesh towards the boundary during perforation of the target by a conical projectile. As seen, the mesh is denser around the projectile nose where the rate of deformation is most intense. Notice also that in these plots, only a part of the complete target plate is shown.

The different residual velocity curves are plotted in Fig. 17. It is interesting to observe that both the ballistic limit velocity and the parameters a and p defining the residual velocity curve (see Table 8) for blunt and hemispherical projectiles using adaptive meshing are close to the corresponding values using a fixed element mesh and the original material constants (see Table 4 and Fig. 6). This gives confidence to the adaptive method used in the simulations. In contrast to both the experimental results and the numerical results using a fixed element mesh and the new fracture strain constants, there is a small difference between the ballistic limit velocities for hemispherical and conical projectiles. However, this difference is not more than 7% and the shapes of the residual velocity curves are very close. If compared to the experimental results, the deviation in ballistic limit velocities using adaptive meshing is 10%, 2% and 4% for blunt, hemispherical and conical projectiles, respectively. The increased deviation in ballistic limit velocity for blunt projectiles may be due to the coarser element mesh used in the adaptive calculations than in the fixed mesh simulations.

Fig. 18 shows that the maximum target deformation from adaptive simulations is similar to those obtained using a fixed element mesh. Furthermore, Fig. 19 indicates that the perforation times obtained from the different numerical simulations are similar and close to the experimental ones estimated from the high-speed camera images (see Part I of the paper). As seen, the perforation time is slightly lower using a fixed element mesh and the new fracture strain constants than for the other models at identical impact velocities.

Since there is only one part in the target plate using adaptive meshing, it is not possible to study local versus global energy absorption during penetration. The energy ratios, defined as $\Delta K / W$, from some of the simulations are given in Fig. 20. This figure shows that the energy ratios for blunt projectiles are almost unity, independent of numerical method, which again shows that there is hardly any energy losses in the simulations even at the highest impact velocities where the number of eroded elements may become considerable. For conical projectiles, on the other hand, much more energy is lost when a fixed mesh is used. As shown in Fig. 20b, nearly 10 % of the energy is lost in a simulation close to the ballistic limit. According to Scheffler and Zukas (2000), losses greater than 10 % in the sliding interface prescription is usually indicative of a serious problem. However, almost no energy is lost in the corresponding simulation using adaptive meshing. Thus, conservation of energy is fulfilled also for conical projectiles when rezoning is introduced. A comparison of time step size histories for the different numerical cases is shown in Fig. 21 for blunt and conical projectiles. In order to have a reliable evaluation, the two adaptive simulations were recalculated using 60 element over the target thickness. Thus, the initial element size was identical in these simulations. However, since there is no refinement and coarsening of the element mesh in the adaptive strategy, the expected superior performance was to some extent absent. The time step size is seen to be almost equal for blunt projectiles, independently of numerical strategy. This indicates that the distortion of the elements in plugging failure is similar in adaptive and fixed mesh calculations, since the required time step is controlled both by the minimum size and number of elements. Using conical projectiles, the situation is somewhat different. Here, the elements in front of the nose tip are severely deformed, and the time step size is reduced accordingly using a fixed element mesh. By way of contrast, the aspect ratio is optimised in the rezoning procedure using adaptive simulations. This is illustrated in Fig. 21b, where a distinct increase in the time step size is seen when critical elements are rezoned. Nevertheless, it is seen from the required CPU-times listed in Table 3, Table 5 and Table 7 that the differences in computational time is not considerable in these simulations, and usually between 1 to 10 CPU-hours on the workstations used in the study.

Finally, a comparison between numerical and experimental results for blunt, hemispherical and conical nosed projectiles are given in Fig. 22. For the two first mentioned, results from simulations using the uniform element mesh and the original fracture strain values are used (see Fig. 6, Table 3 and Table 4). For the conical projectile, on the other hand, results from the adaptive simulations given in Fig. 17, Table 7 and Table 8 are used. As seen, the agreement between numerical and experimental values is in general very good.

5. Concluding remarks and summary

The use of computer codes to solve transient dynamic problems is today commonplace, and a large number of commercial FE codes exist. These codes are applied to problems ranging from fairly low to extremely high damage levels (Scheffler and Zukas, 2000). Thus, it becomes increasingly important to validate that code predictions correspond to the real physical behaviour of a structure impacted by a projectile, especially if different energy absorbing mechanisms and failure modes are expected to appear. In this paper, more than 60 different numerical simulations are reported, using more than 200 CPU-hours on either a HP C360 or a HP J5000 workstation. The numerical results are compared with 24 different high-precision, large-scale impact tests (see Part I of the paper). In other words, both the numerical and experimental evidences are considerable, and this gives confidence to the observations.

In general, close correlation between numerical and experimental results is achieved. Important parameters in the penetration problem such as ballistic limit velocity, residual projectile velocity, shape of residual velocity curve, maximum target deformation, perforation time and energy absorption, are all well predicted numerically if special care is taken. Hence, the computational methodology presented in this paper seems to work well for ductile target perforation by deformable projectiles with different nose shapes in the sub-ordnance velocity regime. The model is formulated within a Lagrangian framework, which has many advantages in ballistic penetration. It is furthermore shown that rezoning plays an important role in order to avoid critical element distortions and severe numerical problems, such as those reported for conical projectiles. Thus, adaptive meshing enlarges the field of application for the Lagrangian formulation and is undoubtedly an attractive alternative to the common practice of element erosion. Some of the main conclusions from the numerical simulations are given below:

- Both the ballistic limit velocity and the residual velocity curve were in agreement with the experimental results for blunt and hemispherical projectiles for a fixed element mesh and the original constitutive model proposed by Børvik et al (1999).
- Numerical problems occurred when conical projectiles were tried simulated using a fixed element mesh and the original material constants. This was due to severe hydrostatic compression just in front of the nose tip, which delayed the element erosion process and finally caused an error termination of the simulation.

- In the first attempt of avoiding this problem, the material constants describing the fracture strain under hydrostatic compression was reduced, causing troublesome elements to erode at an earlier stage. This made it possible to simulate perforation of the target plate also by conical projectiles. Qualitatively, good correlation with the experimental results was obtained. However, a closer examination revealed that the elements in front of the nose tip of hemispherical and conical projectiles were mainly eroded instead of being pushed out laterally as observed experimentally. This caused, among other factors, unacceptable large energy losses in the simulations.
- Adaptive meshing were finally applied. After some minor changes in the rezoning capability available in LS-DYNA, good agreement was obtained. Both the ballistic limit velocity and the residual velocity curve were almost identical for blunt and hemispherical projectile using either a fixed mesh or adaptive meshing. No numerical problems occurred with conical projectiles and the original fracture strain constants when rezoning was allowed, and the energy losses due to eroded elements were small. If compared to the experimental results, the deviation in ballistic limit velocity using adaptive meshing is 10%, 2% and 4% for blunt, hemispherical and conical projectiles, respectively.
- At the highest impact velocities, plastic deformation of the projectile may become severe and this absorbs a lot of the initial kinetic energy. The simple material model used in these simulations for the projectile is not able to describe this behaviour correctly. Thus, the coupled computational model of viscoplasticity and ductile damage should in following simulations also be calibrated for the projectile material.

Acknowledgements

The authors would like to express their gratitude to the Norwegian Defense Construction Service, Central Staff/Technical Division, for their generous financial support of this study.

References

- Bai, Y. and Dodd, B., 1992. *Adiabatic Shear Localization: Occurrence, Theories and Applications*, Pergamon.
- Bammann, D.J., Chiesa, M.L., Horstemeyer, M.F. and Weingarten, L.I., 1990. Failure in Ductile Materials using Finite Element Simulations, In *Structural Crashworthiness and Failure*, edited by N. Jones and T. Wierzbicki, Elsevier Applied Science, pp. 1 - 54.
- Belytschko, T., Krongauz, Y., Organ, D., Fleming, M. and Krysl, P., 1996. Meshless Methods: An Overview and Recent Developments, *Computer Methods in Applied Mechanics and Engineering*, special issue on Meshless Methods, Vol. 139, pp. 3 - 47.
- Belytschko, T., 1996. On Difficulty Level in Non Linear Finite Element Analysis of Solids, *Bulletin Int. Assoc. Comp. Mech.*, No. 2, pp. 6 - 8.
- Berstad, T., Hopperstad, O.S. and Langseth, M., 1994. Elasto-Viscoplastic Constitutive Models in the Explicit Finite Element Code LS-DYNA3D, In: *Proceedings of the Second International LS-DYNA3D Conference*, San Francisco, USA, September 20 - 21.
- Bridgman, P.W., 1952. *Studies in Large Plastic Flow and Fracture*, McGraw-Hill, New York.
- Børvik, T., Langseth, M., Hopperstad, O.S. and Malo, K.A., 1999. Ballistic penetration of steel plates, *International Journal of Impact Engineering*, Vol. 22 (9-10), pp. 855 - 887.
- Børvik, T., Hopperstad, O.S., Berstad, T. and Langseth, M., 2000a. Numerical Simulation of Plugging Failure in Ballistic Penetration, accepted for publication in the *International Journal of Solids and Structures*.
- Børvik, T., Hopperstad, O.S., Berstad, T. and Langseth, M., 2000b. Computational Model of Viscoplasticity and Ductile Damage for Projectile Impact, submitted for publication.
- Børvik, T., Langseth, M., Hopperstad, O.S. and Malo, K.A., 2000c. Effect of projectile nose shape in structural impact, Part I: Experimental study, submitted for publication.
- Camacho, G.T. and Ortiz, M., 1997. Adaptive Lagrangian modelling of ballistic penetration of metallic targets, *Computer Methods in Applied Mechanics and Engineering*, Vol. 142, pp. 269 - 301.
- Hancock, J.W. and Mackenzie, A.C., 1976. On the mechanisms of ductile failure in high-strength steels subjected to multi-axial stress-states, *Journal of the Mechanics and Physics of Solids*, Vol. 24, pp. 147 - 169.
- Johnson, G.R. and Cook, W.H., 1983. A Constitutive Model and Data for Metals Subjected to Large Strains, High Strain Rates and High Temperatures, In: *Proceedings of Seventh Int. Symp. on Ballistics*, The Hague.
- Johnson, G.R. and Cook, W.H., 1985. Fracture characteristics of three metals subjected to various strains, strain rates, temperatures and pressures, *Engineering Fracture Mechanics*, Vol. 21, No. 1, pp. 31 - 48.
- Lemaitre, J., 1996. *A Course on Damage Mechanics*, Second Edition, Springer-Verlag, Berlin.
- Lindholm, U.S. and Johnson, G.R., 1982. Strain rate effects in metals at large shear strains, In: *Proceedings of the 29th Sagamore Army Materials Conference entitled Material Behaviour under High Stress and Ultrahigh Loading Rates*, New York.
- LSTC, 1998. *LS-DYNA Theoretical Manual*, Livermore Software Technology Corporation, CA, USA.
- LSTC, 1999. *LS-DYNA User Manual, Version 950*, Livermore Software Technology Corporation, CA, USA.
- Recht, R.F. and Ipson, R.W., 1963. Ballistic Perforation Dynamics, *Int. J. Applied Mech.* 30, pp. 384 - 390.
- Rice, J.R. and Tracey, D.M., 1969. On the ductile enlargement of voids and triaxial stress fields, *Journal of the Mechanics and Physics of Solids*, Vol. 17, pp. 210 - 217.
- Scheffler, D.R. and Zukas, J.A., 2000. Practical aspects of numerical simulation of dynamic events: material interfaces, *International Journal of Impact Engineering*, Vol. 24, No. 8, pp. 821 - 842.



Fig. 1: Plots of the initial configuration showing the different projectiles (green), the local region (blue) and only a part of the global region (red) of the target plate.

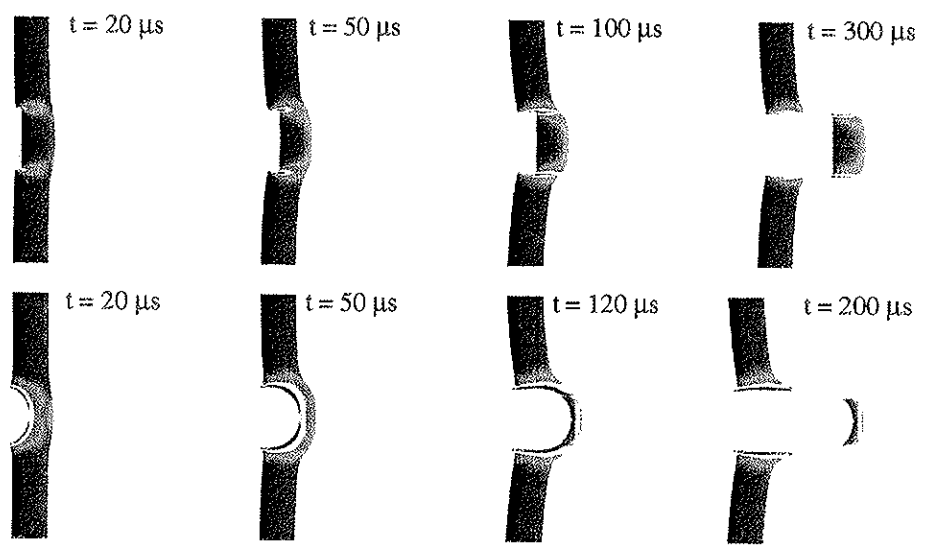


Fig. 2: Perforation of the target plate by blunt (203-60) and hemispherical (300-60) projectiles using a uniform element mesh.

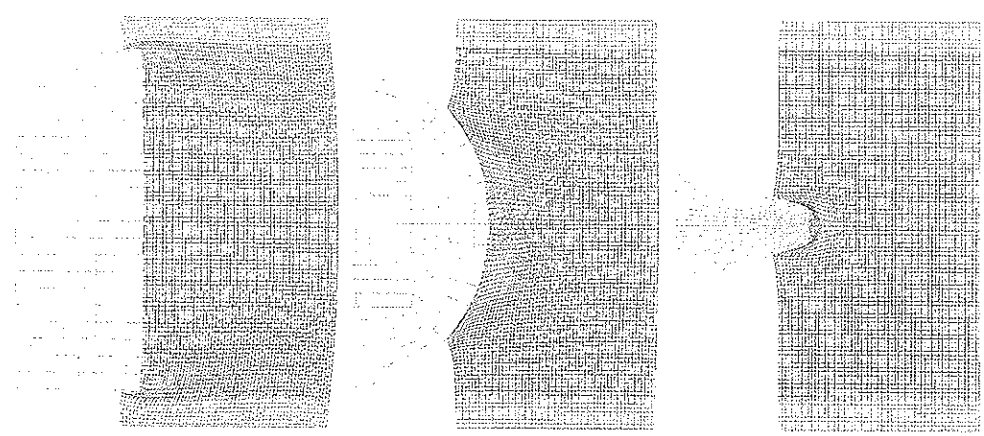


Fig. 3: Element distortion in the target plates just after impact using uniform element meshes.

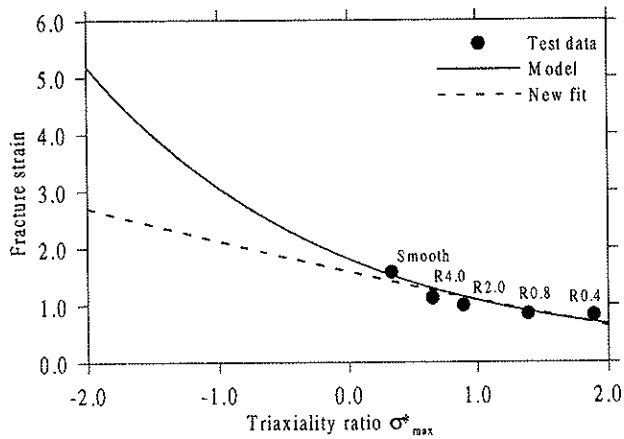


Fig. 4: Fracture strain versus stress triaxiality ratio.

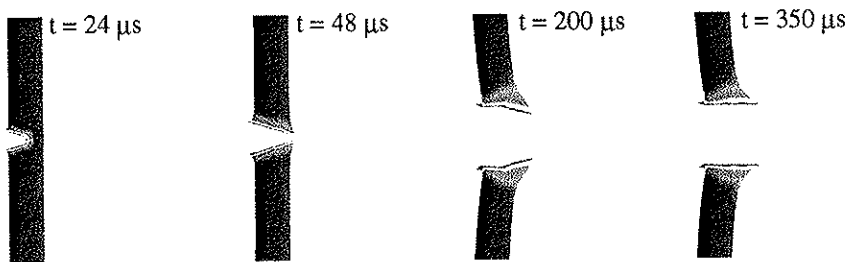


Fig. 5: Perforation of a target plate by a conical projectile (281-60) using a uniform element mesh and the new fracture strain constants.

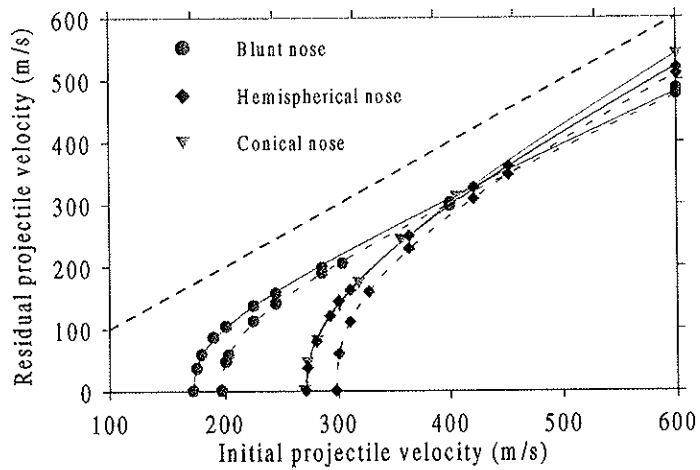


Fig. 6: Ballistic limit curves from numerical simulations using uniform element meshes (solid lines – new fracture strain constants, dotted lines – no reduction).

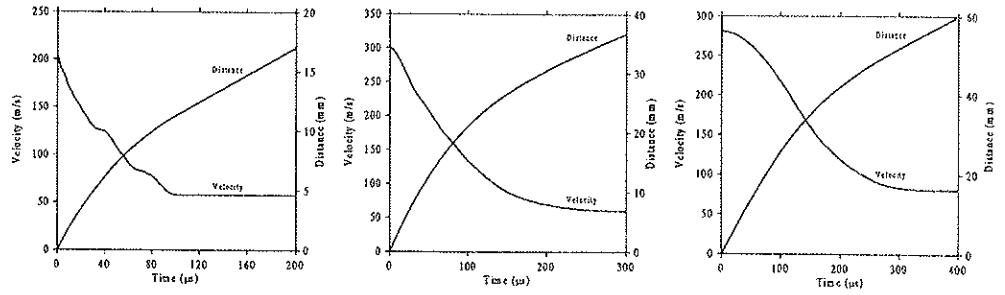


Fig. 7: Velocity-time plots from run a) blunt 203-60, b) hemispherical 300-60 and c) conical 281-60, respectively.

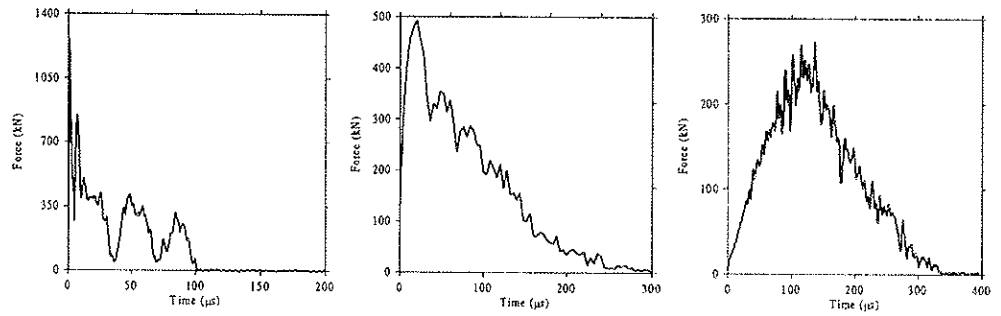


Fig. 8: Force-time plots from run a) blunt 203-60, b) hemispherical 300-60 and c) conical 281-60, respectively.



Fig. 9: Local cross-sections of perforated plates from run a) blunt 203-60, b) hemispherical 300-60 and c) conical 281-60 using uniform element meshes.

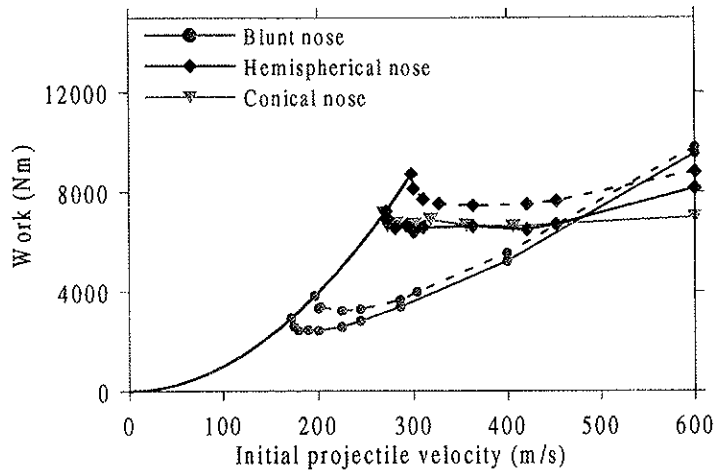


Fig. 10: Change in projectile kinetic energy ($\Delta K = W$) given as a function of initial projectile velocity (solid lines – new fracture strain constants, dotted lines – original fracture strain constants).

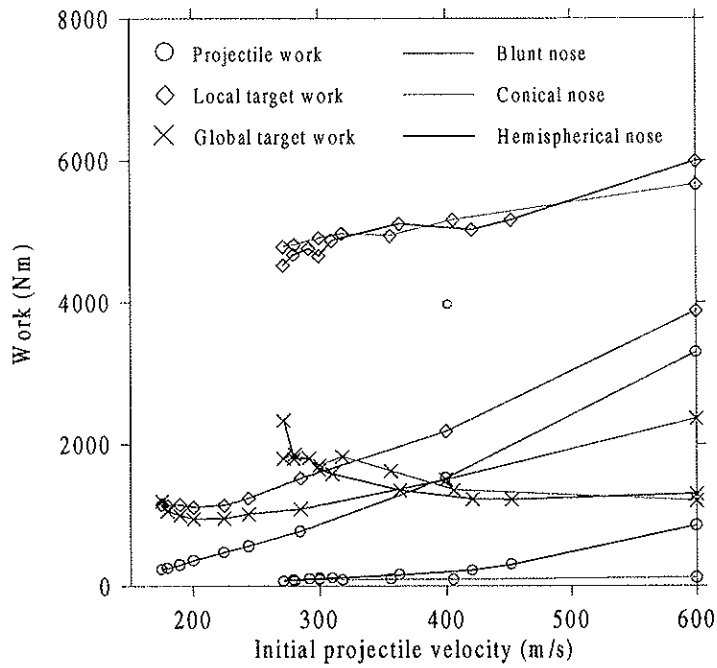


Fig. 11: Energy absorbed in global and local target deformation, and in projectile mushrooming, during penetration.

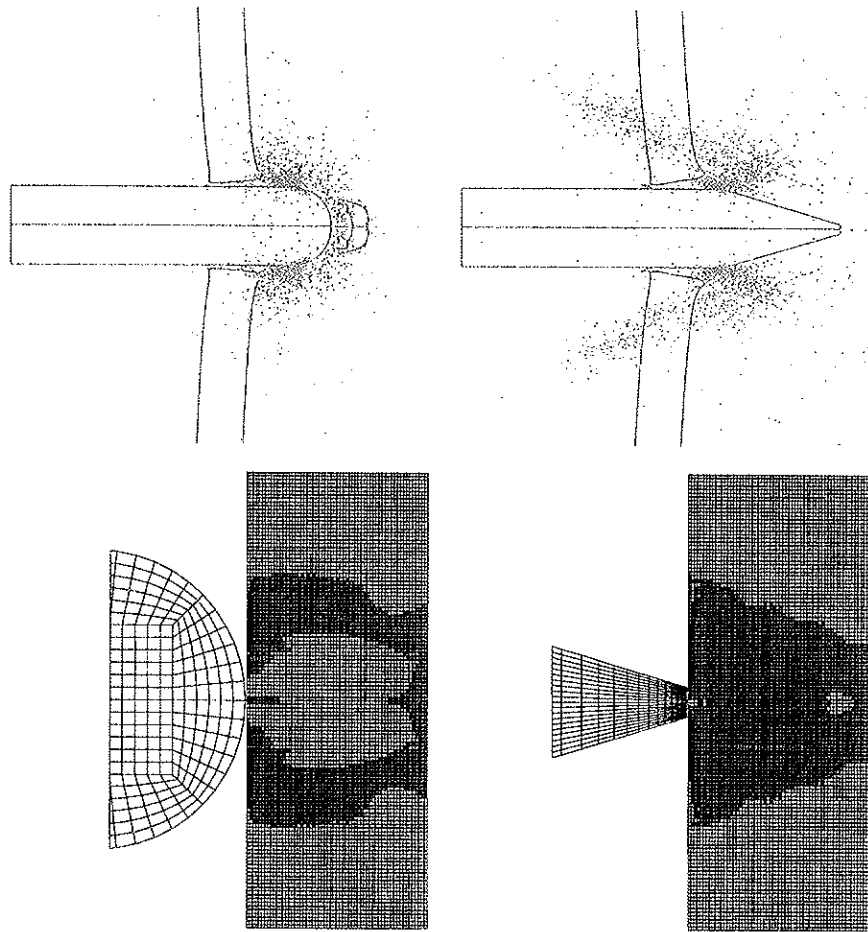


Fig. 12: Plots showing deleted nodes in simulations using hemispherical (300-60) and conical (281-60) projectiles, respectively, and the new failure strain constants.

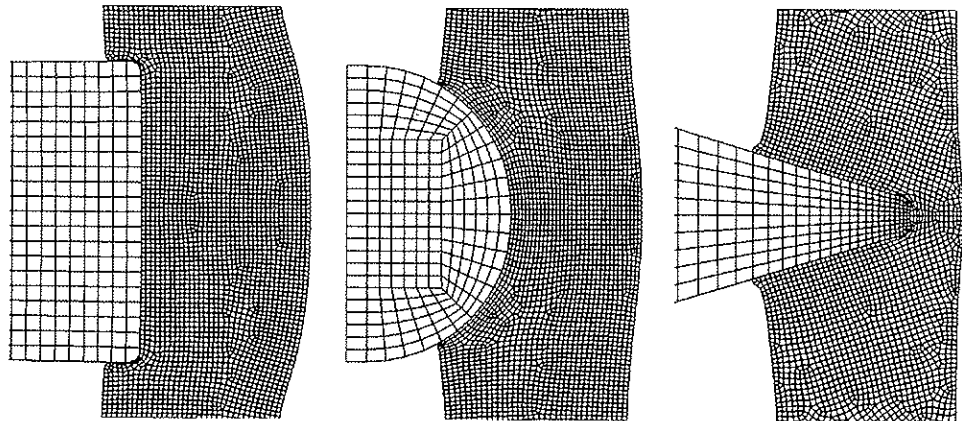


Fig. 13: Details of element meshes just after remeshing in adaptive simulations.

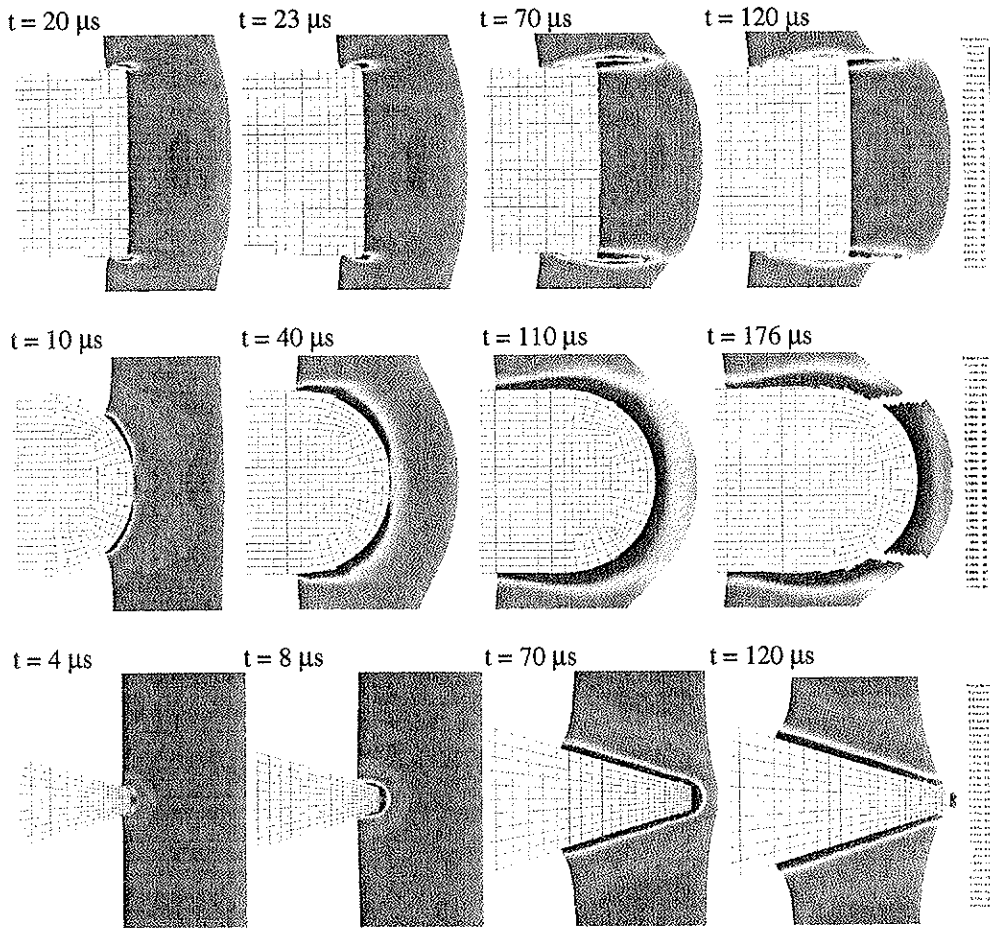


Fig. 14: Close-up of blunt (225-40), hemispherical (300-40) and conical (300-40) projectiles perforating the target plate using adaptive meshing. Fringes of accumulated plastic strain in the user defined range $p = 0$ (blue) to $p = 1.2$ (red) are shown.



Fig. 15: Final cross-section of target plate perforated by conical projectile (run 300-40) using adaptive meshing and plotted with fringes of accumulated plastic strain.

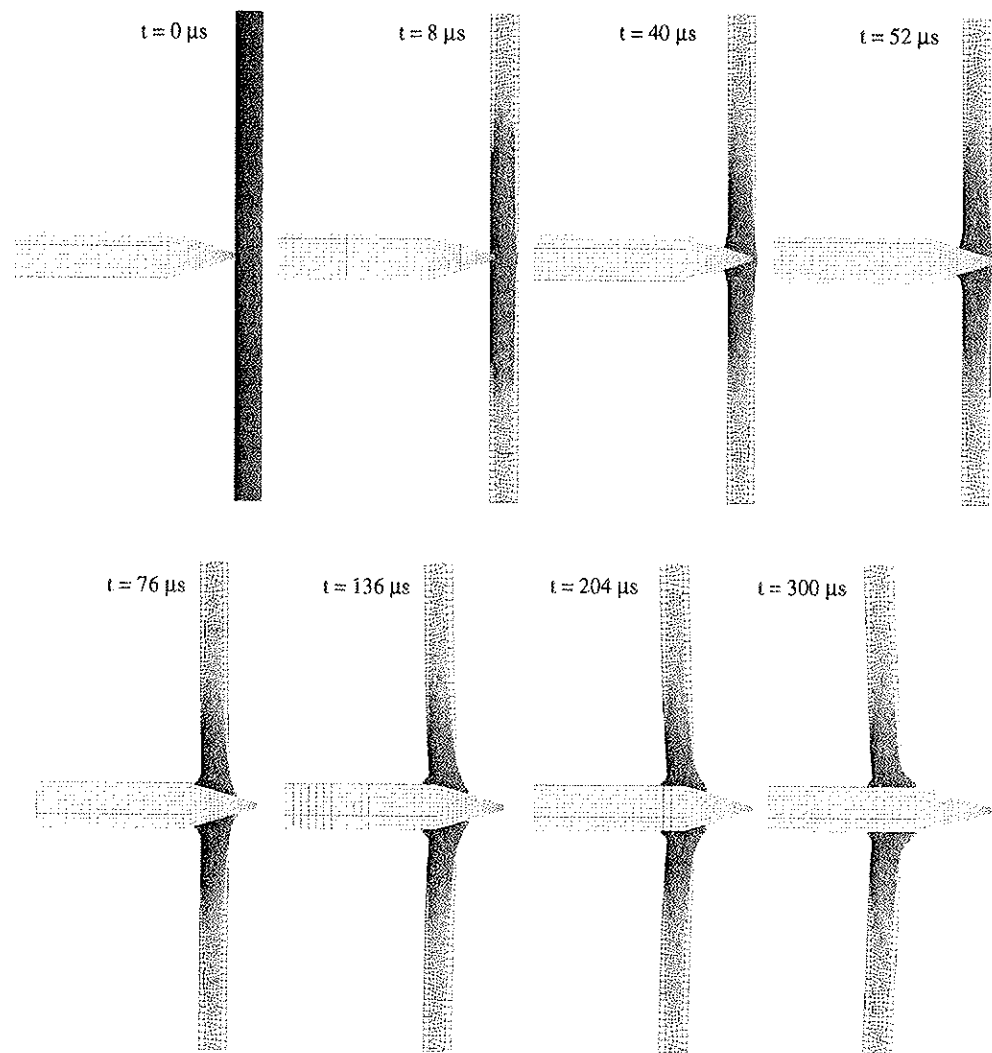


Fig. 16: Outline of target plate perforated by a conical projectile (run 300-40) using adaptive meshing.

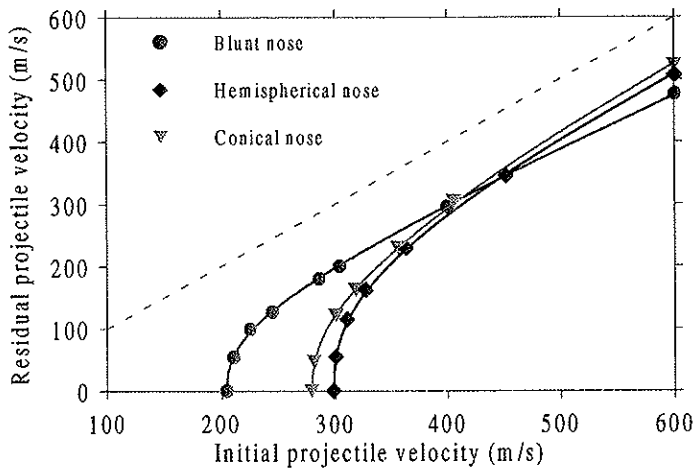


Fig. 17: Ballistic limit curves using adaptive meshing.

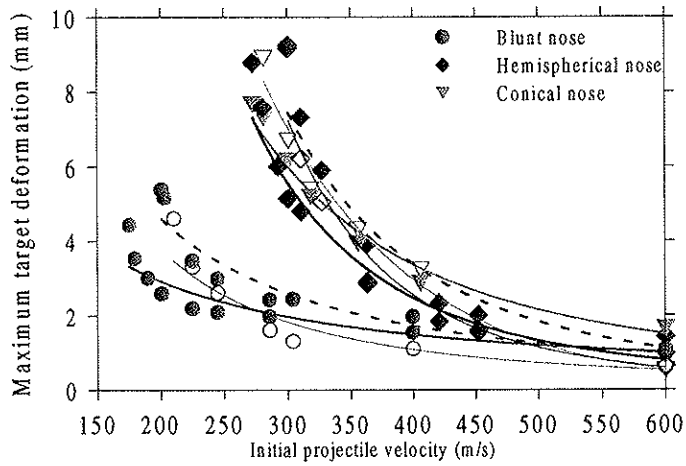


Fig. 18: Maximum target deformation from numerical simulations (dotted lines – original model, thick solid lines – new model, thin solid lines and open legends – adaptive meshing).

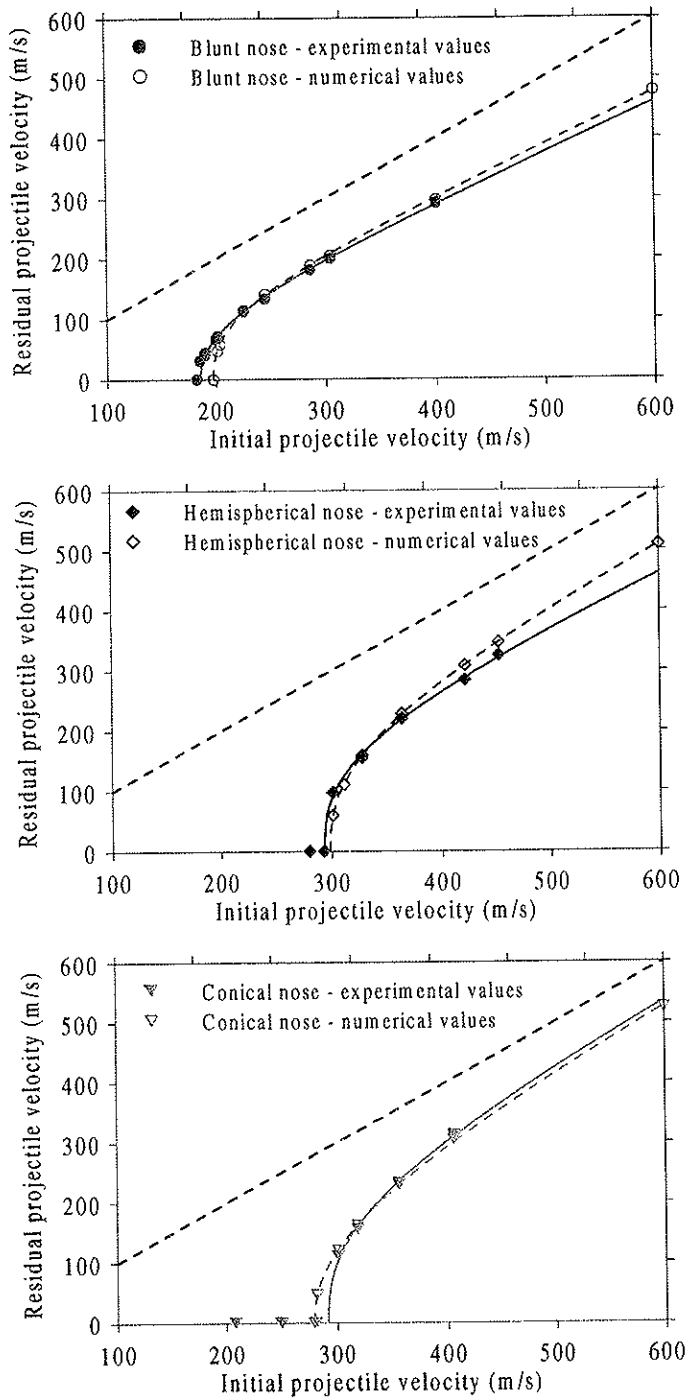


Fig. 22: A comparison between numerical (dotted line) and experimental (solid line) results for blunt, hemispherical and conical nosed projectiles.

Table 1: Material constants for Weldox 460 E steel (Børvik et al, 1999).

Elastic constants and density			Yield stress and strain hardening			Strain-rate hardening		Damage evolution		
E (GPa)	ν	ρ (kg/m ³)	A (MPa)	B (MPa)	n	\dot{P}_0, \dot{T}_0 (s ⁻¹)	C	D _c	P _d	
200	0.33	7850	490	807	0.73	5·10 ⁻⁴	0.0114	0.30	0	
Adiabatic heating and temperature softening						Fracture strain constants				
C _p (J/kgK)	α	$\bar{\alpha}$ (K ⁻¹)	T _m (K)	T ₀ (K)	m	D ₁	D ₂	D ₃	D ₄	D ₅
452	0.9	1.1·10 ⁻⁵	1800	293	0.94	0.0705	1.732	-0.54	-0.015	0

Table 2: Material constants for hardened Arne tool-steel (Børvik et al, 2000b).

E (MPa)	ν	ρ (kg/m ³)	σ_0 (MPa)	E _t (MPa)	Mean ϵ_f (%)
204000	0.33	7850	1900	15000	2.15

Table 3: Numerical results – uniform mesh.

Blunt projectiles – 60 elements over thickness										
v _i (m/s)	v _r (m/s)	v _{rpt} (m/s)	t _r (μs)	El _r (-)	CPU (h)	w _m (mm)	T _m (K)	K _{fp} +W _p (Nm)	K _R +W _I (Nm)	K _{Rf} +W _f (Nm)
600.0	476.8	505	36	257	1.4	0.97	977	22474+3115	3063+4217	150+2441
399.6	297.5	318	40	87	1.3	1.96	869	8747+1630	1310+2238	142+1661
303.5	204.8	242	46	67	1.8	2.43	922	4143+905	810+1729	155+1331
285.4	188.9	230	46	66	1.6	2.41	1072	3528+805	705+1605	150+1230
244.2	140.5	185	56	66	1.7	2.98	844	1954+595	465+1480	185+1195
224.7	111.8	150	68	65	2.0	3.46	1132	1236+462	300+1514	228+1233
202.7	57.6	84	102	63	2.2	5.15	825	329+350	105+1514	338+1495
200.4	47.0	68	117	64	2.9	5.37	810	220+330	52+1439	375+1540

Hemispherical projectiles – 60 elements over thickness										
v _i (m/s)	v _r (m/s)	v _{rpt} (m/s)	t _r (μs)	El _r (-)	CPU (h)	w _m (mm)	T _m (K)	K _{fp} +W _p (Nm)	K _R +W _I (Nm)	K _{Rf} +W _f (Nm)
600.0	508.7	545	42	656	4.9	1.42	1453	25481+870	1040+6163	130+1776
452.0	346.9	402	54*	672	5.8	2.00	1191	11859+300	458+5604	193+1710
420.6	308.2	375	62	705	3.7 ²⁾	2.32	1201	9344+230	378+5551	220+1702
362.9	228.3	238	75*	697	6.1	3.92	1052	5112+154	155+5376	265+1910
326.7	159.0	210	100*	622	8.6	5.89	1036	2461+100	130+5280	392+2150
310.0	110.8	160	124	743	6.9	7.31	1021	1212+82	61+5179	486+2446
300.0	59.6	108	148*	947	12.2	9.16	987	355+70	15+5150	375+2900

* Complete fracture in the element mesh.

Table 4: Numerical ballistic limits for uniform element meshes.

v _{bl} (m/s)	Blunt		Hemispherical			Conical ¹		
	a	p	v _{bl} (m/s)	a	p	v _{bl} (m/s)	a	p
196.4	0.81	2.46	297.3	0.92	2.48	-	-	-

¹ Not obtained due to numerical problems.

Table 5: Numerical results – uniform mesh and new fracture strain constants.

Blunt projectiles – 60 elements over thickness											
v_i (m/s)	v_r (m/s)	v_{rpt} (m/s)	t_f (μ s)	El_f (-)	CPU (h)	w_m (mm)	T_m (K)	$K_{fp}+W_p$ (Nm)	K_n+W_l (Nm)	$K_{fg}+W_g$ (Nm)	
600.0	485.1	525	30	563	2.8	1.07	982	23272+3291	2489+3873	180+2355	
399.6	302.0	327	38	184	1.8	1.53	758	9012+1517	1392+2180	129+1498	
285.4	197.8	219	44	91	1.7	1.96	701	3866+767	663+1515	131+1081	
244.2	156.5	191	48	70	1.3	2.08	672	2425+561	508+1234	136+1010	
224.7	136.5	171	52	68	1.3	2.18	661	1845+473	425+1138	142+950	
200.4	103.5	147	62	64	1.3	2.58	653	1062+357	307+1110	175+945	
189.6	85.7	107	72	63	1.4	3.00	636	728+295	170+1145	209+994	
179.4	58.3	87	96	63	1.6	3.52	650	355+242	113+1131	273+1056	
175.0	35.8	50	126	63	2.1	4.42	654	130+229	42+1148	271+1197	

Hemispherical projectiles – 60 elements over thickness											
v_i (m/s)	v_r (m/s)	v_{rpt} (m/s)	t_f (μ s)	El_f (-)	CPU (h)	w_m (mm)	T_m (K)	$K_{fp}+W_p$ (Nm)	K_n+W_l (Nm)	$K_{fg}+W_g$ (Nm)	
600.0	518.8	565	40	1183	3.2	0.98	1449	26509+852	720+5988	96+1295	
452.0	360.6	380	50	853	1.8	1.55	1200	12806+300	565+5138	130+1216	
420.6	327.0	365	50	874	2.5	1.83	1146	10529+220	302+5019	158+1224	
362.9	248.9	280	72	1303	2.4	2.84	947	6103+155	90+5106	193+1345	
310.0	161.5	167	96	1231	2.9	4.79	948	2568+110	15+4872	335+1580	
300.0	144.7	200	104	1012	3.8	5.13	1488	2066+100	80+4651	347+1635	
292.1	120.0	140	114	1323	6.8	5.99	1003	1425+98	20+4754	320+1800	
280.0	78.9	104	130	1492	5.4	7.57	827	617+80	10+4669	568+1790	
272.0	36.8	98	140	1100	9.7	8.77	1269	136+70	15+4520	225+2332	

* Complete fracture in the element mesh.

Conical projectiles – 60 elements over thickness											
v_i (m/s)	v_r (m/s)	v_{rpt} (m/s)	t_f (μ s)	El_f (-)	CPU (h)	w_m (mm)	T_m (K)	$K_{fp}+W_p$ (Nm)	K_n+W_l (Nm)	$K_{fg}+W_g$ (Nm)	
600.0	539.5	-	26/88	1583	2.9	1.63	847	28382+115	2+5659	102+1200	
405.7	311.7	-	36/144	1570	2.1	2.85	772	9475+87	2+5159	138+1351	
355.6	242.0	-	42/175	1520	4.9	3.91	733	5713+90	2+4938	92+1620	
317.9	172.8	-	48/225	1445	5.6	5.16	821	2916+79	2+4964	172+1821	
300.3	136.1	-	50/260	1445	8.3	6.14	819	1809+78	2+4904	390+1700	
280.9	80.7	-	56/344	1436	9.1	7.27	854	638+67	2+4807	405+1853	
272.0	44.8	-	60/440	1457	9.7	7.65	846	197+62	2+4781	450+1795	

* Time to pierce/time to completely perforate the target.

Table 6: Numerical ballistic limits for uniform element meshes and the new fracture strain constants.

v_{bl} (m/s)	Blunt		Hemispherical			Conical		
	a	p	v_{bl} (m/s)	a	p	v_{bl} (m/s)	a	p
172.0	0.82	2.43	270.6	0.94	2.27	269.0	1.00	2.05

Table 7: Numerical results – adaptive meshing.

Blunt projectiles – 40 elements over thickness						
v_i (m/s)	v_r (m/s)	v_{rpl} (m/s)	t_f (μ s)	EI_f (-)	CPU (h)	w_m (mm)
600.0	476.1	512	36	94	0.6	0.62
399.6	295.1	321	41	42	1.1	1.92
303.5	199.6	234	48	44	1.3	2.09
285.4	179.3	218	53	41	1.6	2.46
244.2	126.6	171	66	46	2.6	3.85
224.7	114.3	157	65	65	8.7	3.66
224.7	98.9	121	78	39	3.3	3.70
210.0	54.0	83	105	41	4.6	5.21

This simulation was carried out using 60 elements over the target thickness.

Hemispherical projectiles – 40 elements over thickness						
v_i (m/s)	v_r (m/s)	v_{rpl} (m/s)	t_f (μ s)	EI_f (-)	CPU (h)	w_m (mm)
600.0	506.7	553	42	157	7.6	0.63
452.0	344.9	400	57	244	1.1	1.59
362.9	228.6	249	81	163	1.6	2.90
326.7	161.5	215	90	117	2.0	5.04
310.0	114.5	146	110	104	2.5	6.20
300.0	54.3	98	150	126	3.1	9.24

Complete fracture in the element mesh.

Conical projectiles – 40 elements over thickness						
v_i (m/s)	v_r (m/s)	v_{rpl} (m/s)	t_f (μ s)	EI_f (-)	CPU (h)	w_m (mm)
600.0	523.0	-	26	157	1.3	0.50
405.7	304.0	-	36	90	1.6	3.21
355.6	228.9	-	40	99	2.1	4.29
317.9	161.3	-	44	69	1.8	5.36
300.3	120.6	-	48	59	2.0	6.68
280.9	46.1	-	61	51	3.1	8.89

Complete fracture in the element mesh.

Table 8: Numerical ballistic limits for adaptive meshing.

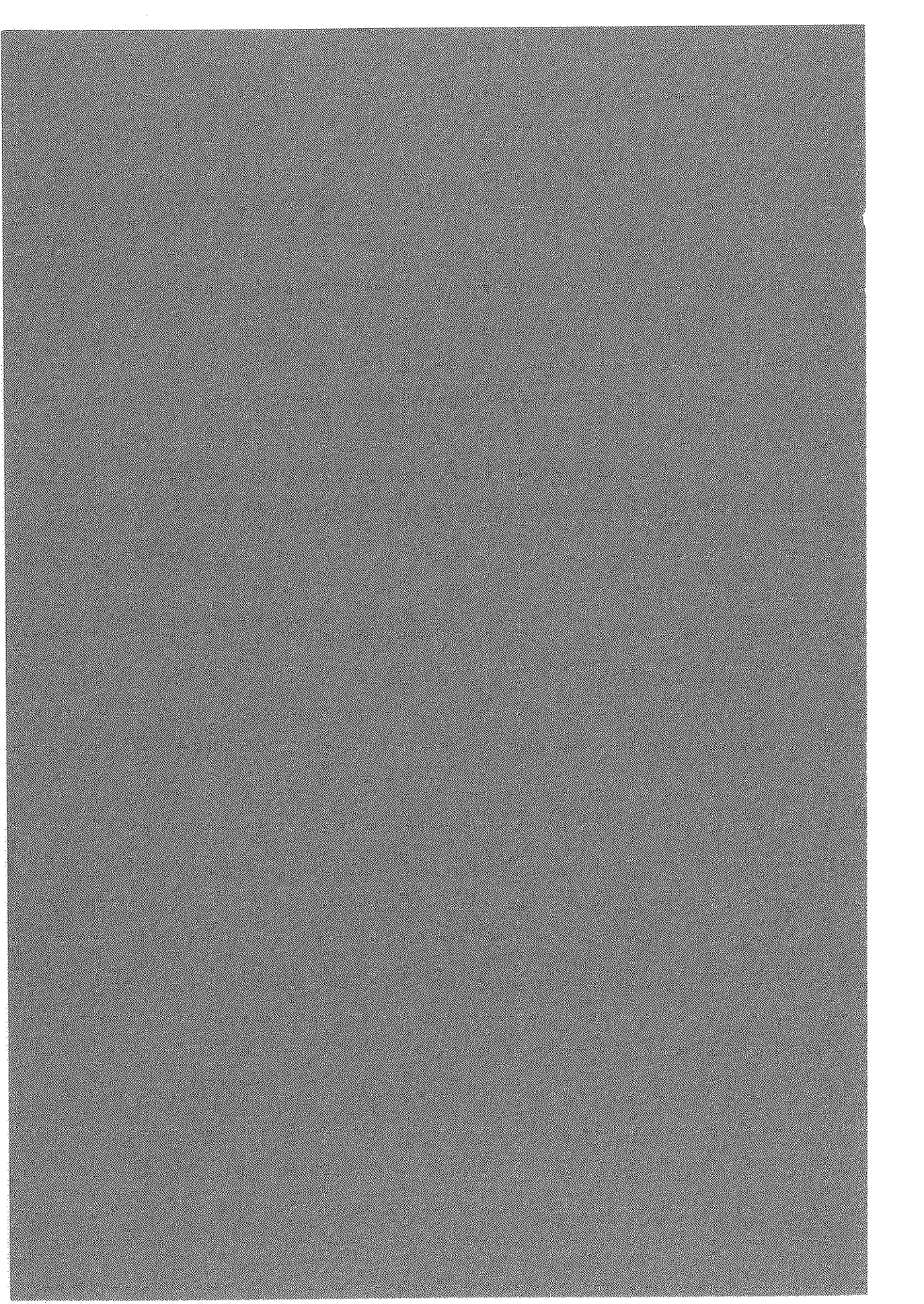
v_{bl} (m/s)	Blunt		Hemispherical			Conical		
	a	p	v_{bl} (m/s)	a	p	v_{bl} (m/s)	a	p
203.8	0.82	2.37	297.8	0.92	2.48	278.3	0.96	2.19

Part VIII

T. Børvik, O.S. Hopperstad, M. Langseth and K.A. Malo.

Effect of Target Thickness in Blunt Projectile Penetration of Weldox 460 E Steel Plates.

Submitted for possible journal publication.



Effect of Target Thickness in Blunt Projectile Penetration of Weldox 460 E Steel Plates

Tore Børvik*, Odd Sture Hopperstad, Magnus Langseth and Kjell Arne Malo

*Structural Impact Laboratory (SIMLab), Department of Structural Engineering, Norwegian University of
Science and Technology, N-7491 Trondheim, Norway.*

Abstract

This paper describes an experimental, analytical and numerical investigation of blunt projectile penetration of circular Weldox 460 E steel plates when varying the target thickness and projectile impact velocity. In the experimental tests, a compressed gas gun was used to launch a sabot mounted blunt projectile at impact velocities well above and just below the ballistic limit of the target plate. Nominal hardness, diameter, length and mass of the projectile were constant in all tests. The target plate was clamped in a rigid circular frame, and the thickness was varied between 6 and 30 mm. Measurements were made of the initial and final velocities, and the ballistic limit curve was constructed for each target thickness tested. In addition, a digital high-speed camera system was used to photograph the penetration event. The experimental findings from the tests are presented and discussed, and the results are used to assess empirical, analytical and numerical models. As will be shown, the method best suited to take the structural response into account when the deformation mode changes from typical thin plate membrane stretching towards thick plate shear localisation, is the finite element approach.

Keywords: Impact; Target thickness; Experiments; Empirical models; Analytical models; Numerical simulations

* Corresponding author. Tel.: + 47-73-59-46-47; fax: + 47-73-59-47-01.

E-mail address: tore.borvik@bygg.ntnu.no (T. Børvik).

Nomenclature

Unless otherwise stated in the text or original references the following notation apply:

ΔD	projectile nose deformation, i.e. $\Delta D = D_f - D_i$	C	strain rate sensitivity constant
ΔL	projectile length reduction, i.e. $\Delta L = L_i - L_f$	D	projectile nose diameter
μ	friction coefficient	d	diameter
θ	impact angle	E	Young's modulus
ϕ	oblique	h	thickness
α	pitch	HRC, R_c	hardness Rockwell C
γ	total yaw	m	mass
β	yaw	p	depth of penetration
ε	strain	P.O.I.	point of impact
σ	stress	r	radius
b	target thickness (Bai-Johnson model)	t	time
		v	velocity
		w	deformation

Subscripts:

0	initial or flow	max	maximum value
bl	ballistic limit	p	projectile
cr	critical	pl	plug
c	cavity	r	residual
e	engineering value	re	rear side value
d	dynamic	t	target or true value
f	final or failure	u	ultimate
fr	front side value	y	yield
i	initial		

1. Introduction

Structural impact problems have become increasingly important for the modern industry. In design of offshore structures, account is taken for accidental loads such as dropped objects, collisions, explosions and penetration by fragments. Most of these accidental loads are also pertinent in design of protective structures in the process industry or fortification installations for defence purposes. In the transport industry, energy absorption and crashworthiness are today critical issues in the design process of vehicles, vessels and aircrafts. In addition, many of the problems found in structural impact are also relevant in metal forming operations. While much of the work carried out by military and industrial research organisations has been classified, many generic investigations are available in the open literature. As pointed out by Goldsmith (1999), the enormous literature on the subject encompasses a variety of different target materials and thicknesses, as well as a host of projectile geometries and a velocity range from about 5 m/s to the hypervelocity domain of up to 15 km/s. Comprehensive reviews on the research into the penetration and perforation of structures by free-flying projectiles can be found in the journal papers by Backman and Goldsmith (1978) and Corbett et al (1996), and in the books by Zukas et al (1982, 1990).

Although many investigations have been presented over the years, the number of papers giving detailed information from ballistic penetration experiments is limited, and the majority of the tests reported are used to validate accompanied theories and models (Corbett et al, 1996). The experimental investigations are roughly divided into three different categories. The first category covers low velocity impact ($v_i < 50$ m/s), where target plates are hit by heavy projectiles using a drop hammer or a pneumatic accelerator. Extensive work in the area has been reported by e.g. Langseth et al (1990-1999). The second category covers the other extreme that is high velocity penetration ($v_i > 1300$ m/s). Here, powder guns, two-stage light gas guns and similar equipment are used to launch low-mass projectiles often against massive target structures. Some of the work in this area can be found in special issues of the International Journal of Impact Engineering containing the proceedings from the Hypervelocity Impact Symposium (Anderson Jr, 1999). The last category covers penetration and perforation in the sub-ordnance and ordnance velocity regime ($50 < v_i < 1300$ m/s), where projectiles of arbitrary mass and shape are launched from compressed gas guns or powder guns. This category has received much attention, and particularly those problems dealing with normal impact of plated metallic structures. Some important contributions in this particular field were listed in a paper by Børvik et al (1999a), and will not be repeated here.

The complexity of the penetration problem, especially if dynamic material behaviour and fracture are taken into account, has limited the use of closed-form analytical solutions. For that reason, work in this area has been considered as experimental in nature (Zukas et al, 1990). Even so, a large number of theoretical studies have been presented in the literature over the years. The theoretical approaches seem to fall into one of the following categories: 1) *Empirical equations* based on curve fits to experimental results, 2) *Analytical models* giving simplified solutions to the problem by assuming certain physical effects to dominate and 3) *Numerical simulations* where the conservation equations are integrated over successive time increments at all points in an element mesh. However, in recent review papers by Goldsmith (1999), Scheffler and Zukas (2000) and Zukas and Scheffler (2000) questions have been asked about the accuracy of the many computational models available. It is therefore necessary to validate computational models against reliable experimental data.

This paper is divided into three major parts. First, experimental details from almost 100 high-precision large-scale impact tests are given. In the tests, blunt projectiles were used to impact Weldox 460 E steel plates clamped in a circular frame. The only variables during the tests were the initial projectile velocity and the target plate thickness. Here, a description of the experimental set-up, instrumentation and the materials involved are also given together with an evaluation of possible experimental errors. In the second part, typical empirical equations and analytical models are used in calculations of the penetration problem. Finally, the last part covers finite element simulations. It will be shown that the numerical approach is an attractive alternative to the more common empirical and analytical solution methods.

2. Experimental set-up

The experimental set-up, instrumentation and measuring methods used in the tests have partly been presented elsewhere (Børvik et al, 1998a, 1999a) and only a summary of the most important features of the equipment is given below. An evaluation of possible errors during a test, both by known and unknown disturbing factors, is also presented. In the tests reported here, conducted under identical conditions, at least four types of experimental errors and uncertainties can be identified. The first error is due to projectile attitude prior to impact, the second is associated with the instrumentation and measurements of the penetration process, while the third is related to the boundary conditions of the target plate. Finally, errors and uncertainties will also appear due to variation in material and geometrical properties.

Compressed gas gun

The compressed gas gun shown in Fig. 1 (Børvik et al, 1998a) was used in all tests to launch the projectile. The main components of the gas gun are the 200 bar pressure tank, the purpose-built firing unit for compressed gas, the 10 m long smooth barrel of calibre 50 mm and the closed 16 m³ impact chamber. The gas gun is designed to launch a 250 g projectile/sabot package to a maximum velocity of 1000 m/s when helium is used as propellant. The projectile is mounted in the sabot (Fig. 6), and inserted into the rear end of the barrel. Mylar membranes are used to separate the firing section from the pressure tank and barrel. Compressed gas is filled into the pressure tank and firing unit simultaneously, but with twice as much pressure in the former. At firing, the firing unit is rapidly evacuated. This sudden increase in pressure gradient over the membrane makes them burst, and the projectile is accelerated throughout the barrel. When the package leaves the muzzle, the sabot is immediately separated from the projectile due to aerodynamic forces. A sabot trap, located about 1.5 m from the muzzle, allows the projectile to pass freely while the sabot parts are stopped. The projectile passes the initial velocity measurement station before it impacts the target clamped in a circular frame after about 2 m of free flight (Fig. 2). To allow high-speed photography during impact, the clamping system is equipped with a 150 mm framing window. If the projectile perforates the target, residual velocities are measured before all free flying bodies are stopped without further damage in a rag-box filled with graded plywood. After testing, the impact chamber is opened for final inspections and measurements.

Measurements

To measure initial projectile velocity (v_i), a photocell system that has two identical light-barriers with LED-light sources on the upper side of the projectile path and detectors on the lower side was used. When the projectile passes between the sources and detectors in the barrier, light is interrupted and signals are given to a digital oscilloscope and a nanosecond counter. The second light-barrier also works as a trigger for the digital high-speed camera system used during testing. A similar system, Fig. 3, was developed to measure residual velocities if perforation occurs. Here, each light source consists of six lasers mounted in line to give parallel beams in a laser curtain. Detectors are mounted in lines to match the laser light sources. When triggered by a moving body, the detector signals are stored on a 100 MHz digital oscilloscope and information regarding velocity and length of all passing objects is

obtained. In all tests, a computer operated digital high-speed camera system was used to photograph the penetration process. The system, which combines an image converter camera capable of framing rates from 2,000 to 20,000,000 frames per second and a high-resolution CCD camera, was used both for visualisation and measurements. The camera system was set perpendicular to the projectile path in the target plane in order to record the projectile both before and after perforation (Fig. 2). To reconstruct a 3D description of the process, mirrors were in some of the tests mounted above the projectile path at an angle of 45° with respect to the centreline of the camera, one on each side of the target. The main features of the gas gun and instrumentation have been presented by Børvik et al (1997, 1998a, 1999a).

Measurements of initial and residual velocities are the primary parameters and hence of vital importance in most ballistic impact related studies. The equipment described above is far from standard, and is for that reason purpose-built for this particular study. Thus, it is necessary to estimate the error associated with these measurements. Both the alignment of the equipment and the standard electronics such as counters, lasers and digital oscilloscopes have been controlled and believed to be of sufficient accuracy (Førre, 2000). The largest uncertainty is related to the distribution of LED-light (which gives a larger spread than laser light) over the detectors in the initial velocity measurement station. In order to check this uncertainty, tests were carried out where projectiles were fired through the impact chamber at different velocities without a target plate. The difference in measured velocity between the initial and residual velocity station was found to be less than 1 %. Accordingly, measured velocities are supposed to be very close to the actual velocity. The computer sub-routine used to determine the velocity-time curve from the digital high-speed camera images (Børvik et al, 1999a) was also checked based on these tests. Due to the sub-pixel resolution, it was found that the accuracy in the measurements was high, and normally within 3-4 % of the velocity measured by the optical measurement systems.

Projectiles and targets

Blunt-nosed circular-cylindrical projectiles were manufactured from Arne tool steel. After machining, they were oil hardened to a Rockwell C value of 53 ($\sigma_y \approx 1900$ MPa) in order to minimise plastic deformations during impact. Nominal hardness (HRC 53), length (80 mm), diameter (20 mm) and mass (0.197 kg) of the projectiles were constant in all tests. Before testing, the projectiles were measured, painted dead black and equipped with fiducial marks for high-speed camera measurements. All target plates within a test series were manufactured

from the same Weldox 460 E steel plate, having a nominal thickness range from 6 to 30 mm. After careful cutting from the larger plate, 21 equally spaced holes were drilled on a 550 mm diameter bolt circle before the target was sandblasted on both sides. The plate was finally sandwiched between the clamping rings and bolted to the frame with an inner clamp diameter of 500 mm. Target thickness, initial imperfections, initial oblique and final deformations were measured *in situ*. The target inserted in the rigid clamping frame is shown in Fig. 2.

A computational model of viscoplasticity and ductile damage for projectile impact has been developed and implemented in the explicit finite element code LS-DYNA (LSTC, 1998, 1999) during this study by Børvik et al (2000c). Four types of tensile tests are required to identify the material constants used in the model. Quasi-static tensile tests are used to identify the elastic constants and the yield stress of the material. Notched-specimen tensile tests define the strain hardening constants, the critical damage and the fracture strain constants. Dynamic tensile tests give the viscoplastic behaviour, while tensile tests at elevated temperatures provide the temperature effect on the stress-strain curve, elastic modulus and fracture strain, respectively. Quasi-static tensile tests were also carried out in order to identify the material constants for the projectile. Here, only engineering mechanical properties for the projectile and target are given in Table 1, while details regarding the material test results and model calibration procedure can be found in Børvik et al (2000c). Fig. 4 shows typical quasi-static tensile stress-strain curves both for the target and projectile material. While the target material displays a very ductile behaviour, the projectile is rather brittle. Some material information is necessary in order to calibrate the analytical models used in Chapter 5, while the fully calibrated computational material model of viscoplasticity coupled with ductile damage will be applied in all numerical simulations of the penetration problem presented in Chapter 6. In the tests, target plates with different thicknesses will be used. This involves material from several deliveries, and scatter in the material properties may appear. In order to reveal such scatter, specimens were machined from 8, 10 and 12 mm thick plates (Børvik et al, 2000c). Coupons were also taken at different locations throughout the thickness (both from the middle and the edge of the plate), and in two different directions (0° and 90°) to the rolling direction of the target material. It was found that scatter in material properties in general was small and is for that reason ignored in following computations.

Both in analytical and numerical calculations it is assumed that the target is fully clamped at the support, even though such boundary conditions are hard to attain experimentally. This assumption is however reasonable, and it is a general perception that the boundary conditions are of minor importance in ballistic penetration by small mass projectiles in the ordnance

velocity regime as long as the target diameter is more than a few projectile diameters. This was verified through numerical simulations. In the analysis, blunt projectiles were used to perforate 6 and 12 mm thick plates at impact velocities close to the ballistic limit when the boundary condition varied from fully clamped to simply supported on a stonewall. No effect on the residual velocity of the projectile was observed due to the change in clamping conditions. The numerical approach used in this study is presented in greater detail in Chapter 6. On the other hand, tests carried out by Corran et al (1983) indicate that the clamping force have a significant effect on the ballistic limit of the target plate. The importance of clamping conditions during penetration for this particular problem was also examined in a quasi-static parametric study reported by Børvik et al (1999b). From the factorial analysis it was found that the plugging force was unaffected and that only a small effect was noticed on the absorbed energy and maximum target deformation when the boundary condition was changes from presumed clamped to simply supported.

Exterior ballistics

Most investigations in penetration dynamics consider normal impact by rigid projectiles on stationary targets, where the velocity vector of the projectile is parallel to its axis of symmetry and normal to the target plane at the point of contact. However, such idealised situations never appear in practice, and some pitch, yaw, oblique and tumbling due to aerodynamic forces and instabilities will always be present, as exemplified in Fig. 5. In the figure, the subscript 0 , f and p refers to initial, final and plug, respectively. An extensive review on the subject of non-ideal projectile impact on targets can be found in Goldsmith (1999). Before impact the attitude of a cylindrical projectile in flight is completely described by a single parameter called total yaw, γ , and defined as the angle from the velocity vector of the projectile's centre of gravity to the longitudinal axis of the projectile. Total yaw is usually determined from two orthogonal attitude components measured in a ballistic range, called pitch, α , if in the vertical plane and yaw, β , if in the horizontal plane, and given as $\gamma = \tan^{-1} (\tan^2 \alpha + \tan^2 \beta)^{1/2}$. The oblique angle, ϕ , is the angle from the target normal to the projectile velocity vector and the impact angle, $\theta = \gamma - |\phi|$, is the angle from the target normal to the symmetry axis of the projectile. Obviously, the impact angle will be equal to the yaw angle when the oblique angle is zero. Tumbling impact, denoted by ω , incorporates yaw and oblique motion as well as an angular motion about an axis through the centre of gravity

orthogonal to the longitudinal axis of the projectile. Even if a number of theoretical and experimental investigations have been reported on the subject, only a few have considered the effect of projectile penetration with yaw. In contrast to oblique, yaw is very hard to control in the laboratory because small yaw angles may be required for projectile trajectory stability. However, from the experimental results reported by Goldsmith (1999), it appears that the penetration process is hardly affected by total yaw angles up to 3-5°. Larger yaw angles may, on the other hand, significantly reduce the penetration capacity of the striker and have to be taken into consideration. Therefore, in a ballistic experiment it is important to be able to measure projectile attitude prior to and during impact in order to see if the angle deviations are small enough to be neglected.

One major disadvantage with the experimental set-up used herein is that the diameter of the barrel is relatively large compared to the diameter of the projectile, and a sabot for guidance and protection of the projectile is required. This sabot has to be completely removed and stopped prior to impact with the target. However, the diameter difference makes massive sabots rather heavy, and tests have revealed that heavy sabots do not separate properly. This enforced the development of the 9-pieced serrated sabot shown in Fig. 6, manufactured from a combination of polycarbonat and foam. The weight of this particular sabot is less than 50 % of the projectile, which was found as a critical value to avoid additional pitch and yaw. It was also learned from Hanchak and Forrestal (1997) that the last meter of the barrel must be both smooth and straight to avoid problems with the sabot separation. Separation of the sabot during flight as the projectile passes the sabot trap is shown in the shadowgraphs presented in Fig. 7. These images also revealed that the originally present titanium plate in the sabot, used to disperse the load from the projectile on the pusher during acceleration, should be removed as it went through the sabot trap and interfered with the projectile.

A method described in Børvik et al (1998a) was developed for angle measurements. Here, the high-speed camera was used to record the projectile both before and after perforation and mirrors were used to give a 3D description. An example where this technique was utilised is given in Fig. 12c), showing perforation of a 10 mm thick plate both in the vertical (lower part of the image) and horizontal (from mirrors in the upper part of the image) planes. A computer sub-routine was developed and used to determine both pitch and yaw angles prior to impact. However, the Ultramac FS501 high-speed camera system is a very complex electro-optical instrument. The image converter process, the non-symmetrical optics and the alignment of both the camera and in particular the mirrors cause aberrations and distortions in the images. A spatial calibration of the camera was recommended to achieve reliable measurements. One

possible spatial calibration routine is given in Børvik et al (1997, 1998a). Unfortunately, the procedure is time consuming and was therefore only accomplished for the 10 mm and for some of the 12 mm thick target tests. It was however revealed from these images that both pitch and yaw were small and well below the critical value. In general, it was noticed that when the pitch was small, so was the yaw. Based on these results, it was assumed that for control reasons it was sufficient to only measure the pitch angle. A simplified method, where the pitch angle of the moving projectile is measured and related to the angle of the stationary support precisely aligned prior to the test, was used in all other tests. In order to measure initial oblique, a collimated laser was inserted in the muzzle of the gun and a mirror was fixed on the target plate surface. The deviation of the reflected laser beam from the centre of the muzzle was measured, and this was used together with the known distance from the laser head to the target plate surface to calculate the oblique angle of the target. Measured pitch, yaw and oblique angles are given in Table 8. As seen, the angle deviations are small and a normal impact can be assumed in these tests.

3. Experimental results

In the presented experimental study, the only parameters varied during the tests are the initial projectile velocity and the nominal target thickness. The effects on the structural response when the impact velocity is varied, while keeping the target thickness constant at $r_p / h_t \sim 1$, has been investigated earlier (Børvik et al, 1999a). Some observations from that particular study are repeated below.

- The target is sensitive to variations in impact velocity near the ballistic limit, and the residual velocity of the projectile is therefore never really small. Thus, the ballistic limit curve exhibits an almost discontinuous “jump” at the ballistic limit velocity. As the impact velocity is increased, the ballistic limit curve approaches the ballistic limit line, i.e. the ballistic limit velocity for a target with zero thickness. The velocity of the plug is always found to be higher than that of the projectile.
- The amount of projectile kinetic energy converted into projectile/target work decreases with increasing impact velocity. At the highest impact velocities, the energy absorption flattens out, indicating that the projectile/target system can not absorb any more energy.

- The target deformation consists of a combination of localised bulging and global dishing, which becomes more and more localised as the impact velocity is increased.
- The permanent target deformation increases with increasing projectile velocity until it reaches a maximum near the ballistic limit. After perforation, the deformation decreases with increasing velocity until it stabilises at a velocity well above the ballistic limit. The maximum deformation during a test is about twice as big as the permanent one.
- The projectile plastic deformation increases with increasing impact velocity. Also the plug thinning, i.e. the difference between the initial and final thickness of the plug, shows an increase with increasing projectile velocity.

Depending on the specific impact configuration, such as target thickness or material and projectile nose shape, various modes of failure may occur during penetration. Backman and Goldsmith (1978) classified these as fracture due to an initial stress wave, radial fracture behind an initial wave in brittle materials, spalling or scabbing, fragmentation, plugging, petaling and ductile hole enlargement. In perforation of metal plates, plugging and ductile hole enlargement seem to be the most significant failure modes. Plugging, which is a failure mode dominated by adiabatic shear banding, takes place with almost no lateral compression in the target material due to the localisation of the deformation in narrow shear zones around the sharp edges of the projectile. However, as the target becomes thick, the material in front of the projectile has to be pushed out laterally in order to form a penetration channel. When the thickness of the remaining target ahead of the advancing projectile approaches some limit, the penetration process changes from hole enlargement to plugging, which is a less energy-consuming failure mode. This will be discussed further in Chapter 6. The metallurgical mechanisms associated with adiabatic shear plug formation and thermoplastic instability were recently investigated by Børvik et al (2000b). The microscopic study showed deformed adiabatic shear bands in 10 to 16 mm thick plates, while transformed adiabatic shear bands were found in thicker plates. In plates thinner than 10 mm, the plugging process was controlled by a combination of localised shear, bending and tension.

In this paper focus will be on the observed variation in ballistic resistance when the target response changes as the thickness increases. Experimental details from about 100 large-scale impact tests with blunt projectiles at striking velocities between 75 and 500 m/s on clamped Weldox 460 E steel plates with a thickness range from 6 to 30 mm are given in Table 8. The measured initial and residual projectile velocities were used to construct the ballistic limit

curves shown in Fig. 8. The solid lines through the data points are calculated based on a model proposed by Recht and Ipson (1963)

$$v_r = a(v_i^p - v_{bl}^p)^{1/p} \quad (1)$$

where the method of least squares was used to obtain a best fit of the model constants a and p to the experimental data. The ballistic limit velocity v_{bl} was calculated as the average between the highest projectile velocity not giving perforation and the lowest projectile velocity giving complete perforation of the target. Table 2 gives the ballistic limit velocities for each target thickness tested, together with the fitted constants a and p from Eq. (1). Much effort was spent in the attempt of defining the ballistic limit as closely as possible, and the accuracy in the determination of the different ballistic limit velocity is indicated in Table 2.

Both the “jump” in residual velocity at the ballistic limit and the slope of the ballistic limit curve seem to decrease with target thickness and initial projectile velocity. Forrestal and Hanchak (1999) predicted a similar distinct jump in perforation of thin plates. The height of the jump is believed to be controlled by the amount of tension at the rear side of the target close to failure. The reduced slope in the ballistic limit curve is probably caused by an increased plastic deformation in the projectile with increased impact velocity and target thickness, as will be discussed later. For targets with a thickness of 20 mm or more, the projectile was severely damaged. The projectile shattered at impact in most tests using 25 or 30 mm thick targets, independent of initial velocity (Table 8), and it was thus not possible to obtain the ballistic limit velocity or curve for these two thicknesses (see Table 2). The projectile also shattered at the highest impact velocities in the 20 mm thick target, and the spread in the experimental results became considerable. For that reason, two ballistic limit curves were fitted to the data points. In the first curve, given as the solid line in Fig. 8, only data from tests at impact velocities below 400 m/s were used in the fit. In the second curve, i.e. the dotted line in Fig. 8, also the data point at an impact velocity of 436 m/s was included. In that particular test, the projectile was more affected by plastic deformation and damage than the other results, and this is probably the reason for the relatively low residual velocity.

Fig. 9 shows experimentally obtained ballistic limit velocities versus target thickness. As seen, a distinct kink appears in the fitted response curve at a target thickness of about 10 mm. This shift in target response appears to be related to the change in deformation mode from typical thin plate membrane stretching towards thick plate shear localisation. Corran et al

(1983) obtained a similar behaviour in penetration tests on steel and aluminium target plates. The effect of this difference in target response during impact is outlined in Fig. 10. It is seen that a doubling of the target thickness from e.g. 6 to 12 mm increases the ballistic capacity of the target by less than 30 %. In-situ measured maximum target deformations are given in Fig. 38. While the permanent deformation is almost twice the target thickness for a 6 mm target, it is hardly measurable for a 16 mm thick plate. In thin plates, both localised bulging and global structural deformation take place. It is assumed that the global deformation mode absorbs a considerable amount of projectile kinetic energy during the impact (Børvik et al, 2000a). In thick plates hardly any global target deformation is measured and most of the projectile kinetic energy has to be absorbed in the highly localised shear zones surrounding the projectile. This is further illustrated in Fig. 11, where permanent deformation profiles for different target thicknesses at an impact velocity close to the respective ballistic limit are shown. Note that no plastic deformation could be measured at the boundary in any of these tests. Target deformation is not a function of plate thickness alone. Impact velocity is also crucial and the deformation reaches a maximum near the ballistic limit independent of target thickness. This was also shown in Børvik et al (1999a) where permanent deformation profiles as a function of impact velocity for 12 mm thick targets were plotted and compared.

High-speed camera images from tests at impact velocities close to the ballistic limits are presented in Fig. 12. As seen, all targets failed by plugging. Fig. 12a) and b) show that the global deformation in 6 and 8 mm thick targets are considerable. The maximum deformation during impact is found to be approximately twice as large as the measured permanent one given in Fig. 38. However, this changes rapidly with target thickness and impact velocity. Fig. 12c) and d) show perforation of 10 and 12 mm thick targets, respectively. In these tests the deformation is much more localised, even if the impact velocity also here is close to the ballistic limit. When the target becomes thick, the deformation becomes extremely localised. This is seen in Fig. 12e) and f), where perforation of 16 and 20 mm thick targets is shown. Here, hardly any global deformation is detected except for the highly localised bulge on the rear side of the target after severe projectile indentation. Note also that due to an unsymmetrical failure mode, the projectile may rotate somewhat in the cavity during penetration even though both pitch and yaw are small. For the thickest plates, the projectile is destroyed. Fig. 12g) and h) show complete break-up of the brittle projectile (Fig. 4) during impact of a 25 and 30 mm thick target plate, respectively, with only a limited target deformation on the rear side. It was not possible to perforate any of the 25 or 30 mm thick targets with the type of projectile used in this study, indicating an upper limit for projectile

capacity. As revealed in Fig. 8 and Table 8, the projectile shattered also for the highest impact velocities in 20 mm thick targets. The reason is the extreme interface force, causing severe circumferential tensile stresses between the projectile nose and the target surface, in blunt projectile penetration of thick plates. This was also seen in a numerical study on the importance of projectile nose shape in structural impact (Børvik et al, 2000e). As seen from the first images in Fig. 12g) and h), the projectile starts to mushroom at impact. However, due to the low fracture strain it is cleaved and completely destroyed during penetration. In an attempt to avoid this complete destruction, several tests were carried out with softer projectiles (HRC 48 and 43). Also these projectiles fractured at impact. If further softened (down to HRC 30), the plastic deformation of the projectile became severe, which again considerably affected the ballistic capability. Shatter was not observed in any of the tests with a target thickness less than 20 mm. Cross-sections of perforated targets close to the ballistic limit are given in Fig. 13. Again, the global deformation decreases and the rear side bulge increases with increasing target thickness. The cavity is smooth and regular in all tests except for the 25 and 30 mm thick plates where the projectile fractured. Here, the target damage is very limited even though the impact velocity of the projectile was much higher than for the other tests. Corresponding projectiles and plugs are shown in Fig. 14. The plastic deformation in the projectile is limited at impact velocities close to the ballistic limit for target thicknesses between 6 and 20 mm. Also the plugs are seen to be both smooth and cylindrical. It was noticed that the plugs have a significant bulge on the distal side, and a variable shear zone height was observed on the surface of the plug in some of the tests. In contrast, Fig. 15 shows a completely shattered projectile after impact with a 30 mm thick target plate.

The velocity-time curve from the penetration experiment is an important quantity both regarding physical understanding and validation of computational models. A computer subroutine (Børvik et al, 1999a) was developed in order to measure the relative displacement of the projectile from the digital high-speed camera images. By computing the centre of gravity based on the intensity of the pixels within each white fiducial mark (see Fig. 12) it is possible to determine the change in velocity with sub-pixel resolution. This method was used to obtain the velocity-time curves presented in Fig. 16, all from tests at an impact velocity near the ballistic limit. The almost linear drop in velocity with time is found to increase both with initial velocity and target thickness. After fracture the curve flattens and shows a constant velocity. Note also that the perforation time is almost constant and about 100 μ s in all tests.

Plug thickness as a function of target thickness and projectile impact velocity is plotted in Fig. 17. As long as the target plate is relatively thin, say $b \leq 12 \text{ mm}$, the thickness of the plug from impact tests close to the ballistic limit is almost identical to the original plate thickness. Thus, plastic compression and lateral material flow before complete formation of the plug is negligible, and it follows that shear banding is the dominant failure mode. For thicker plates a linear reduction in plug thickness with target thickness is found when $b \leq 20 \text{ mm}$ (Fig. 17a). The plug thinning is also seen to increase with impact velocity, and in particular for the thickest plates (Fig. 17b). The diameter of the plug is almost identical to the final diameter of the projectile nose. The increase in projectile nose diameter (ΔD) from all tests is plotted in Fig. 18 as a function of impact velocity. As seen, the deformation is well predicted by a power function. A similar behaviour was found for the reduction in projectile length (ΔL). These observations validate the assumption that projectile deformation takes place at impact, and is more affected by impact velocity than by target thickness. Accordingly, when the impact velocity gets high the amount of energy absorbed in projectile plastic deformation becomes considerable. Several more details from the experimental tests are given in Table 8.

4. Empirical equations

In practical engineering or design, it may be difficult or even impossible to obtain detailed information on a specific penetration problem in a short term. Therefore, in order to have a preliminary prediction of the structural response for a given load, an empirical approach is often used. However, the method may give considerable errors and it is both difficult and hazardous to extrapolate empirical equations outside their often strictly prescribed limits. Also, the empirical approach gives little if any insight into the dynamic structural response or the underlying mechanisms behind the penetration process. Keep in mind that most empirical models are based on least-square curve fits to a limited number of experimental data, often by means of dimensional analysis.

Typical and well-known empirical models frequently found in the literature for the normal impact of steel plates by blunt cylindrical projectiles have been quoted and discussed in Børvik et al (1998b). Results from calculations using some of these formulas are shown in Fig. 19, while their stated limitations are as given in Table 3. It is important to notice that several of the plotted models do not completely satisfy the experimental limitations in this

study. Model results were obtained using typical input data from the penetration tests, where hardened blunt projectiles ($D_p = 20$ mm, $L_p = 80$ mm, $m_p = 197$ g) impacted circular Weldox 460 E steel plates ($d_t = 500$ mm, $\sigma_y = 490$ MPa, $\sigma_u/\sigma_y = 1.2$) of varying thickness in the sub-ordnance velocity regime. Fig. 19 illustrates the severe dispersion in predicted results. For the thinnest plate used in the calculations, the difference in critical velocity between the Recht-Ipson and the SRI model is 340 %. The scatter is also significant for the thickest plate, where the deviation in ballistic limit between the AEA and THOR equations is 260 %. It is seen that the Recht-Ipson model provides the closest fit to the experimental data. This is also the only model that gives a conservative estimate of the target response. However, also the AEA equation is relatively close, while both the BRL and the modified De Marre formulas give reasonable agreement with the experimental results. Nevertheless, it seems clear that special attention must be taken if the empirical approach is to be used in design. For that reason, both the analytical and numerical approach are of greater interest in structural impact, since these more physically based methods lend themselves better to applications over a wider range of problems.

5. Analytical models

Analytical models can range anywhere in complexity from simplified one-dimensional equations based on a single physical mechanism to very advanced two- or three-dimensional models derived from combined local mechanisms, assumed global deformation fields and different failure criteria. Many models have been proposed in the literature, and a thorough review on recent analytical models in the sub-ordnance impact velocity regime can be found in Corbett et al (1996). In contrast, only a few comparisons between model results and experimental data exist. Here, three analytical models developed to calculate the ballistic response of metal plates impacted by blunt projectiles are briefly presented. The models are then used to predict ballistic limit velocities and curves for the problem investigated experimentally. It is important at this stage to emphasise that other models may exist giving better agreement with the experimental results than those chosen in this particular study.

The Wen-Jones model

Wen and Jones (1996) proposed an approximate quasi-static model for the behaviour of punch-impact-loaded metal plates. Based on the principle of virtual work, load-deflection relationships were first obtained and then used to predict the energy absorbing capacity of plates subjected to low velocity impact causing perforation. Many approximations and simplifications were introduced into the analysis. However, the theoretical predictions on fully clamped steel plates were found to be in good agreement with experimental results from Corran et al (1983), Langseth and Larsen (1990) and Wen and Jones (1992, 1994) when material strain rate effects were taken into account. It was further provided that perforation did not occur by adiabatic shear instability. The main equations from the model are given in the appendix, while details in the theoretical description can be found in the original paper.

For this particular problem, necessary input data to the model is given in Table 4. The engineering stress-strain curve from quasi-static tensile tests was used to determine the yield stress σ_y and the ultimate stress σ_u (Fig. 4 and Table 1). The Cowper-Symond coefficients D and q in Eq. (12) were fitted to the experimental data from tensile tests on smooth specimens from the target material at different strain rates (Børvik et al, 1999a). As seen, the calibrated values of D and q are quite different from those given in Jones (1989) for steel. Material constants for the local critical shear strain γ_u , the work-hardening index n and the critical shear stress τ_u are determined in two different ways. First, the method described in the Wen-Jones paper was used. Here, γ_u and n were taken to be the “typical” values of 0.8 and 0.25 for mild steel, respectively, and τ_u was allowed to vary with target thickness as proposed by Langseth and Larsen (1990). The behaviour of a 12 mm thick Weldox 460 E steel plate using these coefficients is plotted as the curve “Calibration I” in Fig. 20. However, this is a rather inaccurate material description if compared to the material tests. Therefore, in the second approach, γ_u , n and τ_u were fitted to a shear stress-strain curve generated from the viscoplastic-damage model proposed by Børvik et al (2000c). This model was calibrated for Weldox 460 E steel and the shear stress is plotted for a strain rate of 10^4 s^{-1} in Fig. 20. The chosen strain rate of 10^4 s^{-1} ensures adiabatic conditions according to Lindholm and Johnson (1982), and this is also a reasonable value for the strain rate in the shear zone although local values may be much higher. A best fit to the viscoplastic-damage model gave the material constants for γ_u , n and τ_u in Table 4. The material behaviour using these values is shown as

the curve “Calibration II” in Fig. 20. It is seen that the latter gives a good description of the local material behaviour during penetration, even though material softening is not included.

Ballistic limit velocities calculated from Eq. (13) with input data as given above and in Table 4 are plotted versus target thickness in Fig. 21. Reasonably good agreement is obtained between the model and the experimentally obtained ballistic limits for plate thicknesses up to 16 mm if the material coefficients are fitted to the “Calibration II”-curve in Fig. 20. For thicker plates, the deviation is considerable. It is also seen that the Wen-Jones model does not describe the kink in the response curve (Fig. 9) with target thickness. Notice that when the static collapse load F_c exceeds the critical value of the transverse load F_u in Eq. (12), the critical transverse displacement of the plate becomes negative and the Wen-Jones model breaks down. Here, this occurs at a target thickness of about 26 mm. Furthermore, the model does not give a separate expression for calculation of the ballistic limit curve after plugging. However, residual projectile velocities can be estimated using the Recht-Ipson model (1963) in Eq. (1) with $a = m_p / (m_p + m_{pl})$, $m_{pl} = \rho \pi r_p^2 h_t$ and $p = 2$. This model gives reasonable agreement with the experimental data as long as the projectile deformation is small.

Finally, the Wen-Jones model gives an interesting relation between projectile indentation and shear failure. It is shown in Eq. (8) that if the critical shear strain γ_u is equal to the fitted value of 1.4, the critical depth of indentation is about $h_t / 2$, i.e. plugging occurs when the projectile has penetrated half the target thickness. This value is used in simplified models as a failure criterion and has been observed both experimentally and numerically (e.g. Børvik et al, 1999a). Here, the extension of the shear zone e is assumed to increase linearly with target thickness. Calculated relative maximum target deformations (W_{ox}) from Eq. (12) versus target thickness are compared with both experimental and numerical values in Fig. 38. The Wen-Jones model seems to give an excellent description of the global target deformation during impact. The model was also used to estimate the average value of the strain rate (see $\dot{\epsilon}_m$ in Eq. (12)). The strain rate was calculated to lie between 1 and 100 s^{-1} . However, this is with the exception of the shear zone, where the strain rate is assumed to be much higher.

The Bai-Johnson model

Bai and Johnson (1982) developed a mechanical model for plugging of metal plates based on adiabatic shear instability. The model consists of three basic elements; the kinetic energy equation connecting the projectile and plug, the constitutive equation and the relationship

between the displacement of the plug and the shear strain. Here, only a short summary of the most important features of the model is given in the appendix. It is referred to the original paper by Bai and Johnson (1982) for a more detailed description of the model.

By assuming the von Mises yield criterion and the normality rule, the material constants required in Eq. (18) were determined in a similar way as for the Wen-Jones model using the calibrated viscoplastic-damage model from Børvik et al (2000c) for an assumed strain rate of 10^4 s^{-1} . A plot of the adiabatic shear stress-strain curve derived from Eq. (18) is shown in Fig. 20, while the constants from the fit are given in Table 5 together with other necessary input data to the model. Furthermore, Bai and Johnson used a very simple failure criterion. They assumed that the penetration process terminates when the penetration depth p equals the target thickness $h_t = b$. However, microscopic examinations of impacted targets have indicated that complete separation of the plug often occurs at a penetration depth p between $b/2$ and b (Woodward, 1984). Ballistic limit curves as obtained from Eq. (15) for $p = b$ are shown in Fig. 22, while ballistic limit velocities calculated from Eq. (17) versus target thickness for $p = b/2$ and $p = b$ are plotted and compared to the experimental data in Fig. 23. It is seen from Fig. 23 that an upper limit for the ballistic resistance of the target is obtained when $p = b$, while good agreement with the experimental data is found for $b \geq 12 \text{ mm}$ when $p = b/2$. The latter corresponds well with the prescribed validity range of the Bai-Johnson model. Another possibility is to include a simple fracture criterion in the model. From Eq. (20) it is found that

$$p_u = \frac{n}{1-n} a \gamma_f \leq b \quad (2)$$

which for Weldox 460 E, where $\gamma_f \approx 2.4$ for $\dot{\epsilon} = 10^4 \text{ s}^{-1}$ and $n = 0.25$ (Table 5), leads to $p_u = 0.8a$. Thus, the penetration depth to failure is independent of target thickness when $b \geq p_u$. The obtained ballistic limit velocities using this criterion is also plotted versus target thickness in Fig. 23, and the results agree reasonably well with the experimental data. For the thinnest plates the fracture mode is not adiabatic shear instability, but rather a combined deformation mode of bending, shear and tension. As seen both in Fig. 11 and Fig. 12, global target deformation is a prominent energy absorbing mode for plates thinner than 12 mm. This mode is not accounted for in the Bai-Johnson model, and the ballistic resistance for the thinnest plates is therefore underpredicted. The shape of the ballistic limit curves in Fig. 22

are in good agreement with the experimental results, considering that projectile deformation which is considerable for the thickest plates (see Fig. 18) is not accounted for in the model.

It is also possible to extract detailed information such as shear strain, penetration force, energy absorption in the shear zone, temperature increase, projectile-plug velocity and shear strain rate as a function of penetration depth p from the Bai-Johnson model. The model was therefore utilised to estimate details associated with the shear plugging in a microscopic study on partially perforated target plates (Børvik et al, 2000b), giving reasonable agreement with the experimental observations. The duration of the penetration process as defined by Eq. (24), i.e. the time until a through-target-crack has occurred so that the shear zone can absorb no more energy, is also of great interest. If $p = b/2$, it is found that the perforation time is almost constant and about 80 μs independent of target thickness. Perforation times from the Bai-Johnson model are compared with other models and the experimental results in Fig. 39.

The Ravid-Bodner model

Ravid and Bodner (1983) proposed an advanced two-dimensional analytical model of the penetration and perforation process for intermediate thick plates struck normally by rigid projectiles, where the analysis parallels procedures used in metal forming operations. Due to the mathematical complexity of the model, no equations are quoted herein and it is referred to the original paper for further details. In the model, elastic effects are neglected, the target material is assumed rigid-viscoplastic and an overall work-rate balance of the rigid projectile/target system is established. The position and motion of the target material are determined at all times during the perforation process, and no empirical information is required. Global target deformation, shock compression, projectile deformation and erosion effects are not included in this paper, but are treated in other works by the authors. The analysis is thus applicable for normal impact of rigid projectiles into ductile targets at velocities from about 200 to 1000 m/s. Target thicknesses could range from fairly thin, i.e. on the order of the projectile diameter, to very thick (Bodner and Ravid, 1998). An essential feature of the analysis is the use of postulated, physically motivated deformation mechanisms in conjunction with the upper bound theorem of plasticity that is modified to include dynamic effects. A plastic flow velocity field is defined in the target that is consistent with the boundary conditions, the geometrical constraints, and continuity and mass conservation requirements. Five successive and interconnected stages of the penetration process, each represented by a distinct plastic flow field that is defined in the original paper, are computed.

Various failure modes are considered throughout the different stages, and a number of plugging modes can occur due to a limiting strain criterion or by adiabatic shear band formation. The available failure modes have been classified as adiabatic shearing, brittle failure in shear, plug formation and ductile failure. The model is self-contained and capable of predicting the exit velocities of the projectile and plug. It also determines the bulge and plug shape, provides the velocity-time and force-time histories of the process, and describes a number of geometrical features during the different deformation states of the target plate. The original model was developed for blunt projectiles, but other nose shapes that required changes in the plastic flow fields were considered in a paper by Ravid et al (1994). This paper also discussed the plastic flow field due to deep penetration and thermal softening.

Due to the mathematical complexity of the model, it requires numerical treatment. Here, the analyses were carried out using the computer program SHAY-1S from Rimat (1992). In the program, only standard input such as geometrical data of the projectile and target and conventional physical and mechanical properties are requested. The model output is arranged in sorted data files, giving typical terminal ballistic data, geometrical data, and scientific values such as strain rate, work rate, etc. Thus, the amount of detailed information provided by the model is extensive, and this may be used for validation purposes. In the analyses, the target material is assumed to be rigid-plastic with a flow stress defined as a function of strain rate. Ravid and Bodner suggested that work hardening should be considered by taking the flow stress σ_0 as the average value of plastic work over the full strain range. Here, a somewhat simpler approach is adopted and σ_0 is calculated as

$$\sigma_0 = (\sigma_y + \sigma_u) / 2 \quad (3)$$

where σ_y and σ_u are the yield and engineering ultimate stress, respectively, at a given strain rate. The strain rate dependence of the flow stress is given by the expression

$$\sigma_d = \sigma_0 [1 + C \log_{10} \dot{\epsilon}_{eff}] \quad (4)$$

where σ_d is the dynamic flow stress, σ_0 is the quasi-static flow stress, C is a material constant and $\dot{\epsilon}_{eff} = \dot{\epsilon} / \dot{\epsilon}_0$ where $\dot{\epsilon}$ is the actual strain rate and $\dot{\epsilon}_0 = 5 \cdot 10^{-4} \text{ s}^{-1}$ is taken as the quasi-static strain rate. Values of C have been fitted to the experimental data from tensile tests

at elevated rates of strain (Børvik et al, 2000c), both when $\sigma_\theta = \sigma_y$ and when σ_θ is as given by Eq. (3). The former was used in this study because it gives a conservative estimate of the flow stress. Based on earlier observations using blunt projectiles (Børvik et al, 2000c), frictional effects are neglected, i.e. $\mu_f = \mu_l = \mu_p = 0$. Based on von Mises the model assumes that failure occurs when $\gamma = \gamma_f$, where $\gamma_f = \sqrt{3}\varepsilon_f$ and ε_f is the true (logarithmic) strain to failure measured from the maximum reduction of cross-section area in a standard tensile test. This is a major simplification to the failure process during shear plugging. Both Table 1 and Fig. 4 indicate that Weldox 460 E is a very ductile material. The true strain to failure measured in a quasi-static tensile test is about 160 %, which is reduced to 120 % at a strain rate of 10^4 s^{-1} (Børvik et al, 1999a). These values are unsuitable to the Ravid-Bodner model, which was developed for moderately ductile materials such as armour steel. A condition such as the Considère's criterion for diffuse necking at maximum load (Dieter, 1988), i.e. where the rate of strain hardening equals the stress, may be more applicable for this model. For Weldox 460 E this criterion is realised at a true strain ε_n of about 20 % (see Fig. 4). The variation of ε_n with strain rate has earlier been found to be small (Børvik et al, 2000c). Assuming von Mises material, the shear stress-plastic strain curve used in the Ravid-Bodner model is plotted in Fig. 20 for an estimated strain rate of 10^4 s^{-1} . The material behaviour using this model is quite different from the other models. Even though the model is self-contained, indicating that there is no demand for empirical constants, one empirical input parameter regarding the fracture mode is needed. Here, the almost cylindrical plug as shown in Fig. 14 is close to the P2 condition described in the paper by Ravid and Bodner (1983), and is therefore used in all simulations. Also the AS (adiabatic shearing) option was tested, but it did not provide adequate results in these calculations. This option, which leads to a discontinuity in velocity between the different surfaces, is recommended when adiabatic shear bands are expected in the target. That adiabatic shear bands may appear in the target plates due to the penetration process was revealed in a micro-mechanical study by Børvik et al (2000b). Necessary input data to the Ravid-Bodner model is given in Table 6.

Calculated ballistic limit curves are given in Fig. 24. The computational step in all calculations was chosen equal to 0.1 mm, since the solution was found too coarse using the recommended value of 1 mm. In contrast to the experimental results, the "jump" in residual velocity at the ballistic limit seems to increase with target thickness and initial projectile velocity. Since projectile plastic deformation is not accounted for in the model, the ballistic limit curves approaches the ballistic limit line for a target of zero thickness as the velocity is

increased. Ballistic limit velocities versus target thickness are plotted in Fig. 25. The discrepancy between model predictions and experimental results are considerable in the intermediate thickness range. At the extreme ends, on the other hand, the model predictions correspond fairly well with the plotted trend line based on the experimental data. A number of factors may be responsible for the deviation in the results. Also thickness or material property variations of the target, non-perfect impacts, shock waves, etc, may influence the outcome. However, since the model is not able to describe global target deformation, it seems obvious that it fails to describe the kink in the response curve when the deformation mode changes.

Predicted histories of projectile velocity and resisting force versus penetration time for different target thicknesses are given in Fig. 26. For these curves, the impact velocity of the projectile is approximately 5 % above the respective ballistic limits. In the velocity-time curves in Fig. 26a), the drop in velocity after impact shows a weak linear increase with target thickness, while the perforation time is almost constant. It appears that the different curves do not intersect, and the minimum residual projectile velocity is seen to increase linearly with target thickness. Computed perforation times for different target thicknesses are plotted and compared with the experimental data in Fig. 39. An increase in velocity drop indicates an increase in interface force, as shown in the corresponding force-time curves in Fig. 26b). The projectile indentation during stage 1 is found to be very short ($t \sim 1 \mu s$) for the thinnest targets, but increases considerably as the targets grow thick. Thus, a plateau of constant force is obtained for the thickest plates during this time period. The resisting force then starts to fall in stage 2 (bulge formation) and stage 3 (bulge advancement) due to target mass movement in front of the projectile. A rapid drop in the resisting force occurs in stage 4 (plug formation and exit) due to separation of the plug from the target plate. This is seen to take place almost at the same time, independent of target thickness. Stage 4 continues until the plug is fully ejected from the target. Here, the resisting force in stage 5 (projectile exit) is zero due to the neglecting of frictional effects.

6. Numerical Simulations

As indicated in Chapter 3, both the energy absorbing mechanisms and the failure process itself will change during penetration when the target response changes from typically thin plate global deformation towards thick plate shear localisation. It is hence important to investigate if a numerical approach using finite elements is able to describe the structural

response. This is vital for FE codes that are intended for design of protective structures, and is further made topical since both the empirical equations given in Chapter 4 and the analytical models presented in Chapter 5 fail to do so. The validation is carried out by simulating all experimental tests presented in Chapter 3 using LS-DYNA, which is a general-purpose, finite element code for analysis of large deformation dynamic response of structures based on explicit time integration, and is therefore suitable for the type of problem under investigation. No attempts are made herein to describe the many algorithms involved in the code, and it is referred to the manuals of LS-DYNA (LSTC, 1998, 1999) for information regarding the numerical scheme.

Finite element models

In a similar way as for the experimental tests, the only variables in the numerical analyses were the initial projectile velocity and the target thickness. For each simulation, a fixed mesh of 4-node 2D axisymmetric elements with one-point integration and stiffness based hourglass control was used. Fig. 28 gives a plot of the nominal geometry of the projectile and the initial element model for a 12 mm thick plate, showing a section of the target plate and the blunt projectile just prior to impact. The target consist of two parts (see Fig. 28) in order to study global versus local energy absorption during penetration (Børvik et al, 2000a). In each run the target plate was fully clamped at the support, while the projectile was given an initial velocity identical to the one measured in the corresponding experiment. The initial size of the smallest element in the impact region was $0.125 \times 0.1 \text{ mm}^2$ in all simulations for target thicknesses equal to or less than 12 mm, giving from 40 (4 mm thick targets) to 120 (12 mm thick targets) elements throughout the plate thickness. For thicker targets, the element size in the impact region was increased to $0.25 \times 0.2 \text{ mm}^2$ in order to reduce the computational time. This gave from 80 (16 mm thick targets) to 150 (30 mm thick targets) elements through the thickness. Contact was modelled using an automatic 2D single surface penalty formulation available in LS-DYNA. In accordance with experimental observations in Børvik et al (2000d), frictional effects were neglected for blunt projectiles.

A coupled computational model of viscoplasticity and ductile damage was proposed by Børvik et al (2000c) for numerical simulations of the penetration problem. The model is based on work by Johnson and Cook (1983, 1985), Camacho and Ortiz (1997) and Lemaitre (1990, 1992). It includes linear thermoelasticity, the von Mises yield criterion, the associated flow rule, isotropic strain hardening, strain rate hardening, softening due to adiabatic heating,

softening due to isotropic damage evolution and a failure criterion. Model constants have been identified for the target material of Weldox 460 E steel by conducting standard tensile tests on smooth and notched specimens at room temperature, dynamic tests at room temperature and strain rates between 10^{-4} and 10^{+3} s^{-1} , and tests on smooth specimens at temperatures between 20 and 500°C (Børvik et al, 2000c). The calibrated constitutive model was used to generate the stress-strain curves shown in Fig. 27 for different rates of strain at constant hydrostatic tension ($\sigma^* = \sigma_m / \sigma_{eq} = 1/3$, where σ_m is the mean stress). The equation for the equivalent von Mises stress σ_{eq} is also given in Fig. 27. Here, the first bracket describes material degradation due to damage, the second gives the strain hardening, the third defines the effect of strain rate, while the last bracket gives the effect of temperature softening on σ_{eq} . To allow crack growth during penetration, the model is coupled with an element-kill algorithm in LS-DYNA that removes damaged elements from the mesh when the damage variable reaches its critical value. The projectile was simply modelled as a bilinear elastic-plastic von Mises material with isotropic hardening. Material constants for the target and projectile are listed in Børvik et al (2000c). These constitutive relations enter into the numerical model in all simulations.

Earlier simulations have indicated that the actual problem involving shear localisation and plugging for blunt projectiles is mesh size sensitive (Børvik et al, 2000a, 2000c). To check this, the ballistic limit velocity for several target thicknesses was determined when the number of elements over the thickness varied. The numerical result seems to converge towards a limit solution when the number of elements over the target thickness is sufficiently large, see Fig. 29a). Thus, the mesh size dependency seems not to be pathological. Note also that the numerical results change from non-conservative to conservative estimates of the ballistic limit when the number of elements over the target thickness increases. As seen in Fig. 29b), the mesh sensitivity is most distinct close to the ballistic limit. At higher velocities, the results are far less affected by mesh size. The mesh sensitivity could be expected since the width of the adiabatic shear band is typically in the order of 10^1 - $10^2 \mu\text{m}$ (Bai and Dodd, 1992, Børvik et al, 2000b). Here, the CPU-time of the simulations varied from 10 minutes (8 mm thick target; 20 elements through thickness; initial velocity of 600 m/s) to approximately 50 hours (16 mm thick target; 160 elements through thickness; initial velocity of 230 m/s) on a HP C360 workstation. In order to reduce the computational time, which is affected both by the element size and number, the element size was somewhat enlarged towards the clamp. A further

reduction of the element size in the impact region is for the time being restricted due to limitations in the computational resources.

Numerical results

Ballistic limit curves based on the numerical results are constructed in Fig. 30. If these are compared to the experimental curves in Fig. 8, some minor differences are seen. Probably due to the simplified material model for the projectile, giving a too small plastic deformation of the nose during impact, the slope of the calculated ballistic limit curves is slightly steeper than in the corresponding experimental curves for the thickest targets. No fracture criterion is included in the material model for the projectile. Hence, the ballistic limit curves for 20, 25 and 30 mm thick target plates could be simulated without problems. The jump in residual velocity at the ballistic limit seems to decrease slightly with target thickness, as also observed experimentally, and the agreement between numerical and experimental ballistic limit curves is in general good. Both the ballistic limit curves and ballistic limit velocities were estimated from a least square fit of the model constants in the Recht-Ipson model in Eq. (1) to the numerical residual velocities. Values of a , p and v_{bl} from the fits are given in

Table 7. Ballistic limit velocities are plotted against target thickness and compared to experimental values in Fig. 31. The agreement is excellent and the numerical predictions are within 5 % of the corresponding experimental value for all target thicknesses. The simulations also give a precise description of the observed kink in response curve with target thickness.

Plots showing perforation of target plates with different thicknesses are given in Fig. 32, where fringes of accumulated plastic strain are plotted on the deformed geometry. It is seen that the extension of the localised plastic zone increases and the global target deformation decreases with increasing target thickness (see also Børvik et al, 2000b). These plots compare well with the high-speed camera images in Fig. 12. Thus, the numerical approach seems to capture the overall physical behaviour during plugging. Details of shear localisation, crack propagation and complete failure in the element mesh from one simulations of a 20 mm thick target are shown in Fig. 33. The number of eroded elements in simulations using blunt projectile is normally small. In general, as the initial projectile velocity is increased, so is the number of eroded elements. For the thinnest targets, where much tension is present during failure, the number of eroded elements is relatively higher than for thicker plates dominated by shear. As the target becomes thick, the extension of the plastic zone causes more than one element column to erode. This can be seen from the fracture patterns in Fig. 34 for different

target thicknesses at impact velocities close to the ballistic limit. Even so, the loss of energy in the simulations is small and normally not more than 1-2 % of the initial kinetic energy. The energy loss due to element erosion has been discussed in more detail by Børvik et al (2000e).

Calculated histories of projectile velocity and interface force are plotted in Fig. 35. If the velocity-time curves are compared with those measured from the high-speed camera images in Fig. 16, the behaviour is found to be similar, while they differ quite much from those obtained by the Ravid-Bodner model in Fig. 26a). Still, they all indicate that the perforation time is constant and independent of target thickness when the impact velocity is close to the ballistic limit. The small areas of constant velocity seen for all target thicknesses in Fig. 35a) are due to the temporary loss of contact between the projectile and plug during penetration. This is probably the reason for the observed difference in projectile and plug residual velocity (Børvik et al, 1999a). The extensive drop in velocity over a short time period implies a large interface force at impact (Fig. 35b). In a similar way as for the Ravid-Bodner model (Fig. 26), the force varies little during the indentation process. This may be the reason for the projectile break-up in the thickest targets. In thinner plates, on the other hand, the impulse is not strong enough to cause projectile fragmentation. Once the material in front of the projectile starts to move, the force falls off rapidly. From Fig. 35b) it is seen that the force does not drop to zero immediately after fracture. The force continues to act as long as the plug and projectile nose are within the target due to contact between the bodies (Fig. 33).

Permanent plug thickness versus initial target thickness from the simulations is plotted in Fig. 36 and several interesting features are obtained. First, the computed thinning of the plug is almost linear and in close agreement with the experimental values to a target thickness of about 20 mm (see also Fig. 17a). Then, for thicker plates the plug thinning seems to flatten out, indicating a constant plug thickness. Børvik et al (2000d, 2000e) studied the effect of projectile nose shape on the failure mode in targets both experimentally and numerically. They found that in 12 mm thick Weldox 460 E steel plates, plugging due to adiabatic shear banding was the most effective failure mode. From a simplified model by Woodward (1984), it can be shown analytically that plugging is more favourable than ductile hole enlargement for a target thickness less than $\sqrt{3}d_p / 2$, which in this particular study is about 17 mm. Such behaviour is indicated in Fig. 36. For targets with a thickness above 20 mm, the material in front of the projectile is pushed aside during indentation due to ductile hole enlargement. Thus, when the thickness of the target in front of the projectile has been sufficiently reduced, plugging will again be the dominant failure mode and a plug failure occurs.

The amount of energy absorbed in local and global target deformation (see Fig. 28) and in projectile mushrooming in simulations at impact velocities close to the respective ballistic limits is shown Fig. 37 for different target thicknesses. For the thinnest plates, most of the energy is absorbed in global deformation. However, as the thickness is increased, more and more energy is absorbed in localised shearing. At a target thickness of 10 mm, the curves intersect and more energy is absorbed in local than in global deformation. This is also where the deformation mode was found to change (see Fig. 9) and where adiabatic shear bands were first detected (Børvik et al, 2000b). Up to a thickness of 16 mm, the amount of local work continues to increase, while the amount of global work decreases. Afterwards, the ratio between the two curves is about constant. The amount of energy absorbed in the projectile increases linearly to a target thickness of about 20 mm. This is where the projectile starts to fracture in the tests. The energy absorption then flattens out and becomes constant at about 20 % of the total work. Relative deformations versus target thickness from the numerical simulations have been plotted and compared to the experimental data and results from the Wen-Jones analytical model in Fig. 38, and the agreement is good. Finally, perforation times versus target thicknesses are given in Fig. 39. Here, the experimental data points have been estimated from the high-speed camera images and are therefore only approximate. However, both the experimental and numerical data indicate that the perforation time is reduced with increasing target thickness to 20 mm, in contrast to calculations from the analytical models.

7. Concluding remarks

This paper is concerned with the ballistic penetration and perforation of circular Weldox 460 E steel plates with a thickness range from 4 to 30 mm impacted by blunt cylindrical projectiles in the velocity range of 75-500 m/s. The study is divided into three major parts. First, experimental details from almost 100 high-precision large-scale impact tests are given. In the tests, the only variables were the initial projectile velocity and the target thickness. In the second part, empirical equations and analytical models are briefly discussed, and then used to estimate ballistic limit velocities and curves. The last part gives results and findings from more than 150 finite element simulations of the problem investigated experimentally. Some important observations and conclusions from the study are listed below.

- Experimentally, both the “jump” in residual velocity at the ballistic limit and the slope of the ballistic limit curve decrease with target thickness and initial projectile velocity.
- A distinct kink in the ballistic response curve was obtained at a target thickness of about 10 mm. The change in target response seems related to a change in deformation mode with target thickness, from thin plate global deformation towards thick plate shear localisation.
- While the maximum target deformation was nearly twice the thickness for the thinnest plates, hardly any global deformation could be measured for plates of 16 mm or thicker. Projectile deformation, on the other hand, increased strongly with target thickness and impact velocity. At thicknesses above 20 mm, the projectile fractured at impact with only limited damage on the target plate. The perforation time was found to be fairly constant for all target thicknesses at impact velocities close to the ballistic limit.
- Calculations using empirical equations revealed an extensive spread in model results and a considerable difference between predictions and experiments. It is realised that most empirical models result from curve fits to a limited number of experimental data and do not provide any physically based description. Even though the empirical approach is still frequently used for design purposes, mainly due to the absence of reliable analytical models for preliminary calculations, they should not be used without special care.
- Some typical analytical models were also used in calculations of the ballistic event. Unfortunately, none of these were able to describe the structural response correctly when the target thickness changed from thin to thick, even though all models gave results in reasonable agreement with the experimental data. The reason why the analytical models fail to describe the structural response may be a poor description of the material behaviour under impact loading or the fact that most analytical models assume one physical mechanism to dominate the problem. Hence, it was found that the Wen-Jones model gives a good prediction of the global target deformation and reasonable results for target thicknesses equal to or less than 12 mm. The Bai-Johnson model, on the other hand, gives a physical description of shear instability, and results in reasonable agreement with the experimental data for target thicknesses above 12 mm. Although the Ravid-Bodner model also showed deviation compared to the experimental results, it is by far the most general of the analytical models used. It is expected to give better results when the impact velocity is increased, such as the case of armour piercing bullets impacting hard steel targets.
- A large number of numerical simulations have been carried out using LS-DYNA. When the numerical results are compared with the experimental data, excellent agreement is

found. Both the ballistic limit curves and in particular the ballistic limit velocities are precisely determined using numerical simulations. Also the overall physical behaviour of the target plate during impact is very well described.

- The amount of detailed information from the numerical simulations is overwhelming, and in general much more extensive than what is available from analytical models. In particular the ability of visualising the penetration process in combination with a large number of history variables is advantageous. From the numerical results in this and similar papers, it seems reasonable to state that a verified and validated numerical model can be used both to increase the physical understanding of the penetration problem and to extend the limited experimental database.

Acknowledgements

The financial support of this study by the Norwegian Defence Construction Service, Central Staff/Technical Division, Oslo, Norway, is gratefully acknowledged.

References

- Anderson Jr CE, Wilbeck JS, Wenzel AE, Westine PS, Lindholm US, 1995. A Short Course on Penetration Mechanics: Authors, Course Notes, Southwest Research Institute, San Antonio, USA.
- Anderson Jr CE (Ed), 1999. Hypervelocity Impact, Proceedings of the 1998 Symposium, International Journal of Impact Engineering 23 (1), pp. 1-1024.
- Backman, ME, Goldsmith, W, 1978. The Mechanics of Penetration of Projectiles into Targets, International Journal of Engineering Science 16, pp. 1 – 99.
- Bai YL, Johnson W, 1982. Plugging: Physical Understanding and Energy Absorption, Metals Technology 9, pp. 182-190.
- Bai YL, Dodd B, 1992. Adiabatic Shear Localization. Occurrence, theories and applications. Pergamon Press.
- Bodner SR, Ravid M, 1998. Review and Some Applications of 2D Analytical Models of Ballistic Penetration, Proceedings Transient loading and response of structures, International Symposium honouring Mr. Arnfinn Jenssen, Trondheim, Norway, 25 – 27 May.
- Børvik T, Vestli K, Langseth M, 1997. Determination of Projectile Path during Ballistic Penetration by use of a High-Speed Digital Camera, Proc Association for High-Speed Photography and Photonics Conference, Cambridge, UK, April.

- Børvik T, Holen K, Langseth M, Malo KA, 1998a. An Experimental set-up used in Ballistic Penetration, Proceedings of Fifth International Symposium on Structures under Shock and Impact, pp. 683-692, Thessaloniki, Greece, 24 – 26 June.
- Børvik T, Langseth M, Hopperstad OS, Malo KA, 1998b. Empirical Equations for Ballistic Penetration of Metal Plates, Fortifikatorisk Notat No. 260/98, The Norwegian Defence Construction Service, Central Staff-Technical Division, Oslo mil/Akershus, 0015 Oslo, Norway.
- Børvik T, Langseth M, Hopperstad OS, Malo KA, 1999a. Ballistic Penetration of Steel Plates, International Journal of Impact Engineering 22 (9-10), pp 855 - 887.
- Børvik T, Langseth M, 1999b. Quasi-Static Penetration of Steel Plates, Proc from Integrity, Reliability, Failure: An International Conference, University of Porto, Portugal, 19-22 July.
- Børvik T, Hopperstad OS, Berstad T, Langseth M, 2000a. Numerical Simulation of Plugging Failure in Ballistic Penetration, accepted for publication in the International Journal of Solids and Structures.
- Børvik T, Leinum JR, Solberg JK, Hopperstad OS, Langseth M, 2000b. Observations on shear plug formation in Weldox 460 E steel plates impacted by blunt-nosed projectiles, accepted for publication in the International Journal of Impact Engineering.
- Børvik, T., Hopperstad, O.S., Berstad, T. and Langseth, M., 2000c. Computational Model of Viscoplasticity and Ductile Damage for Projectile Impact, submitted for publication.
- Børvik T, Langseth M, Hopperstad OS, Malo KA, 2000d. Effect of Projectile Nose Shape in Structural Impact, Part I: Experimental Study, submitted for publication.
- Børvik T, Hopperstad OS, Berstad, T, Langseth, M, 2000e. Effect of Projectile Nose Shape in Structural Impact, Part II: Numerical Simulations, submitted for publication.
- Camacho GT, Ortiz M, 1997. Adaptive Lagrangian Modelling of Ballistic Penetration of Metallic Targets, Int J Comp Meth Appl Mech Engng 142, pp 269-301.
- Corbett GG, Reid SR, Johnson W, 1996. Impact Loading of Plates and Shells by Free-Flying Projectile, International Journal of Impact Engineering 18 (2), pp 141 - 230.
- Corran RSJ, Shadbolt PJ, Ruiz C, 1983. Impact Loading of Plates – An Experimental Investigation, International Journal of Impact Engineering 1 (1), pp 3 - 22.
- Dieter GE, 1988. Mechanical Metallurgy, McGraw-Hill Book Company, UK.
- Forrestal MJ, Hanchak SJ, 1999. Perforation on HY-100 steel plates with 4340 R_c 38 and maraging T-250 steel rod projectiles, International Journal of Impact Engineering 22 (9-10), pp 923 - 933.
- Førre B, 2000. Private communication. Department of Physics, Norwegian University of Science and Technology (NTNU), E-mail: bernt.forre@phys.ntnu.no
- Goldsmith W, 1999. Non-ideal projectile impact on targets, Int J Impact Engineering 22 (2-3), pp 95 - 395.
- Hanchak SJ, Forrestal MJ, 1997. Private communication.
- Johnson GR, Cook WH, 1983. A Constitutive Model and Data for Metals Subjected to Large Strains, High Strain Rates and High Temperatures, Proceedings of Seventh Int. Symposium on Ballistics, The Hague.
- Johnson GR, Cook WH, 1985. Fracture Characteristics of Three Metals Subjected to Various Strains, Strain Rates, Temperatures, and Pressures, International Journal Engineering Fracture Mechanics 21, pp 31-48.
- Jones N, 1989. Structural Impact, Cambridge University Press.

- Jowett, J, 1986. The Effects of Missile Impact on Thin Metal Structures, UKAEA Safety and Reliability Directorate Report No SRDR 378.
- Langseth M, Larsen PK, 1990. Dropped Objects' Plugging Capacity of Steel Plates: An Experimental Investigation, *International Journal of Impact Engineering* 9 (3), pp 289 - 316.
- Langseth M, Larsen PK, 1992. The Behaviour of Square Steel Plates subjected to a Circular Blunt Ended Load, *International Journal of Impact Engineering* 12 (4), pp .
- Langseth M, Larsen PK, 1994. Dropped Objects' Plugging Capacity of Aluminium Alloy Plates, *International Journal of Impact Engineering* 15 (3), pp 225 - 241.
- Langseth M, Hopperstad OS, Berstad T, 1999. Impact loading of plates. Validation of numerical simulations by testing, *International Journal of Offshore and Polar Engineering* 9 (1), pp.
- Lemaitre J, Chaboche J-L, 1990. *Mechanics of solid materials*, Cambridge University Press.
- Lemaitre J, 1992. *A Short Course in Damage Mechanics*, Springer-Verlag.
- Lindholm US, Johnson GR, 1982. Strain-rate effects in metals at large shear strains, *Proceedings of the 29th Sagamore Army Material Research Conference "Material behaviour under high stress and ultrahigh loading rates"*, J. Mescall and V. Weiss (Eds.), 19-23 July, New York, pp 61-79.
- LSTC, 1998. *LS-DYNA Theoretical Manual*.
- LSTC, 1999. *LS-DYNA User's Manual, Version 950*.
- Neilson AJ, 1985. Empirical Equations for the Perforation of Mild Steel Plates, *International Journal of Impact Engineering* 3 (2), pp. 137-142.
- Norwegian Defence Construction Service (NDCS), 1990. *Handbook in Fortification, Part I: Weapons effect* (in Norwegian), Central Staff - Technical Division, Oslo mil/Akershus, 0015 Oslo, Norway.
- Ravid M, Bodner SR, 1983. Dynamic Perforation of Viscoplastic Plates by Rigid Projectiles, *Int. J. Impact Engng.* 21 (6), pp. 577-591.
- Ravid M, Bodner SR, Holzman I, 1994. Penetration into thick Targets – Refinement of a 2D Dynamic Plasticity Approach, *Int. J. Impact Engng* 15 (5), pp 587-603.
- Recht RF, Ipson TW, 1963. Ballistic Perforation Dynamics, *J. Appl. Mech.* 30, pp. 384 - 390.
- Rimat – Advanced Technologies Ltd, 1992. *SHAY 1S – Dynamic Perforation of Viscoplastic Plates by Rigid Projectiles*, Version 3.2, Hod Hashron, Israel.
- Scheffler DR, Zukas JA, 2000. Practical aspects of numerical simulations of dynamic events: material interfaces, *International Journal of Impact Engineering* 24 (8), pp 821 – 842.
- Wen H-M, Jones N, 1992. Semi-Empirical Equations for the Perforation of Plates Struck by a Mass, *Structures Under Shock and Impact (SUSI) II*, pp 369-380, Ed. PS Bulson, Computational Mechanics Publications.
- Wen H-M, Jones N, 1994. Experimental Investigation into the Dynamic Plastic Response and Perforation of a Clamped Circular Plate Struck Transversely by a Mass, *Proc Instn Mech Engrs., Journal of Mechanical Engineering Science*, Vol. 208 (C2), pp 113 - 137.
- Wen H-M, Jones N, 1996. Low-Velocity Perforation of Punch-Impact-Loaded Metal Plates, *Journal of Pressure Vessel Technology* 118, pp 181 – 187.
- Woodward RL, 1984. The Interrelation of Failure Modes Observed in the Penetration of Metallic Targets, *International Journal of Impact Engineering* 2 (2), pp 121 – 129.
- Zukas JA et al, 1982. *Impact Dynamics*, John Wiley and Sons, New York.
- Zukas JA et al, 1990. *High Velocity Impact Dynamics*, John Wiley and Sons, New York.

Appendix

The Wen-Jones (1996) model

Consider a clamped circular plate having an outer radius R and thickness H loaded at the centre by a blunt circular punch with diameter $d = 2a$. It is assumed that a transverse velocity (or displacement) field for a rigid, perfectly plastic plate can be written as

$$W = W_0 \text{ for } r \leq a \quad \text{and} \quad W = W_0 \left[\frac{\ln(r/R)}{\ln(a/R)} \right] \text{ for } a \leq r \leq R \quad (6)$$

where W is the transverse displacement of the plate at a radius r and W_0 is the transverse displacement at the periphery of the punch-plate interface. Taking local indentation Δ into account and utilising the principle of virtual work, an approximate quasi-static load-displacement relationship can be established as

$$W_t = W_0 + \Delta = \frac{F - F_c}{K_m} + \left(\frac{F}{F_u} \right)^{1/n} \Delta_c \quad (7)$$

where W_t is the total transverse displacement of the punch, F is the applied load between the punch and plate, $F_c = (4/\sqrt{3})\pi M_0 [1 + (1 + \sqrt{3}/2) \ln(R/a)]$ is the plate's static collapse load for infinitesimal displacements and $K_m = 2\pi N_0 / \ln(R/a)$ is the membrane stiffness of the plate. $N_0 = \sigma_y H$ and $M_0 = \sigma_y H^2 / 4$ are the fully plastic membrane force and bending moment per unit length, respectively, and σ_y is the static uniaxial tensile yield stress. $F_u = \tau_u A_s$ gives the critical shear force at plugging failure, where $\tau_u = \sigma_u [0.41(H/d) + 0.42]$ may be taken as the critical shear stress for steel plates (Langseth and Larsen, 1990). Finally, n is the work-hardening index of the material defined from the constitutive expression $\tau = \tau_u (\gamma / \gamma_u)^n$. The relation between the punch indentation Δ and the shear strain γ is assumed as

$$\Delta = e\gamma = \frac{1 + \sqrt{3}}{8} H\gamma \quad (8)$$

where e is the half-width of the localised shear band, obtained using moment equilibrium for an axisymmetrically loaded circular plate. Thus, the critical indentation Δ_c of the punch when shear failure occurs

is $\Delta_c = e\gamma_u$, in which γ_u is the critical shear strain. The energy is assumed absorbed by the system when statically loaded as

$$E_t = E_{bm} + E_s = \frac{F_u^2 - F_c^2}{2K_m} + \frac{F_u \Delta_c}{1+n} \quad (9)$$

or equivalent

$$\frac{E_t}{\sigma_y d^3} = A \left(\frac{H}{d} \right) + B \left(\frac{H}{d} \right)^2 + C \left(\frac{H}{d} \right)^3 \quad (10)$$

where

$$\begin{aligned} A &= 0.138\lambda^2 \ln(R/a) \\ B &= 0.270\lambda^2 \ln(R/a) + 0.451\lambda\gamma_u / (1+n) \\ C &= 0.132\lambda^2 \ln(R/a) + 0.440\lambda\gamma_u / (1+n) - (\pi/12)\ln(R/a) \left[1 + (1 + \sqrt{3/2}) / \ln(R/a) \right]^2 \end{aligned} \quad (11)$$

Here, E_{bm} is the energy dissipated by bending and membrane stretching, E_s is the energy dissipated by shear deformations, and $\lambda = \sigma_u / \sigma_y$ where σ_u is the ultimate tensile stress. It was further assumed that a quasi-static model was suitable for metal plates impacted by relatively large masses travelling at relatively low velocities. Material strain rate sensitivity was taken into account using the Cowper-Symonds empirical equation

$$\sigma_d = \sigma_y \left[1 + \left(\frac{\dot{\epsilon}_m}{D} \right)^{1/q} \right], \quad \dot{\epsilon}_m = \frac{2W_{os}V_c}{3\sqrt{2}Ra \ln^2(a/R)}, \quad W_{os} = \frac{F_u - F_c}{K_m} \quad (12)$$

where σ_d is the dynamic yield stress, D and q are material constants, $\dot{\epsilon}_m$ is the mean strain rate when the plate fails in shear plugging, V_c is the critical velocity or ballistic limit, and W_{os} is the critical transverse displacement at failure. At the ballistic limit, the amount of energy absorbed by the system is $E_t = E_p = \frac{1}{2}GV_c^2$, where G is the projectile mass. Thus, an approximate expression of the ballistic limit for the target is found from Eq.(10) as

$$V_c = \sqrt{\frac{2\sigma_y d^3}{G} \left[\left(1 + \left(\frac{2W_{os}V_c}{3\sqrt{2}DRa \ln^2(a/R)} \right)^{1/q} \right) \cdot \left[A \left(\frac{H}{d} \right) + B \left(\frac{H}{d} \right)^2 + C \left(\frac{H}{d} \right)^3 \right] \right]^{1/2}} \quad (13)$$

The Bai-Johnson (1982) model

Consider the normal impact of an infinite circular plate with thickness b and density ρ by a blunt, cylindrical projectile with radius a and mass M . The distance r is zero in the centre of the plate and $r = a$ at the periphery of the projectile. It is assumed that only simple shear deformation occurs along the direction of the moving projectile during the penetration process, and friction and stress wave effects are neglected. The displacement of the plate element at $r = a$, which equals the penetration depth p of the projectile, can be obtained by the integral

$$p = -\int_{\infty}^{\alpha} \gamma dr \quad (14)$$

This limits the validity of the model to systems where the ratio of projectile diameter to target thickness is about unity. The conservation laws give the relationship between the initial velocity of the projectile v_0 and the current velocity of the projectile and plug v as

$$v = \left\{ \frac{M^2}{(M+m)^2} v_0^2 - \frac{2e}{(M+m)} \right\}^{1/2} \quad (15)$$

where $m = \pi a^2 b \rho$ is the mass of the plug. The energy e absorbed in the shear zone as a function of penetration depth p is calculated as

$$e(p) = \int_0^p 2\pi a b \tau_s(\bar{p}) d\bar{p} \quad (16)$$

where τ_s is the shear stress at distance $r = a$, which is at the plug boundary. The function $\tau_s = \tau_s(p)$ is derived below. An expression for the ballistic limit or critical impact velocity v_{0c} , which implies zero residual velocity of the projectile, is readily obtained as

$$v_{0c} = \left\{ 2e_u (M+m) / M^2 \right\}^{1/2} \quad (17)$$

where $m = \pi a^2 b \rho$ is the mass of the plug, $e_u = e(p_u)$ is the ultimate energy absorbed in the shear zone during the impact event, and p_u is the ultimate penetration beyond which no energy is consumed. Bai and Johnson used as a criterion for shear instability that temperature softening should outbalance strain and strain-rate hardening, i.e. that an increment in shear stress was equal to or less than zero in the loading process. They also assumed that the effect of strain rate variation under adiabatic conditions could be ignored. Using these assumptions, an explicit expression of the shear stress in terms of the shear strain was proposed as

$$\tau = \tau_M \left(\frac{\gamma}{\gamma_u} \right)^n \exp \left\{ \frac{n}{1+n} \left[1 - \left(\frac{\gamma}{\gamma_u} \right)^{n+1} \right] \right\} \quad (18)$$

where γ_u and τ_M denote the critical shear strain and the maximum shear stress at incipient thermoplastic shear instability, i.e. at $d\tau=0$, and n represents the strain hardening exponent. In the derivation of the constitutive relation, it was assumed that $K=1$, i.e. the portion of plastic work converted into heat equals unity. The differential equation of the target plate, assuming the deformation of the plate beyond the plug to be quasi-static, gives the relation between the shear stress τ and the distance r . Using the constitutive relation, an expression

for the shear strain γ as a function of distance r is obtained. Since this expression turns out to be rather involved, Bai and Johnson proposed an approximation in the form

$$\frac{\gamma}{\gamma_a} = \left(\frac{a}{r}\right)^{1/n} \quad (19)$$

The relation between the shear strain γ_a at distance $r = a$ (i.e. in the adiabatic shear band) and the penetration depth p follows as

$$\gamma_a(p) = \frac{1-n}{n} \frac{p}{a} \quad (20)$$

Time differentiation of Eq. (20) gives the shear strain rate in the adiabatic shear band

$$\frac{d\gamma_a}{dt} = \frac{1-n}{n} \frac{dp_a}{dt} = \frac{1-n}{n} \frac{v_a}{a} \quad (21)$$

Combining the above equations, it is possible to express the shear stress τ_a in terms of the penetration depth p

$$\tau_a(p) = \tau_m \left(\frac{1-n}{n\gamma_a} \frac{p}{a}\right)^n \exp\left\{\frac{n}{1+n} \left[1 - \left(\frac{1-n}{n\gamma_a} \frac{p}{a}\right)^{n+1}\right]\right\} \quad (22)$$

It is further possible to obtain an expression for the temperature θ_a at the plug boundary, $r = a$, as a function of the penetration depth p

$$\theta_a(p) = \theta_0 + \frac{1-n}{na} \frac{1}{\rho C_V} \int_0^p \tau_a(\bar{p}) d\bar{p} \quad (23)$$

where θ_0 is the initial temperature of the target and K equals unity. The penetration time t against penetration depth p can finally be calculated from the relation $dp/dt = v$ as

$$t(p) = \int_0^p \frac{1}{v(\bar{p})} d\bar{p} \quad (24)$$

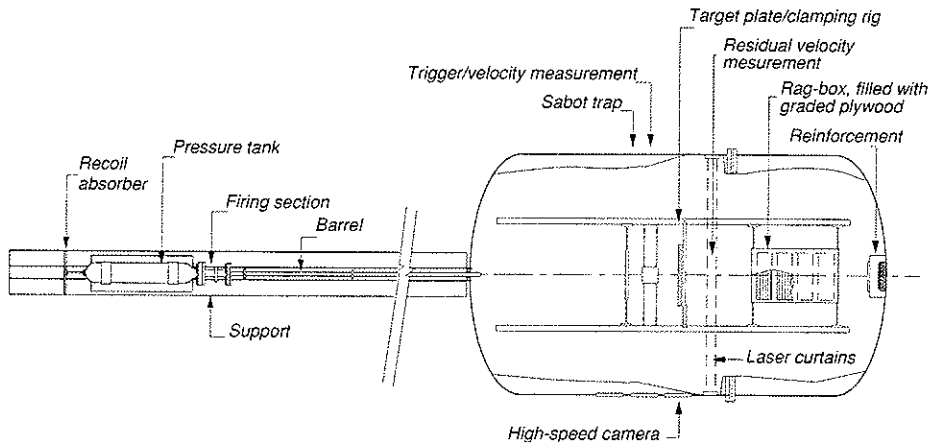


Fig. 1: Sketch of compressed gas gun.

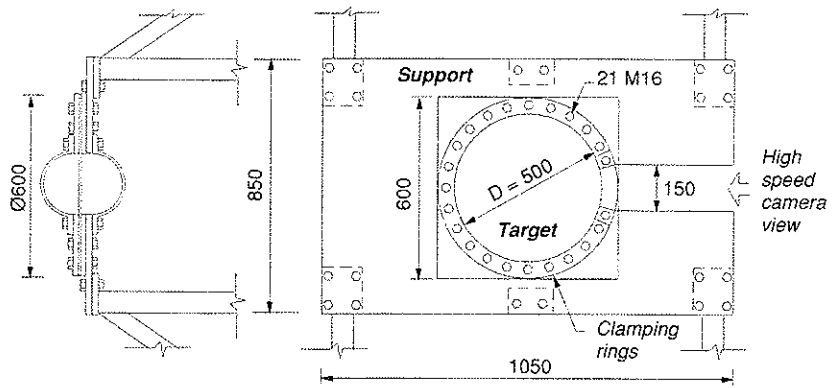


Fig. 2: Target clamped in frame.

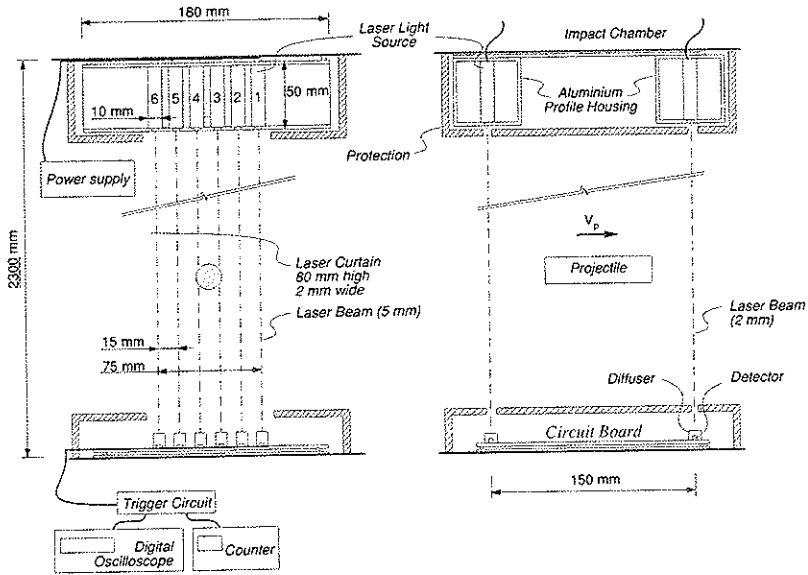


Fig. 3: Residual velocity measurement station.

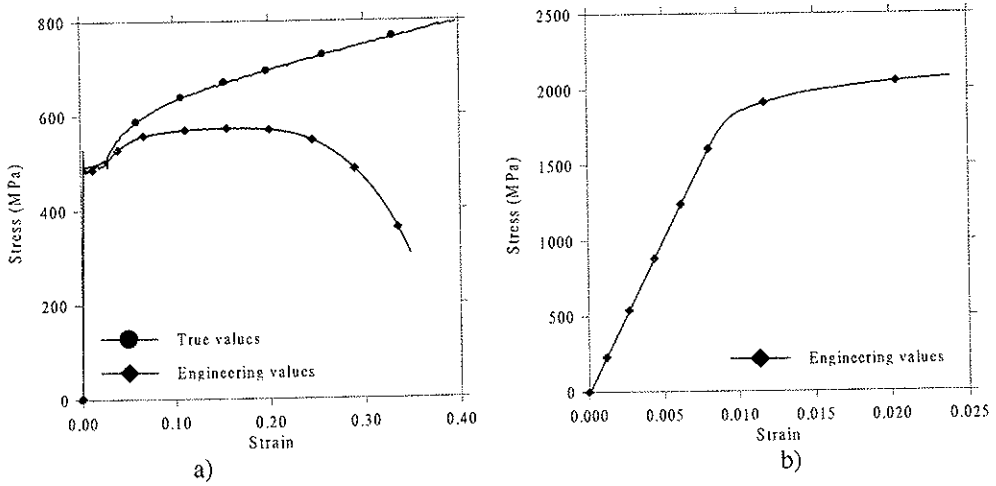


Fig. 4: Typical quasi-static tensile stress-strain curves for a) Weldox 460 E (target material) and b) hardened Arne tool steel (projectile material).

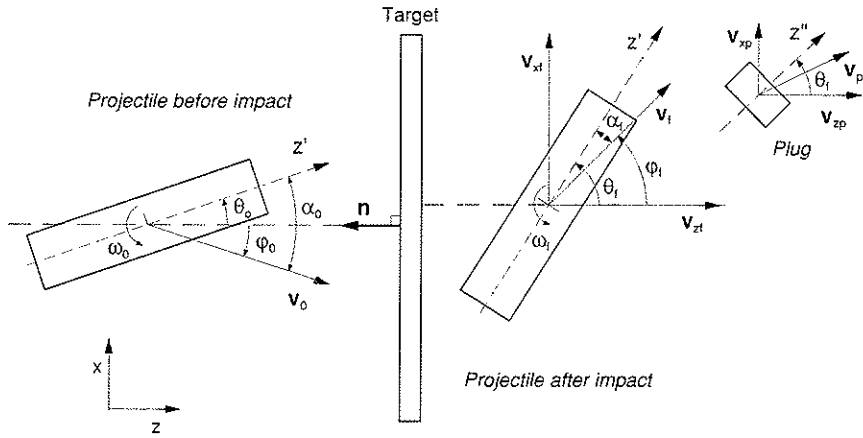


Fig. 5: Definition of projectile attitude during perforation (vertical plane).

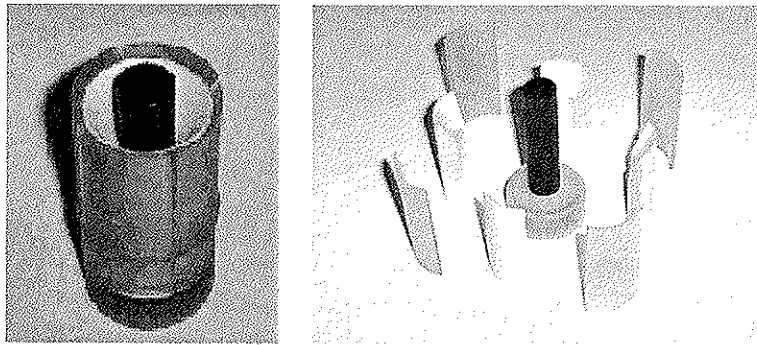


Fig. 6: Projectile sabot design.

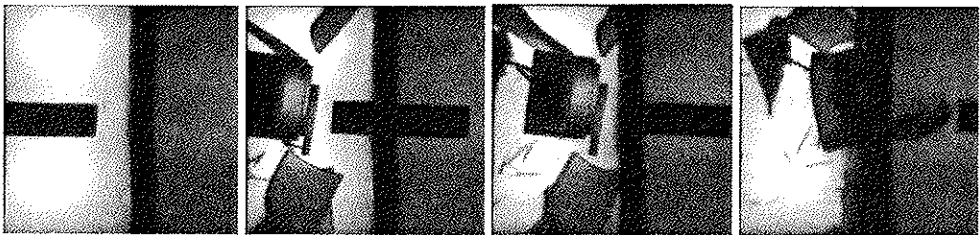


Fig. 7: Projectile passage through the sabot trap, while the separated sabot pieces are stopped.

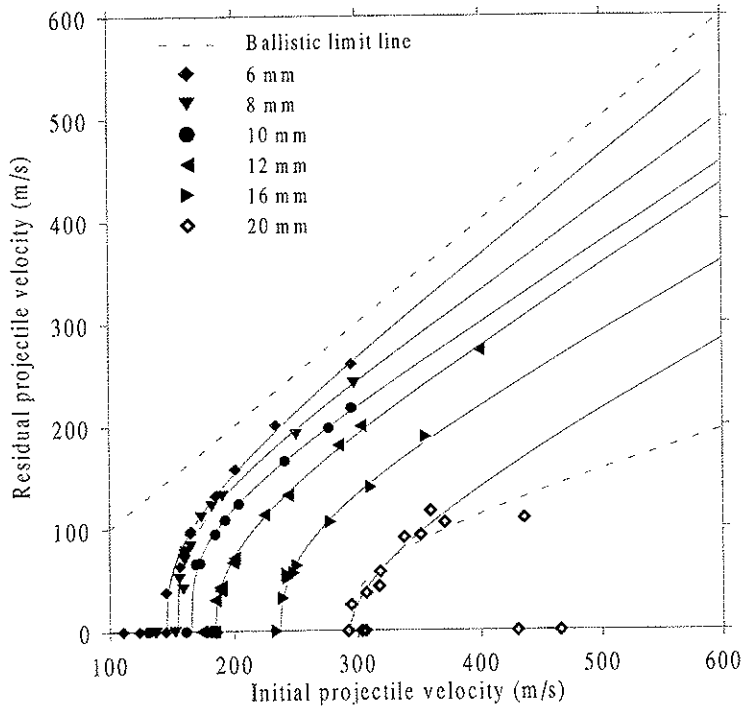


Fig. 8: Experimental ballistic limit curves.

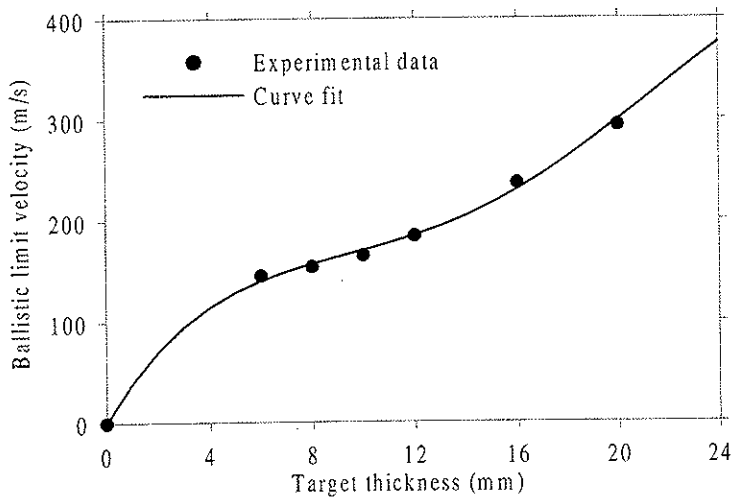


Fig. 9: Ballistic limit velocity versus target thickness.

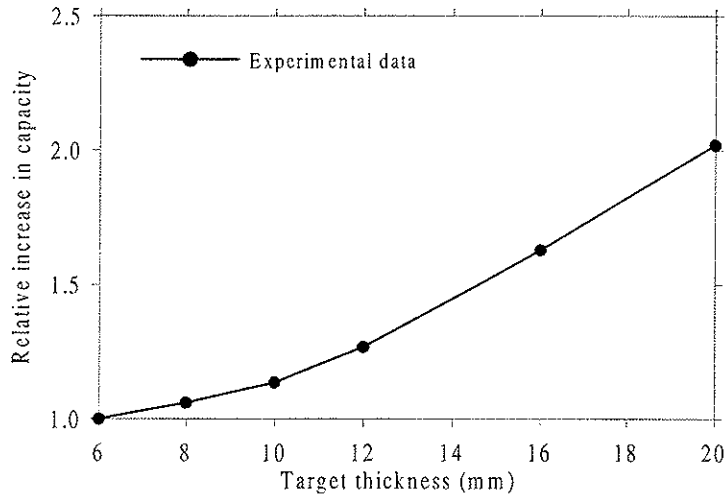


Fig. 10: Relative increase in ballistic limit velocity with target thickness.

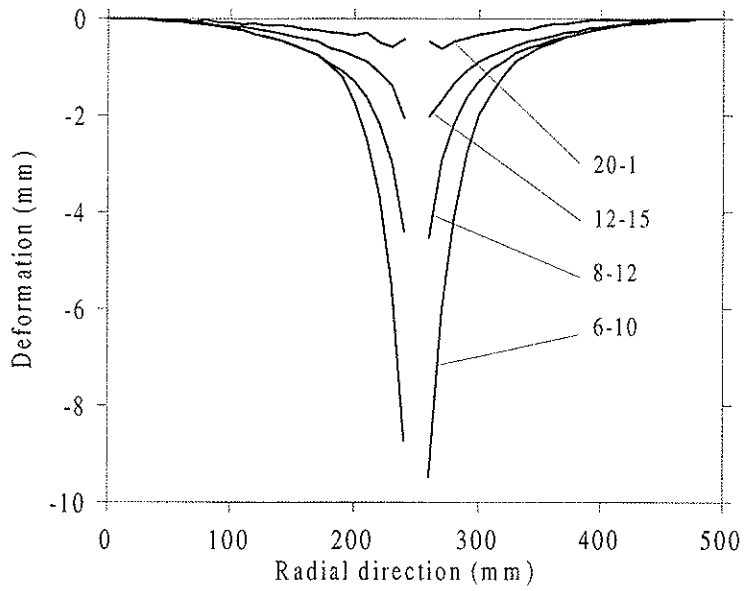
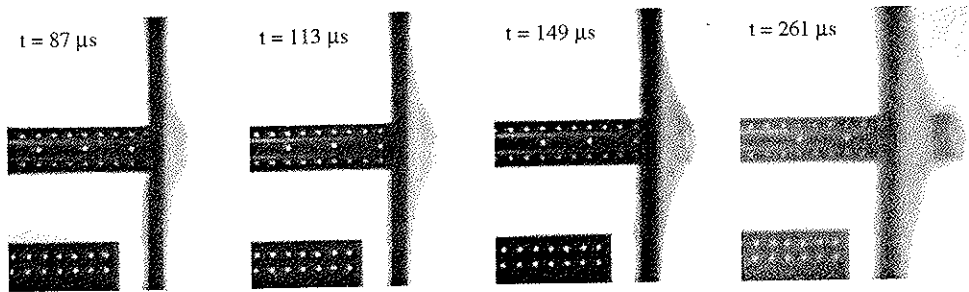
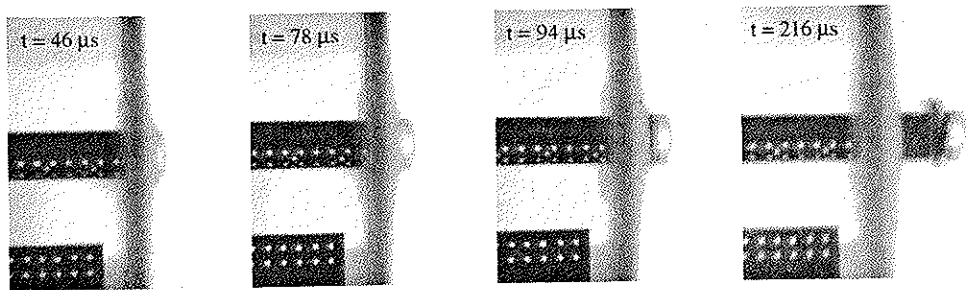


Fig. 11: Measured permanent target deformation profiles at impact velocities close to the ballistic limits.

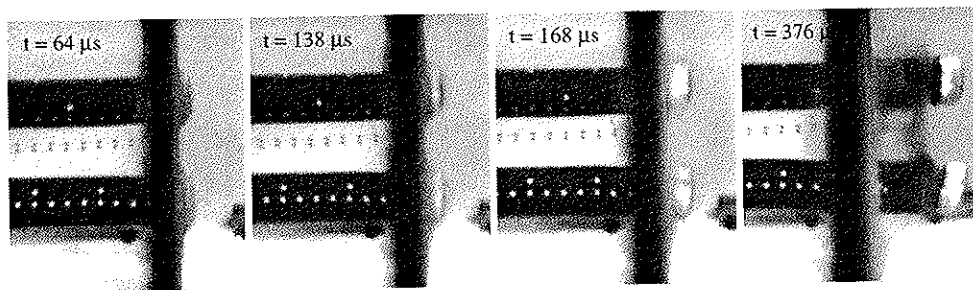
a) Test # 6-11 ($v_i = 156.6$ m/s, $v_r = 63.5$ m/s, $v_{rpl} = 87.0$ m/s, $v_i/v_{bl} = 1.076$):



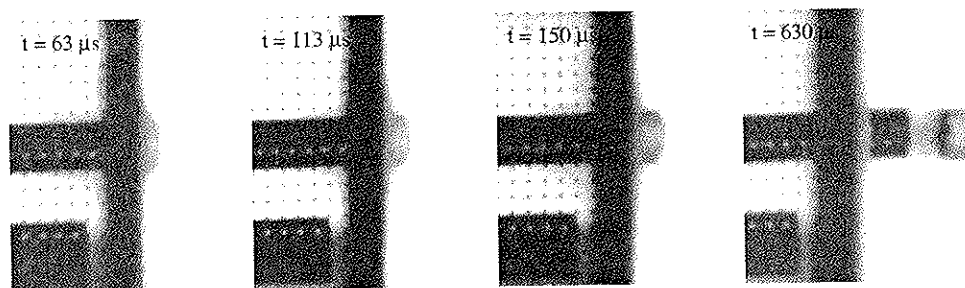
b) Test # 8-8 ($v_i = 173.7$ m/s, $v_r = 112.0$ m/s, $v_{rpl} = 131.0$ m/s, $v_i/v_{bl} = 1.126$):



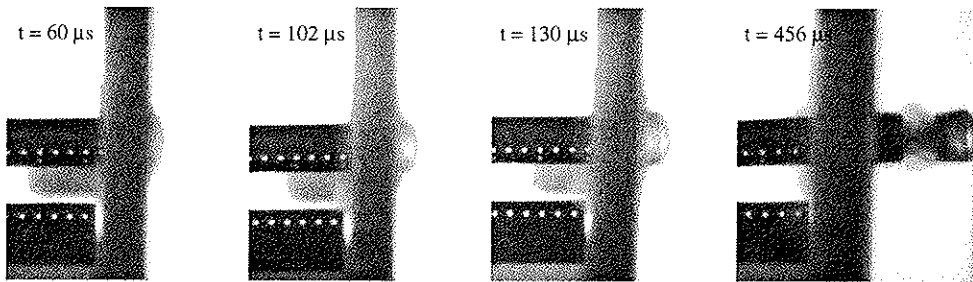
c) Test # 10-7 ($v_i = 184.9$ m/s, $v_r = 94.8$ m/s, $v_{rpl} = 125.8$ m/s, $v_i/v_{bl} = 1.119$):



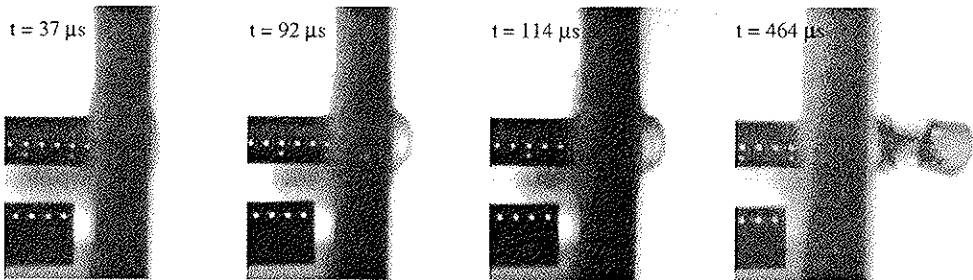
d) Test # 12-16 ($v_i = 189.6$ m/s, $v_r = 42.0$ m/s, $v_{rpl} = 64.0$ m/s, $v_i/v_{bl} = 1.028$):



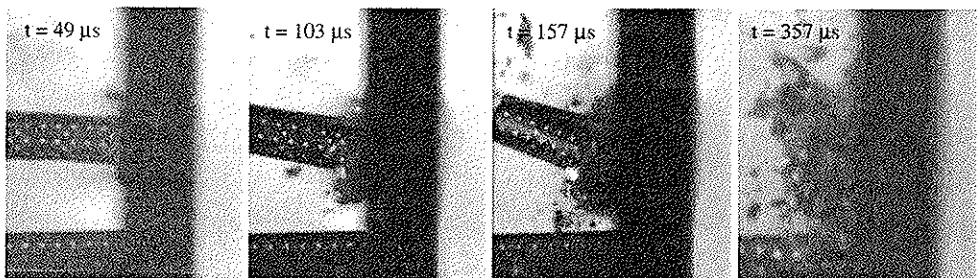
e) Test # 16-6 ($v_i = 242.4$ m/s, $v_r = 55.5$ m/s, $v_{rpl} = 94.3$ m/s, $v_i/v_{bl} = 1.023$):



f) Test # 20-4 ($v_i = 307.2$ m/s, $v_r = 37.1$ m/s, $v_{rpl} = 83.2$ m/s, $v_i/v_{bl} = 1.045$):



g) Test # 25-5 ($v_i = 411.4$ m/s, $v_r = 0$ m/s, $v_{rpl} = 0$ m/s):



h) Test # 30-3 ($v_i = 452.0$ m/s, $v_r = 0$ m/s, $v_{rpl} = 0$ m/s):

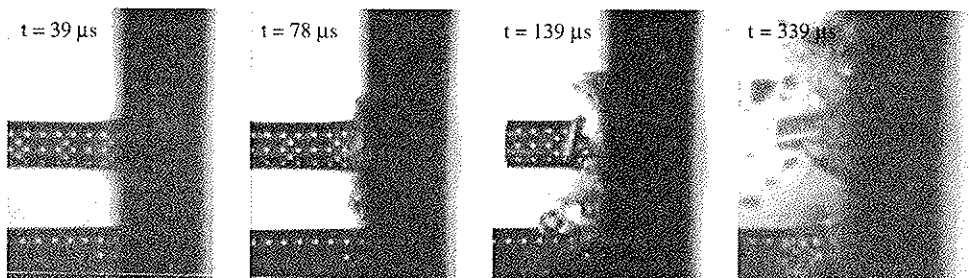


Fig. 12: Some high-speed camera images from tests at impact velocities close to the ballistic limit for different target thicknesses.

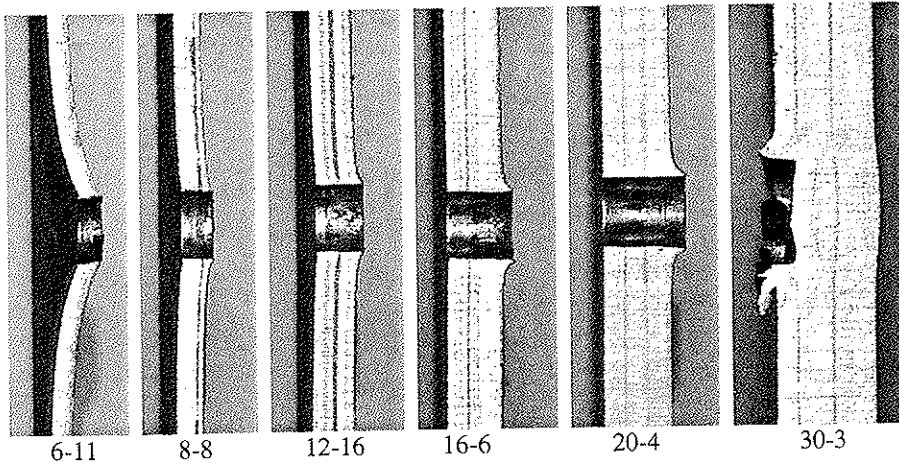


Fig. 13: Cross-sections of perforated and penetrated targets of varying thickness.

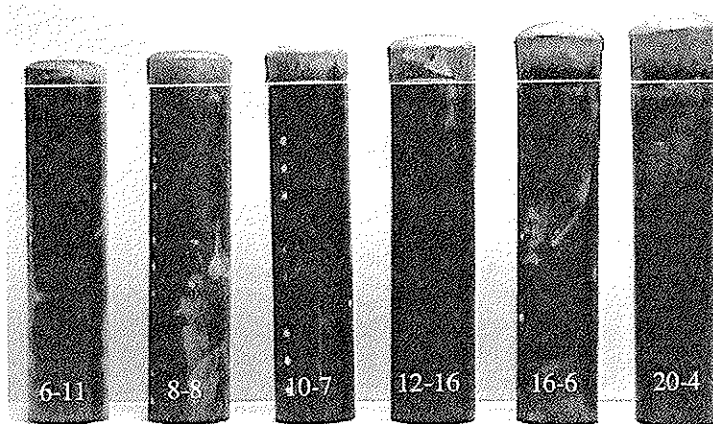


Fig. 14: Projectiles and plugs from tests in targets with varying thickness.

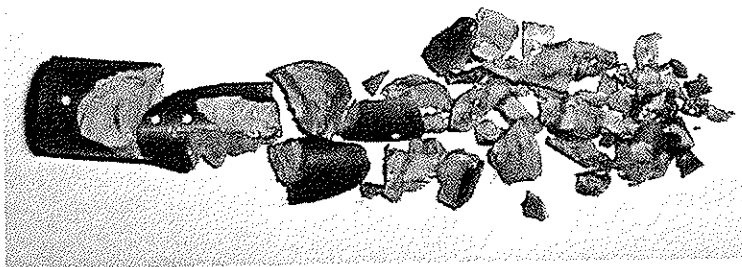


Fig. 15: Shattered projectile after impact of 30 mm thick target plate (test # 30-3).

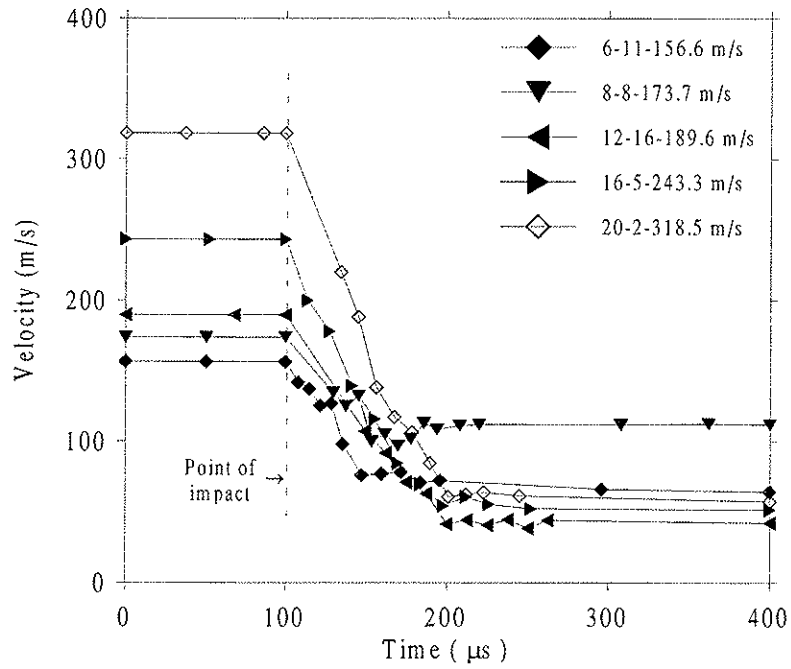


Fig. 16: Velocity-time curves measured from high-speed camera images.

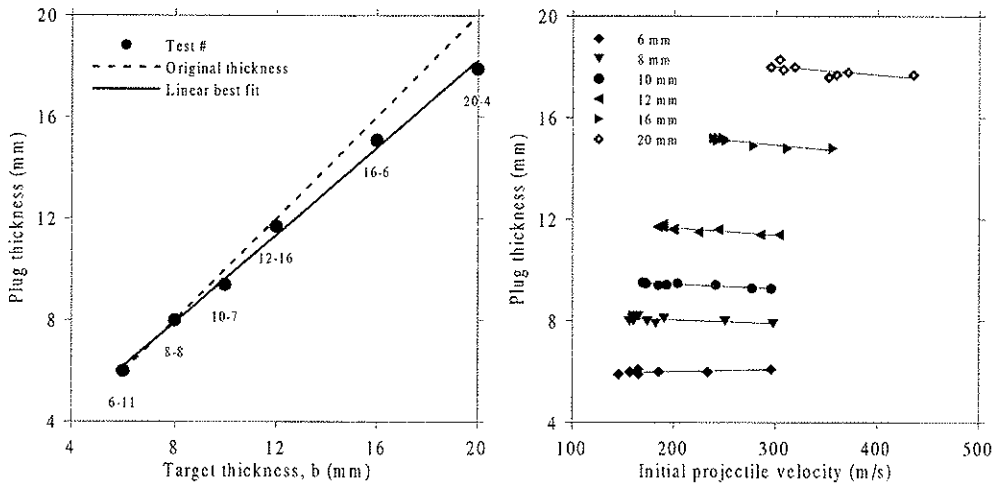


Fig. 17: Plug thickness as function of a) target thickness and b) projectile impact velocity.

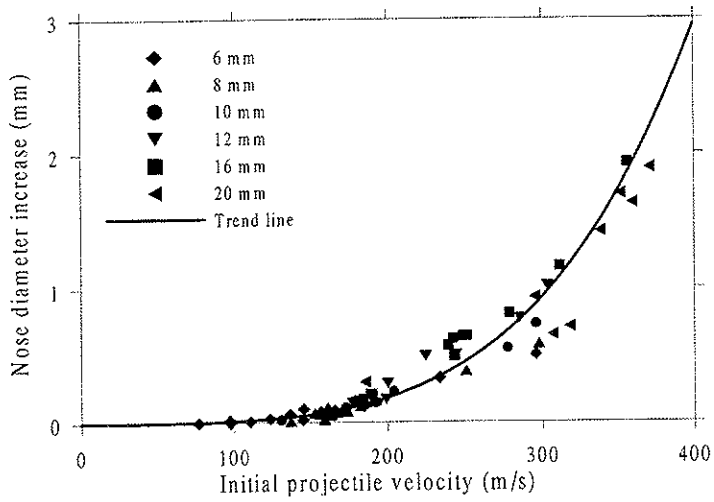


Fig. 18: Projectile nose diameter increase (ΔD) versus initial projectile velocity.

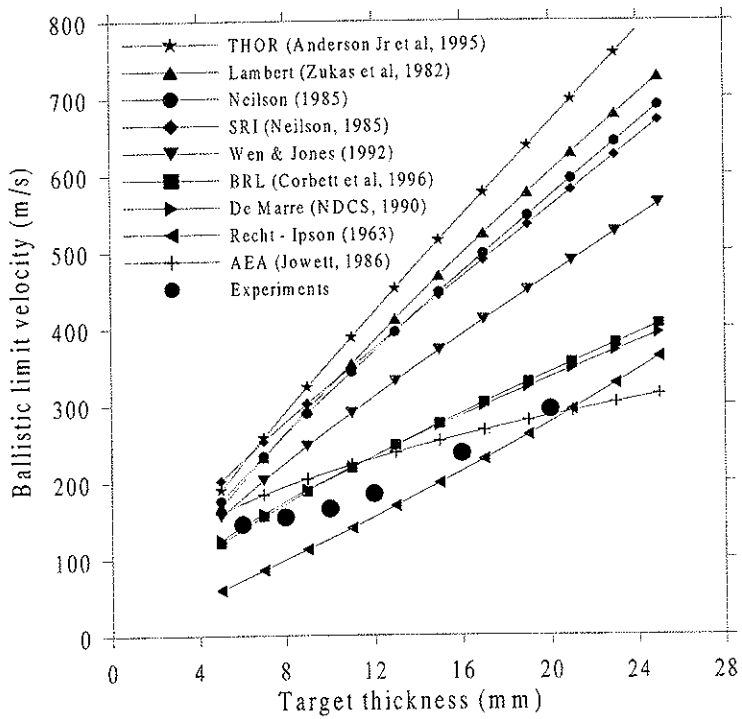


Fig. 19: Comparison between data from empirical models and experimental results.

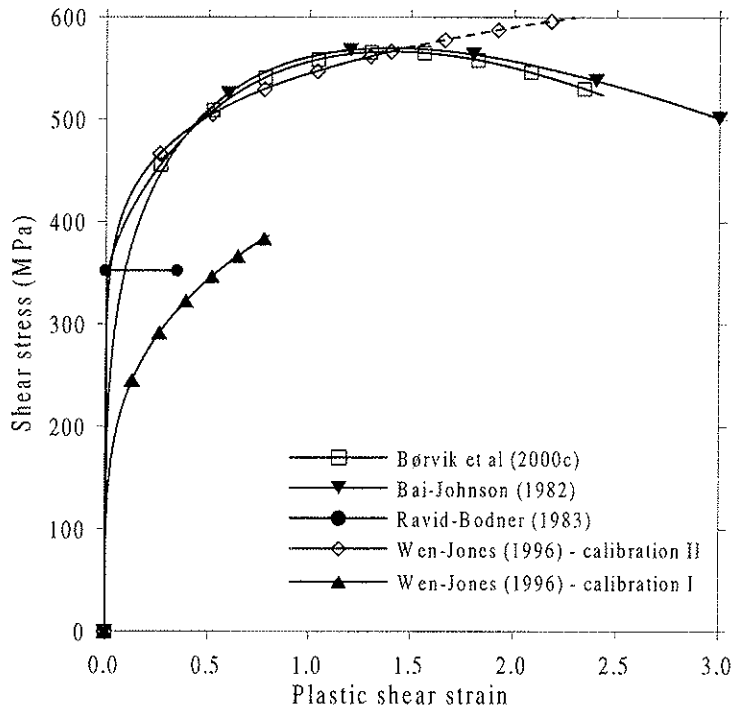


Fig. 20: Material behaviour from different constitutive relations.

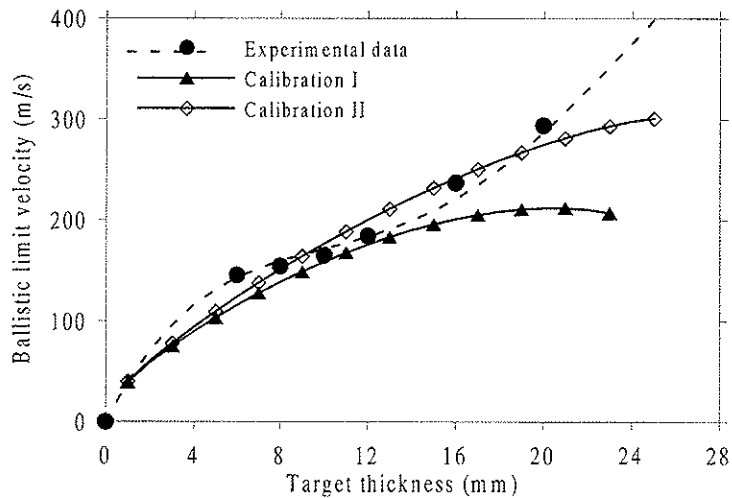


Fig. 21: Ballistic limit velocity versus target thickness obtained from the Wen-Jones model.

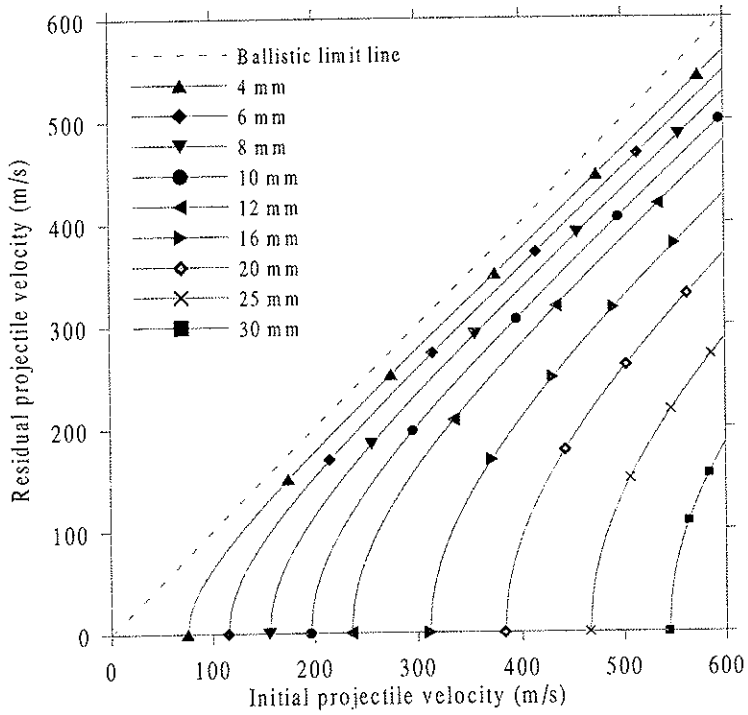


Fig. 22: Ballistic limit curves obtained from the Bai-Johnson model.

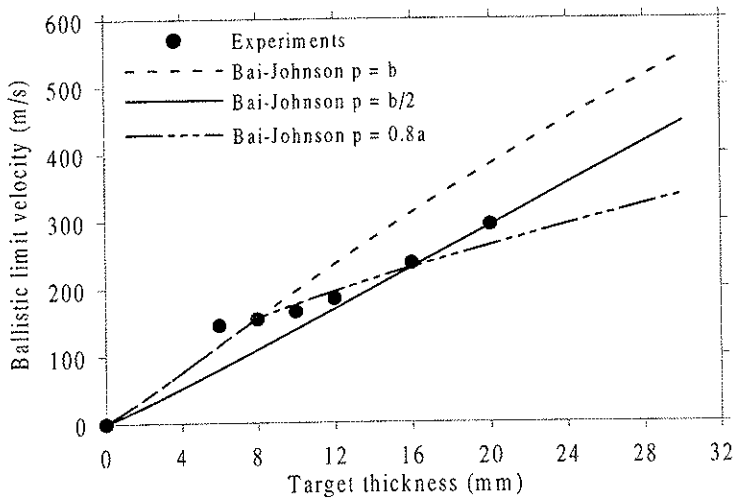


Fig. 23: Ballistic limit velocity versus target thickness obtained from the Bai-Johnson model.

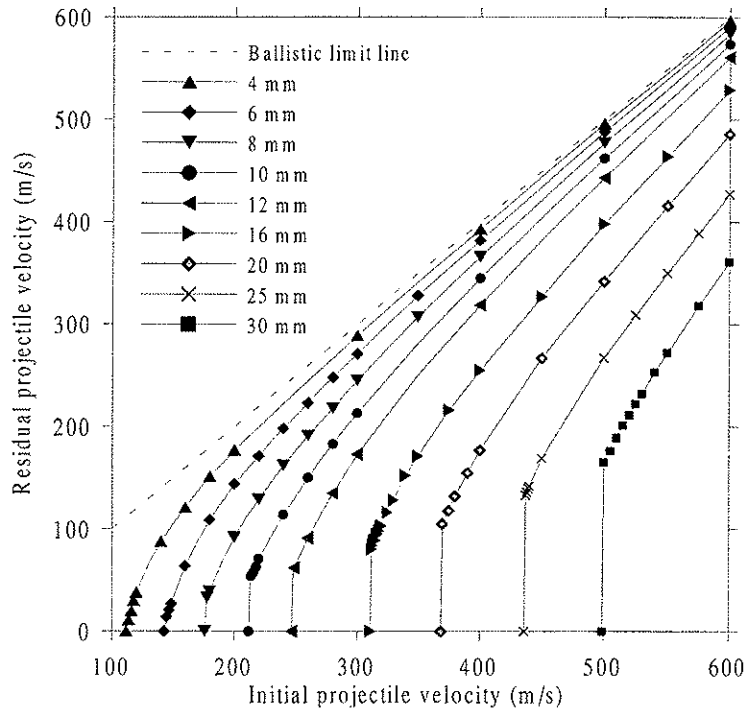


Fig. 24: Ballistic limit curves obtained from the Ravid-Bodner model.

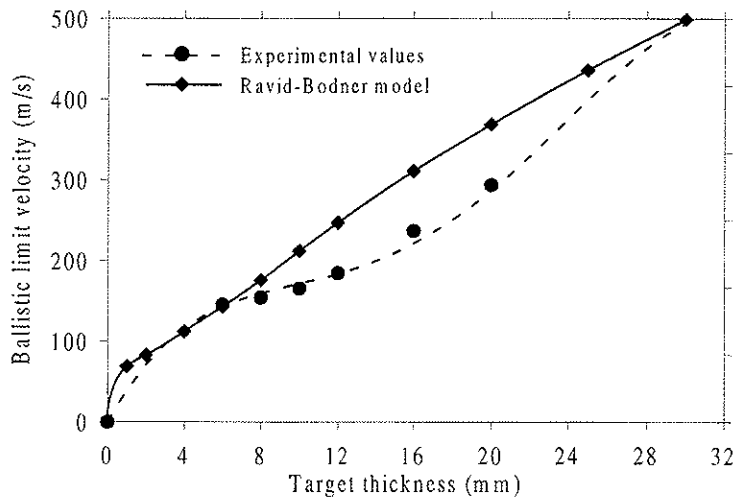


Fig. 25: Ballistic limit velocities versus target thickness from the Ravid-Bodner model.

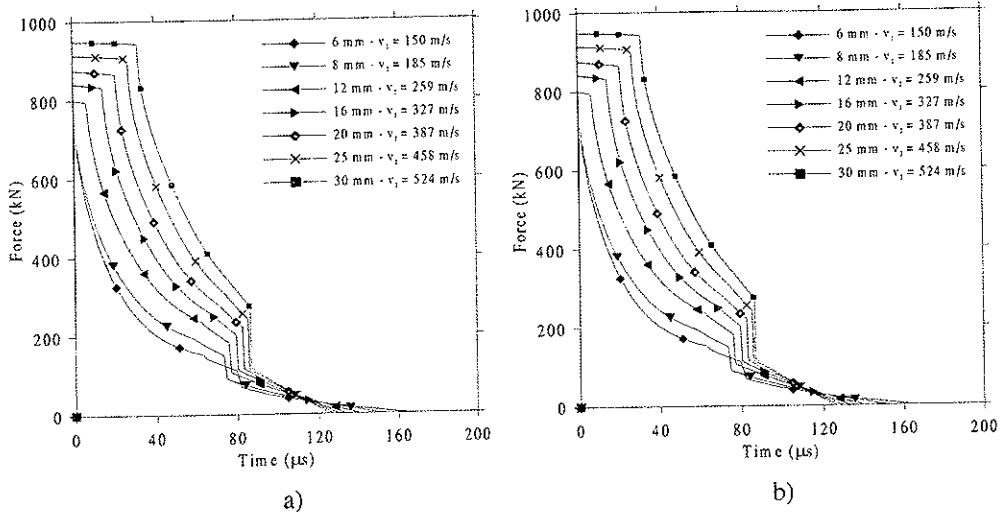


Fig. 26: Predicted projectile a) velocity and b) resisting force versus time for targets of different thickness during perforation using the Ravid-Bodner model.

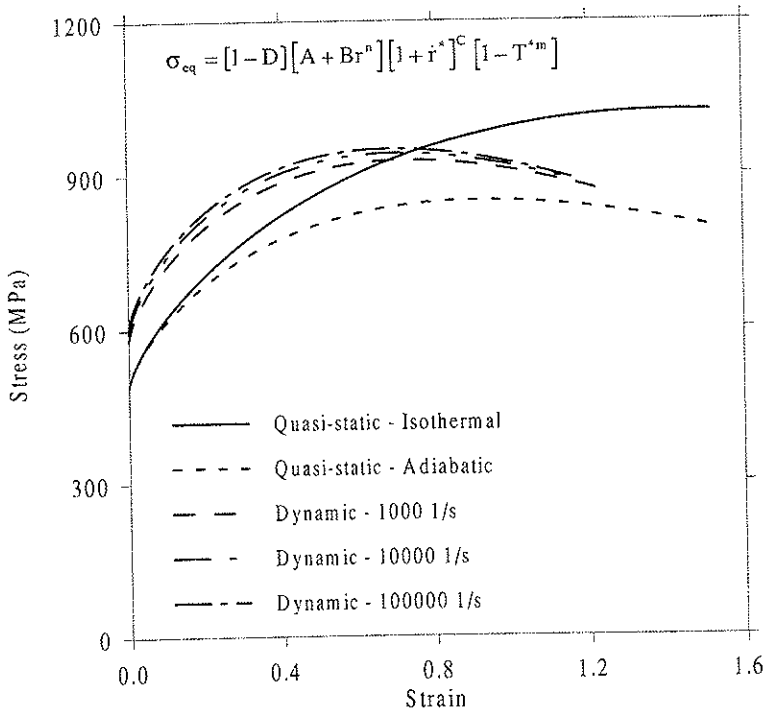


Fig. 27: Calculated quasi-static and dynamic stress-strain curves for Weldox 460 E steel based on the calibrated viscoplastic-damage model developed by Børvik et al (2000c).

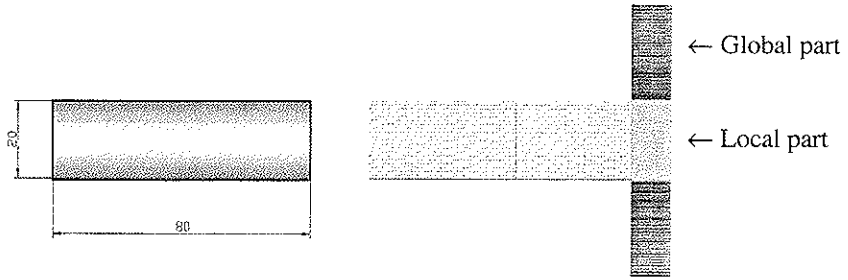


Fig. 28: Geometry of projectile and a plot of the initial FE model showing the local part and a section of the global part of the target.

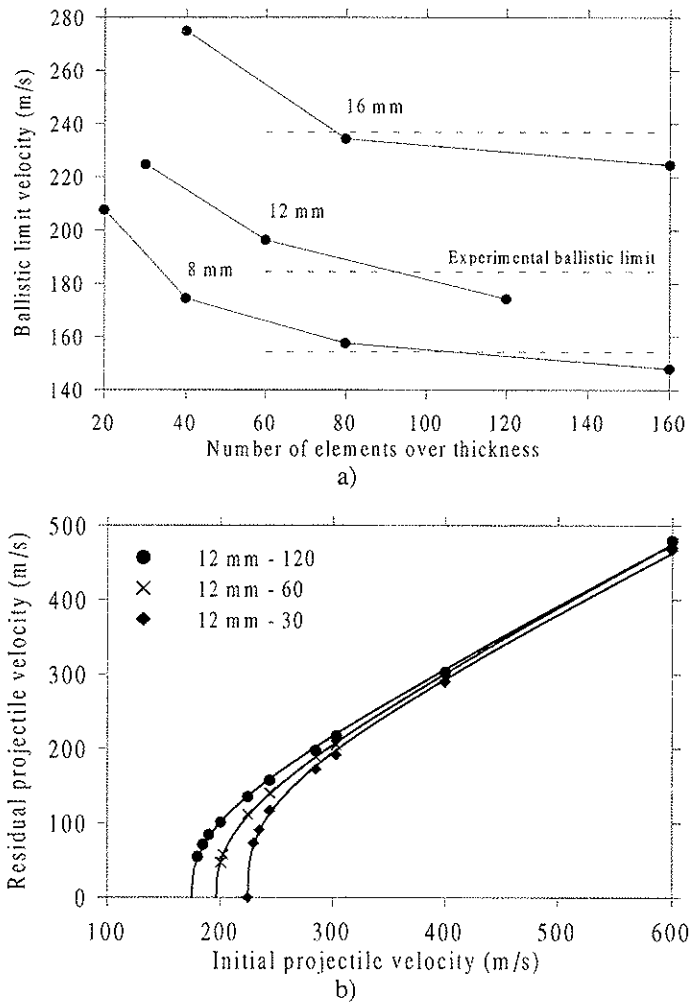


Fig. 29: Mesh sensitivity of numerical simulations.

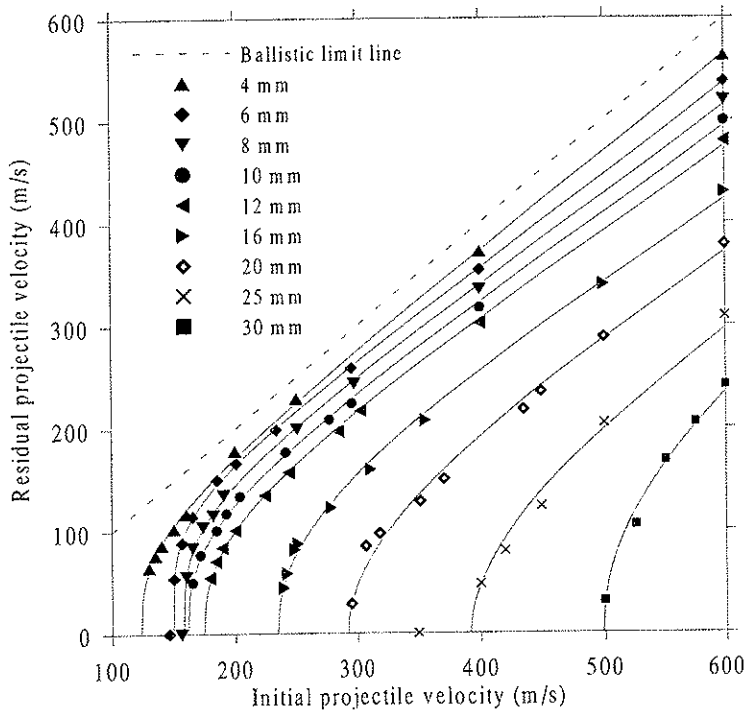


Fig. 30: Ballistic limit curves obtained from numerical simulations.

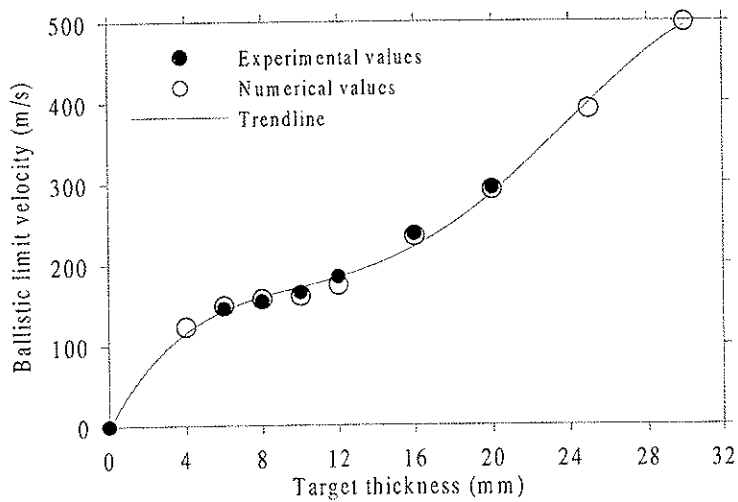


Fig. 31: Ballistic limit velocity versus target thickness from numerical simulations.

4-150

$t = 50 \mu\text{s}$



$t = 90 \mu\text{s}$



$t = 120 \mu\text{s}$



$t = 200 \mu\text{s}$



6-157

$t = 50 \mu\text{s}$



$t = 87 \mu\text{s}$



$t = 100 \mu\text{s}$



$t = 200 \mu\text{s}$



10-185

$t = 30 \mu\text{s}$



$t = 64 \mu\text{s}$



$t = 90 \mu\text{s}$



$t = 230 \mu\text{s}$



12-190

$t = 30 \mu\text{s}$



$t = 63 \mu\text{s}$



$t = 90 \mu\text{s}$



$t = 300 \mu\text{s}$



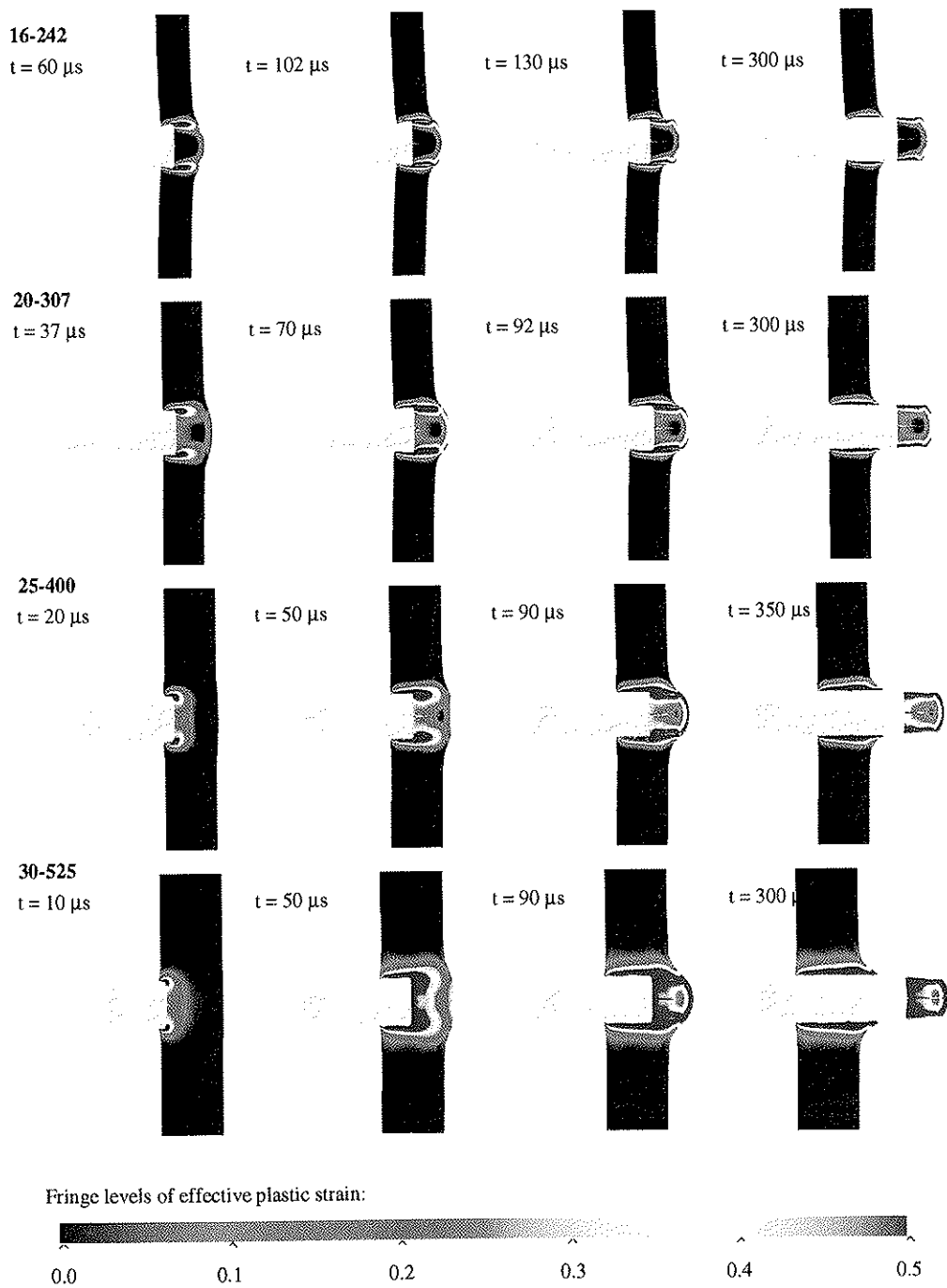


Fig. 32: Numerical simulations of plugging plotted as fringes of effective plastic strain.

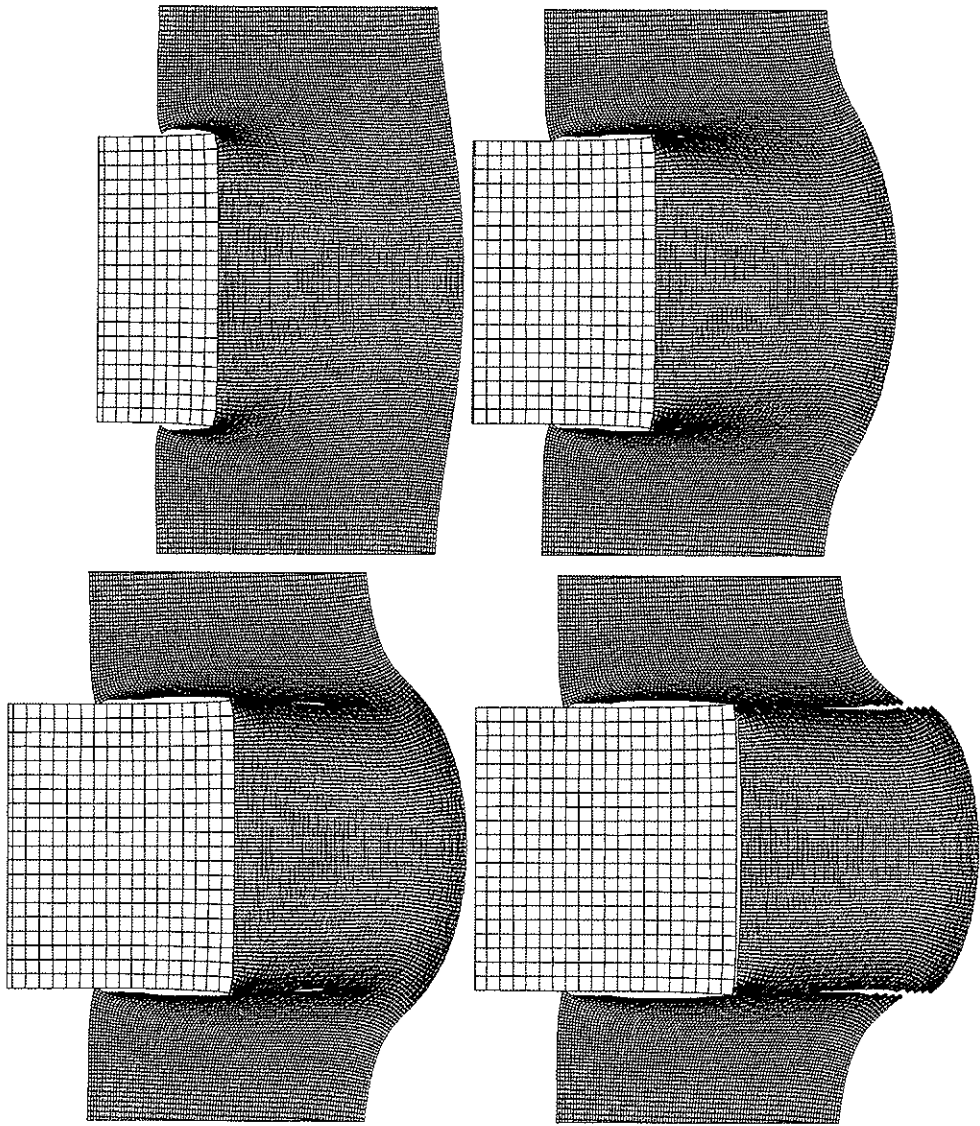


Fig. 33: Details of the crack propagation and failure in Run # 20-307.

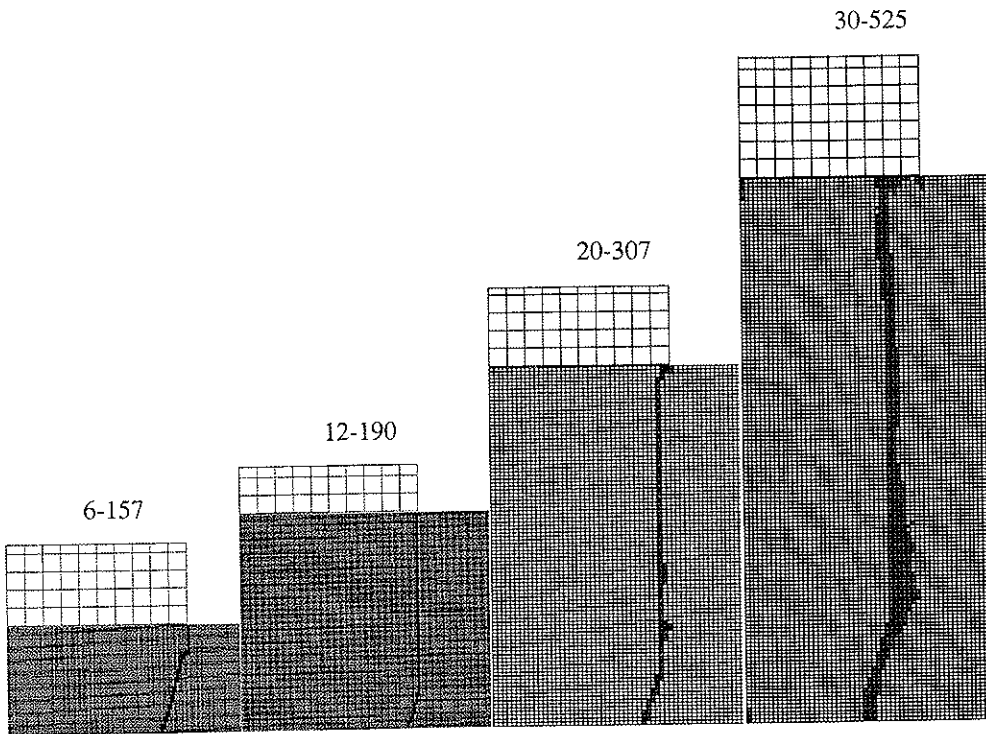


Fig. 34: Plots of removed elements forming the fracture patterns for different target thicknesses at impact velocities close to the respective ballistic limit velocity.

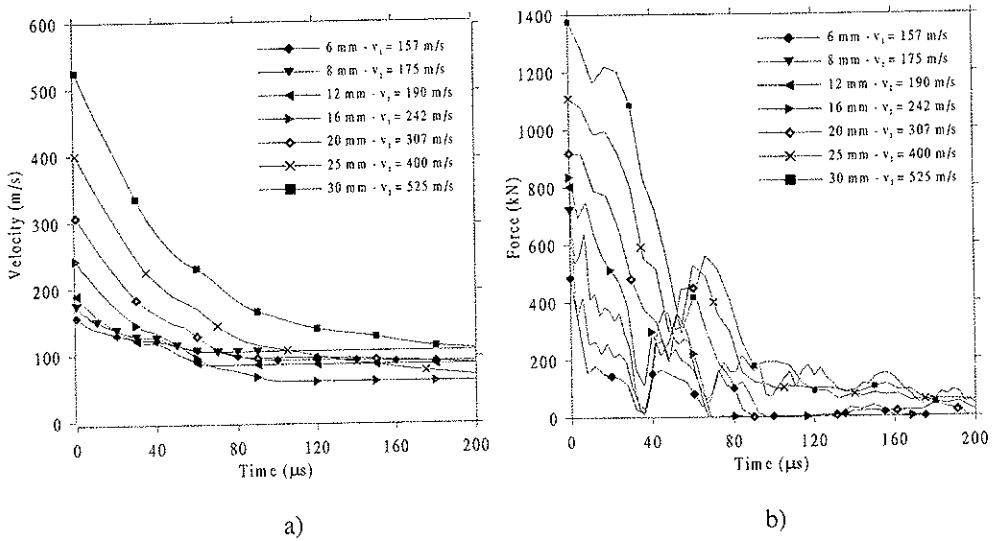


Fig. 35: Projectile a) velocity and b) interface force versus time for targets of different thickness during perforation from numerical simulations at impact velocities about 5% above the respective ballistic limit velocity.

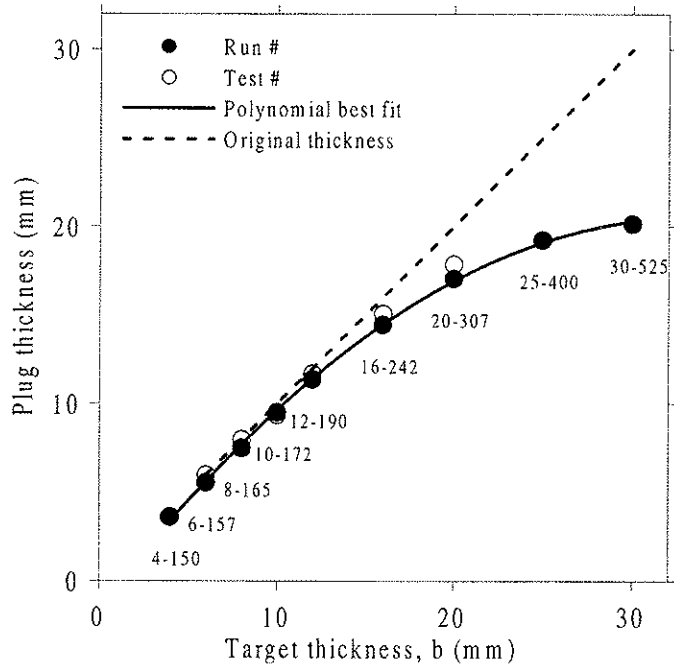


Fig. 36: Plug thickness versus target thickness from numerical simulations at impact velocities close to the respective ballistic limits (see also Fig. 17 and Fig. 32).

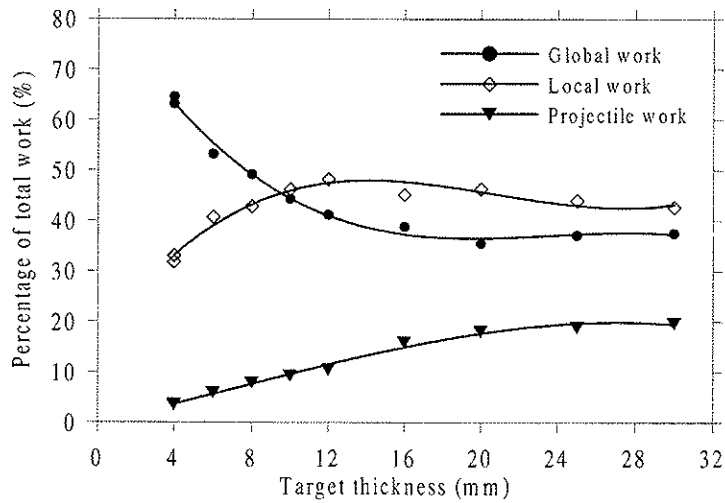


Fig. 37: Energy absorbed in local and global target deformation and in projectile mushrooming as a function of target thickness, from numerical simulations at impact velocities close to the respective ballistic limits.

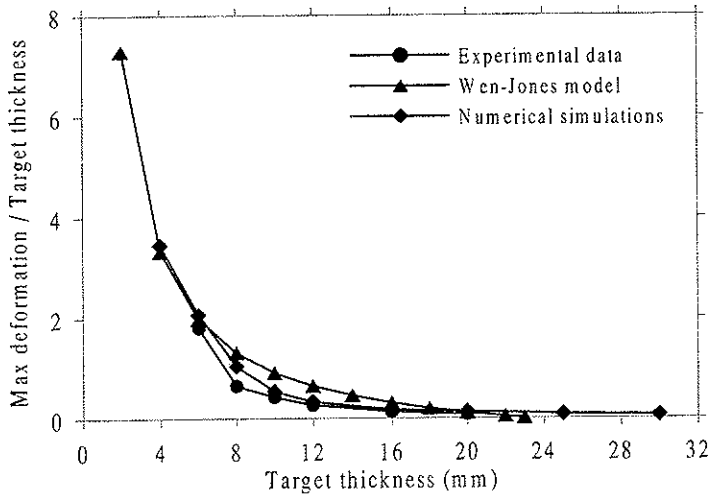


Fig. 38: Relative maximum target deformation versus target thickness.

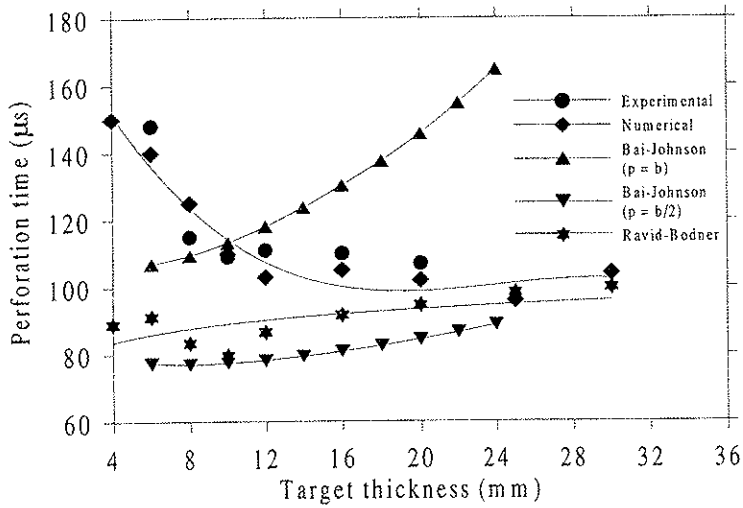


Fig. 39: Perforation times versus target thickness at impact velocities close to the respective ballistic limits.

Table 1: Quasi-static engineering mechanical properties of target and projectile.

Material	E (MPa)	σ_v (MPa)	σ_u (MPa)	ϵ_{fc}	ϵ_{ff}
Target	200000	490	580	0.35	1.58
Projectile	204000	1900	2080	0.024	0.024

Table 2: Experimentally obtained ballistic limit velocities versus target thickness.

	Target thickness (mm)						
	6	8	10	12	16	20	25 - 30
v_{bl} (m/s)	145.5	154.3	165.3	184.5	236.9	293.9	-
Accuracy (m/s)	± 0.15	± 1.75	± 4.05	± 0.25	± 2.60	± 1.35	-
a	0.94	0.84	0.76	0.74	0.63	0.57 (0.34)	-
p	2.71	3.30	3.23	2.42	2.40	1.78 (2.85)	-

* Perforation was not obtained in any of these tests due to projectile fragmentation.

Table 3: Stated limits for experiments and empirical models (Børvik et al, 1998b).

	Limits						
	h_i / D_p	h_i / L_p	L_p / D_p	d_i / D_p	d_i / h_i	σ_u (MPa)	v_i (m/s)
Experiments	0.3 - 1.5	0.08 - 0.38	4	25	17 - 83	580	100-500
THOR	-	-	< 3	-	-	-	-
De Marre	-	-	-	-	-	-	200-900
SRI	0.1 - 0.6	0.002 - 0.05	10 - 50	5 - 8	8 - 100	-	21 - 122
BRL	-	-	-	-	-	-	-
Neilson	0.14 - 0.64	-	> 13	4 - 22	-	-	-
AEA	0.1 - 0.65	-	2 - 8	> 12	-	315 - 483	40 - 200
Wen & Jones	0.4 - 1.6	-	-	40	25 - 100	340 - 440	< 20
Recht & Ipson	< 0.5	< 0.5	-	-	-	-	-
Lambert	See Børvik et al (1998b) for database.						

Table 4: Input to the Wen-Jones model.

Target material properties (Weldox 460 E) and projectile constants									
σ_v (MPa)	σ_u (MPa)	D (s ⁻¹)	q	τ_u (MPa)	γ_u	n	G (kg)	d (m)	R (m)
490	580	$4.6 \cdot 10^7$	7.33	570	1.4	0.12	0.197	0.020	0.25

Table 5: Input to the Bai-Johnson model.

Target material properties (Weldox 460 E) and projectile constants							
τ_u (MPa)	γ_u	n	ρ (kg/m ³)	C_v (J/kgK)	θ_0 (K)	M (kg)	a (m)
570	1.4	0.25	7850	452	293	0.197	0.010

Table 6: Input to the Ravid-Bodner model.

Target material properties (Weldox 460 E) and projectile constants								
σ_v (MPa)	σ_0 (MPa)	C_v	C_0	μ	L_p (mm)	D_p (mm)	ρ (kg/m ³)	ϵ_u
490	550	0.0337	0.0254	0.0	80	20	7850	0.20

Table 7: Numerically obtained ballistic limit velocities versus target thickness.

	Target thickness (mm)								
	4	6	8	10	12	16	20	25	30
v_{bl} (m/s)	123.3	149.1	157.6	161.1	174.3	234.4	291.9	391.4	498.5
a	0.94	0.89	0.86	0.83	0.80	0.74	0.72	0.68	0.66
p	2.91	4.09	3.40	2.81	2.59	2.31	1.95	1.86	2.13

Table 8: Experimental details from penetration tests.

Test #	v_i (m/s)	v_c (m/s)	v_{imp} (m/s)	m_p (g)	m_{pt} (g)	P.O.I. (mm)	ϕ_0 (°)	α_0 / β_0 (°)	w_{max} (mm)	d_{ip} / d_{ire} (mm)	h_{im} (mm)	h_c (mm)	h_{pl} (mm)	d_{pp} / d_{pmax} (mm)	ΔD (mm)	ΔL (mm)	ΔR_c (-)	t_f (s)
6-1	296.0	260.2	-	196.8	14.3	2.4D/2.7L	0.24	- ²⁾	0.93	20.5/20.8	6.03	9.7	6.1	20.6/21.1	0.50	0.32	3.0	- ²⁾
6-14	233.9	201.0	240.5	197.0	14.0	1.1U/2.3L	0.09	0.7D	1.73	20.2/20.4	6.07	8.3	6.0	20.4/20.8	0.33	0.19	1.0	- ³⁾
6-15	201.3	157.9	175.8	196.6	13.8	1.0U/1.2R	0.10	- ²⁾	2.43	20.2/20.3	6.01	8.0	6.0	20.3/20.6	0.20	0.15	2.2	- ²⁾
6-2	185.4	132.2	169.4	196.5	13.6	2.2U/2.0R	0.14	0.3U	3.06	20.2/20.3	6.10	7.9	6.0	20.2/20.6	0.15	0.14	2.0	50
6-4	165.3	98.0	111.8	196.5	12.5	2.6U/2.0R	0.18	1.1U	7.56	20.2/20.4	6.05	8.6	5.9	20.2/20.3	0.09	0.08	1.0	87
6-13	165.0	95.9	119.7	196.5	12.8	0.7U/2.8R	0.06	0.1D	6.80	20.0/20.2	6.03	7.9	6.1	19.8/20.5	0.05	0.03	0	90
6-11	156.6	63.5	87.0	196.5	12.3	0.7U/3.9R	0.17	0.1D	9.16	20.4/20.5	6.02	7.8	6.0	20.0/20.2	0.08	0.02	0	119
6-12	145.6	38.1	49.5	196.6	12.0	2.6D/0.7R	0.18	0.8D	9.29	20.4/20.5	5.99	7.6	5.9	20.3/20.4	0.10	0.06	3.0	148
6-10	145.3	0	0	196.7	0	1.9U/3.0R	0.06	0.4U	10.84	20.1/-	6.07	3.0 ⁵⁾	-	-/-	0.02	0.02	0.7	-
6-9	137.0	0	0	196.7	0	0.5U/1.8R	0.06	0.5D	10.01	20.1/-	6.00	2.4 ⁵⁾	-	-/-	0.06	0.02	1.0	-
6-6	124.0	0	0	196.3	0	1.5U/1.2R	0.20	0.8U	8.52	20.1/-	6.02	1.8 ⁵⁾	-	-/-	0.03	0.03	2.0	-
6-8	111.1	0	0	196.6	0	1.1D/2.7R	0.11	0.8D	7.70	20.1/-	5.92	1.4 ⁵⁾	-	-/-	0.01	0.04	4.7	-
6-3	97.6	0	0	195.9	0	2.3U/0.7L	0.12	0.5U	5.94	20.0/-	5.97	1.1 ⁵⁾	-	-/-	0	0.02	1.3	-
6-5	97.3	0	0	196.8	0	0.6U/0.7R	0.11	0.9U	6.11	20.1/-	5.96	1.2 ⁵⁾	-	-/-	0.02	0.02	1.3	-
6-7	76.7	0	0	196.9	0	2.7U/2.5R	0.12	0.5D	4.05	20.0/-	5.94	0.7 ⁵⁾	-	-/-	0	0	1.0	-
8-13	298.0	241.4	261.2	196.8	18.7	1.0R	0.23	0.3D	0.98	20.4/20.7	8.03	11.1	7.9	20.7/21.3	0.58	0.47	3.7	28
8-1	250.8	191.7	222.7	196.8	18.8	0.8U/2.8R	0.14	0.9D	1.02	20.4/20.4	8.02	10.3	8.0	20.2/20.8	0.38	0.38	0	35
8-2	190.7	132.3	168.2	196.5	18.6	1.8D/1.8R	0.11	1.0D	2.31	20.3/20.3	8.06	10.4	8.1	20.4/20.8	0.15	0.10	1.3	51
8-14	182.2	122.6	143.4	196.8	18.1	1.8U/1.9R	0.11	- ²⁾	2.40	20.2/20.2	8.08	11.2	7.9	20.3/20.5	0.12	0.14	3.3	- ²⁾
8-8	173.7	112.0	131.0	196.3	18.5	0.8U/0.4R	0.18	0.1U	2.64	20.2/20.2	8.09	10.2	8.0	20.3/20.8	0.08	0.10	0.7	82
8-5	165.2	83.7	99.1	196.6	18.5	1.8U/2.1R	0.19	0.5U	3.69	20.3/20.3	8.04	10.1	8.2	20.5/20.6	0.07	0.12	0	107
8-9	161.1	78.7	95.4	196.6	18.5	1.0U/1.5R	0.13	0.4U	3.05	20.1/20.2	8.02	10.0	8.1	20.4/20.4	0.11	0.09	0	104
8-3	160.7	76.0	102.8	196.4	18.2	2.8U/2.3L	0.14	1.3U	3.91	20.1/20.2	8.10	10.2	8.2	20.3/20.5	0.11	0.09	1.3	109
8-11	160.2	70.2	82.5	196.8	18.2	2.0U/1.2R	0.15	0.6U	3.93	20.2/20.3	8.05	10.2	8.0	20.3/20.4	0.09	0.15	1.3	104
8-10	160.0	71.6	98.7	197.0	18.6	1.6U/2.6R	0.21	0.7U	2.96	20.1/20.3	8.04	10.0	8.2	20.7/20.8	0.05	0.07	0	100
8-6	159.0	41.7	83.6	196.6	18.2	1.6U/1.6L	0.14	0.8U	5.04	20.3/20.6	8.01	9.9	8.1	20.3/20.9	0.02	0.05	0.3	106
8-12	156.0	52.0	86.0	196.9	18.3	1.2U/1.5R	0.14	0	4.52	20.2/20.7	8.09	10.1	8.0	20.4/21.1	0.06	0.12	2.0	108
8-7	152.5	0	0	196.3	0	2.3U/0.1R	0.10	0.8U	5.02	20.3/-	8.00	3.8 ⁵⁾	-	-/-	0.07	0.05	1.3	-
8-4	137.4	0	0	196.9	0	2.8U/2.3L	0.21	0	4.85	20.1/-	8.10	2.9 ⁵⁾	-	-/-	0.01	0.02	1.0	-

¹⁾ No measurements available, ²⁾ No images available, ³⁾ Very poor image quality, ⁴⁾ The projectile is destroyed during impact, ⁵⁾ Projectile indentation, ⁶⁾ Projectile fragmentation, ⁷⁾ Projectile embedded in target, ⁸⁾ Too small to be measured accurately.

Table 8: Experimental details from penetration tests (continued).

Test #	v_i (m/s)	v_r (m/s)	v_{rpl} (m/s)	m_{rp} (g)	m_{pl} (g)	P.O.I. (mm)	ϕ_0 (°)	α_0 / β_0 (°)	w_{max} (mm)	d_{gr} / d_{rec} (mm)	h_{im} (mm)	h_c (mm)	h_{pl} (mm)	d_{gr} / d_{plmax} (mm)	ΔD (mm)	ΔL (mm)	ΔR_c (-)	t_f (s)
10-9	296.0	217.5	251.3	196.7	22.1	2.9D/0.2L	0.36	0.3U/0.1L	0.99	20.5/20.6	9.8	13.2	9.28	20.8/21.5	0.73	0.70	2.0	27
10-6	277.5	197.9	235.0	197.2	22.2	2.3D/1.0R	0.56	0.4D	1.16	20.4/20.7	9.7	- ¹⁾	9.29	20.6/21.5	0.55	0.51	2.6	40
10-1	241.5	165.9	203.8	196.4	22.1	0.2D/0.7L	- ¹⁾	0.1U	1.07	20.3/20.4	9.7	12.9	9.42	20.3/21.2	0.41	0.43	2.0	67
10-2	204.0	124.2	162.0	197.3	22.4	0.1D/0.4R	0.23	0.1U/0.3R	1.61	20.3/20.5	9.7	12.4	9.48	20.4/20.8	0.23	0.25	2.7	3 ²⁾
10-5	192.9	108.6	145.4	196.5	22.2	1.8D/0.5L	0.25	0.3D/0.1R	1.82	20.3/20.4	9.7	12.3	9.42	20.4/20.5	0.15	0.22	1.3	3 ³⁾
10-7	184.9	94.8	125.8	196.9	21.8	2.7D/0.2R	0.10	0.4D/0.5L	2.53	20.3/20.4	9.7	12.5	9.41	20.3/20.6	0.13	0.22	1.0	48
10-8	172.6	66.8	95.9	196.9	21.9	0.5D/0.7L	0.12	0.6U/0.1R	2.75	20.2/20.3	9.7	- ¹⁾	9.47	20.3/20.4	0.11	0.18	2.3	113
10-4	171.6	66.4	94.7	195.8	22.1	1.8D/2.0R	0.20	0.2D/0.1R	2.86	20.2/20.3	9.7	12.8	9.51	20.3/20.6	0.08	0.16	1.7	99
10-11	169.3	66.0	93.2	197.0	22.2	1.7D/1.7L	0.14	0.4D/0.3R	3.14	20.2/20.3	9.7	12.5	9.52	20.3/20.4	0.07	0.16	1.3	109
10-3	161.2	0	0	196.5	0	0.4D/0.1R	0.15	0.3D/0.3R	4.28	20.1/-	9.7	- ¹⁾	-	-/-	0.06	0.05	1.0	-
10-10	131.3	0	0	197.1	0	4.1D/1.4R	0.16	2.3D/0.8R	3.49	20.1/-	9.8	2.6 ⁵⁾	-	-/-	0.02	0.03	0.7	-
12-1	303.5	199.7	242.3	196.6	27.6	3.1R/0.4U	0.28	0.1U/0.1R	1.01	20.7/20.9	12.1	16.9	11.4	21.0/21.9	1.01	0.90	0.7	82
12-3	285.4	181.1	224.7	197.3	27.6	2.6R/0.5D	0.11	- ²⁾	1.22	20.6/20.8	12.0	15.6	11.4	20.7/21.7	0.77	0.70	0.6	2 ⁴⁾
12-2	244.2	132.6	187.7	196.9	28.1	2.7L/0.8D	0.17	0.6U/1.0R	1.22	20.4/21.2	12.1	15.1	11.6	20.7/21.7	0.50	0.53	0.7	124
12-10	224.7	113.7	169.0	196.9	27.3	0.7R/3.1D	- ¹⁾	0.1U	- ¹⁾	20.6/20.7	12.0	15.0	11.5	20.5/21.2	0.49	0.47	1.7	72
12-4	200.4	71.4	103.7	197.0	27.8	0.2L/1.1U	0.18	0.9U/1.1L	2.08	20.4/20.9	12.0	14.9	11.6	20.4/21.4	0.29	0.28	2.3	97
12-5	199.1	67.3	104.0	196.9	27.8	1.2L/2.8D	0.14	- ²⁾	1.92	20.3/20.7	12.1	14.7	11.6	20.4/21.3	0.17	0.22	0	2 ⁵⁾
12-12	189.6	43.7	71.8	196.9	27.9	1.1L/3.5D	0.11	1.7D	1.98	20.4/20.8	12.1	14.9	11.8	20.4/21.3	0.19	0.28	0	131
12-16	189.6	42.0	64.0	196.7	27.7	1.9R/0.3U	0.13	0.7U	2.06	20.3/20.6	12.1	14.6	11.7	20.4/21.2	0.17	0.22	2.7	127
12-13	189.2	40.1	66.8	196.7	28.0	3.5L/0.8D	0.09	1.1D	1.87	20.4/20.6	12.1	14.8	11.7	20.4/21.4	0.21	0.34	0	134
12-7	188.8	43.2	66.9	196.9	27.8	1.8R/1.9D	0.23	0.7D/0.5R	2.32	20.4/20.7	12.1	15.2	11.7	20.6/21.3	0.19	0.27	0	133
12-15	184.3	30.8	45.3	196.8	27.8	1.9L/4.1U	0.17	0.5D	2.04	20.4/20.7	12.1	14.7	11.7	20.5/21.3	0.17	0.20	0.6	111
12-9	181.5	0	0	196.7	0	0.7L/1.0U	0.13	- ²⁾	3.20	20.2/-	12.1	5.5 ⁵⁾	-	-/-	0.11	0.24	1.0	-
12-11	179.4	0	0	196.8	0	0.5R/1.1U	0.13	0.1D	2.81	20.1/-	12.0	5.3 ⁵⁾	-	-/-	0.16	0.13	1.0	-
12-14	177.3	0	0	197.0	0	3.5R/1.0U	0.15	0.8U	2.95	20.2/-	12.1	5.1 ⁵⁾	-	-/-	0.15	0.13	1.7	-
12-8	173.7	0	0	196.1	0	0.6U	0.19	1.6U/1.3L	2.93	20.2/-	12.1	4.6 ⁵⁾	-	-/-	0.14	0.22	0	-

¹⁾No measurements available, ²⁾No images available, ³⁾Very poor image quality, ⁴⁾The projectile is destroyed during impact, ⁵⁾Projectile indentation, ⁶⁾Projectile fragmentation, ⁷⁾Projectile embedded in target, ⁸⁾Too small to be measured accurately.

Table 8: Experimental details from penetration tests (continued).

Test #	v_i (m/s)	v_r (m/s)	v_{pl} (m/s)	m_p (g)	m_{pl} (g)	P.O.I. (mm)	ϕ_0 (°)	α_0 / β_0 (°)	w_{max} (mm)	d_{pr} / d_{inc} (mm)	h_{in} (mm)	h_c (mm)	h_{pl} (mm)	d_{app} / d_{minor} (mm)	ΔD (mm)	ΔL (mm)	ΔR_c (-)	t_f (s)
16-9	356.0	189.1	236.5	196.1	35.1	1.2R/2.1U	0.26	0	0.29	21.7/22.6	16.0	22.9	14.8	21.0/22.3	1.93	1.59	3.2	72
16-1	311.5	140.0	184.4	196.7	35.9	3.2R/1.8D	0.35	0.2D	0.38	20.6/21.3	16.0	20.9	14.8	20.7/22.2	1.16	1.57	0.3	87
16-7	278.5	106.5	141.5	197.5	36.2	2.1R/1.9D	0.10	0.8D	0.94	20.7/20.8	16.0	20.6	14.9	21.5/22.1	0.81	1.13	0.6	86
16-2	251.2	64.0 ^{b)}	- ^{b)}	196.6	36.2	1.1R/2.0D	0.31	0.4U	1.05	20.6/20.8	16.0	19.8	15.1	20.7/22.1	0.64	0.88	1.5	99
16-4	248.6	56.6	100.2	196.8	35.5	1.4R/0.4D	0.13	- ^{b)}	0.87	20.5/21.2	16.0	20.1	15.2	20.4/21.8	0.64	0.89	2.4	- ^{b)}
16-5	243.3	52.0	93.8	196.4	35.8	2.0R/1.2U	0.06	0.4D	0.32	20.5/21.1	16.0	20.4	15.2	20.4/21.4	0.49	0.83	0.7	103
16-6	242.4	55.5	94.3	196.9	36.6	2.3R/0.3D	0.26	0.5U	- ^{b)}	20.5/20.9	16.0	19.9	15.1	20.7/21.7	0.62	0.81	1.0	99
16-8	239.5	32.3	83.8	196.5	36.1	1.0R/1.0U	0.32	0.1D	0.38	20.5/21.2	16.0	19.6	15.2	20.5/21.9	0.57	0.81	- ^{b)}	110
16-3	234.3	0	0	196.1	0	2.0R/1.7U	0.06	1.6D	- ^{b)}	20.8/-	16.0	9.5 ^{b)}	-	-/-	0.28	0.22	-	-
20-15	465.7	0 ^{b)}	0	196.3	0	2.0R/1.5U	0.14	0.5D	1.51	-/-	20.0	-	-	-/-	-	-	-	- ^{b)}
20-12	435.6	110.0	143.5	196.4	45.6	0.8L/7.0D	0.11	1.0D	0.52	21.4/21.7	20.1	26.4	17.7	21.3/23.1	1.84	2.83	2.5	-
20-14	430.0	0 ^{b)}	0	197.1	0	4.1R/0.6U	0.28	0.7D	1.19	-/-	20.1	-	-	-/-	-	-	-	-
20-13	370.9	105.8	159.9	196.4	46.0	2.2R/6.1D	0.16	0.3U	0.64	21.5/21.8	20.1	27.5	17.8	21.5/22.9	1.89	2.79	2.0	74
20-7	359.6	117.1	152.1	196.0	44.4	3.0U	0.34	1.1D	0.60	21.4/21.9	20.0	26.5	17.7	21.3/22.7	1.63	2.31	0.8	92
20-5	351.7	93.5	145.1	196.9	47.1	4.1R/0.1U	0.21	0	0.76	21.3/22.3	20.1	26.1	17.6	21.7/23.4	1.7	2.53	3.2	94
20-6	338.3	91.2	132.3	196.1	44.4	4.1R/2.6U	0.18	0.1U	0.59	21.3/22.0	20.1	26.1	17.8	21.3/23.0	1.42	2.13	1.0	101
20-2	318.5	57.8	111.4	196.9	44.4	2.5R/0.8U	0.23	0.3U	0.82	20.8/21.5	20.1	25.9	18.0	20.9/22.5	0.71	1.72	2.2	108
20-1	317.8	43.6	- ^{b)}	196.2	44.3	1.9R/0.5U	0.34	0.1U	0.72	21.2/21.7	20.0	26.5	18.0	21.0/22.5	1.07	0.99	2.0	117
20-4	307.2	37.1	83.2	196.7	45.4	0.1R/2.1U	0.11	0.1U	0.92	21.0/22.0	20.0	25.2	17.9	21.0/22.4	0.65	1.74	1.7	107
20-10	306.6	0 ^{b)}	35.8	196.5	46.5	-	0.35	0.5D	-	-/22.1	20.1	11.2 ^{b)}	17.9	20.4/22.6	0.92	0.84	-	105
20-3	303.8	0 ^{b)}	- ^{b)}	196.8	47.8	0.3L/0.7U	0.14	1.2D	-	-/22.2	20.0	14.3 ^{b)}	18.3	21.1/23.5	0.89	0.81	-	110
20-8	295.2	25.6	66.7	197.1	44.8	0.3L/0.7U	0.12	1.0D	0.94	20.8/21.9	20.0	24.9	18.0	20.9/22.2	0.93	1.32	0.8	- ^{b)}
20-9	292.5	0	0	196.9	0	1.0R	0.10	0.8U	1.02	-/-	20.0	- ^{b)}	-	-/-	0.75	0.68	-	-
20-11	185.4	0	0	196.8	0	1.1D/8L	0.34	0.5U	0.82	20.3/-	20.1	4.1 ^{b)}	-	-/-	0.3	0.56	2.4	-

^{b)}No measurements available, ^{c)}No images available, ^{d)}Very poor image quality, ^{e)}The projectile is destroyed during impact, ^{f)}Projectile indentation, ^{g)}Projectile fragmentation, ^{h)}Projectile embedded in target, ⁱ⁾Too small to be measured accurately.

Table 8: Experimental details from penetration tests (continued).

Test #	v_i (m/s)	v_r (m/s)	v_{pl} (m/s)	m_p (g)	m_{pl} (g)	P.O.I. (mm)	ϕ_0 (°)	α_0 / β_0	w_{max} (mm)	d_{pl} / d_{rec} (mm)	h_{im} (mm)	h_c (mm)	h_{pl} (mm)	d_{pp}/d_{pmax} (mm)	ΔD (mm)	ΔL (mm)	ΔR_c (-)	t_f (s)
25-5	411.4	⁶⁾	-	196.8	-	6.0L/5.0U	0.13	1.7D	⁸⁾	-	25.1	-	-	-/-	-	-	-	-
25-4	388.0	⁷⁾	-	196.9	-	3.2L/1.2D	0.06	1.0D	⁸⁾	-	25.2	¹⁾	-	-/-	-	-	-	-
25-6	386.8	⁶⁾	-	197.0	-	3.0L/0.5D	0.29	0.1D	⁸⁾	-	25.0	-	-	-/-	-	-	-	-
25-2	362.7	⁷⁾	-	196.6	-	6.0R/1.0U	0.47	1.3D	⁸⁾	-	25.1	17.3 ⁵⁾	-	-/-	-	-	-	-
25-1	356.5	⁷⁾	-	196.6	-	2.0L	0.27	0	⁸⁾	-	25.3	16.1 ⁵⁾	-	-/-	-	-	-	-
25-3	319.9	⁶⁾	-	197.0	-	4.0R/3.0U	0.14	1.0U	⁸⁾	-	25.1	-	-	-/-	-	-	-	-
30-3	450.0	⁶⁾	-	196.7	-	4.0U	0.18	0	⁸⁾	-	29.9	-	-	-/-	-	-	-	-
30-2	423.8	⁶⁾	-	196.7	-	1.0R	0.20	0	⁸⁾	-	30.0	-	-	-/-	-	-	-	-
30-5	400.9	⁶⁾	-	196.6	-	7.0L/6.0U	0.26	2.1D	⁸⁾	-	30.1	-	-	-/-	-	-	-	-
30-4	395.6	⁶⁾	-	196.7	-	3.0R/2.0D	0.11	0.8D	⁸⁾	-	30.1	-	-	-/-	-	-	-	-
30-1	353.2	⁶⁾	-	196.6	-	1.0L/1.0U	0.19	0.9D	⁸⁾	-	30.1	10.1 ⁵⁾	-	-/-	-	-	-	-

¹⁾ No measurements available, ²⁾ No images available, ³⁾ Very poor image quality, ⁴⁾ The projectile is destroyed during impact, ⁵⁾ Projectile indentation, ⁶⁾ Projectile fragmentation, ⁷⁾ Projectile embedded in target, ⁸⁾ Too small to be measured accurately.

